M.G. Aguilera Chaves

Numerical modelling of flow depths and velocities at the crest of a rubble mound breakwater using OpenFOAM®

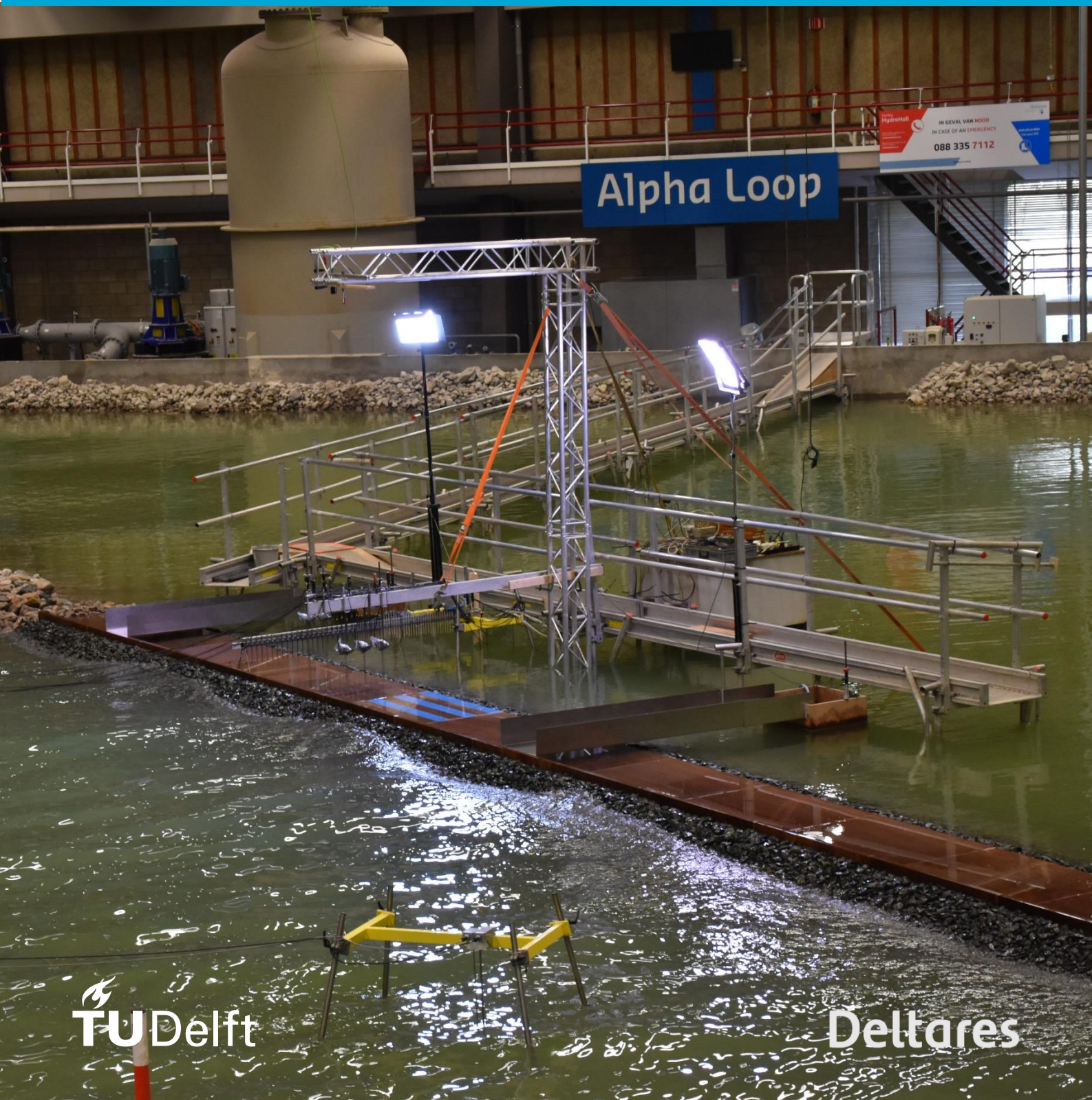

TU Delft

Deltares

Numerical modelling of flow depths and velocities at the crest of a rubble mound breakwater using OpenFOAM®

By

M.G. Aguilera Chaves
(5459826)

in partial fulfilment of the requirements for the degree of

Master of Science
in Civil Engineering

at the Delft University of Technology,
to be defended publicly on Monday, September 25th, 2023 at 15:00 hrs.

Thesis committee: Prof. dr. ir. Marcel R.A. van Gent (TU Delft & Deltares)
Dr. ir. Patricia Mares Nasarre (TU Delft)
Ir. Menno P. de Ridder (Deltares)

TU Delft

Deltares

Preface

This research project marks the end of my master studies in Civil Engineering at the Delft University of Technology. A journey that started much earlier, in 2017, when I set coming to study to this university as one of my life goals. At that moment (2017), just a few months after finishing my bachelor studies at the University of Costa Rica, my dream seemed almost unachievable (due to monetary constraints). However, time was kind to me, and in 2021, I was awarded the Justus and Louise van Effen Excellence Scholarship. I will forever be thankful to the Justus and Louise van Effen Foundation for giving me the opportunity to follow the high level of education at the Delft University of Technology. I hope to pay it forward in the future.

I express my sincerest thanks to my thesis committee. Starting with my Chair, Marcel van Gent, for giving me a warm welcome from the moment I showed interest in carrying out my thesis on the subject of breakwaters. I appreciate him for building the founding pillars of this challenging project, and for the insightful feedback throughout. Also, I owe a great debt of gratitude to Menno de Ridder for all the support he offered me during our weekly meetings. His expertise in numerical modelling in OpenFOAM®, and his overview of the project guided me to take the right steps towards the successful completion of this thesis. In addition, I am profoundly grateful to Patricia Mares Nasarre for her assistance during the development of this research. Her keen attention to details contributed immensely to improve the quality of the final product.

My thesis was executed in collaboration with the Coastal Structures and Waves (CSW) department at Deltares. Deltares provided me with the resources, tools, and a great work environment which enabled me to realize this project. From CSW, I am especially thankful to Marisol Irías Mata and Joost den Bieman for taking the time to answer my questions regarding numerical modelling in OpenFOAM® and physical model experiments with rubble mound breakwaters.

I would also like to thank my family and friends for all their support during the whole duration of the master program. Their encouragement made the start of my life in the Netherlands much easier. Over the past two years they have been my infinite source of joy and precious moments, and reminders that I have to believe in myself. I am forever indebted.

M.G. Aguilera Chaves
Delft, September 14th, 2023

Abstract

Climate change is increasing pressure on shallow coastal waters. In these regions, breakwaters are built to alter the sediment transport, or protect threatened habitats and port facilities. The rising sea level and its effect on wave heights is causing more water to overtop these structures. Increasing amounts of overtopping discharge can compromise the security of people, machinery or equipment located at the crest of the breakwaters. The overtopping flow causes a peak force that drives an instability on these subjects. The overtopping flow, meaning the flow depths and velocities, depends on the hydrodynamic conditions and structure geometry. Up to date, there is limited data that characterize these flow depths and velocities for a wide range of wave conditions and breakwater configurations. In principle, it is possible to perform physical model tests to fill this gap. Nevertheless, many tests would be required to cover several possible wave conditions and breakwater geometries. Physical model tests are known to be expensive and time-consuming. Furthermore, extracting the flow depths and velocities from experiments is complex and most intrusive measuring instruments can alter the flow. An alternative or addition to physical model experiments is the use of numerical models. In this research, a numerical model based in OpenFOAM® is used to evaluate the effects of different wave conditions and protrusion heights on the flow depths and velocities occurring during wave overtopping events at rubble mound breakwaters.

The numerical model was validated with physical model tests performed on a rubble mound breakwater with two configurations: 1) with a crest wall and with a berm, and 2) with a crest wall and without a berm. Overall, the numerical model simulated the incident waves accurately, but overestimated the mean overtopping discharge. The overprediction of the overtopping discharge and the different methodologies of computation of the flow velocities made it difficult to validate the overtopping flow. However, the numerical model was still valuable to study the physical processes occurring during overtopping events, and the trends on the modelled flow depths and velocities when changing the wave conditions and protrusion heights.

From sensitivity analyses carried out to extract the flow depths and velocities from the numerical model, it was found that wave gauges and probes can be used. They were placed along (and over) the crest. Care has to be taken with respect to where to place the lower tip of the wave gauges on the horizontal part of the crest wall. Other methods to compute the flow velocities are considered not to be reliable. For the specific set-up of the numerical model, it was found that the most extreme events impact the horizontal part of the crest wall in between the measuring devices. Therefore, for some of the measuring instruments, the flow depths and velocities are extracted when the events are still in the air or at the moment of collision with the crest (e.g., Figure 1a). In these cases, the trends had a different behavior than the expected one once the events are propagating attached to (and along) the horizontal part of the crest wall. One of the processes that caused the differences in the trends under these circumstances, was a return flow (flow in the seaward direction) that happened after the moment of impact against the horizontal part of the crest wall (see Figure 2). To the author's knowledge, this is the first time that this process has been observed during wave overtopping events on rubble mound breakwaters with a crest wall. More detailed analysis and future validation is required for the extreme events, as well as for the mentioned return flow.

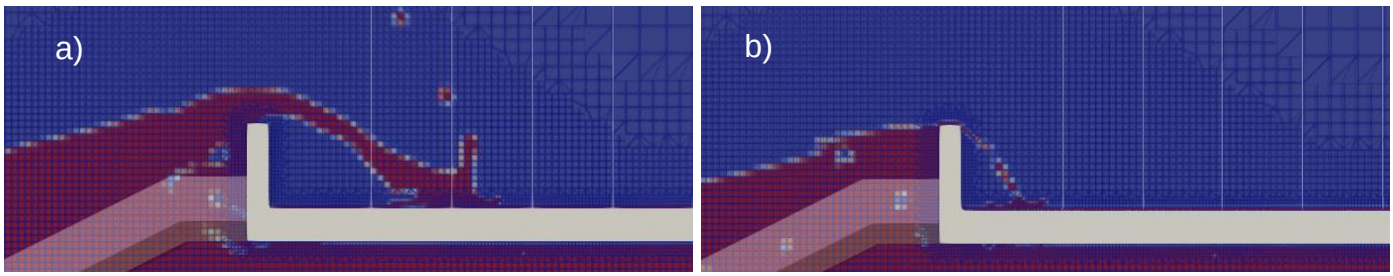

Figure 1. Impact of an event against the crest a) in between and b) before the measuring devices. The white lines show the horizontal locations of the measuring instruments.

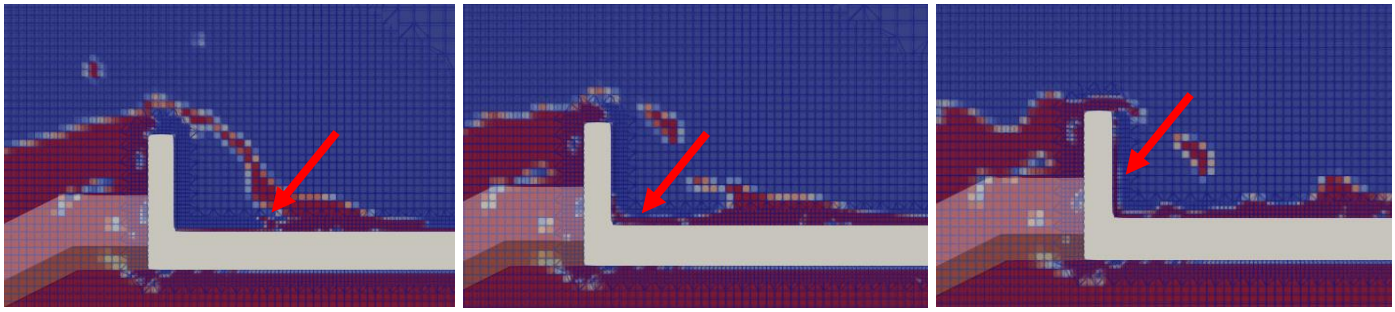

Figure 2. Flow in the seaward direction after the collision of the event with the crest.

Events associated to high exceedance probabilities showed trends aligned with the expected tendencies (for events that are propagating attached to and along the crest). This is because, these events were produced by smaller wave heights. Hence, the overtopping events collided with the horizontal part of the crest wall before the first measuring devices (e.g., Figure 1b). For these events with high exceedance probabilities, it was observed that the flow depths and velocities increased the larger the significant wave height and the lower the wave steepness. Also, the flow depths and velocities decreased the longer the distance was with respect to the seaward boundary. In addition, for a smaller protrusion height, more events were captured, and their flow depths and velocities were larger.

Some drawbacks in the application of the numerical model were identified. Nevertheless, it is still possible to improve the model. After that, the numerical model can become a powerful tool in combination with physical model tests when it comes to the evaluation of risk caused by climate change on new and existing coastal structures.

Contents

1. Introduction 17
1.1. Relevance 17
1.2. Rubble mound breakwaters background 18
1.3. Research outline 20
1.3.1. Research Objective 20
1.3.2. Research Questions 20
1.4. Literature review 21
1.5. Reading guide 25
2. Methodology 26
2.1. Description of physical model tests 26
2.2. Description of the numerical model set-up 31
2.2.1. Applied hydrodynamic model 31
2.2.2. General configuration of the numerical flume 31
2.2.3. Mesh 32
2.2.4. Wave generation and absorption 34
2.2.5. Boundary conditions 35
2.2.6. Turbulence model 36
2.2.7. Measurement of surface elevation 36
2.2.8. Measurement of overtopping discharges 37
2.2.9. Flow depths and velocities output request 37
2.2.10. Overview of changes in the numerical model 42
2.3. Goodness of fit measures used to validate the numerical model 44
2.4. Description of additional simulations to investigate the influence of two parameters on the computed flow depths and velocities 44
2.4.1. Simulations to study the impact of changing wave conditions 44
2.4.2. Simulations to study the effect of varying protrusion height 45
2.5. Determination of individual extreme events 46
3. Preferred method of extraction of flow depths and velocities 48
3.1. Flow depths 48
3.2. Flow velocities 49
4. Validation of the numerical model 52
4.1. Incident waves 52
4.2. Wave overtopping discharge 53
4.3. Validation of the flow depths and velocities 54
5. Influence of two parameters on the modelled flow depths and velocities 56
5.1. Observed physical processes 56
5.2. Variations in the wave conditions 60
5.2.1. Influence of the wave conditions on the flow depths 60
5.2.2. Influence of the wave conditions on the flow velocities 64

5.3. Variations in the protrusion height 67
6. Discussion of results 73
7. Conclusions and recommendations 76
7.1. Conclusions 76
7.1.1. Optimal method of extraction of the flow depths and velocities at the crest of a rubble mound breakwater using OpenFOAM® 76
7.1.2. Accuracy of flow depths and velocities, modelled with OpenFOAM®, at the crest of a rubble mound breakwater 76
7.1.3. Physical processes occurring during the wave overtopping events 77
7.1.4. Effects of changing the wave conditions and protrusion height on the flow depths and velocities at the crest of a rubble mound breakwater 77
7.2. Recommendations 78
8. References 80

A. Description of the porosity model used to model the wave-structure interaction in OpenFOAM® 84
B. Grid sensitivity analysis for wave propagation 86
C. Extraction of flow depths and flow velocities from the numerical flume 94
C.1. Mass continuity 94
C.2. Flow depths 95
C.3. Flow velocities 105
C.3.1. Method 1: Discharge sheets and wave gauges 105
C.3.2. Method 2: Probes 108
C.3.3. Method 3: Planes 108
C.4. Grid sensitivity analysis for the computation of flow depths and velocities 111
D. Comparison between measured and computed wave energy spectra 117
E. Additional results concerning the numerical modelled flow depths and velocities 119
E.1. Incapability of the numerical model to resolve thin flow depths 119
E.2. Additional aspects regarding the computation of flow velocities 120
E.3. Consistency check in the flow depth and velocity timeseries 120
E.4. Observed trends from flow depth timeseries with and without protrusion 123
F. Modelled and measured flow depths and velocities 125

List of Figures

Figure 1. Impact of an event against the crest a) in between and b) before the measuring devices. The white lines show the horizontal locations of the measuring instruments. 6
Figure 2. Flow in the seaward direction after the collision of the event with the crest. 7
Figure 3. Standard rubble mound breakwater cross-sections. 19
Figure 4. Rubble mound breakwater with a crest wall (crest element) and a berm. 20
Figure 5. Model set-ups used for the validation of the numerical model. The top panel shows the cross-section with the crest wall and without the berm, and the lower panel shows the cross section with the crest wall and with the berm. 26
Figure 6. Layout of the physical model within the Delta Basin. GRSM01, GRSM02 and GRSM03 are the wave gauges used to compute the incident waves. The berm is shown in dashed lines in the cross-section presented in the upper right corner. 27
Figure 7. Equipment used to measure the average overtopping discharge. 28
Figure 8. Flow depths and velocities measuring devices. 29
Figure 9. Step gauge and layer thickness gauge set-up in 2DV. The dimensions and elevations are given in mm. 29
Figure 10. Final configuration of the numerical flume. The berm considered in the second configuration is presented in dashed lines. 32
Figure 11. Final mesh used in the numerical model. a) General view. b) Close-up of the mesh of 2 cm of thickness surrounding the crest element. 33
Figure 12. Variation of $\boldsymbol{\alpha R}(\mathbf{XR})$ at the inlet and outlet relaxation zones. 35
Figure 13. Boundary names. 35
Figure 14. Wave gauges used for the separation of incident and reflected waves. The blue wave gauge is placed at the same location as the physical wave gauge GRSM02. The red wave gauge is where the incident and reflected waves are computed. 36
Figure 15. Sheet used to capture the overtopping discharges during the simulations. 37
Figure 16. Numerical coordinates of the instruments and the start of the crest wall. Final configuration with individual measuring devices separated at 12 cm intervals. 38
Figure 17. Wave gauges used to capture the flow depths in the numerical flume. 39
Figure 18. Set-up of discharge sheets and wave gauges for the computation of depth-averaged flow velocities. The red lines indicate the wave gauges, and the gray surfaces represent the discharge sheets. 40
Figure 19. Probes used for the extraction of flow velocities. The mesh around the crest element is finer, which causes a shorter spacing between consecutive probes than in upper regions of the domain. Not all the probes placed in the 20 cm above the horizontal part of the crest wall are shown. 40
Figure 20. Set-up of planes to extract the flow velocities in the numerical flume. 42
Figure 21. Modifications in the protrusion height to evaluate its respective influence in the computed flow depths and velocities. 46
Figure 22. Procedure followed to identify individual events. The dashed lines indicate the start (red) and end (green) of each event. The red dots show the maximum per event. 47
Figure 23. Flow depths at the location x = 16.44 m and for the test Th00155. The lower tip of the wave gauges was located at a) the bottom, b) the top, c) and the middle of the horizontal component of the crest element. 49
Figure 24. Flow velocities obtained with the three proposed methods. 50
Figure 25. Depth-averaged flow velocities timeseries for the location x = 16.32 m with variations in the mesh around the crest element of the breakwater. 51
Figure 26. Comparisons of computed and measured non-dimensional mean overtopping discharges. Here H_{m0} corresponds to the target value of the experiments, but the mean overtopping discharge (q) is the measured one. 53
Figure 27. Evolution of one event after overtopping the breakwater with and without protrusion. Simulation with H_{m0} = 0.16 m and s_{op} = 0.015. The panels show the indicator function (it is red for water and blue for air). The black dots represent the probes located at 20 cm over the horizontal

component of the crest wall. The vertical white lines indicate the location of the wave gauges. The regions with less opacity show the armor and filter layers. 58
Figure 28. Vertical and horizontal velocities of an event while overtopping the breakwater with highest protrusion ($R_c – A_c$ = 0.08 m). Simulation with H_{m0} = 0.16 m and s_{op} = 0.015. The black dots represent the probes located at 20 cm over the crest. The vertical black lines indicate the wave gauges. The regions with less opacity show the armor and filter layers. 59
Figure 29. Vertical and horizontal velocities of an event while overtopping the breakwater without protrusion ($R_c – A_c$ = 0 m). Simulation with H_{m0} = 0.16 m and s_{op} = 0.015. The regions with less opacity show the armor and filter layers. 59
Figure 30. Event acceleration in the horizontal direction after the impact against the horizontal part of the crest element. Simulation with H_{m0} = 0.16 m and s_{op} = 0.015. a) largest protrusion ($R_c – A_c$ = 0.08 m), b) no protrusion ($R_c – A_c$ = 0 m). The black dots show the probes located at 20 cm over the horizontal part of the crest wall. The vertical black lines indicate the wave gauges. The less opaque regions present the armor and filter layers. 59
Figure 31. Flow depth exceedance curves for varying distances from the vertical part of the crest wall. The left panel shows the results for the simulation with H_{m0} = 0.08 m and s_{op} = 0.015, and the right panel for H_{m0} = 0.16 and s_{op} = 0.027. The curves were calculated in terms of the percentage of incoming waves. A line of 45 degrees indicates a Rayleigh distribution. 61
Figure 32. Flow depth exceedance curves for all simulated wave conditions at different positions from the vertical part of the crest wall. The curves were calculated in terms of the percentage of incoming waves. A line of 45 degrees indicates a Rayleigh distribution. 62
Figure 33. Flow depths exceeded by 2% of the incoming waves at different positions with respect to the vertical part of the crest wall. Results for all the wave conditions. 63
Figure 34. Example of situations when the events impact the horizontal part of the crest wall in between the measuring devices. The black lines indicate the position of the wave gauges and the black dots, the highest probes in the numerical flume. The regions with less opacity show the armor and filter layers. 63
Figure 35. Flow velocity exceedance curves for various places from the vertical part of the crest wall. The left panel shows the results for the simulation with H_{m0} = 0.08 m and s_{op} = 0.015, and the right panel for H_{m0} = 0.16 and s_{op} = 0.027. The curves were calculated in terms of the percentage of incoming waves. A line of 45 degrees indicates a Rayleigh distribution. 65
Figure 36. Flow velocity exceedance curves for all simulated wave conditions at different places with respect to the vertical part of the crest wall. The curves were calculated in terms of the percentage of incoming waves. A line of 45 degrees indicates a Rayleigh distribution. 66
Figure 37. Zoom in to the high exceedance probability part of the exceedance curves computed at various distances from the vertical component of the crest wall. The black rectangle encloses the region of interest. Simulation with H_{m0} = 0.12 m and s_{op} = 0.015. 67
Figure 38. Examples of situations when the flow depths and velocities are extracted when the events are in the air or at the moment of impact against the crest. The black lines indicate the position of the wave gauges and the black dots, the highest probes in the numerical flume. The less opaque regions show the armor and filter layers. 67
Figure 39. Flow depth exceedance curves for all simulated cases with H_{m0} = 0.16 m, with different wave steepness and protrusion heights. The curves were calculated in terms of the percentage of incoming waves. A line of 45 degrees indicates a Rayleigh distribution. 69
Figure 40. Flow velocity exceedance curves for all simulated cases with H_{m0} = 0.16 m, with different wave steepness and protrusion heights. The curves were calculated in terms of the percentage of incoming waves. A line of 45 degrees indicates a Rayleigh distribution. 70
Figure 41. Zoom in to the high exceedance probability part of the flow depth exceedance curves obtained for different protrusion heights and wave steepness. Results for every location with respect to the vertical part of the crest wall. 71
Figure 42. Zoom in to the high exceedance probability part of the flow velocity exceedance curves obtained for different protrusion heights and wave steepness. Results for every location with respect to the vertical part of the crest wall. 72

Figure 43. Example of entrapped air during wave propagation and impact with the vertical part of the crest wall. Simulation with H_{m0} = 0.16 m and s_{op} = 0.04. The regions with less opacity indicate the armor and filter layers. 73
Figure 44. Example of water spreading into several cells and converging into less cells. Simulation with H_{m0} = 0.16 m and s_{op} = 0.04. The vertical black lines and the black dots show the position of the wave gauges and the highest probes. The regions with less opacity indicate the armor and filter layers. 74

Figure B- 1. a) Numerical flume set-up to evaluate the influence of the grid on the wave propagation. b) Close-up of the area of refinement around the water surface. The coordinates are specified in meters. WG = wave gauge. 87
Figure B- 2. Effect of different grid sizes around the water level on the wave propagation. The circles represent the results of the test with the low wave height (Hm0 = 0.08 m) and low wave steepness (s_{op} = 0.015), and the triangles, the results of the test with the high wave height (Hm0 = 0.12) with high wave steepness (s_{op} = 0.040 m). The blue colors are obtained with a base mesh of 0.04 m x 0.04 m, and the green colors, with a base mesh of 0.06 m x 0.06 m. 88
Figure B- 3. Grid effect on a) the significant wave height along the flume computed with the total surface elevation, b) the wave spectrum of the incident waves, and c) the exceedance curve of the incident waves. BM = base mesh, MWL = mesh around the water level. 89
Figure B- 4. Additional changes to the numerical model to evaluate convergence in the wave propagation. a) Variation 1. b) Variation 2. c) Variation 3. d) Variation 4. e) Variation 5. 91
Figure B- 5. Effect of the additional variations of the numerical model on a) the significant wave height along the flume, b) the wave spectrum of the incident waves, and c) the exceedance curve of the incident waves. 93

Figure C- 1. Cumulative overtopped volume passing through all the discharge sheets. All the lines are plotted in black. 94
Figure C- 2. Set-up of wave gauges with their lower tip at the bottom part of the crest wall. 95
Figure C- 3. Surface elevation histogram for all wave gauges and computational time steps when the lower tip of the wave gauges is placed at 0.80 m. 96
Figure C- 4. Set-up of wave gauges with their lower tip at the upper part of the crest wall. 96
Figure C- 5. Surface elevation histogram for all wave gauges and computational time steps when the lower tip of the wave gauges is placed at 0.85 m. 97
Figure C- 6. Flow depth time series at x = 16.20 m (coordinates of the numerical flume) when the lower tip of the wave gauge is placed at the bottom edge (a) and upper edge (b) of the horizontal part of the crest element. 98
Figure C- 7. Output of the numerical flume for different moments in time. a) at 220 s, b) at 240 s, and c) at 260 s. The white plane indicates the wave gauge positioned at x = 16.20 m. 99
Figure C- 8. Flow depth time series at x = 16.48 m (coordinates of the numerical flume) when the lower tip of the wave gauge is placed at the bottom edge (a) and upper edge (b) of the horizontal part of the crest wall. 100
Figure C- 9. Output of the numerical flume for different instants. a) at 200 s, b) at 220 s, c) at 240 s, and d) at 260 s. The white plane indicates the location of the wave gauge at 16.48 m. 101
Figure C- 10. Configuration of wave gauges with their lower tip at the middle of the horizontal part of the crest wall. 101
Figure C- 11. Flow depth time series at x = 16.44 m (coordinates of the numerical flume) when the lower tip of the wave gauge is placed at the top (a) and at the middle (b) of the horizontal component of the crest wall. 102
Figure C- 12. Example of the method of extraction of the flow depths by the numerical wave gauges. Simulation with H_{m0} = 0.12 and s_{op} = 0.015. a) Instant t = 205.9 s when the flow depth of the overtopping event is being measured at the first wave gauge (x = 16.08 m). b) Flow depth timeseries around the same instant in time (t = 205.9 s). 103

Figure C- 13. Cumulative overtopping discharge when: a) the discharge sheets were defined starting at 0.85 m, b) the discharge sheets were defined starting at 0.80 m. All the lines are plotted in black. 104
Figure C- 14. Configuration of the numerical flume with an impermeable breakwater (test with ID Th00402d). The gray and red regions indicate the relaxation zones..... 105
Figure C- 15. Depth-averaged flow velocities obtained with discharge sheets and wave gauges at the locations a) x = 16.32 m, and b) x = 16.56 m. 106
Figure C- 16. Flow depth histogram for all computational timesteps and all the wave gauges. ... 107
Figure C- 17. Histogram of the difference in timesteps at which the flow depths and discharges are extracted. 108
Figure C- 18. Depth-averaged flow velocities obtained with the probes and planes at the locations a) x = 16.20 m, and b) x = 16.68 m. 109
Figure C- 19. Maximum depth-averaged flow velocities at each location and for all computational timesteps. The distance is giving with respect to the intersection in between the crest and the seaward slope (x = 15.69 m, in numerical coordinates). 110
Figure C- 20. Variations in the mesh around the crest for the grid sensitivity analysis. Case with a) original finest mesh with grid cells of $\Delta x = \Delta y = 0.005$ m and thickness of 2 cm, b) original finest mesh with 20 cm of thickness, c) finest mesh removed. 112
Figure C- 21. Numerical flume set-up to perform the grid sensitivity analysis around the crest. The gray and red regions represent the relaxation zones. The lengths indicated as shorter refer to the corresponding lengths of the original set-up for the test Th00402d..... 112
Figure C- 22. Depth-averaged flow velocities timeseries for the location x = 16.32 m with variations in the mesh around the crest of the breakwater. 113
Figure C- 23. Maximum depth-averaged flow velocities at each location and for all computational timesteps. A bit more than 250 waves were considered. The distance is given with respect to the intersection between the seaward slope and the crest (x = 15.69 m). 114
Figure C- 24. Flow depths timeseries for the location x = 16.32 m with variations in the mesh around the crest of the breakwater..... 115
Figure C- 25. Maximum flow depths at each location and for all computational timesteps. A bit more than 250 waves were considered. The distance is given with respect to the intersection between the seaward slope and the crest (x = 15.69 m). 116

Figure D- 1. Comparison of measured and computed wave energy spectra associated to the breakwater configuration without the berm. The ID of the tests is indicated above each plot. 117
Figure D- 2. Comparison of measured and computed wave energy spectra associated to the breakwater configuration with the berm. The ID of the tests is indicated above each plot. 118

Figure E- 1. Flow depth timeseries at different locations with respect to the vertical component of the crest wall. Case with H_{m0} = 0.08 and s_{op} = 0.027. The timeseries at x = 16.08 m is not shown. .. 119
Figure E- 2. Example of non-physical droplet. Simulation with H_{m0} = 0.16 m and s_{op} = 0.015. The regions with less opacity indicate the armor and filter layers..... 120
Figure E- 3. Example of high air flow velocities. Simulation with H_{m0} = 0.16 m and s_{op} = 0.04. The black lines and the black dots show the position of the wave gauges and highest probes. The regions with less opacity indicate the armor and filter layers. 120
Figure E- 4. Comparison between the discharge, flow depth and velocity timeseries for the simulation with H_{m0} = 0.08 m and s_{op} = 0.015. 121
Figure E- 5. Comparison between the flow depth and flow velocity timeseries for the simulation with H_{m0} = 0.16 m and s_{op} = 0.015. The peak flow depths and velocities are highlighted with vertical lines, in red and green, respectively. 122
Figure E- 6. 100 seconds of the flow depth timeseries of the simulation performed with H_{m0} = 0.16 m and s_{op} = 0.015, with and without protrusion, R_c-A_c = 0 m, and 0.08 m, respectively. 124

Figure F- 1. Comparison of exceedance curves obtained from the measured and simulated flow depths (left panels). The right panels show a zoom in to the exceedance curves computed from the

measurements. The labels indicate the distance with respect to the vertical part of the crest wall. 127
Figure F- 2. Comparison of exceedance curves obtained from the measured and simulated flow depths (left panels). The right panels show a zoom in to the exceedance curves computed from the measurements. The labels indicate the distance with respect to the vertical part of the crest wall. 128
Figure F- 3. Comparison of exceedance curves obtained from the measured and simulated flow velocities (left panels). The right panels show a zoom in to the exceedance curves computed from the results of the numerical model. The labels indicate the distance with respect to the vertical part of the crest wall. 130
Figure F- 4. Comparison of exceedance curves obtained from the measured and simulated flow velocities (left panels). The right panels show a zoom in to the exceedance curves computed from the results of the numerical model. The labels indicate the distance with respect to the vertical part of the crest wall. 131

List of Tables

Table 1. Tests used for validation of computed incident waves and overtopping discharges. 30
Table 2. Tests used for validation of computed flow depths and velocities. 30
Table 3. Mesh resolution for different regions. 33
Table 4. Cases related to the variation in the wave conditions..... 45
Table 5. Cases related to the variations in the protrusion height..... 45
Table 6. Comparison of measured and computed spectral parameters. 52

List of symbols

- α: slope angle of the structure [°].
- α_F: coefficient in expression for a [-].
- α_R: Relaxation function in the relaxation zone [-].
- β: Angle of wave attack [°].
- β_F: coefficient in expression for b [-].
- γ_b: factor to account for berm influence in the expression to calculate the mean overtopping discharge [-].
- γ_f: factor to account for the influence of roughness in the equation to estimate the mean overtopping discharge [-].
- γ_p: factor to account for influence of the recurved parapet in the equation to estimate the mean overtopping discharge [-].
- γ_β: factor to account for influence of oblique waves in the expression to estimate the mean overtopping discharge [-].
- γ_v: factor to account for influence of the crest wall in the formula to calculate the mean overtopping discharge [-].
- $\mathcal{E}$: Used to indicate an overtopping discharge sheet in the expression that calculates flux of water through this element in OpenFOAM® [-].
- Δx: Grid size in the horizontal direction [m].
- Δy: Grid size in the vertical direction [m].
- ϕ_F: Flux of water cross a face [m^3/s].
- μ: Dynamic molecular viscosity [kg/m/s].
- ρ: Density of the fluid [kg/m^3].
- ∇: Divergence operator, $\nabla = \frac{\partial}{\partial x} + \frac{\partial}{\partial y} + \frac{\partial}{\partial z}$.
- a: Resistance coefficient in the Darcy-Forchheimer equation [s/m].
- A_c: Crest level of the armor with respect to the still water level [m].
- b: Resistance coefficient in the Darcy-Forchheimer equation [s^2/m^2].
- B: Berm width in the seaward slope of the structure [m].
- B_L: Vertical distance measured from the level of the armour at the crest to the berm level [m].
- C_m: Added mass coefficient that accounts for the transient interaction between the grains and the water [-].
- d: Water depth [m].
- D_{50}: Median diameter of the stones [m].
- D_{n50}: Nominal median diameter of the stones [m].
- f: Representation of cell faces in expression used to estimate the flux of water through an overtopping discharge sheet in OpenFOAM® [-].
- F: Indicator function of the VOF method.
- F_p: Friction and pressure forces the porous media exerts on the flow [N].
- g: Acceleration due to gravity [m/s^2].
- h_c: Flow depth at the breakwater crest during wave overtopping events [m].
- $h_{c2\%}$: Flow depth exceeded by 2% of the incoming waves [m].
- H_{m0}: Incident spectral significant wave height, $H_{m0} = 4\sqrt{m_0}$ [m].
- KC: Keulegen-Carpenter number that considers the effect of the oscillatory flow in the Darcy-Forchheimer equation [-].
- L_{0p}: deep-water wave length [m].
- n: porosity [-].
- p*: excess pressure [Pa].
- q: mean overtopping discharge [$m^3/s/m$].

- Q: non-dimensional mean overtopping discharge [-].
- R_c: freeboard (including the height of the crest wall, if present) relative to the still water level [m].
- S_f: Non-unit normal vector to the cell faces used in the expression to estimate the flux of water through an overtopping discharge sheet in OpenFOAM® [-].
- $s_{m-1,0}$: wave steepness based on the wave height H_{m0} and the wave period $T_{m-1,0}$ [-].
- s_{op}: Fictitious wave steepness. Wave steepness based on the wave height H_{m0} and the peak period T_p [-].
- t: time [s].
- $T_{m-1,0}$: spectral wave period based on the ratio of the spectral moments m_{-1} and m_0 of the incident wave spectrum [s].
- T_p: Peak period [s].
- u: Velocity field in Cartesian coordinates (u = u, v, w) [m/s].
- u_c: Flow velocity at the breakwater crest during wave overtopping events [m/s].
- $u_{c2\%}$: Flow velocity exceeded by 2% of the incoming waves [m/s].
- u_f: Filter velocity vector in Cartesian coordinates [m/s].
- u_m: Maximum oscillating velocity [m/s]
- x: Cartesian coordinate vector (x,y,z) [m].

1. Introduction

1.1. Relevance

Coastal Engineering is a field of Civil Engineering that focuses on the study of the processes that occur in the coastal zone. Based on the understanding of these dynamics, solutions are proposed to protect the natural and built environments, located in the coasts, against flooding and erosion. The type of measure to be executed depends on the vulnerability level and the land use, therefore, on the social, economic, and cultural value of the coast and the amount of available budget (Bosboom and Stive, 2022). The protections can be classified in soft vs hard, and temporal vs permanent ones. Soft measures are characterized for allowing the natural processes to continue, for example, sand nourishments or sediment bypass systems. Examples of hard measures are series of groins, series of breakwaters, submerged breakwaters, revetments, seawalls and sea dikes. They can decrease the rate of sediment erosion or completely prevent it, in the alongshore or cross-shore directions of the coast.

Concerning the breakwaters, some of them have the function of changing the longshore transport rates under normal and extreme conditions. This is the case of the shore-normal breakwaters or the shore parallel offshore emerged and submerged breakwaters (Bosboom and Stive, 2022). There are breakwaters which purpose is to protect habitats threatened by sea forces (Van den Bos and Verhagen, 2018). A common use of breakwaters is to provide shelter at port entrances and access channels. There, they are constructed to counteract sedimentation, decrease the currents, and reduce the wave action behind them. Hence, they offer suitable conditions for maneuverability of vessels, safe port operations, and reduced downtime.

Breakwaters are designed to prevent any failure mechanism during their lifetime. In this context, failure happens when the structure is no longer capable of fulfilling its function. In the past, many design formulas have been obtained based on physical models. Nevertheless, their range of applicability is limited to the breakwater configuration and hydrodynamic conditions that were tested (specific wave and water level conditions). When a more complex breakwater geometry is proposed, usually additional laboratory tests must be performed to evaluate its capability to withstand the design conditions, under the specific project circumstances. However, there are situations in which executing physical model tests is not possible either by limitations in time or budget. In this case, it is attractive to apply numerical tools to verify the new design. Even so, numerical models need to be validated with physical model tests, but once the validation is successful, these tools can be utilized to study other configurations that were not tested in the experiments. Nowadays, the use of numerical models is possible due to the increase in computer power. Numerical modelling offers other opportunities that are not available when performing physical model tests, for example, the possibility to carry out parallel computations, which allow getting faster results. In addition, the positioning of numerical measuring devices does not distort the flow, and there is no limitation in the number of measuring instruments that can be located in the numerical domain. It is also feasible to obtain output of solution variables from the entire numerical domain, for a specific moment in time, if needed.

Traditionally, the crest level of a breakwater is designed based on the mean overtopping discharge. This is the total volume of water discharged over the structure during the entire storm duration per unit of width, q ($m^3/s/m$). However, the overtopping discharge is distributed unevenly during the duration of a storm. In one large wave, a considerable volume can pass over the crest of the breakwater[1]. These extreme events can compromise the safety of the people, traffic or equipment positioned at the crest of the breakwater. In this context, the aim of the breakwater is to provide shelter to the port facilities behind, prevent fatalities and diminish material loses.

[1] Franco et al. (1994) suggested that the overtopping volumes per individual wave were a better hydraulic parameter than the mean overtopping discharge for the evaluation of damage on the crest of a breakwater.

Safety in the region protected by the breakwater can be assessed by computing the flow depths and velocities during the overtopping events and determining if their magnitude compromises the stability of the people or equipment located on the structure. Such approach has been carried out by some researchers in recent years. For example, Bae et al. (2016) and Sandoval et al. (2017) defined instability thresholds for pedestrians subjected to overtopping flow based on the product of the flow velocity and flow depth. Also, Cao et al. (2022) proposed a probabilistic model to estimate the probability of instability of a pedestrian during his/her visit to a coastal structure due to an overtopping event.

When overtopping becomes dangerous, its reduction can be achieved by rising the crest level, but also by adding a berm on the seaward slope of the structure, or by constructing a crest wall. Testing different breakwater configurations (i.e., changing the crest level, adding a crest wall or a berm) with a numerical model is faster and cheaper than with physical model tests. The effect of these changes can be analyzed to identify their impact on the overtopping discharge and associated flow depths and velocities at the crest of the breakwater. This way, an optimum can be found between acceptable damage and initial investment. Numerical models can also be helpful when analyzing the compliance of existing infrastructure with new safety levels, and test adaptations if necessary. This is particularly useful now that shallow coastal zones are suffering increasing pressure due to climate change, and heavier loading (higher waves and water level) is expected due to sea level rise.

1.2. Rubble mound breakwaters background

A rubble mound breakwater is a conventional type[2] of breakwater characterized by presenting a flexible structure. This flexibility is achieved due to its composition of heaps of loose elements. A typical cross-section of a rubble mound breakwater consists of an armor layer, a filter layer, a core, and a toe berm. Figure 3 presents some standard rubble mound breakwater cross-sections. The main changes between these cross-sections are concentrated on the slope at the rear side, depending on the degree of overtopping and transmission[3].

The armor layer can be composed of concrete units or quarry stone. Its elements are the largest in size in the whole structure since the armor must withstand the wave attack during the design conditions. The filter layer is directly placed under the armor layer. These elements are designed not to pass through the voids of the armor layer. In occasions, more than one filter layer is necessary. Below the filter layer, the core is located. This is the part of the breakwater with the largest amount of material. “Quarry run” is commonly employed for its construction. The toe berm is the component that provides the lower support to the armor layer (Van den Bos and Verhagen, 2018).

Other elements that are added to the cross-sections of rubble mound breakwaters are berms and crest walls. It has been shown that these components can have an effect on the average overtopping discharge (see Van Gent et al., 2022) which is advantageous as possible solutions to the negative impacts of sea level rise. The crest wall reduces the overtopping discharge only when it is added on top of a breakwater, increasing the crest elevation (Van Gent et al., 2022) but not compared to a rubble mound breakwater without a crest wall that have the same total crest elevation. Figure 4 shows a rubble mound breakwater with a crest wall and a berm. In this case, the berm is an adaptation measure to an existing breakwater to compensate for sea level rise. In occasions, a recurved parapet is added to the top of the crest wall to further reduce overtopping. This last element is not investigated in the present research.

[2] The other conventional type of breakwater are the monolithic/vertical breakwaters. The main difference they have with respect to rubble mound breakwaters is that their cross-section behaves as one solid block. Some examples include caissons, a block wall, or a masonry structure (Van den Bos and Verhagen, 2018).
[3] Wave transmission is the phenomenon which creates a reduced wave action in the structure slope at the rear side due to wave energy passing over and through the breakwater (Van den Bos and Verhagen, 2018).

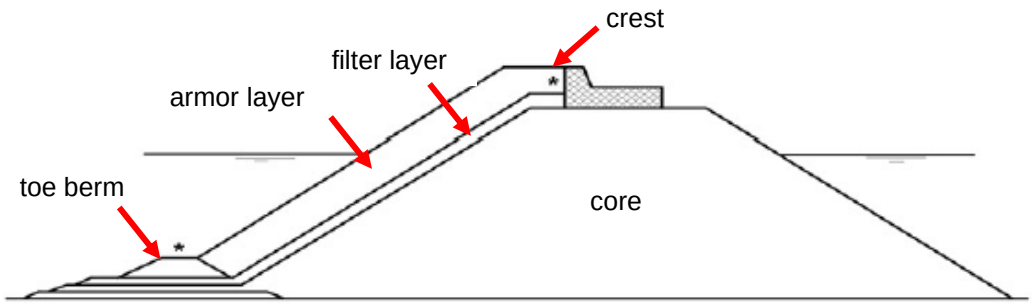

(a) Rubble mound breakwater – light overtopping (with cap block)

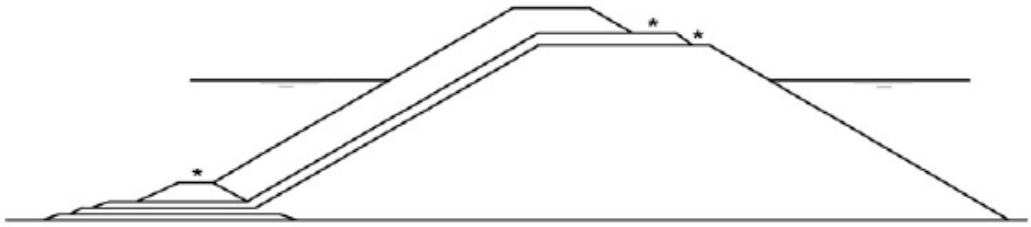

(b) Rubble mound breakwater - light overtopping

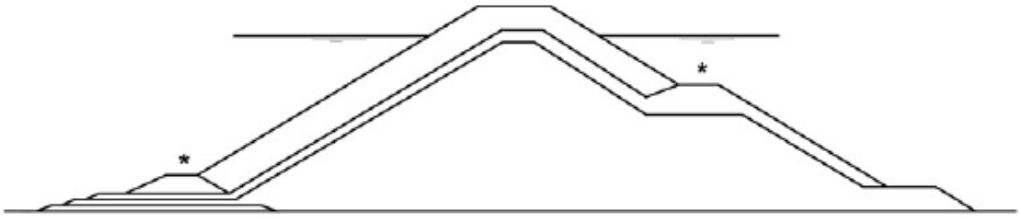

(c) Rubble mound breakwater - moderate overtopping

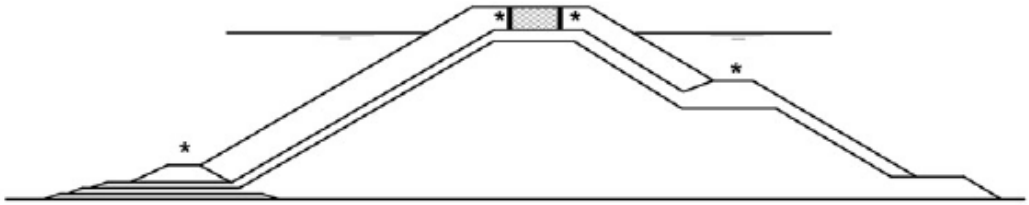

(d) Rubble mound breakwater - moderate overtopping (with cap block)

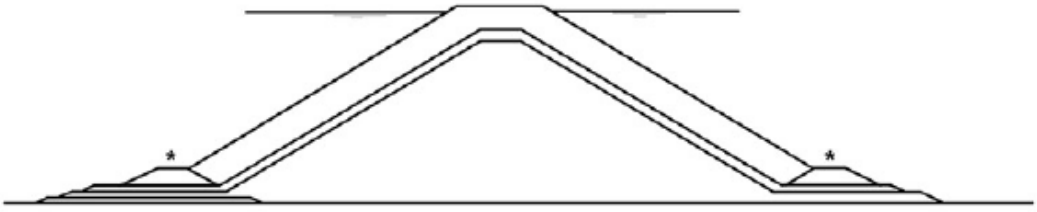

(e) Rubble mound breakwater - severe overtopping

Figure 3. Standard rubble mound breakwater cross-sections.

Source: Van den Bos and Verhagen (2018)

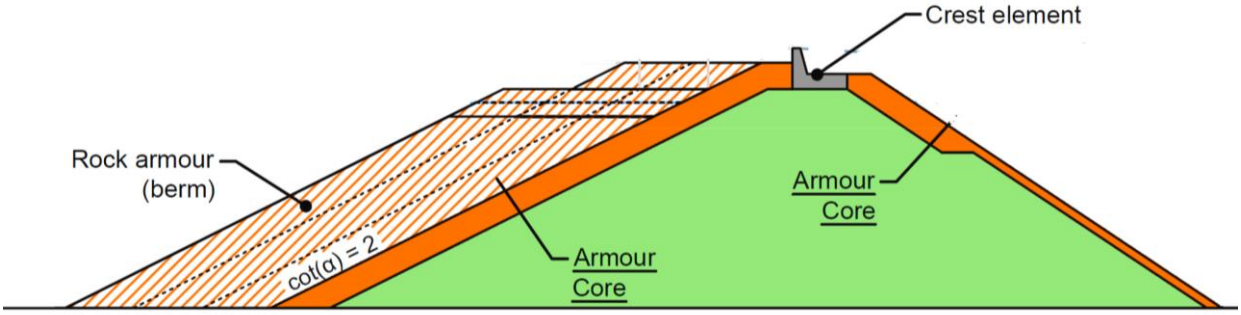

Figure 4. Rubble mound breakwater with a crest wall (crest element) and a berm.

Source: Van Gent et al. (2022)

1.3. Research outline

The pressure caused by sea level rise on shallow coastal waters requires finding fast, efficient, and cheap methods to evaluate the risk imposed on the people, or equipment at the crest of the breakwater during wave overtopping events. A numerical model can help to fill this gap. In this view, the following outline is proposed for the present research:

1.3.1. Research Objective

Investigate, with the application of an OpenFOAM® numerical model, how different rubble mound breakwater[4] configurations and hydrodynamic conditions affect the flow depths and velocities at the crest of the structure during wave overtopping events.

1.3.2. Research Questions

To achieve the previous defined objective, various research questions have been proposed. They consist of a main question, which is further divided into a series of sub-questions, which together form a step-by-step guide for this research.

Central Question

How do different rubble mound breakwater configurations and hydrodynamic conditions affect the flow depths and velocities, modelled with OpenFOAM®, at the crest of the structure under wave overtopping events?

Sub-questions

1. What is the optimal methodology to extract the flow depths and velocities at the crest of a rubble mound breakwater using OpenFOAM®?
2. How accurate is OpenFOAM® in reproducing flow depths and velocities occurring at the crest of a rubble mound breakwater?
3. What are the physical processes occurring during wave overtopping events?
4. What are the effects of changing the wave steepness and significant wave height on the flow depths and velocities at the crest of a rubble mound breakwater?
5. How do different protrusion heights affect the flow depths and velocities at the crest of a rubble mound breakwater?

[4] The scope of this research is limited to non-reshaping rubble mound breakwaters. Any configuration with a berm treated in this document refers to a set-up with a statically stable berm.

1.4. Literature review

In this section, the relevant literature related to the objective of study of this research is presented.

Over the last years, the increased computational resources have allowed numerical modelling to become an attractive alternative in simulating wave-structure interactions. These tools are known as Computational Fluid Dynamics models. They employ numerical schemes and different solver techniques to simulate schematizations involving fluid flows. These models are based on simplifications of the Navier-Stokes equations. Nowadays, it is not practical to solve the Navier-Stokes equations, which considers all the turbulence scales, directly with the current capacity of computers.

Nonlinear Shallow Water equations (NLSW) models have been used, in a depth-averaged form, to compute wave propagation and interaction with permeable coastal structures (see Kobayashi and Wurjanto, 1989; Wurjanto and Kobayashi, 1993; Van Gent, 1994; and Van Gent, 1995a), and impermeable coastal structures (see for instance Shiach et al., 2004; Tuan and Oumeraci, 2010). They can simulate wave trains of 1,000 waves rapidly (Losada et al., 2008), which makes them computationally efficient. Nevertheless, they assume hydrostatic pressure, which implies that vertical accelerations are neglected, and vertical velocities are small. This limits the capacity to accurately describe wave interaction with coastal structures with overtopped crest walls and to compute heavy wave impacts on vertical walls (Tuan and Oumeraci, 2010). Other restrictions of these models are that the offshore boundary condition of the numerical model has to be located close to the structure to satisfy the shallow water limit, the introduction of semi-empirical methods to simulate wave breaking, and modeling of porous flow, and the difficulty of simulating complicated free surfaces, like overturning waves (Losada et al., 2008). Models have also been developed to consider the non-hydrostatic pressure in the NLSW. This is the case of SWASH (Zijlema et al., 2011). It has been used to compute wave overtopping over impermeable structures with a very shallow foreshore (Suzuki et al., 2017). It has been proven to reproduce mean overtopping discharges with a good accuracy, and instantaneous wave overtopping when incident wave time series are correctly reproduced. Nonetheless, it is still a depth integrated model.

Models based on simplified versions of the Navier-Stokes equations[5] have been used in combination with free surface tracking techniques. Two of these techniques are the Volume of Fluid method (VOF), which is Eulerian; and the Smooth Particle Hydrodynamic method (SPH), which is Lagrangian (Suzuki et al., 2017). Both methods are capable of tracking large free surface deformations accurately, but the VOF techniques are more computational efficient than the SPH models (Losada et al., 2008). Even though the volume of fluid method is more computational expensive than models based on the NLSW equations, the free surface can attain arbitrarily complex geometries. For example, this framework can handle overturning waves and slamming forces on structures (Jacobsen et al., 2015), which makes it advantageous for the purposes of study of this research.

Several models based on simplifications of the Navier-Stokes equations, which make use of the VOF approach to model the free surface, have been developed to simulate wave interactions with porous media (including coastal structures). The first one was implemented by Van Gent et al. (1994), followed by other developments such as COBRAS (Liu et al., 1999; Hsu et al., 2002; Lin and Karunarathna, 2007), IH-3VOF (Del Jesus et al., 2012; Lara et al., 2012), ComFlow (Wellens et al., 2010), and FLOW-3D (Vanneste and Troch, 2015). Other recent numerical model contributions for coastal engineering problems have been implemented in OpenFOAM®, they are the ones by Higuera et al. (2013a, 2013b, 2014) (IHFOAM) and Jensen et al. (2014) (waves2foam).

[5] An example corresponds to the Reynolds Averaged Navier-Stokes equations (RANS).

OpenFOAM®, originally developed by Weller et al. (1998), is a Reynolds Averaged Navier-Stokes (RANS) model which applies the VOF technique to track the free surface. It is a two-phase numerical tool (it resolves the flow for air and water), which consists of a finite volume approach with a collocated variable arrangement on generally unstructured grids. It is distributed under an open-source license which allows the user to have access to a series of helpful libraries and packages. One of these packages is the mentioned waves2Foam.

It has been shown that OpenFOAM® is able to model long time series of irregular waves of 500-1000 waves (Jacobsen et al., 2015). The capability of OpenFOAM® to accurately model wave propagation, transformation over a complex bathymetry, reflection in the presence of impermeable structures, and reflection and dampening with permeable structures has also been demonstrated (see Jacobsen et al., 2015).

Concerning overtopping modelling using OpenFOAM®, some studies can be found in literature where simulations were performed in simple coastal structures. Higuera et al. (2014) presents a 2D-3D hybrid methodology to model overtopping over a high-mound breakwater subjected to oblique irregular long-crested waves. However, only 110 seconds were simulated, which from a statistical point of view is not sufficient to analyze overtopping. Jensen et al. (2014) modelled wave overtopping under irregular waves for an impermeable smooth structure, and a rubble mound breakwater, both with a straight slope. They used their porosity model (explained in the same paper), and the relaxation zones technique (Jacobsen et al., 2012) for the generation and absorption of waves. Their numerical model proved to accurately estimate overtopping. Patil (2019) modelled wave overtopping events over a coastal dike with a shallow foreshore. In his thesis he integrated waves2Foam with the isoAdvection scheme developed by Roenby et al. (2016). He called this approach the waveFlow solver. He showed that the accuracy of the numerical overtopping predictions is improved when the sharp interface capture technique (waveFlow) is used instead of the original diffusive interface capture method (interFoam solver) included in OpenFOAM®. Even though a small underprediction in the overtopping values was found when waveFlow was used, the results were more in accordance with the experimental measurements. When interFoam was employed, overprediction in the overtopping discharges was observed, which can be attributed to the diffusive nature of the interface. In addition, the splashing phenomena of the overtopping events was better captured when the waveFlow solver was employed.

Regarding modelling of overtopping discharges on complex coastal structures, Chen et al. (2021) explored the capacity of OpenFOAM® to calculate the mean overtopping discharge at impermeable dikes with a berm and roughness elements at the seaward slope. Similar to the approach taken by Patil (2019), Chen et al. (2021) combined waves2Foam with the isoAdvection scheme developed by Roenby et al. (2016). In their work, they showed that the estimation of the mean overtopping discharge with OpenFOAM® is accurate for a smooth straight slope, slightly overestimated for a smooth bermed slope, and considerably overestimated for a slope with protruding elements. They attributed the excess of discharge to a numerical underestimation of the energy dissipation by OpenFOAM®. Nevertheless, they concluded that the overtopping estimation with OpenFOAM® for simple and complex dike structures was, at least, as accurate as the one obtained with empirical formulations. Chen et al. (2022) investigated the combined effect of oblique waves and a berm with varying width in the mean overtopping discharge at dikes. For this purpose, they set-up a 3D model in OpenFOAM®. The numerical results were analyzed qualitatively since the runtime of the simulations was defined as 200 seconds, which is not sufficient for an accurate representation of the overtopping distribution. Irías Mata and Van Gent (2023) validated a numerical model with measurements taken from physical model tests with a rubble mound breakwater with different configurations. They found that even though OpenFOAM® overestimated the mean overtopping discharge, it was able to reproduce the overtopping trend depending on the geometry of the breakwater. With the validated model, they further investigated the influence of different configurations on the mean overtopping discharge by varying the wave steepness, seaward slope, berm, crest wall and recurved parapet; their effect was analyzed individually and combined.

The effect of the presence or absence of a detailed turbulence closure to model wave interactions with porous structures have been studied in the past. It has been demonstrated that not including a detailed turbulence closure model is valid in the occasions when no or little wave breaking occurs outside the porous structure in the modelled situations (see Higuera et al., 2013a, 2013b; Jensen et al., 2014). Also, several authors have shown that turbulence inside the porous media can be modelled only by means of the Darcy-Forchheimer equation (explained in section 2.2.1), and a good reproduction of the wave height, wave transformation and dissipation within the porous media is obtained (see Van Gent, 1995a, 1995b; Jensen et al., 2014; Jacobsen et al., 2018; Molines et al., 2019; Irías Mata, 2021; Irías Mata and Van Gent, 2023). When the resistance coefficients, α_F and β_F, of that equation are calibrated from physical model tests, they already include the turbulence effects. If a turbulence model is applied to the numerical simulations, it adds extra resistance. Hence, applying the resistance coefficients found from physical model tests is no longer valid, and these coefficients should be calibrated instead.

When it comes to estimating the mean overtopping discharge with formulations based on physical model tests, up until recently, this parameter could be calculated for simple rubble mound configurations only (see EurOtop, 2018 and its previous versions). One recent set of equations that was proposed to estimate the mean overtopping discharge on rubble mound breakwaters with more complex configurations[6] is given by Van Gent et al. (2022). In their formulas they consider the influence of a berm, crest wall, structure slope and wave steepness. For this purpose, they performed physical model tests where all these effects were included. Besides the limitations associated with the range of validity of the tested variables, their equations can only be applied in situations when no severe wave breaking occurs on the foreshore. These authors found that a lower wave steepness and freeboard results in more wave overtopping. Also, for the same non-dimensional freeboard, rubble mound breakwaters with a crest wall experience more wave overtopping. In addition to this, a wider and higher berm reduces wave overtopping for the same non-dimensional freeboard, and the reducing effect depends on the wave steepness (the reduction is larger for waves with higher wave steepness).

With respect to the estimation of flow depths (h_c) and velocities (u_c) on the crest of coastal structures during wave overtopping events, the majority of efforts have been put in the creation of experimental formulations from physical model tests with dikes (see Van Gent, 2002a; Schüttrumpf et al., 2002; Van der Meer et al., 2010; and Van Bergeijk et al., 2019). Mares-Nasarre et al. (2019) were the first to propose a method to estimate these parameters on the crest of rubble mound breakwaters. Their formulations to estimate h_c and u_c exceeded by 2% of incoming waves are based on existing equations to calculate these variables for dikes. These equations indicate that h_c exceeded by 2% of the incoming waves depends on the significant wave height (H_{m0}), the Iribarren number ($Ir_{m-1,0}$)[7], and the crest freeboard (R_c). Mares-Nasarre et al. (2019), suggested approximating u_c exceeded by 2% of incoming waves as a function of the squared root of h_c exceeded by 2% of the incoming waves. The trends in these formulas are such that the flow depths and velocities are larger for increasing H_{m0} and $Ir_{m-1,0}$, and for decreasing R_c. Mares-Nasarre et al. (2019) calibrated the empirical coefficients of their equations using measurements obtained from physical model tests with overtopped rubble mound breakwaters under depth-limited breaking wave conditions. In addition, they proposed Exponential and Rayleigh distributions, for the approximation of h_c and u_c with exceedance probabilities below 2%, respectively. They also found that h_c and u_c were not correlated for the same extreme overtopping event.

Mares-Nasarre et al. (2020) concluded that the foreshore slope (m) also has an influence on h_c and u_c exceeded by 2% of the incoming waves. Later, Mares-Nasarre et al. (2021) trained and simulated Feedforward Neural Network models to analyze the influence of a set of explanatory variables on h_c

[6] The author refers to complex breakwater configurations to the ones where additional components are included (e.g., a crest wall, a berm, a recurved parapet, etc).
[7] Iribarren number computed with the significant wave height and the spectral wave period.

and u_c exceeded by 2% of the incoming waves. These explanatory variables corresponded to the foreshore slope (m), the crest freeboard (R_c), the Iribarren number ($Ir_{m-1,0}$), and the water depth (d). Based on this model, they proposed new equations for the estimation of h_c and u_c exceeded by 2% of the incoming waves. They validated the shape of the distributions that were proposed in their first work (Mares-Nasarre et al., 2019) to describe h_c and u_c with exceedance probabilities lower than 2%. Additionally, they updated the calibration coefficients for these distribution functions. The equations proposed by Mares-Nasarre et al. (2019, 2021) are valid for the middle of the crest only since this was the place where the measurements were taken in the experiments.

There are several studies where human stability is assessed during flood flows (e.g., Abt et al., 1989; Jonkman and Penning-Rowsell, 2008; and Xia et al., 2014). The instability threshold for these conditions were defined as the product of the flow velocity (u) and the flow depth (h). Bae et al. (2016) performed tests on dummies and humans subjected to overtopping flow. They were standing facing the flow with their legs slightly opened. The tested structure was a breakwater with a vertical wall and a crest covered with pieces of wood. From their results, they defined uh-criteria for instability of children and adults for two severity levels: 1) tiptoe clearance, and 2) slipping and tumbling. Sandoval et al. (2017) also defined uh thresholds based on videos on the internet of real situations of people losing stability under wave overtopping events. However, these uh limits are not directly applicable to overtopping flow because the peak impact force is the result of an “slamming effect” which is absent in steady flow (Cao et al., 2022). Also, the peak flow depth and velocity might not even be simultaneous in time (Mares-Nasarre et al., 2019). Furthermore, overtopping flow depends on the incoming wave, and the geometry of the structure. Therefore, many tests are still needed under different wave conditions and configurations to define universally applicable uh-criteria for overtopping flow (Cao et al., 2021b).

Cao et al. (2022) proposes a risk assessment framework to evaluate the likelihood that a pedestrian will be mobilized by the largest overtopping event during his/her visit time to the crest of a coastal structure. Their approach is applicable on smooth impermeable revetments with a seaward slope or vertical seawalls; and for non-breaking waves arriving at the structure toe. The information on the sea state, structure and pedestrian are used to estimate the peak driving force caused by the overtopping flow, which is subsequently used to compute an instability factor. The uncertainty is accounted for in a critical instability factor. Some sources of uncertainty for the pedestrian failure under overtopping flow are the body position with respect to the flow, clothing, skin softness, and the friction between the surface and the shoes (Bae et al., 2016; Cao et al., 2022).

The peak force caused by the overtopping flow on a human body used in the risk assessment framework by Cao et al. (2022), was developed and calibrated in their previous studies (see Cao et al., 2021a, 2021b; Chen et al., 2021). For a smooth and impermeable seawall, it depends on the wave height at the structure toe, the Iribarren number, the seaward slope of the structure, the relative freeboard (R_c/H), and a representative diameter of the person. With a different parametrization of the formula, in terms of the characteristics of the overtopping flow, they showed there is a dependency of this force on the flow depth at the leading edge of the crest. This force decreases exponentially with the distance from the leading edge of the crest. The length scale of decay is associated to the flow depth at the leading edge. Furthermore, in one of their studies (Cao et al., 2021b) they found that the flow depth at the leading edge of the crest increases with the Iribarren number and decreases with the relative freeboard (R_c/H). The influence of the breaker parameter is such that for the same R_c/H ratio, plunging breakers produce thinner flow depths and higher speeds than surging breakers at the crest.

Calculating the probability of instability of a pedestrian under certain wave conditions and for different rubble mound breakwater configurations is out of the scope of this research. Nevertheless, computing the flow depths and velocities at the crest of a rubble mound breakwater is definitely a first step in building a database to tune a robust probabilistic model such as the one proposed by Cao et al. (2022) for revetments, but applied to rubble mound breakwaters. As was mentioned by

Cao et al. (2022), one of the biggest problems in the applicability of the uh-criteria, is not having these values under a wide range of tests with different structure configurations and wave conditions. A validated numerical model can help to fill this gap; and provide a database to calibrate the coefficients of formulas to evaluate the stability not only of pedestrians, but also traffic and equipment.

1.5. Reading guide

Regarding the structure of this document, chapter 1 presents all the components of the introduction, which have already been covered. Chapter 2 includes the methodology for the validation and set-up of the numerical model in OpenFOAM®, as well as the description of further sensitivity analysis performed to evaluate their impact on the modelled flow depths and velocities. Chapter 3 treats the preferred method of extraction of the flow depths and velocities, at the crest, from the numerical model. The validation of wave propagation, overtopping discharge, and the flow depths and velocities at the crest are included in Chapter 4. Chapter 5 comprises the explanation of the physical processes occurring during the wave overtopping events, and the effect of changing the wave conditions and protrusion height on the modelled flow depths and velocities. The discussion of results, conclusions and recommendations for future research are covered in Chapters 6 and 7, respectively. At the end of the document, a series of Appendices (A to F), show complementary and more detailed information concerning the numerical modelling of flow depths and velocities with OpenFOAM®.

2. Methodology

2.1. Description of physical model tests

To perform the validation of the numerical model, physical model tests carried out in the Delta Basin at Deltares, in the Netherlands, were used. Two rubble mound breakwater setups were tested on a horizontal foreshore: a) a breakwater with a crest wall and without a berm, and b) a breakwater with a crest wall and with a berm (upper and lower panels of Figure 5, respectively). Both cross sections had a seaward slope of 1:2, and a rear slope of 1:1.5. The structure was composed by a permeable core (d_{n50} = 6.5 mm), a filter layer (d_{n50} = 17 mm) with a thickness of $2d_{n50}$, and an armor layer (d_{n50} = 33 mm) with a thickness of $2d_{n50}$. The crest wall was placed on top of the core material. The freeboard relative to the still water level was 97 mm and 150 mm, excluding and including the crest wall, respectively. The berm width was 500 mm and was placed 50 mm below the still water level. The width and the position of the berm, and the height of the crest wall remained unchanged while performing the tests. The configuration with the berm was representative of a case when a new breakwater with a berm is constructed since the berm was composed of the three materials (core, filter, and the armor layer). The armor stones were glued together to prevent displacement during the execution of the tests.

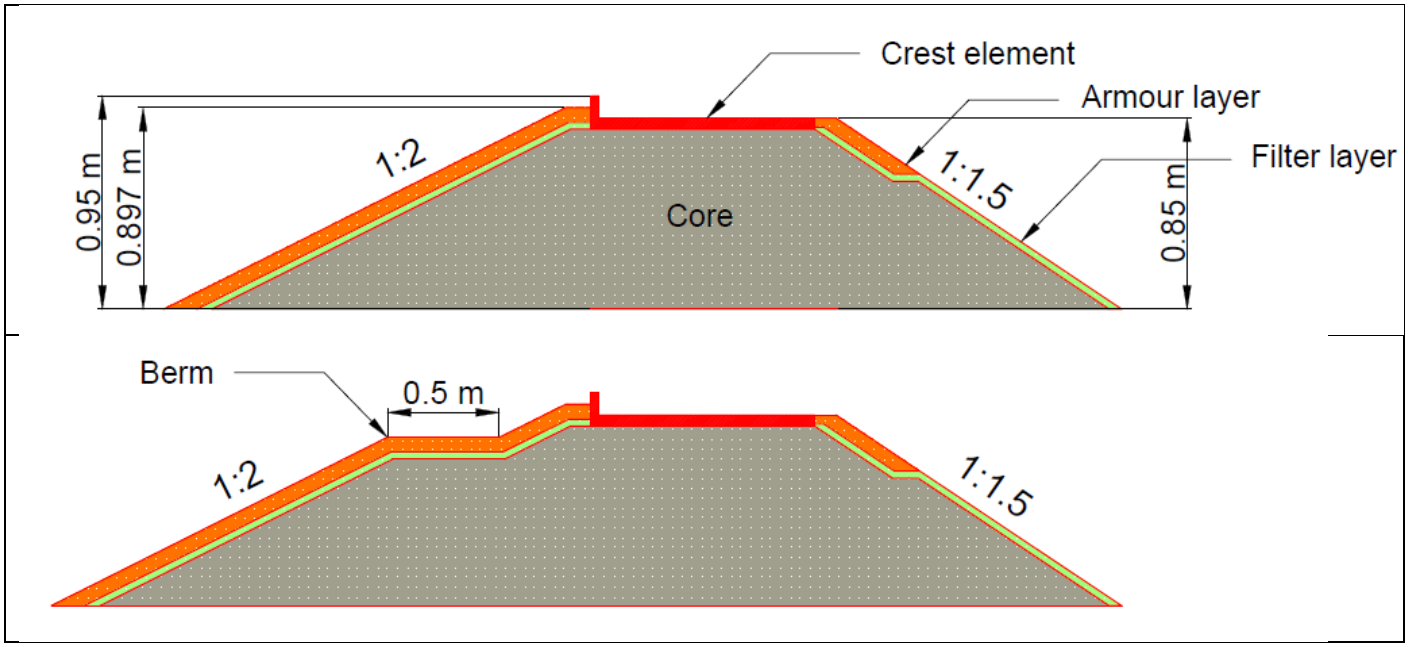

Figure 5. Model set-ups used for the validation of the numerical model. The top panel shows the cross-section with the crest wall and without the berm, and the lower panel shows the cross section with the crest wall and with the berm.

Figure 6 presents the position of the physical model within the Delta Basin. The basin is 50 m long and 50 m wide, with a maximum water depth of 1.0 m. A segment of 18.3 m of the breakwater was constructed for the tests. To generate the waves, a multi-directional wave board with 100 paddles was employed. It is equipped with an active reflection compensation mechanism, which prevents waves reflected from the breakwater to re-reflect at the wave paddles and propagate again towards the structure. Also, a system with the second order steering of the wavemakers motion is included. With it, second order effects of the first higher and first lower harmonics of the wave field are considered, which guarantees that generated waves are representative of natural occurring waves. The angle between the axis of the breakwater and these wave generators was 37.5º.

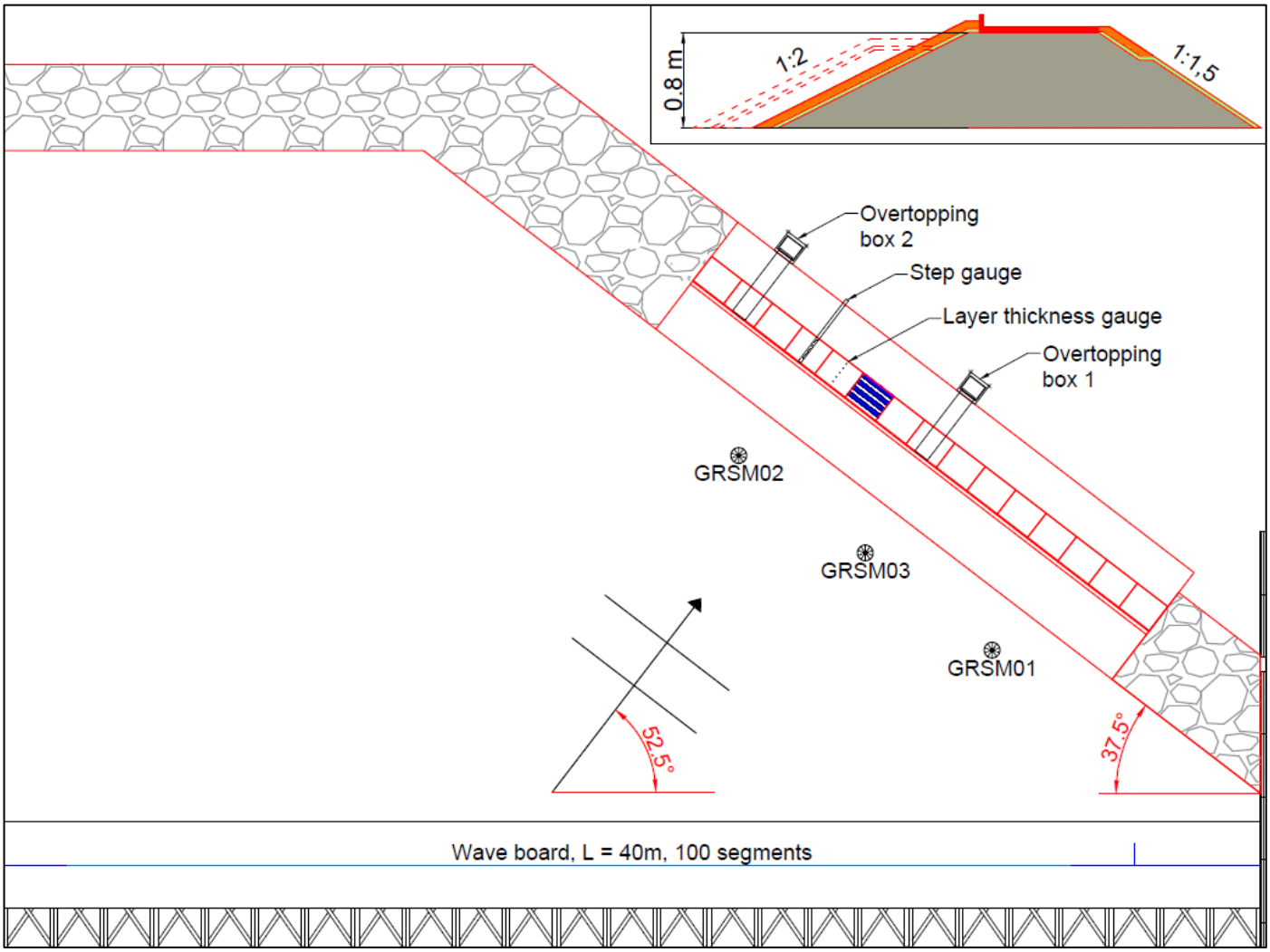

Figure 6. Layout of the physical model within the Delta Basin. GRSM01, GRSM02 and GRSM03 are the wave gauges used to compute the incident waves. The berm is shown in dashed lines in the cross-section presented in the upper right corner.

During the physical modelling campaign, different wave directions, and even directional spreading were tested. Nevertheless, the description of the tests will be limited to long crested normal incident waves since the focus of this study is on 2DV numerical modelling. For these tests, the incident wave height was varied, and two diff8erent wave steepness were considered. Irregular waves based on the JONSWAP spectrum with a peak enhancement factor of 3.3 were applied. Each test consisted of 1000 waves[8]. The water depth was kept as h = 0.80 m. Therefore, only one freeboard was tested. In total, 16 tests were performed under perpendicular wave attack (8 for the setup without the berm, and 8 with the berm).

The overtopping discharge was measured by collecting the water passing over the crest wall of the structure through a couple of overtopping chutes and boxes (see Figure 6 and Figure 7). Inside the overtopping boxes, wave gauges were installed to measure the water levels. The multiplication of the difference in the water level and the dimensions of the overtopping boxes (0.5x0.6 m) gave the overtopping discharge per wave. Average overtopping discharges were obtained for the total duration of each test.

[8] Traditionally, 1000 waves have been used to compute mean overtopping discharges. They are considered to be representative of the duration of a storm.

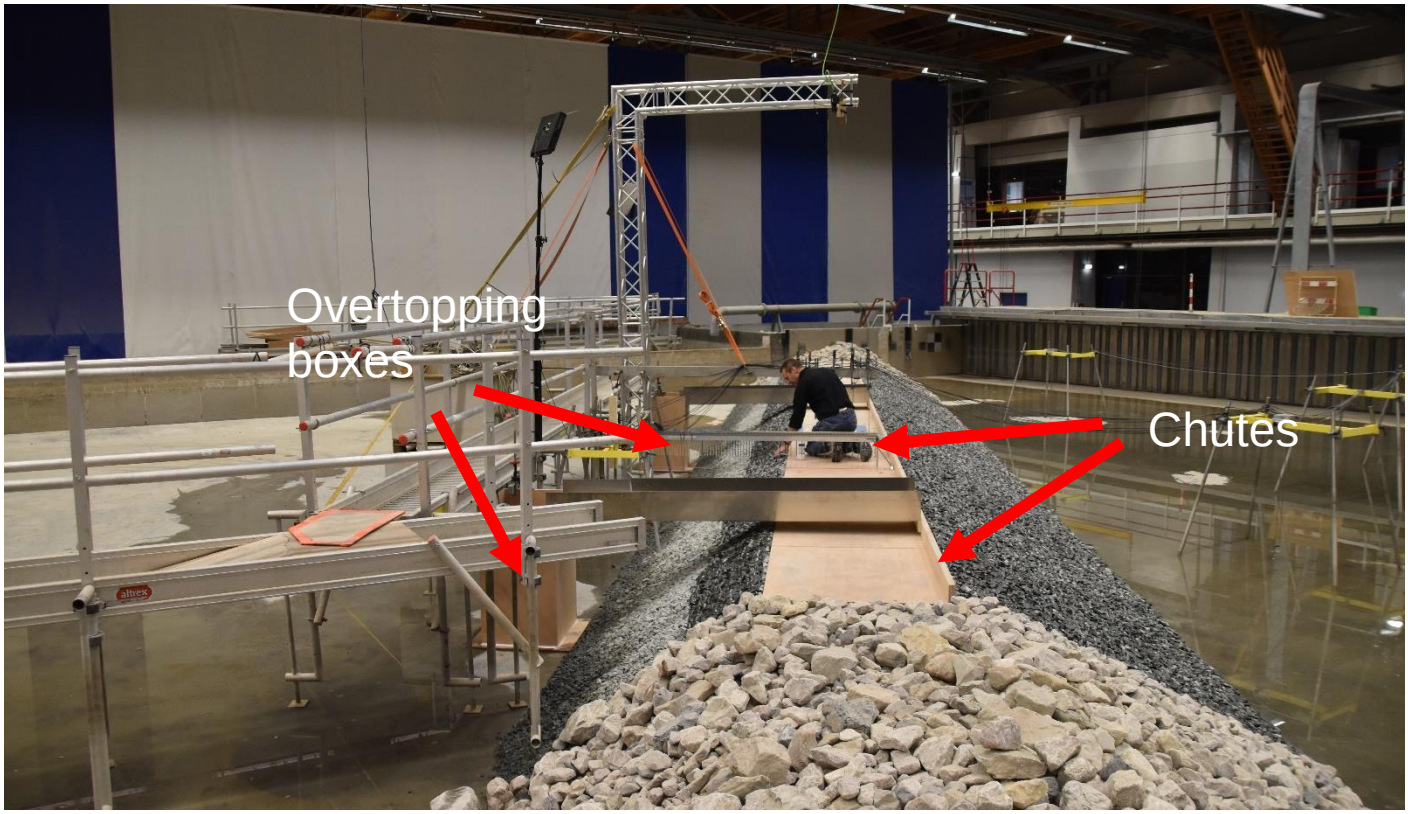

Figure 7. Equipment used to measure the average overtopping discharge.

Three directional wave gauges (GRSM01, GRSM02, and GRSM03 shown in Figure 6) were positioned in a plane parallel to the axis of the structure, near the toe of the breakwater. They were used to separate incident and reflected waves during the execution of the tests, and to estimate the spectral parameters (H_{m0} and $T_{m-1,0}$) of the incident waves. When the method to compute these parameters is used with the structure in place, the results cannot be trusted. The presence of the breakwater causes a lot of reflection, which contaminates the results. Normally, a calibration procedure is executed where the tests are repeated with the same wave-paddle velocity signal, after removing the structure. Without the presence of the breakwater, cleaner spectral parameters are computed. However, this calibration procedure was not performed before carrying out this research.

Two devices were used to measure the flow depths and velocities at the horizontal part of the crest wall, a step gauge and a layer thickness gauge (see Figure 8). The step gauge is constituted of many pins in a straight line. The output of this measuring device is not continuous in time for all the pins. At each timestep, the device gives output only for the highest wet pin. There were some pins located outside the plateau behind the crest wall that never received a signal (see Figure 8). From this device, the moving front of each wave could be identified and hence, its velocity could be estimated. The layer thickness gauge is composed of five metal rods. In this case, the output was based on the wet height of each pin over time. Then, the flow depth timeseries at the location of each of the five pins could be obtained. From the layer thickness gauge, it was also possible to estimate flow velocities. For this purpose, the velocity was computed as the time it took for the wave front to move in between two consecutive pins. Hence, the velocities were representative of four locations along the horizontal part of the crest element, instead of five. Figure 9 presents a 2DV set-up of the layer thickness and step gauges used in the laboratory.

The step gauge has the downside that when there were two events passing through its pins, the signal was only captured for one of them. The one that caused the highest wet pin. Then, its output is not completely reliable. Instead, a signal is obtained for each of the five metal rods composing the layer thickness gauge. For this reason, only the velocities computed from the layer thickness gauge are used for validation of the numerical model.

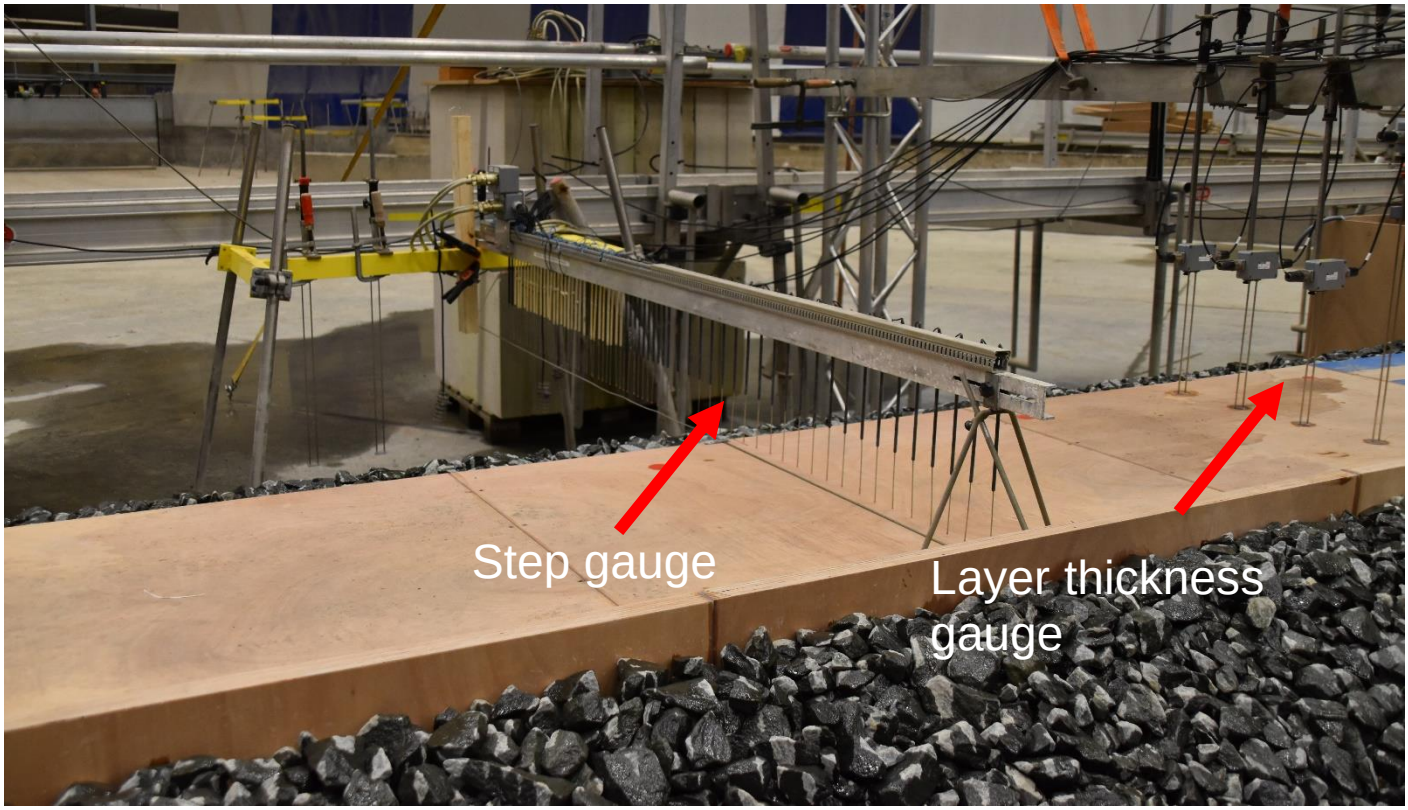

Figure 8. Flow depths and velocities measuring devices.

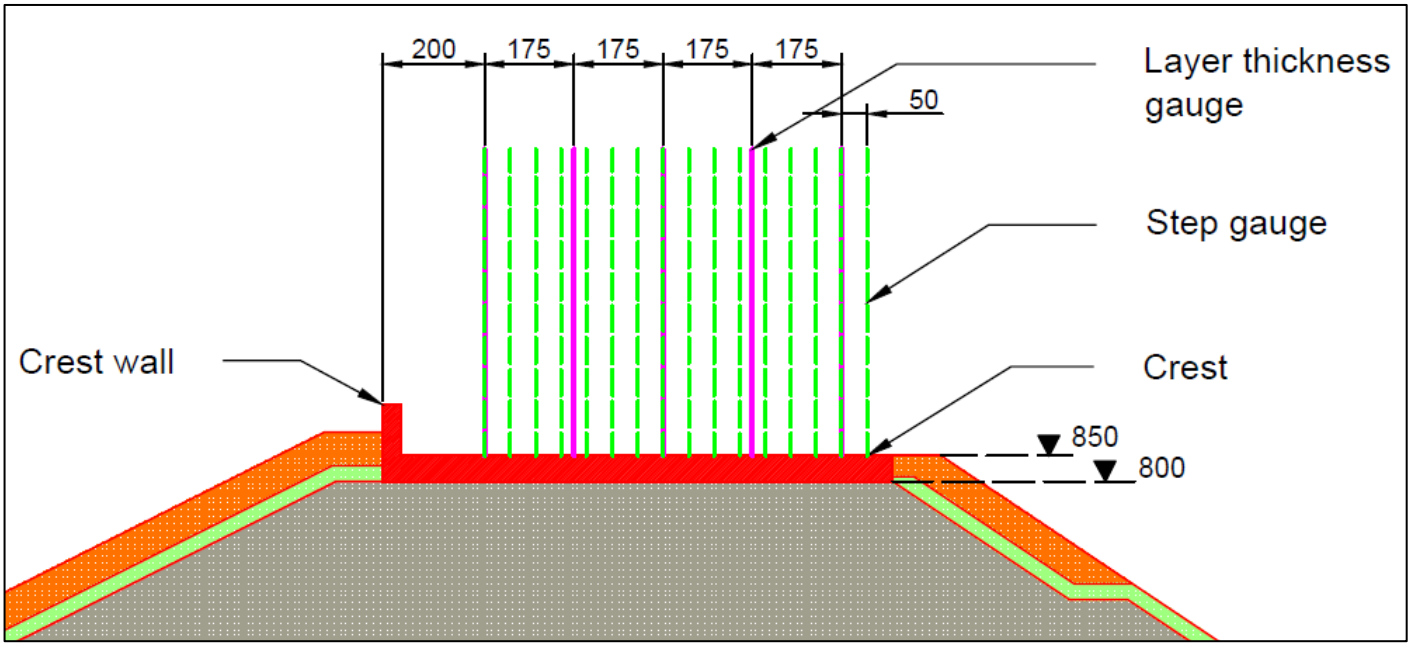

Figure 9. Step gauge and layer thickness gauge set-up in 2DV. The dimensions and elevations are given in mm.

Originally, the definition of the tests to be used for validation of the numerical model was based on a criterion dependent on the non-dimensional mean overtopping discharge (Q). As a starting point, tests having Q in between 10^{-6} and 10^{-3} were chosen. Non-dimensional overtopping discharges smaller than 10^{-6} are less relevant in practice, and scale effects might be present (Van Gent et al., 2022). 10^{-3} was defined as an upper limit to help distinguish individual overtopping events with the measurement equipment. The set of tests meeting these conditions is presented in Table 1. They were used to validate the numerical model regarding the prediction of incident waves and overtopping discharges.

Table 1. Tests used for validation of computed incident waves and overtopping discharges.

Wave conditions to be simulated in OpenFOAM®, case without berm

Test ID	d [m]	H_{m0} [m]	H_{m0}/d [-]	T_p [s]	s_{op} [-]	q [l/s/m]	Q [-]
Th00151b	0,80	0,08	0,100	1,85	0,015	0,003	3,7E-05
Th00155	0,80	0,10	0,125	2,07	0,015	0,110	1,1E-03
Th00401	0,80	0,08	0,100	1,13	0,040	0,001	2,1E-05
Th00402d	0,80	0,12	0,150	1,39	0,040	0,051	3,9E-04

Wave conditions to be simulated in OpenFOAM®, case with berm

Test ID	d [m]	H_{m0} [m]	H_{m0}/d [-]	T_p [s]	s_{op} [-]	q [l/s/m]	Q [-]
ThB00155	0,80	0,10	0,125	2,07	0,015	0,006	5,7E-05
ThB00152	0,80	0,12	0,150	2,26	0,015	0,081	6,2E-04
ThB00406	0,80	0,14	0,175	1,50	0,040	0,014	8,7E-05
ThB00403	0,80	0,16	0,200	1,60	0,040	0,045	2,3E-04

The set of tests used to validate the numerical flow depths and velocities was redefined. Tests producing very thin flow depths or only a few overtopping events were discarded. Very thin flow depths contain scale effects. Little overtopping events inhibit drawing conclusions from the associated exceedance curves. In this case, the non-dimensional mean overtopping discharges has values in between 10^{-4} and 10^{-3}. A total of six tests were picked for validation purposes of the flow depths and velocities. They are presented in Table 2.

Table 2. Tests used for validation of computed flow depths and velocities.

Wave conditions to be simulated in OpenFOAM®, case without berm

TestID	d [m]	H_{m0} [m]	H_{m0}/d [-]	T_p [s]	s_{op} [-]	q [l/s/m]	Q [-]
Th00402d	0,80	0,12	0,150	1,39	0,040	0,051	3,9E-04
Th00406	0,80	0,14	0,175	1,50	0,040	0,240	1,5E-03
Th00403c	0,80	0,16	0,200	1,60	0,040	0,490	2,4E-03

Wave conditions to be simulated in OpenFOAM®, case with berm

TestID	d [m]	H_{m0} [m]	H_{m0}/d [-]	T_p [s]	s_{op} [-]	q [l/s/m]	Q [-]
ThB00152	0,80	0,12	0,150	2,26	0,015	0,081	6,2E-04
ThB00156	0,80	0,14	0,175	2,44	0,015	0,229	1,4E-03
ThB00403	0,80	0,16	0,200	1,60	0,040	0,045	2,3E-04

In the tables above, q and Q stand for mean overtopping discharge, and non-dimensional mean overtopping discharge, respectively. The parameters H_{m0}, T_p, and s_{op} correspond to the target values. The q values are the measured mean overtopping discharges, and the Q values are computed from the measured mean overtopping discharges with the target significant wave heights.

2.2. Description of the numerical model set-up

2.2.1. Applied hydrodynamic model

OpenFOAM®, a two-phase model (water and air), was used in this research to model the flow depths and velocities at the crest of a rubble mound breakwater with different configurations. It employs a numerical method based on a finite volume discretization on a collocated grid arrangement. To simulate the wave-structure interaction, the package waves2foam was applied. It includes a method for the generation and absorption of waves, the relaxation zone technique developed by Jacobsen et al. (2012). It also incorporates the resistance-type porosity model by Jensen et al. (2014), based on Van Gent (1995a), for the simulation of the flow in the porous media. A brief description of this porosity model is given in Appendix A.

Following the suggestions by Larsen et al. (2019) and Patil (2019), the variant of the VOF method that was applied here, corresponds to the isoAdvection scheme developed by Roenby et al. (2016). The advantage of this algorithm is that it keeps a sharp interface between the air and water, and it prevents wiggles around the free surface and overestimated velocities near the wave crests. The sharp interface allows to accurately capture the overtopping events.

2.2.2. General configuration of the numerical flume

In this research, only 2DV numerical modelling was carried out. 3D modelling is too computationally expensive to simulate wave propagation and overtopping events for the duration of a storm. Regarding the representative storm duration, the common practice is to use 1000 waves to produce a reliable overtopping distribution. Using 1000 waves[9] is necessary when dealing with situations for which a low percentage of overtopping events occur.

The consequence of performing 2DV numerical modelling is that only normal incident waves can be considered, and effects such as directional spreading or wave transformation due to a non-alongshore homogeneous bathymetry cannot be taken into account. Since the distance from the wave paddles till the rear side of the breakwater in the physical model tests was short enough (in the order of 15 m), it was feasible to perform the numerical simulations solely with OpenFOAM®. In other words, it was not necessary to couple it to another solver to decrease the demand on the computational resources.

The numerical flume was configured to simulate some of the tests with normal incident waves effectuated during the physical model campaign in the Delta Basin. The height of the numerical flume was conservatively fixed as 1.60 m to avoid escape of water through the atmosphere boundary during the simulations (see section 2.2.5). Relaxation zones were located at the inlet and outlet boundaries of the domain. They were used to generate and absorb waves. Since the physical model tests were performed in a 3D environment (see Figure 6), in principle, any perpendicular transect to the breakwater could be picked for the numerical simulations. This was advantageous because the length of the relaxation zones could be varied depending on the simulated wave characteristics. To determine the length of both relaxation zones, a sensitivity analysis was effectuated (see Appendix B). With it, the effect on the wave propagation, of using the deep water wave length vs the actual wave length to define the length of the relaxation zones, was quantified. Finally, the length of the inlet relaxation zone was fixed (at least) as the actual wave length calculated with the peak period

[9] Simulations with 1000 waves were used for the validation of wave propagation, overtopping discharge, and the exceedance curves of the flow depths and velocities. Nevertheless, when performing sensitivity cases, the author executed simulations with less waves. The number of waves used for these variations changed depending on the process to analyze (wave propagation, extraction of flow depths and velocities). For detailed information in this respect, refer to section 2.2.10.

and the water depth, and the length of the outlet relaxation zone was set (at least) as half the same wave length.

Since the length of the numerical flume was varied depending on the simulated wave characteristics, to ease the configuration, the numerical domain was built in terms of coordinates. They were fixed for the breakwater structure, the end of the inlet relaxation zone and the start of the outlet relaxation zone. To separate incident and reflected waves, the method by De Ridder et al. (2023) was used. For this purpose, six wave gauges were positioned between the end of the inlet relaxation zone and the toe of the breakwater. They were located at 1.59 m, 1.91 m, 2.41 m, 3.01 m, 3.34 m, and 4.04 m, respectively, from the toe of the breakwater (configuration without the berm). Their locations were fixed after performing one sensitivity case, where a longer distance between the first numerical wave gauge and the end of the inlet relaxation zone was considered (see Appendix B). The closest wave gauge to the breakwater had the same location as the wave gauge in the physical model tests. This method (De Ridder et al., 2023) calculates the time signal of the incident and reflected waves at the location of the first gauge in the positive x-direction. Therefore, it was assumed that this signal is equivalent to the one captured at the position of the physical wave gauge. Figure 10 shows the final configuration of the numerical flume.

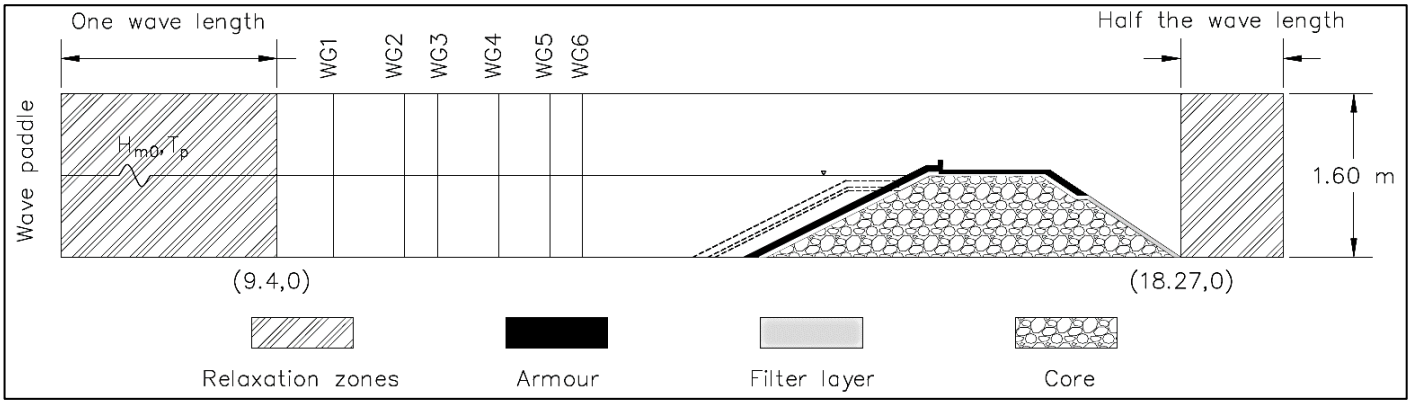

Figure 10. Final configuration of the numerical flume. The berm considered in the second configuration is presented in dashed lines.

2.2.3. Mesh

The blockMesh and snappyHexMesh utilities were used to create the mesh. The base mesh was generated with the blockMesh tool. Then, the mesh was refined in areas near the water level and around the crest wall by means of the snappyHexMesh tool. The mesh characteristics were determined through two grid sensitivity analyses. The first grid sensitivity analysis was effectuated to identify the coarsest grid that did not longer have a strong impact in the wave propagation process. With it, the dimensions of the grid cells of the base mesh and the mesh around the water level were defined. The purpose of the second grid sensitivity analysis was to determine the impact in the computed flow depths and velocities when the mesh around the crest wall was varied. The detailed explanation of the first and second grid sensitivity analyses can be found in Appendix B and C.4, respectively.

In this section, the mesh description will be limited to the final grid (based on the outcome of the grid sensitivity analyses). It consisted of a base mesh of 4x4 cm. Most of the base mesh was composed of square cells, except for a lower block, in the deepest part of the water column, which had a grading in the vertical direction of 0.8. This means that the upper cells of that block had a vertical dimension that was 0.8 times smaller than the vertical dimension of the cells at the bottom of the same block. Around the water surface, an area was created for which two refinement levels were applied with respect to the base mesh. This mesh consisted of square cells of 1x1 cm. Consequently, the number of cells per wave height ranged between 8 and 16. Also, the cell aspect ratio was equal to 1 on the cells around the water surface, which is needed for a good representation of the wave propagation

and wave breaking processes (Jacobsen et al., 2012). The height of the area of refinement around the water level was defined in such a way, that it contained the highest waves of all the modelled wave conditions.

Surrounding the crest wall, three refinement levels with respect to the base mesh were effectuated. Hence, the mesh around this impermeable element was composed of cells of 0.5x0.5 cm. The thickness associated to this finest mesh was 2 cm. It was identified that this finest mesh was necessary for a better estimation of the flow depths and velocities occurring during the overtopping events (see Appendix C.4). In addition, the crest wall was removed from the numerical domain through the snappyHexMesh utility.

Table 3 and Figure 11 presents the description of the final mesh. This set-up was applied to all the validation and final sensitivity cases (variations in the wave conditions and breakwater geometry) to avoid causing a bias in the results due to the use of different grid sizes.

Table 3. Mesh resolution for different regions.

Mesh region	Grid size $\Delta x \times \Delta y$ [cm × cm]
Base mesh	4 x 4
Mesh near the water surface	1 x 1
Mesh around the crest wall	0.5 x 0.5

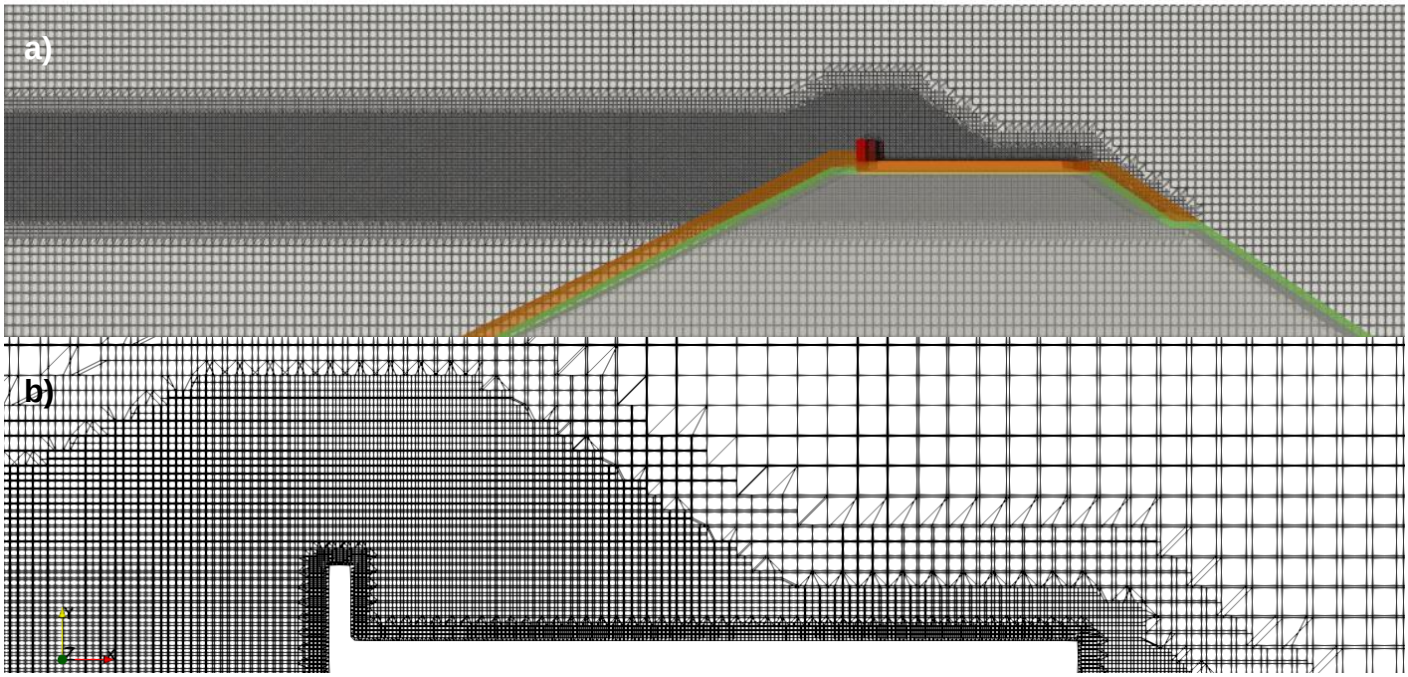

Figure 11. Final mesh used in the numerical model. a) General view. b) Close-up of the mesh of 2 cm of thickness surrounding the crest element.

2.2.4. Wave generation and absorption

A brief description of how the waves were generated and absorbed, through the relaxation zones of the waves2Foam package, is given in this section. For detailed information, refer to Appendix B of the waves2Foam manual (Jacobsen, 2017) and the article on the waves2Foam toolbox (Jacobsen et al., 2012).

The physical model tests were executed in a 3D environment, and the waves were generated with 100 paddles. Therefore, it was not possible to input the wave-paddle velocity signal into the numerical domain. Instead, the irregular waves were created, through the inlet relaxation zone, based on a JONSWAP spectrum with a peak enhancement factor of 3.3 (in the same manner as the generated waves of the physical model experiments). The input significant wave height was calibrated, in such a way, that the incident significant wave height at the position of the first numerical wave gauge had a similar magnitude as the target incident significant wave height at the location of the physical wave gauge GRMS02 (see Figure 6).

The generation of irregular waves included in the waves2Foam package is based on the first order irregular wave theory. It consists of simple superposition of first order linear waves:

$$\eta = \sum_{i}^{N} \alpha_i \cos(\omega_i t - k_i x + \varphi_i) \qquad \text{Equation 1}$$

Where η is the surface elevation, N is the number of wave components, α_i, ω_i, k_i, and φ_i are the amplitude, the radial frequency, the wave number, and the phase of the i'th wave component, respectively.
A non-equidistant discretization of the frequency axis of the JONSWAP spectrum was used, the cosine stretching method, with 100 components. This method utilizes a finer discretization in the region of the spectrum that contains more energy, which saves computational time compared to simulations when an equidistant discretization of the spectrum is used. This is because less components are required to avoid repetition of the signal, and to properly describe the wave height and wave period distributions. The evaluation of the signal was performed by means of the split method (termed irregularFast in the waves2Foam package). The split method reformulates the equation that computes the surface elevation based on the linear superposition of wave components (Equation 1). This enables the evaluation of the x-coordinate as a pre-processing step rather than at each computational timestep. Therefore, it is more computational efficient than when the direct evaluation of the irregular wave signal is carried out. Additionally, a seeding was prescribed for the generation of random phases of 0. The indication of a seeding value is necessary to guarantee the reproduction and comparison of results (the same set of random phases is always used).

As mentioned before, the incident irregular wave field prescribed with waves2Foam is of first order. Nowadays, the inclusion of second order effects in the numerical computations (in OpenFOAM®) is computational expensive[10]. This differs with respect to the generated incident waves in the physical model tests since the second order effects were included there.

[10] The evaluation of the wave signal depends on the number of wave components (N). When second-order effects are included, the number of second order components is N^2. Therefore, their inclusion result in more computational effort. Furthermore, the evaluation of the relaxation zone is more expensive than the evaluation of the wave signal itself. A more detailed explanation regarding this matter is found in Appendix B of the waves2foam manual (Jacobsen, 2017).

The relaxation zones work by weighting the computed and target solutions of the indicator function, F[11], and the velocity field, u, by means of a relaxation function $\alpha_R(X_R)$. The variation of $\alpha_R(X_R)$, and its application to update F and u each computational time step is presented below. Figure 12 presents the schematic variation of for the inlet and outlet relaxation zones.

$$\alpha_R(X_R) = 1 - \frac{\exp(X_R^{3.5}) - 1}{\exp(1) - 1} \text{ for } X_R \in [0,1] \quad \text{Equation 2}$$

$$F = \alpha_R F_{computed} + (1 - \alpha_R) F_{target} \quad \text{Equation 3}$$

$$u = \alpha_R u_{computed} + (1 - \alpha_R) u_{target} \quad \text{Equation 4}$$

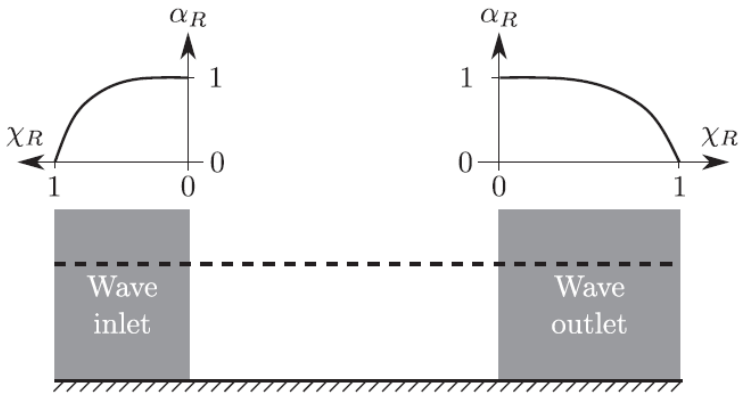

Figure 12. Variation of $\alpha_R(X_R)$ at the inlet and outlet relaxation zones.

Source: Jacobsen et al. (2012)

2.2.5. Boundary conditions

For the wet part of the inlet boundary, the boundary condition is given analytically according to the potential wave theory, as this is the boundary where the waves are generated through the inlet relaxation zone. For the wet part of the outlet boundary, the boundary condition is such that the velocity is equal to zero, as the waves are absorbed through the outlet relaxation zone in this boundary. For the upper boundary, a so call atmospheric boundary condition is defined. It permits air, and water to flow out, but only air is allowed to flow in. At the bottom boundary (and in impermeable parts of the domain), a slip boundary condition is used. No boundary condition is applied on the faces on the front and back of the numerical model. The figure below specifies the names of the boundaries for reference.

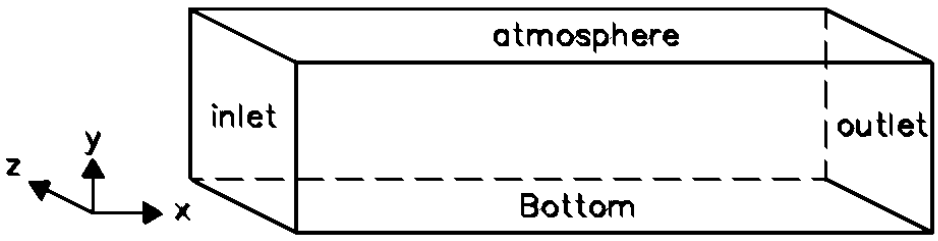

Figure 13. Boundary names.

[11] The indicator function (F) keeps track of two fluid considered in OpenFOAM®, air and water. F is 0 for air and 1 for water, and it can hold intermediate values when both fluids are mixed. Refer to Appendix A for a more detailed explanation.

2.2.6. Turbulence model

Following the approach by several authors (Van Gent, 1995a, 1995b; Higuera et al., 2013a, 2013b; Jensen et al., 2014; Jacobsen et al., 2018; Molines et al., 2019; Irías Mata, 2021; Irías Mata and Van Gent, 2023), no detailed turbulence closure model was applied in any of the simulations; instead, a constant eddy viscosity has been applied. These authors proved that the absence of a detailed turbulence model is valid when little wave breaking occurs (like the cases considered in this research), and because the turbulence effects inside the porous media are already included in the resistance coefficients of the Darcy-Forchheimer equation (see section 1.4 above). The resistance coefficients that were employed in the simulations are the same values proposed in Van Gent (1995a), α_F = 1000 and β_F = 1.1. However, they can be calibrated to take into account the extra resistance caused in the numerical model due to non-physical damping (see Irías Mata and Van Gent, 2023). For a fully turbulent flow, like the one that happens in the porous media within a breakwater, the non-linear term of the Darcy-Forchheimer is dominant in the friction generation. Hence, the non-physical dissipation can be reduced by lowering β and/or increasing KC. The latter option was effectuated in the numerical simulations carried out in this research, where a very large KC number (10,000) was used. The nominal median grain sizes of the three different layers that composed the breakwater were set equal to the ones used in the physical model tests (d_{n50} = 6.5 mm for the core, d_{n50} = 17 mm for the filter layer, and d_{n50} = 33 mm for the armor layer). A porosity value of n = 0.40 was assumed.

2.2.7. Measurement of surface elevation

To measure the surface elevation over the whole length of the numerical domain, wave gauges were placed at each 10 cm. Also, for the separation of incident and reflected waves, 6 wave gauges were located between the end of the inlet relaxation zone and the breakwater. They were placed at 1.59 m, 1.91 m, 2.41 m, 3.01 m, 3.34 m, and 4.04 m, respectively, from the toe of the breakwater (configuration without the berm). For the wave gauges, which were destined to track the wave propagation along the flume, the surface elevation was sampled at a constant timestep, equal to 0.01 s. With a timeseries at constant intervals it was possible to directly compute the wave energy spectra. Figure 14 presents the wave gauges used to determine the spectral parameters of the incident waves.

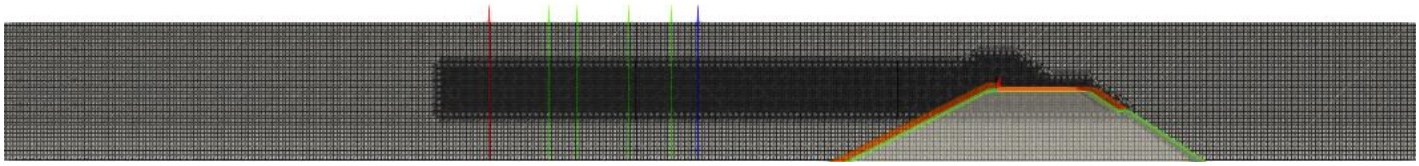

Figure 14. Wave gauges used for the separation of incident and reflected waves. The blue wave gauge is placed at the same location as the physical wave gauge GRSM02. The red wave gauge is where the incident and reflected waves are computed.

2.2.7.1. Spin-up time in the surface elevations

At the beginning of all the simulations, it takes time to obtain a stable surface elevation. This phenomenon is called spin-up time, and it can be estimated as the time it takes for the waves to propagate from the wave paddle, all the way to the breakwater and back. In a postprocessing step of the model results, this time was computed by means of the linear wave theory. Nevertheless, the author decided to reassign the spin-up time as 90 seconds whenever the propagation time was shorter than this value. In this way, there was consistency between the starting time for analysis of both, the physical model tests, and the numerical simulations. It was always checked that at least 1000 waves were obtained.

2.2.8. Measurement of overtopping discharges

To measure the amount of water that is going through a specific part of the domain, a discharge sheet ($\mathcal{E}$) is placed in the position of the cell faces, in the direction perpendicular to the flow. Typically, a sheet is long enough to cover several cell faces (f). The model captures the flux of fluids (air and water) going through each of these cell faces. Then, the flux of water going through the cells is obtained from the rearrangement of an expression that forms part of the solution to the advection equation of the indicator function. This expression contains both, the flux of water and the flux of fluids (see Jacobsen, 2017 for more details). Finally, the total discharge of water is calculated by summing up the individual water discharge through each of the cell faces, as shown in Equation 5:

$$q^* = \sum_{f \in \mathcal{E}} \phi_{F,f} \frac{S_f}{\|S_f\|_2} \qquad \text{Equation 5}$$

Where S_f is the non-unit normal vector to the face, and ϕ_F is the flux of water cross a face, and q is the instantaneous volume flux in m^3/s.

As it is suggested in the waves2foam manual (see Jacobsen, 2017), the overtopping discharges were requested at each computational timestep. This is necessary because overtopping is a very fast phenomena, and it can happen that the process is not well captured at a post-processing step (e.g., the peak of the overtopping event is missed). Figure 15 presents the discharge sheet used to measure the overtopping discharges in the numerical flume. It was placed on top of the crest wall.

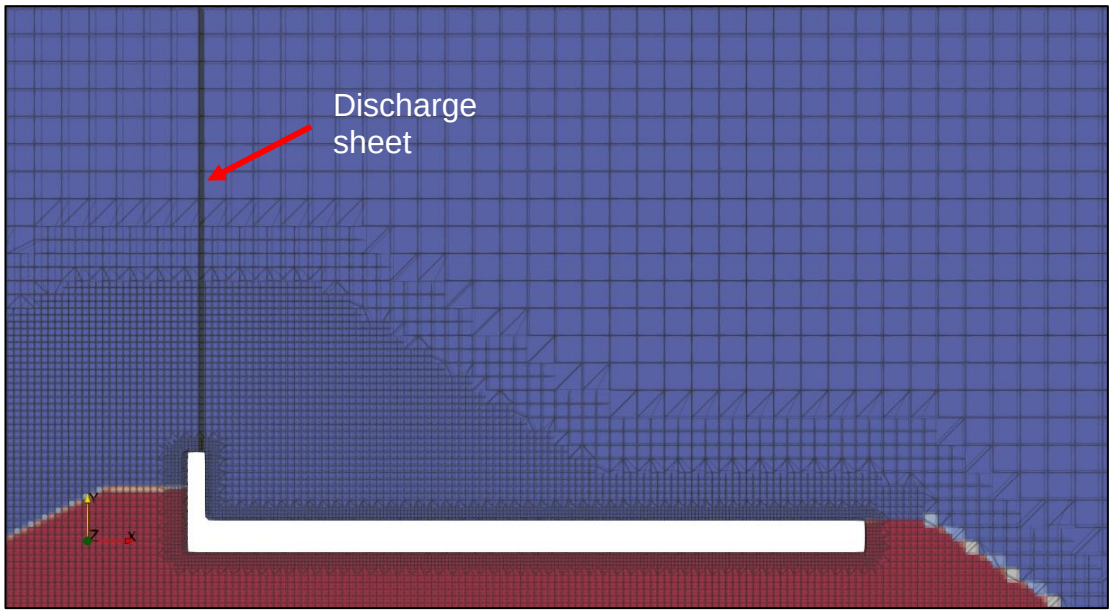

Figure 15. Sheet used to capture the overtopping discharges during the simulations.

2.2.9. Flow depths and velocities output request

In order to have complementary information, all instrumentation used to request the flow depths and velocities during the wave overtopping events, were located in the same horizontal positions on the crest. Even though there are devices that can be placed anywhere in the domain, there are others that are limited by the mesh. For example, planes can only be located in the cell faces. Since the coarsest mesh consists of grid cells with a horizontal dimension of 4 cm, the spacing between individual measuring devices had to be in multiples of 4 cm. This means that it was not possible to align the numerical instrumentation with the physical one utilized in the test campaign in the Delta Basin (see Figure 9).

In principle, placing the measuring devices very close to each other was attainable. However, the postprocessing of the results was lengthier, especially for the planes (this is explained in more detail in section 3 and in Appendix C.3.3). In addition, when the numerical domain was partitioned to distribute the computation into different processors, whenever the division fell in the same place as a discharge sheet, OpenFOAM® collapsed. The possibility of this occurring was higher when the instruments were placed closer to each other (e.g., 4 cm).

For the reasons mentioned above, the author decided to place the individual devices at 12 cm intervals as final configuration[12]. The distribution of these instruments almost covered the entire distance where the layer thickness gauge and step gauge were located in the physical model tests. Overall, the devices were placed from x = 16.08 m till x = 16.80 m in the coordinates of the numerical domain (18 cm and 90 cm from the start of the crest wall (x = 15.90 m), respectively, see Figure 16). Although the numerical devices were not arranged in the same manner as the instruments used during the execution of the physical model tests, it does not affect the final goal of this research, which is to analyze the overall trend of the extreme events.

As stated in the waves2foam manual (see Jacobsen, 2017), the overtopping process is fast. For this reason, it is recommended to capture the overtopping discharges in runtime (at each computational timestep). Therefore, the same approach is taken for the evaluation of the devices intended to measure the flow depths and velocities during the overtopping events.

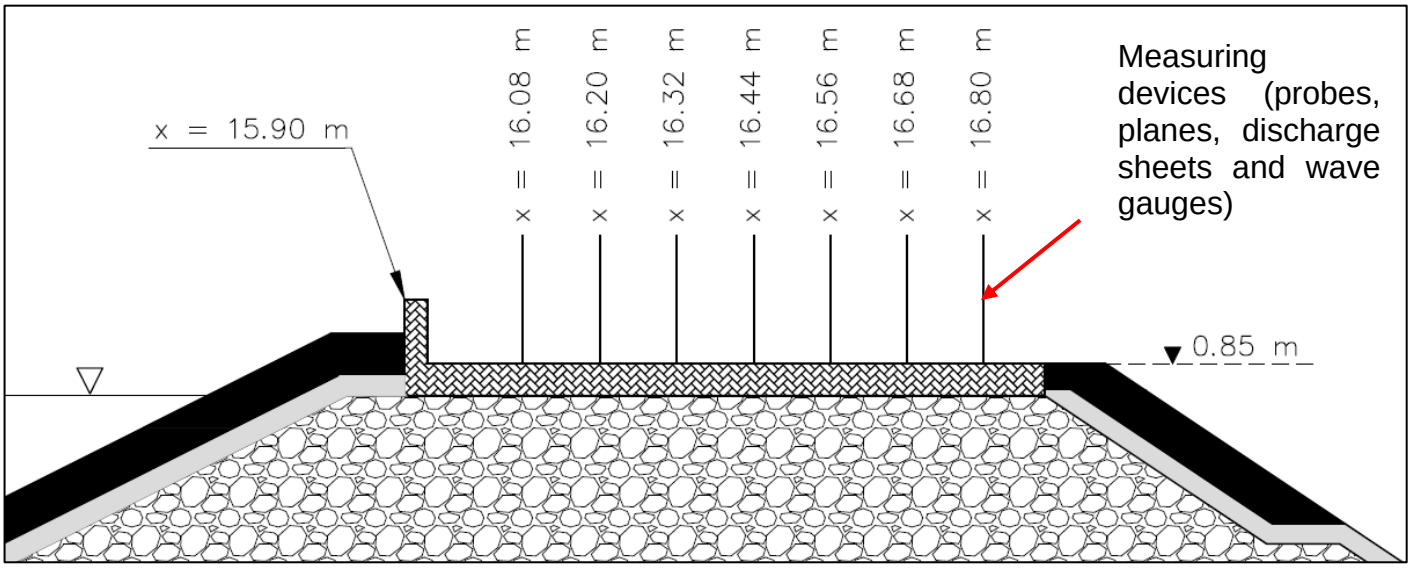

Figure 16. Numerical coordinates of the instruments and the start of the crest wall. Final configuration with individual measuring devices separated at 12 cm intervals.

[12] 12 cm was the final separation of the instruments, but for the initial sensitivity cases that were performed to extract the flow depths, shorter separation distances were used (4 cm). Refer to section 2.2.10 for a more detailed overview of the set-ups used for each step in the sensitivity and validation processes of the numerical model.

2.2.9.1. Measurement of flow depths

Wave gauges were placed at the horizontal part of the breakwater crest to measure the flow depths during overtopping events. As mentioned before, in their final configuration, they were separated equidistantly at 12 cm intervals, starting from x = 16.08 m till x = 16.80 m (in numerical coordinates, see Figure 16). The lower tip of the wave gauges was located at the elevation 0.85 m, which corresponds to the elevation at the top of the horizontal part of the crest element. The final position of the wave gauges was defined after executing some sensitivity cases to find the way to correctly extract the flow depths. A summary of these sensitivity cases is presented in section 3, and a more detailed explanation of the followed process is shown in Appendix C.2. Figure 17 presents the (final) configuration of these wave gauges.

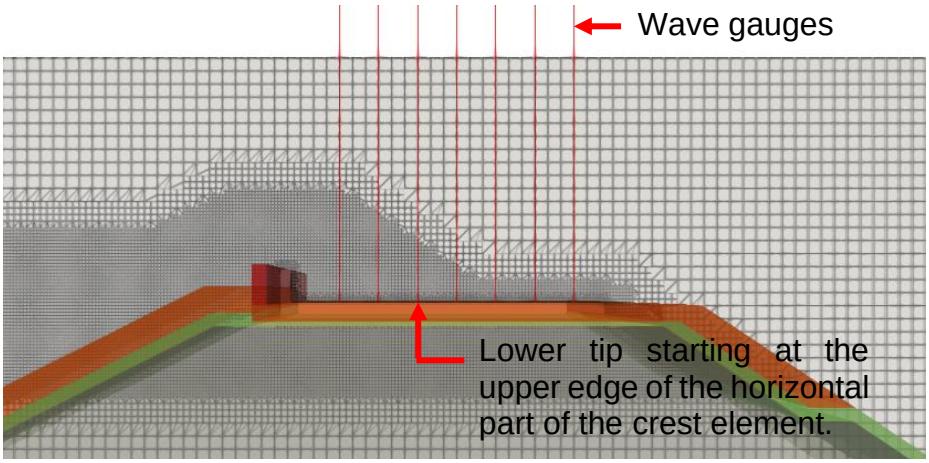

Figure 17. Wave gauges used to capture the flow depths in the numerical flume.

2.2.9.2. Measurement of flow velocities

Three different methods were utilized to extract the flow velocities during the wave overtopping events: 1) with a combination of discharge sheets and wave gauges, 2) with probes[13], and 3) with planes. A more detailed description of the followed procedure is given below.

Method 1: using discharge sheets and wave gauges

Discharge sheets and wave gauges were located at the same horizontal positions, at each 12 cm, from x = 16.08 m till x = 16.80 m, as described in section 2.2.9. The output was requested in runtime. Hence, it was possible to calculate depth averaged flow velocities by simply dividing the overtopping discharge over the flow depth for each computational timestep, as shown in Equation 6. Figure 18 presents the numerical set-up of discharge sheets and wave gauges used in this method.

$$u_{ci} = \frac{q_i^*}{h_{ci}} \qquad \text{Equation 6}$$

Where u_c is the depth-averaged flow velocity, q* is the instantaneous overtopping discharge, and h_c is the flow depth. Each computational time step is denoted by the subindex i. The water volume flux extracted from the discharge sheets, in OpenFOAM®, is given in m^3/s. However, the instantaneous discharge was divided by the width of the numerical flume in a postprocessing step. In this case, the dimensional analysis of Equation 6 is correct.

[13] Note that here, probes refer to numerical probes. They shall not be confused with the probes that are used in physical model experiments.

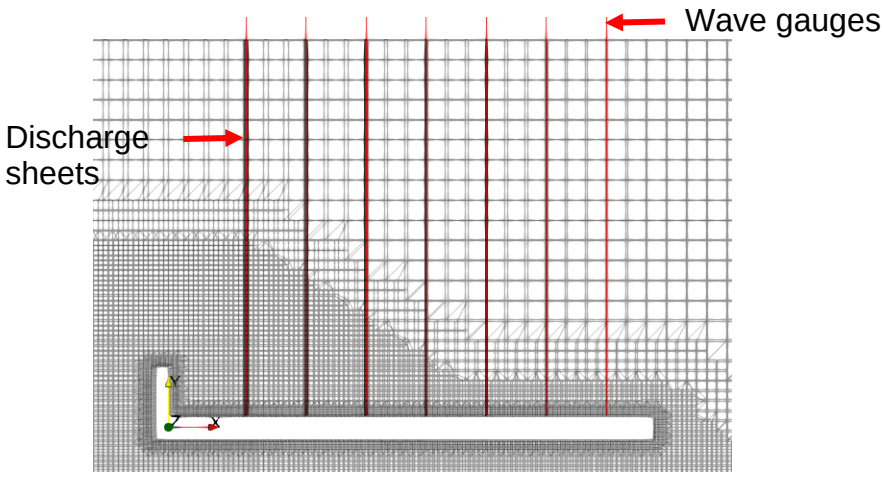

Figure 18. Set-up of discharge sheets and wave gauges for the computation of depth-averaged flow velocities. The red lines indicate the wave gauges, and the gray surfaces represent the discharge sheets.

Method 2: using probes

Probes were placed at intervals of 12 cm in the horizontal direction, from x = 16.08 m till x = 16.80 m in the coordinates of the numerical flume, as described in section 2.2.9. Wherever it was possible, the probes were located at the cell centers in the vertical direction. In transition zones where the size of the vertical dimension of the cells is increasing in the horizontal direction, various probes were placed in the same cell. In addition, the probes were not created all the way from the upper edge of horizontal part of the breakwater crest till the highest cells in the numerical flume. It was assumed that the probes were not needed in elevations corresponding to virtual flow depths larger than 20 cm. In other words, the probes covered the elevations of the numerical domain from y = 0.85 m till 1.05 m. It can happen that during the overtopping events, some droplets are ejected above the region covered by the probes. Therefore, the velocities of these droplets are not captured. It is assumed that their impact on the flow velocities is negligible and that the main event occurs in (maximum) the first 20 cm above the horizontal part of the crest element. Figure 19 presents some of the probes used to capture the flow velocities during the wave overtopping events.

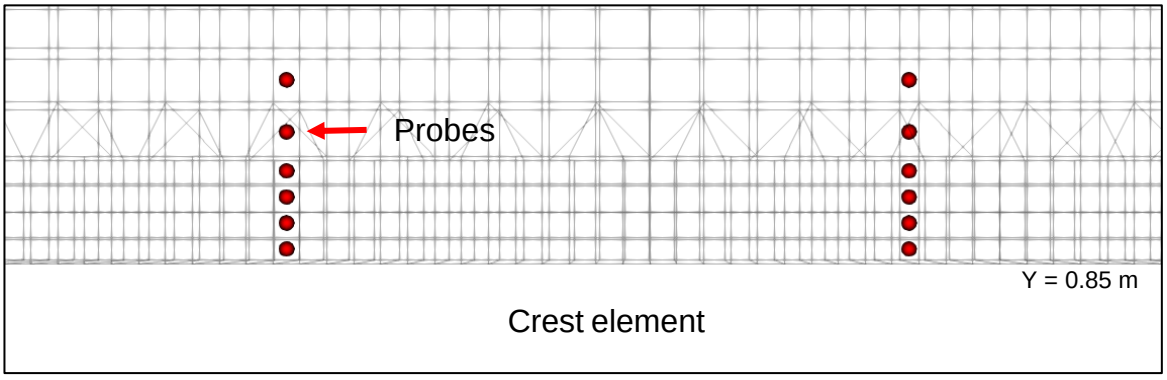

Figure 19. Probes used for the extraction of flow velocities. The mesh around the crest element is finer, which causes a shorter spacing between consecutive probes than in upper regions of the domain. Not all the probes placed in the 20 cm above the horizontal part of the crest wall are shown.

The probes extract the velocity of the fluid in the specific coordinates where they are defined. However, these devices don't distinguish if the velocities are related to air, water, or a mixture of the two. To tackle this challenge, besides the velocity, the indicator function was also requested at each computational step for all the probes. The indicator function is 0 for air and 1 for water, and any value in between suggests that a particular cell contains a mixture of both fluids (see Appendix A). The flow that occurs during an overtopping event consist mostly of water, but air is also present. As a starting point, and specifically to compare the different methods of extracting the flow velocities (see

2.2.10 for more details), it was decided to further postprocess the velocities for the probes for which an indicator function larger than 0.7 would be obtained at each computational timestep. Using this approach, the depth-averaged velocities were computed as shown in Equation 7:

$$u_{ci} = \frac{\sum_{j=1}^{j=N} u_{cji} * \Delta y_j}{\sum_{j=1}^{j=N} \Delta y_j} \qquad \text{Equation 7}$$

Where u_c is the depth-averaged flow velocity, j represents each of the positions in the y-axis where the probes are located (in the same x-coordinate), N is the total number of locations in the vertical direction, i indicates each computational timestep, and Δy refers to the distance between consecutive probes in the vertical direction.

As it can be observed from the previous equation, the depth averaging is carried out by considering that each velocity is representative of the vertical distance corresponding to the separation in between two consecutive probes. Nevertheless, a more appropriate method would be to consider the real water layer contained in the vertical distance in between two consecutive probes. This water layer can be obtained from multiplying this vertical distance (Δy) with the indicator function (F). With this improvement, the depth-averaged flow velocities were estimated according to Equation 8. In addition, it was observed that the numerical model was able to solve flow depths when they were at least half the vertical size of the finest grid (0.0025 m). Consequently, to get rid of noise occurring in the flow velocity signal, the velocities were postprocessed when their associated indicator function was, at least, 0.5.

$$u_{ci} = \frac{\sum_{j=1}^{j=N} u_{cji} * \Delta y_j * F_{ji}}{\sum_{j=1}^{j=N} \Delta y_j * F_{ji}} \qquad \text{Equation 8}$$

Where F represents the indicator function. This equation was used to carry out the grid sensitivity analysis around the crest wall and to evaluate the influence that changing some parameters had on the modelled flow velocities (see section 2.2.10 for a more detailed explanation).

Filtering the flow velocities by means of the indicator function had other advantages besides reducing the noise caused by the inaccuracies of the model. Visual inspection of the hydrodynamics of the numerical flume during the overtopping events showed that sometimes, non-physical droplets with a small indicator function appeared. Additionally, the air flow presented velocities higher than the ones of water. Considering flow velocities when the indicator function was, at least, 0.5 allowed to remove errors generated for these reasons. Appendix E.2 shows examples of the non-physical droplets and high air flow velocities.

It is noteworthy to mention that before coming up with the final methodology to compute the depth-averaged velocities from the probes, another option was tried. It consisted in computing the depth-averaged velocities for the layer of water up till its interface. For this purpose, for each computational timestep, the probes were checked from bottom to top (at each horizontal location). When an indicator function smaller than 0.01 was found, it was considered as the interface between air and water. Then, only the velocities pertaining to the probes located below this position (and including the interface) were further postprocessed in the depth-averaged process. The indicator function was also taken into consideration in the formula to compute the depth-averaged velocities (as shown in Equation 8). Also, to avoid noise in the timeseries, at each computational timestep it was verified that at least one probe (in the same horizontal location) had an indicator function no less than 0.5. It was found that this method didn't work for certain conditions. One of such conditions was when there were air bubbles in the middle of the layer of water. Then, the method considered this air bubble as the interface, and velocities located on top of this air bubble were ignored.

Method 3: using planes

Planes were placed in the crest region, from x = 16.08 m till x = 16.80 m, separated at each 12 cm, as explained in section 2.2.9. With the planes, the output is requested at edges of the cell faces where they are located. Figure 20 presents the set-up of the planes in the numerical flume. The planes covered the total vertical dimension of the domain. Then, the output was requested in regions of the domain where there was no interest in extracting it (inside the porous structure, for example). Therefore, during the postprocessing step, the analysis of flow velocities was limited to the region covering 20 cm above the horizontal part of the crest wall (similarly to the probes).

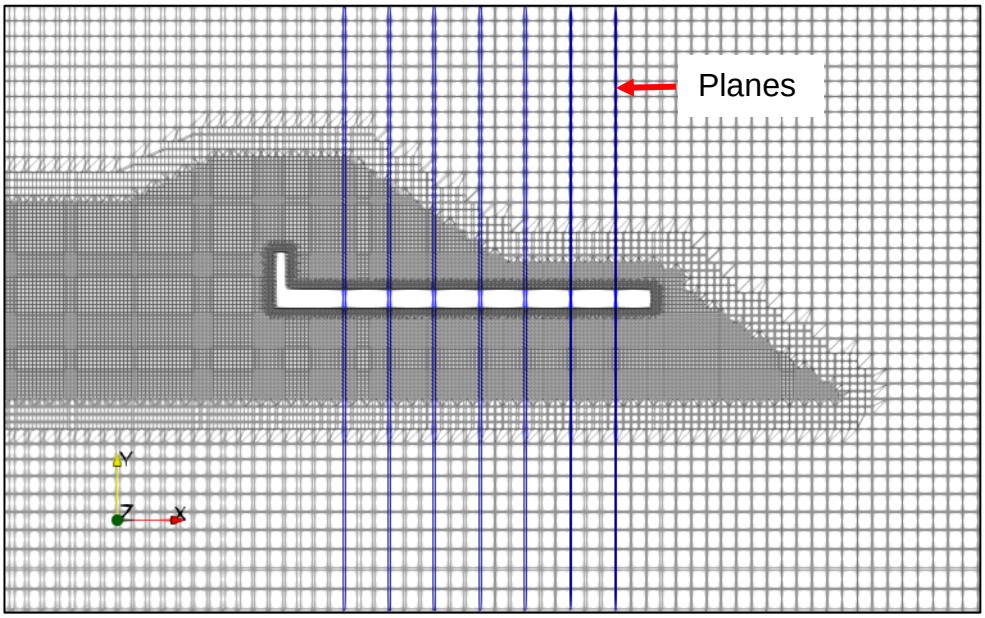

Figure 20. Set-up of planes to extract the flow velocities in the numerical flume.

In the same manner as for the probes, the planes do not differentiate if the velocities are associated to air, water, or a mixture of both. Here, the same original strategy utilized for the probes of postprocessing the velocities when the associated indicator function surpassed 0.7 was used. Hence, Equation 7 was also used to compute the depth-averaged flow velocities (refer to section 2.2.10 for more details).

2.2.10. Overview of changes in the numerical model

This section offers a guide to the reader of all the variations carried out through the different stages of the numerical model set-up (and associated sensitivity analyses), validation, and further sensitivity analyses where variations in the wave conditions and breakwater geometry were effectuated. The objective of this section is to help the reader to better follow the report. The conclusions that were drawn from each of these steps are not presented here but in other sections of the document.

a) Grid sensitivity analysis for wave propagation: All the cases were run with, at least, 250 waves. The length of the inlet relaxation zone was defined as the largest deep-water wave length of all the tests performed under normal incident waves in the Delta Basin campaign. The length of the outlet relaxation zone was fixed around 2 m. The 2 m are not related to a particular portion of the wave length of any of the tests. It was chosen to be short because even if it was not completely non-reflective, most of the wave energy reflected at the outlet relaxation zone would get dissipated at the porous structure. The distance between the end of the inlet relaxation zone and the first numerical wave gauge (from left to right) was set as 0.55 m. Different grid cells sizes for the base mesh and the mesh around the water level were tested.

b) Other variations for wave propagation: Continuation of the previous step. The size of the grid cells of the different mesh components was fixed, except for one case where gradation[14] was effectuated at the top and bottom of the mesh. The cases were run with 250 waves, at least. The length of the inlet and outlet relaxation zones were varied. The distance between the end of the inlet relaxation zone and the first numerical wave gauge (from left to right) was also changed.

c) Calibration of incident waves: The configuration of the numerical flume was fixed from the results of the sensitivity cases for wave propagation. The incident waves were calibrated to obtain the target H_{m0} at the position of the first numerical wave gauge. The tests were run with 500 waves. It was observed that the H_{m0} obtained with 500 waves was similar to the one obtained with 1000 waves. The maximum absolute percentage of error was around 2% or even smaller.

d) Validation of incident waves and mean overtopping discharge: In this part it was relevant to obtain a reliable distribution for the incident waves and mean overtopping discharge. Therefore, the validation of the incident waves and mean overtopping discharge were carried out with 1000 waves. The numerical flume was fixed according with the results obtained from the sensitivity cases of wave propagation.

e) Sensitivity cases regarding the set-up of the numerical instruments to compute the flow depths and velocities: The numerical flume was fixed according to the results obtained from the sensitivity cases of wave propagation. The spacing between adjacent measuring devices was changed (initially, 4 cm were used, and the final separation was fixed at 12 cm). The position of the wave gauges was varied in the vertical with respect to the horizontal part of the crest element as part of the sensitivity cases. More than 250 waves were used in the sensitivity cases regarding the position of the wave gauges. For the computation of the flow velocities with the probes and the planes, Equation 7 was used. The velocities with an indicator function smaller than 0.7 were filtered out. Only around 70 waves were used for the sensitivity cases related to the computation method of flow velocities (discharge sheets and wave gauges, probes, and planes). An impermeable breakwater was used to compare the methods of estimation of depth-averaged flow velocities.

f) Grid sensitivity analysis for the computation of flow depths and velocities: The numerical flume was fixed according with the results obtained from the sensitivity cases of wave propagation. Nevertheless, the mesh around crest wall was changed. The cases were run for, at least, 250 waves. To analyze the effect of the grid changes on the calculation of the depth-averaged flow velocities, Equation 8 was used.

g) Validation of flow depths and velocities: The set-up of the numerical flume included the last findings obtained from the grid sensitivity performed around the crest element. The validation of the flow depths and velocities was effectuated with 1000 waves to get reliability in the distribution of the exceedance curves.

h) Sensitivity cases to determine the influence of different wave conditions and protrusion heights on the estimation of flow depths and velocities: The cases were run with the final numerical flume configuration (including the final mesh around the crest wall). 1000 waves were used since the interest was on the distributions of the extreme events. The depth-averaged flow velocities were computed using Equation 8.

[14] Gradation refers to a progressive change in cell size in one particular direction.

2.3. Goodness of fit measures used to validate the numerical model

Three parameters were used to compare the fit of the computed values with respect to the measured ones, the relative error, the bias, and the RMSE. The relative error shows the difference of the computed value with respect to the expected value (in percentage). The bias is defined as the averaged ratio of predicted over measured values, and the RMSE gives an indication of the spreading of the calculated with respect to the measured values. The lower the value of these three indicators, the closer the computed values are with respect to the measured ones. Equation 9, Equation 10, and Equation 11 present the expressions to compute the relative error, the bias and RMSE.

$$\text{relative error } (\%) = \left(\frac{\text{measured value} - \text{computed value}}{\text{measured value}}\right) * 100 \qquad \text{Equation 9}$$

$$\text{Bias} = \frac{\sum_{i=1}^{n_{tests}} \left(\frac{\text{computed value}}{\text{measured value}}\right)}{n_{tests}} \qquad \text{Equation 10}$$

$$\text{RMSE} = \sqrt{\frac{\sum_{i=1}^{n_{tests}} (\log(\text{measured value}) - \log(\text{computed value}))^2}{n_{tests}}} \qquad \text{Equation 11}$$

2.4. Description of additional simulations to investigate the influence of two parameters on the computed flow depths and velocities

With the validated numerical model (see Chapter 4), additional simulations were effectuated to study the effect of changing the wave conditions and the protrusion height on the flow depths and velocities. For this purpose, a total of 15 simulations, with 1000 waves each, were carried out. The breakwater configuration with the crest wall and without the berm was used. The water depth at the seaward boundary of the breakwater, and the structure slope were maintained for all the simulations. They were kept as in the physical model tests (d = 0.80 m, and a seaward slope of 1:2). In the following, a more detailed description of the variation cases is presented.

2.4.1. Simulations to study the impact of changing wave conditions

To study the effect of the variation in the wave conditions on the flow depths and flow velocities, three different wave heights were analyzed in combination with three different wave steepness. The wave heights were defined in such a way that they were within the range of wave heights considered for the physical model tests. It was decided to model the smallest and highest wave heights of these experiments (H_{m0} = 0.08 and 0.16 m, respectively), and the one in between these two (H_{m0} = 0.12 m). With respect to the wave steepness, the two original wave steepness present in the physical model tests were considered in the simulations (s_{op} = 0.015 and s_{op} = 0.04). The third modelled wave steepness was defined as the one in between these two (s_{op} = 0.027). The protrusion height was fixed as 0.053 m, such as in the physical model tests. The resulting 9 cases are summarized in Table 4.

Table 4. Cases related to the variation in the wave conditions.

Case ID	H_{m0}/d [-]	H_{m0} [m]	T_p [s]	s_{op} [-]
1	0.1	0.08	1.85	0.015
2	0.1	0.08	1.38	0.027
3	0.1	0.08	1.13	0.04
4	0.15	0.12	2.26	0.015
5	0.15	0.12	1.69	0.027
6	0.15	0.12	1.39	0.04
7	0.2	0.16	2.61	0.015
8	0.2	0.16	1.95	0.027
9	0.2	0.16	1.60	0.04

The results of changing the wave conditions are shown in section 5.2.

2.4.2. Simulations to study the effect of varying protrusion height

The impact of changing the height of the protrusion was also analyzed in combination with varying wave steepness. Three different protrusion cases were considered: no protrusion (R_c-A_c = 0 m), same protrusion as in the original physical model tests (R_c – A_c = 0.053 m), and a higher protrusion (R_c – A_c = 0.08 m). Where R_c is the vertical distance between the still water level and the top of the crest wall, and A_c is the vertical distance between the still water level and the seaward armor crest level. The same three wave steepness considered in 2.4.1 were modelled. The wave height was not varied in the simulations. It was decided to work with the highest wave height (H_{m0} = 0.16 m) to ensure the numerical model would be able to solve the flow depths and velocities even for the cases with more protrusion (R_c – A_c = 0.08 m). The resulting 9 cases are shown in Table 5.

Table 5. Cases related to the variations in the protrusion height.

Case ID	H_{m0}/d [-]	H_{m0} [m]	T_p [s]	s_{op} [-]	R_c-A_c [m]
10	0.2	0.16	2.61	0.015	0.00
11	0.2	0.16	1.95	0.027	0.00
12	0.2	0.16	1.60	0.04	0.00
13	0.2	0.16	2.61	0.015	0.053
14	0.2	0.16	1.95	0.027	0.053
15	0.2	0.16	1.60	0.04	0.053
16	0.2	0.16	2.61	0.015	0.08
17	0.2	0.16	1.95	0.027	0.08
18	0.2	0.16	1.60	0.04	0.08

The three cases that have a protrusion of R_c-A_c = 0.053 m also were part of the set of simulations presented in Table 4. For this reason, 15 simulations were performed (instead of 18). Figure 21 depicts each of the modifications in the protrusion height, to help the reader comprehend what each of them involve.

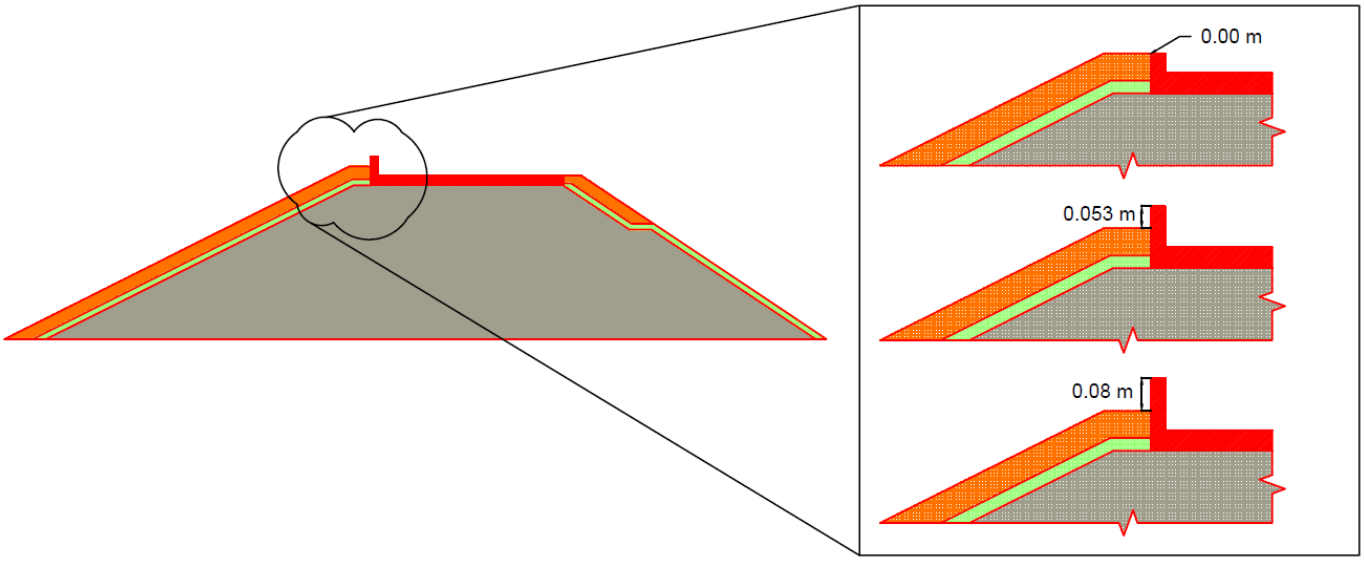

Figure 21. Modifications in the protrusion height to evaluate its respective influence in the computed flow depths and velocities.

The results of modifying the protrusion height can be consulted in section 5.3.

2.5. Determination of individual extreme events

To comply with the objectives of this research and present the influence of different parameters on the flow depths and velocities, calculating the exceedance curves of these variables is necessary. To obtain the exceedance curves, and any point that belongs to them (e.g., the flow depths and velocities exceeded by 2% of the incoming waves), it is necessary to identify the individual events. In this section, the approach that was used to determine such events is discussed.

The automated methodology that was used to separate individual events works in a similar manner to the "peak over threshold method"[15]. Given a timeseries of flow depths or flow velocities, the following steps were taken:

a) First, a threshold was defined. Determining the threshold value depended on the type of timeseries itself. In the case of the flow depths timeseries, an almost constant layer of water was visible during the whole simulation time. This thin layer of water was formed due to the incapability of the overtopped water to infiltrate through the impermeable crest element. Therefore, the threshold value had to be higher than this constant thin water layer. In addition to this, the threshold value had to be defined a bit higher, due to the presence of a tail at the end of each event. For the flow velocities timeseries, the definition of the threshold depended entirely on the event tails.
b) Then, a routine was created that checked the signal at each computational timestep. When a value larger than the threshold was detected for the first time, it was taken as part of the first event. Successive signal values larger than the threshold were considered as part of the same event. Due to numerical wiggles, the signal dropped below the threshold, but in successive timesteps, it surpassed the threshold again. In these occasions, the method was able to identify that these sudden and short drops were part of the same event.

[15] A detailed statistical analysis to determine whether the separated events were really independent was not performed in this research.

c) Next, to identify separate events, the routine examined if the time in between two consecutive signal values larger than the threshold was longer than half the mean wave period of the incident waves.
d) After that, the routine checked that the minimum event duration was at least three computational timesteps. If an event was found with a shorter duration, it was discarded. It is supposed that in this case, the short event duration was caused by an error in the measuring device.
e) Finally, the maximum value per valid event was found and saved.

With the maximum value per event, computing the exceedance curves was possible. The procedure to arrive to the exceedance curves won't be treated here. It is pertinent to mention that the exceedance curves were calculated in terms of the percentage of incoming waves (around 1000 waves). Figure 22 presents an outline of the process followed to determine the individual events and their associated maximum value.

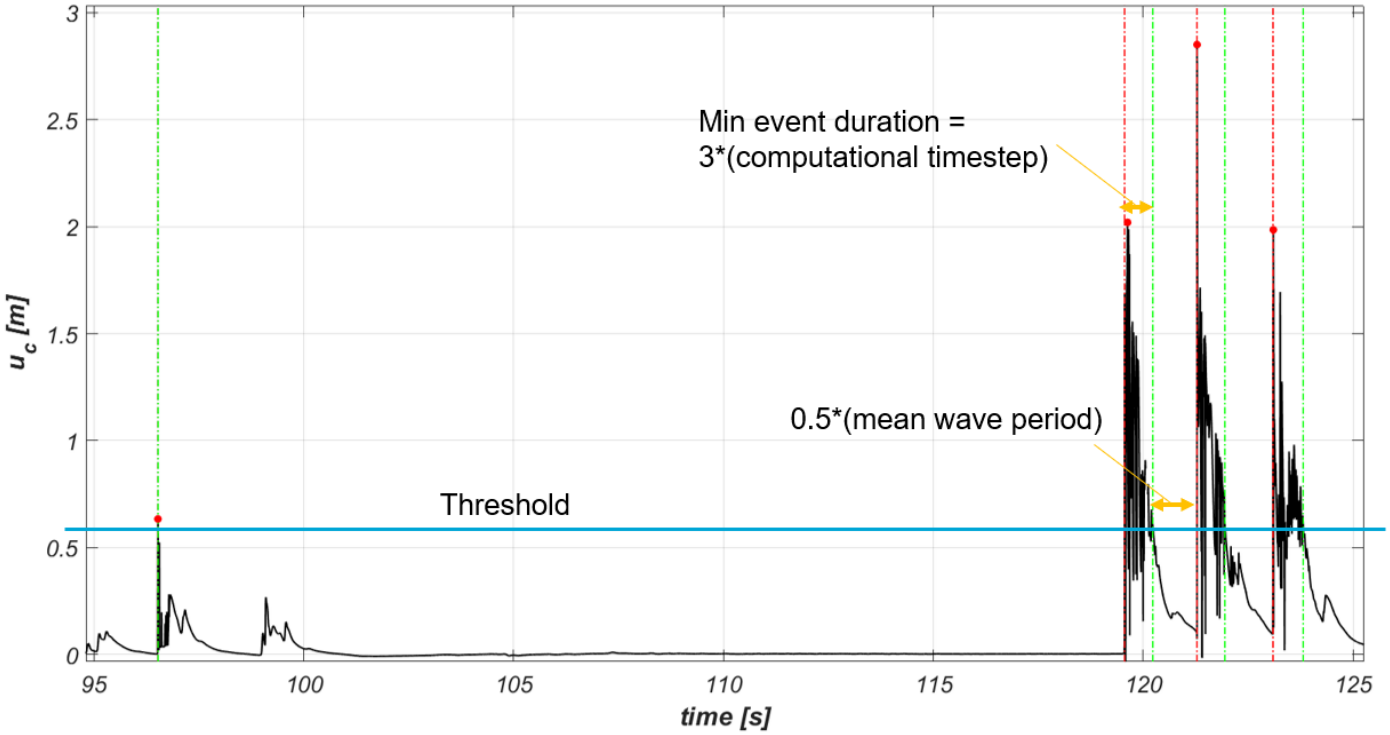

Figure 22. Procedure followed to identify individual events. The dashed lines indicate the start (red) and end (green) of each event. The red dots show the maximum per event.

It is relevant to mention that the threshold was varied in between the simulated cases. The threshold was defined iteratively based on the wave conditions, and the magnitude of the resulting flow depths and velocities (including the thickness of the constant layer of water that was formed on top of the horizontal part of the crest element). The events identified by this automated methodology were visually inspected to ensure that most of them were captured. For this purpose, the flow depth or velocity timeseries was plotted along with identifiers associated to the start and end of each event, and their maximum values (see Figure 22).

This automatic approach was used to detect the individual events for most of the simulations. For the simulations executed with very small wave heights (Hm0 = 0.08 m), there were only a few events capable of overtopping the structure. For the specific case of the flow depth timeseries, the thin constant layer of water varied significantly with time, which complicated the definition of a constant threshold. Therefore, the maximum values of the most extreme events were picked manually by the author.

3. Preferred method of extraction of flow depths and velocities

3.1. Flow depths

As mentioned in section 2.2.9.1, the flow depths were calculated by means of wave gauges placed in the crest region. Some sensitivity cases were effectuated to determine if the flow depths were extracted correctly. For this purpose, the placement of the wave gauges was varied in the vertical with respect to the position of the horizontal component of the crest wall. The lower tip of the wave gauges was located at the bottom, at the middle and at the top of the horizontal part of the crest element. An example of the resulting flow depths timeseries is presented in Figure 23. In this case, they are shown for the location x = 16.44 m (see Figure 16), and for the test Th00155 (see Table 1). The top, the middle and the bottom panels show the extracted flow depths when the wave gauges are placed at the bottom, the top and the middle of the horizontal part of the crest element. It can be observed that the middle and lower panels have coincident timeseries. The same behavior was observed for the other wave gauges located along the crest. When the lower tip of the wave gauges is located at the bottom of the crest element, negative flow depths were obtained.

OpenFOAM® saved the hydrodynamics output of the entire numerical flume each 20 seconds. This output was used to further validate the computed flow depths when the lower tip of the wave gauges is placed at the middle and the top of the horizontal part of the crest wall. For the sake of brevity, the associated figures are not presented in this section. Nevertheless, these comparisons can be found in Appendix C.2. It was concluded that when the wave gauges are placed starting at the middle and at the top of the horizontal component of the crest wall, the flow depths are computed correctly. It is believed that when the lower tip of the wave gauges is located at the bottom edge of the crest element, the flow depths are polluted with the water flow that occurs in the porous region below the crest wall. The author decided to stick to the approach of placing the lower tip of the wave gauges always at the top of the horizontal part of the crest wall for further validation and sensitivity cases. This configuration is also suggested for researchers in the verge of performing similar studies in OpenFOAM®. This is because the minimum required distance in between the lower tip of the wave gauges and the bottom of the crest element is unknown, and it might be grid sensitive. The reader is referred to Appendix C.2 for a detailed explanation of the step-by-step sensitivity analysis carried out to extract the flow depths.

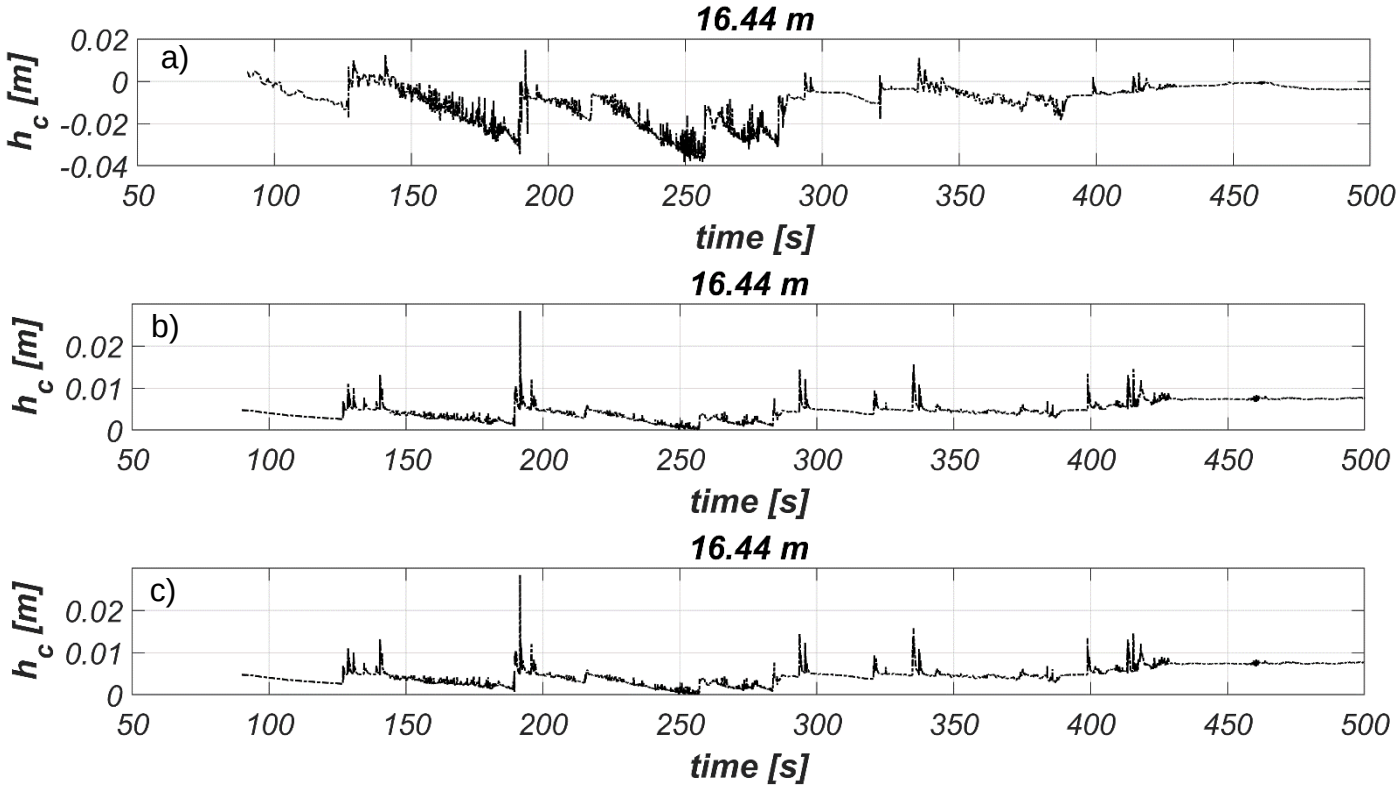

Figure 23. Flow depths at the location x = 16.44 m and for the test Th00155. The lower tip of the wave gauges was located at a) the bottom, b) the top, c) and the middle of the horizontal component of the crest element.

3.2. Flow velocities

As explained in section 2.2.9.2, three methods were employed to extract flow velocities (depth-averaged): wave gauges and discharge sheets, probes, and planes. A test with an impermeable breakwater was utilized to compare the flow velocities computed with the three options. It turned out that when the discharge sheets and wave gauges are used, very high non-physical flow velocities happen at certain computational timesteps. It was found that this problem is caused by very thin flow depths or by very high overtopping discharges that occur in the simulations. In the first case, the division of the overtopping discharges over these thin flow depths result in non-realistic flow velocities. In the second case, when very high overtopping discharges are divided by (not very small) flow depths, also very high flow velocities are obtained.

To calculate the flow velocities by means of the probes and planes, Equation 7 was used. At this stage, only the flow velocities occurring at the same time and position as indicator functions higher than 0.7 were further postprocessed. It was discovered that the flow velocities computed from the probes and planes are very similar. They do not seem to be overestimated. These last two methods are more reliable than the one using discharge sheets and wave gauges, as the flow velocities are extracted directly from the numerical model. Figure 24 presents an example of the flow velocities obtained for a specific location (x = 16.32 m, in numerical coordinates, see Figure 16) with the three proposed methods. Finally, the probes are the recommended method given that it takes less time to postprocess the output from OpenFOAM®. The reader is referred to Appendix C.3 for a more detailed explanation on the procedure followed to arrive to these conclusions.

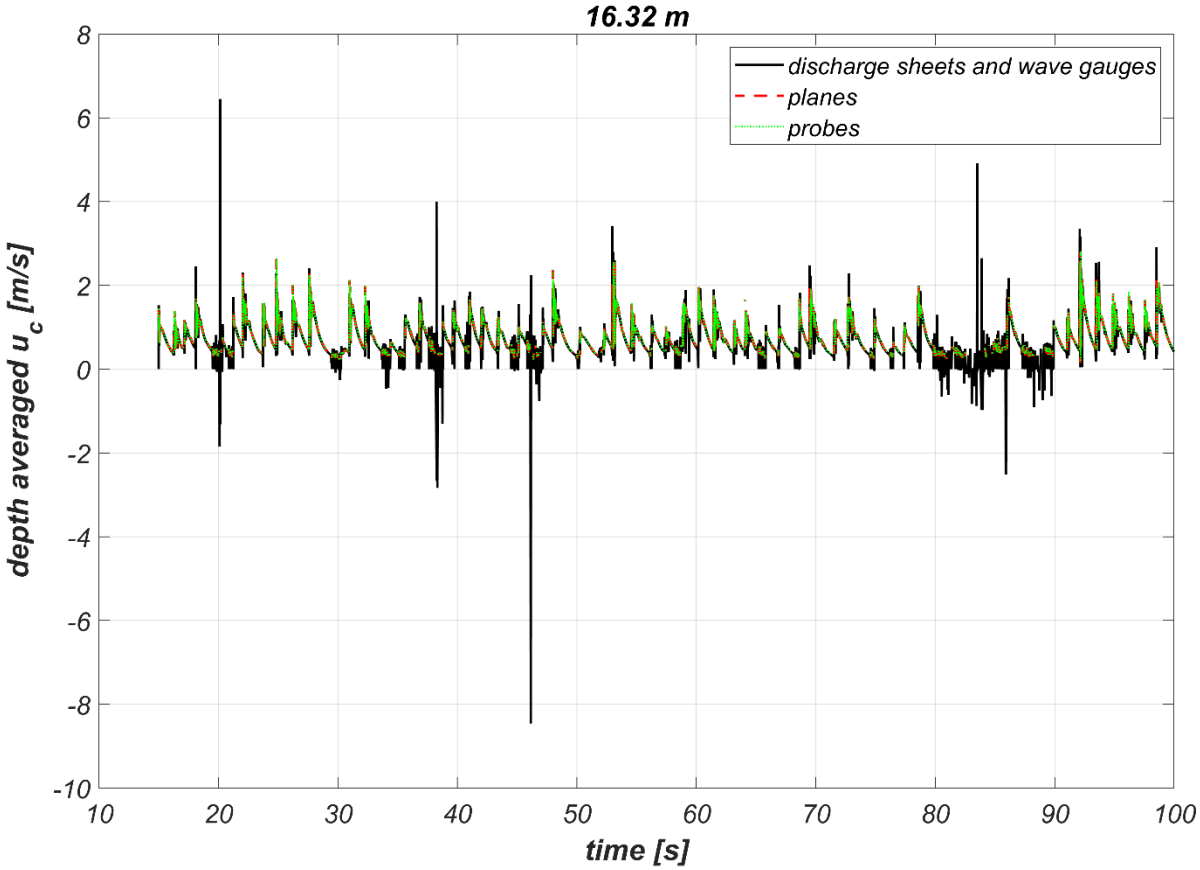

Figure 24. Flow velocities obtained with the three proposed methods.

Besides the sensitivity analysis executed to determine which was the most appropriate approach to extract the flow velocities, a grid sensitivity analysis was also performed. This one comprised identifying the coarsest mesh enclosing the crest element that showed the better balance in between accuracy and computational time to estimate the flow velocities (and flow depths). This sensitivity analysis is explained in detail in Appendix C.4, respectively. Equation 8 was used to compute the flow velocities.

From the sensitivity analysis performed on the mesh surrounding the crest element, it was found that cell sizes of 0.5 cm x 0.5 cm were required to solve the flow depths and velocities more accurately. When the mesh around the crest wall is kept with the same characteristics as the mesh around the water level (grid cells of 1 cm x 1 cm), there was a lot of noise generated due to the incapability of the numerical model to solve small flow depths and velocities. Increasing the thickness of the fine mesh enclosing the crest element, did not result in an improvement of the estimation of the flow depths and velocities. Figure 25 presents the results of the influence of different mesh characteristics around the crest wall on the timeseries of the depth-averaged flow velocities. To keep the report brief, the same result is not presented for the flow depths. In this case, the reader is referred to Appendix C.4, which also contains a more detailed explanation of the conducted grid sensitivity analysis (around the crest element).

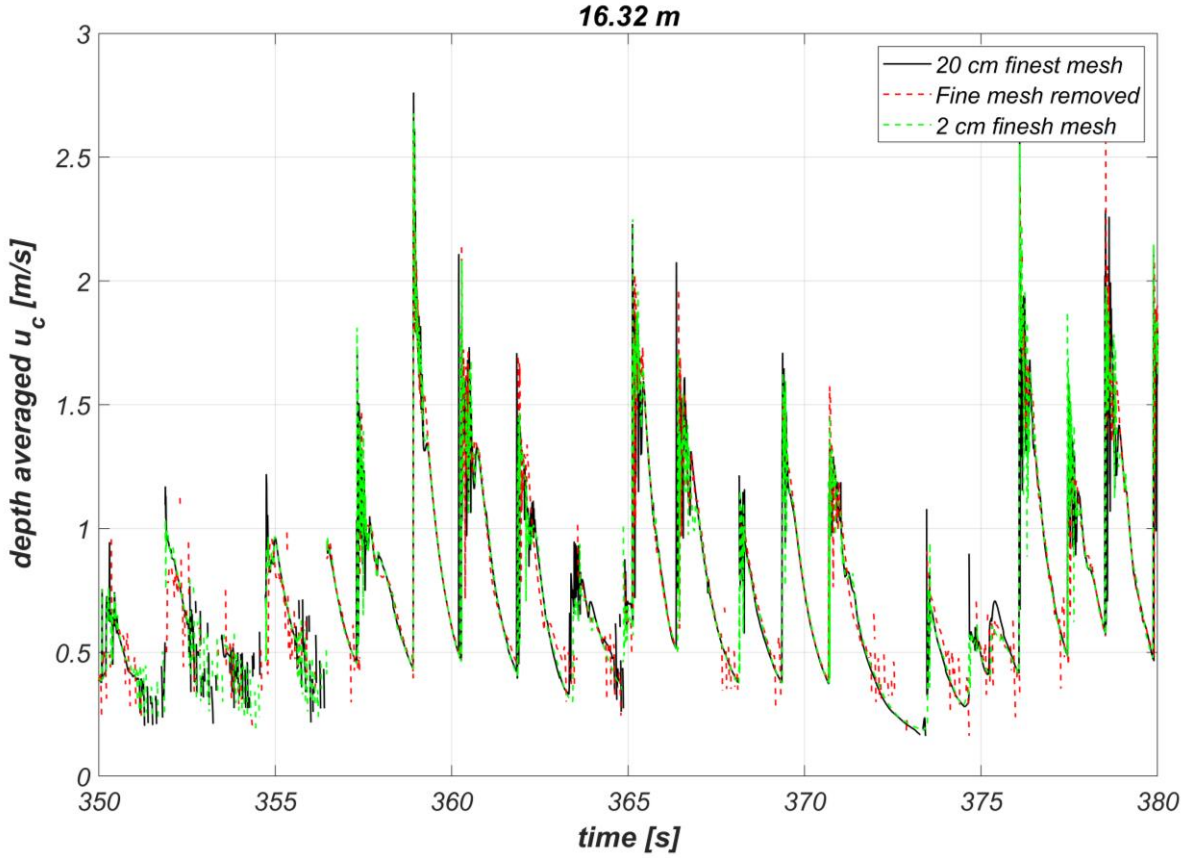

Figure 25. Depth-averaged flow velocities timeseries for the location x = 16.32 m with variations in the mesh around the crest element of the breakwater.

4. Validation of the numerical model

As was explained in section 2.1, some of the tests effectuated in a campaign in the Delta Basin, at Deltares, were picked to validate the numerical model. One set of tests was used to compare the incident waves and overtopping discharge of the physical model tests and numerical model (see Table 1). A different set of tests was utilized to compare the modelled and measured flow depths and velocities (see Table 2). In the following sections the results of the validation process are shown.

4.1. Incident waves

To generate the waves in OpenFOAM®, the input significant wave height was calibrated to obtain the target incident significant wave height at the position of the first numerical wave gauge (from left to right in the numerical domain). It was not attempted to calibrate the input significant wave height to obtain the measured incident significant wave height at the position of the physical wave gauge, as the later real values were not known during the execution of this research (see section 2.1).

Given the fact that the wave paddle velocity signal of the tests was not used to create the waves in the numerical model, it was not possible to compare the time signal measured at the position of the physical wave gauge GRSM02. Instead, the validation of the capability of OpenFOAM® in computing the incident waves was performed from a statistical perspective.
Table 6 shows the comparison, including the relative error, between the measured and computed spectral parameters at the position of the physical wave gauge GRSM02.

Table 6. Comparison of measured and computed spectral parameters.

Test ID	Berm	Measured data		Computed data		Relative error	
		H_{m0} (m)	$T_{m-1,0}$ (s)	H_{m0} (m)	$T_{m-1,0}$ (s)	H_{m0}	$T_{m-1,0}$
Th00151b	No	0.076	1.698	0.080	1.749	-5.09%	-2.96%
Th00155	No	0.094	1.870	0.101	1.946	-7.62%	-4.06%
Th00401	No	0.082	1.084	0.076	1.179	8.05%	-8.82%
Th00402d	No	0.114	1.294	0.118	1.378	-4.06%	-6.54%
ThB00155	Yes	0.106	1.910	0.101	1.942	5.56%	-1.63%
ThB00152	Yes	0.131	2.075	0.121	2.124	7.56%	-2.37%
ThB00406	Yes	0.137	1.420	0.145	1.492	-6.18%	-5.06%
ThB00403	Yes	0.145	1.500	0.155	1.571	-6.99%	-4.73%

Note: The spectral parameters were estimated based on the data measured at the physical wave gauge GRSM02.

Negative values of the relative error indicate that the computed values are larger than the measured ones. The errors fluctuate between positive and negative in the case of the incident significant wave height (bias of 1.01), which suggest that overall, there is no systematic overprediction or underprediction of this parameter. On the other hand, all the errors in $T_{m-1,0}$ are negative, which indicate that the numerical spectral wave periods are larger than the measured ones (bias of 1.05). The higher computed $T_{m-1,0}$ values are associated to a larger concentration of wave energy in the lower frequencies, and less concentration of wave energy in the higher frequencies of the wave energy spectra. This can be observed when the computed and measured wave energy spectra are compared (see Appendix C).

4.2. Wave overtopping discharge

Since the time series of the surface elevation of the numerical model runs and the tests are different, it is not possible to compare the computed and measured individual overtopping events. However, the overtopping discharges can be compared with statistical parameters. For this purpose, the validation of the numerical model regarding the simulation of overtopping discharges was effectuated by comparing the non-dimensional mean overtopping discharge from the tests and the numerical simulations (see Figure 26). It is observed that despite the computed incident significant wave height is very close to the target value, the non-dimensional mean overtopping discharge is overpredicted for all the simulated tests except one (i.e., the one with smallest discharge). Overprediction of the wave overtopping discharges by OpenFOAM® has also been found in other studies (e.g., Chen et al., 2021; Irías Mata and Van Gent, 2023). It can also be observed from Figure 26 that the non-dimensional mean overtopping discharges are even larger with respect to the measured values in the cases where the berm is present. It seems the applied numerical model is underpredicting the dissipation capacity of the berm. Underprediction of the berm dissipation was also found by Chen et al. (2021).

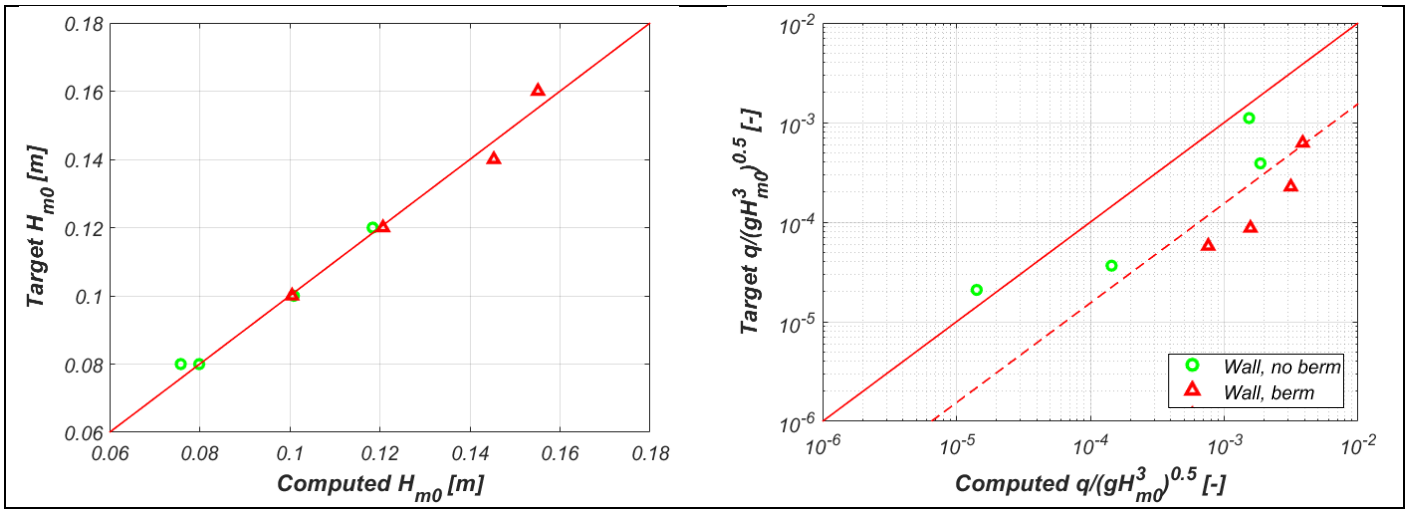

Figure 26. Comparisons of computed and measured non-dimensional mean overtopping discharges. Here H_{m0} corresponds to the target value of the experiments, but the mean overtopping discharge (q) is the measured one.

The bias for the 8 modelled tests was a factor 7.8, which suggest that the numerical model overpredicts the non-dimensional mean overtopping discharge by a factor 7.8 on average. The bias can be visualized as the dashed line presented in Figure 26. It seems the bias estimated here is quite large compared to other studies concerning prediction of the mean overtopping discharge with OpenFOAM® (e.g., Irías Mata and Van Gent, 2023). However, in this case, the bias is partially caused by the model itself, but also by the uncertainty in the input data. The later refers to the absence of the calibrated measured spectral parameters of the physical model tests at the time of performing these numerical activities. The RMSE of these 8 cases was calculated as 0.84. When the most recent empirical equation to predict mean overtopping discharges is used (Van Gent et al., 2022)[16], it is found that the bias and RMSE correspond to 0.48 and 0.97, respectively. Here again, the uncertainty in the input data affects the result of these two fit estimators. When comparing the goodness of fit estimators of both methods of calculation of the mean overtopping discharge, it can be concluded that the empirical formulas (by Van Gent et al., 2022) have a better prediction of the mean overtopping discharge (due to the smaller bias) but with more spreading when compared to the numerical prediction with OpenFOAM® (due to the larger RMSE).

[16] Since the real spectral parameters were not known at the moment of carrying out this research, $T_{m-1,0}$ was estimated from the formula T_p=1.1* $T_{m-1,0}$, which holds for irregular waves in deep water based on a JONSWAP spectrum with a peak enhancement factor of 3.3.

There are some possible causes for the overprediction of the numerical mean overtopping discharge. The first one is related to the spectral wave periods ($T_{m-1,0}$). As was already discussed in section 4.1, the numerical spectral wave periods are higher than the measured ones. A high spectral wave period generates a lower wave steepness, and it is known that a lower wave steepness causes more overtopping discharge (see Van Gent et al., 2022; Irías Mata and Van Gent, 2023). The second reason is associated with the non-physical damping caused by the numerical model. It adds extra resistance which does not allow water to penetrate the porous media. Hence, water overtops the structure instead. As was explained in section 2.2.6, this mechanism can be counteracted by calibrating the resistance coefficients of the Darcy- Forchheimer equation.

Future research should be performed to determine if the absence of a detailed turbulence model affects the modelling of wave breaking outside the breakwater and in the seaward slope of it. It remains to be verified if the inaccuracies on the prediction of wave breaking have an effect on the overtopping discharge. The influence of non-physical entrapped air on the computed wave overtopping should also be studied.

4.3. Validation of the flow depths and velocities

To determine how accurate the numerical model reproduces the flow depths and velocities, exceedance curves were computed for six physical model tests. These exceedance curves were computed for variable distances with respect to the vertical part of the crest wall. The tests that were used for the validation were previously presented in section 2.1. In this section, a summary of the most relevant conclusions regarding the comparison of the modelled and measured flow depths and velocities will be mentioned. The results and corresponding detailed explanation are shown in Appendix F.

Regarding the flow depths, their method of extraction is similar in the numerical model and in the physical model tests. The numerical and physical wave gauges sum all the water they find in the vertical, at each timestep, and reference it with respect to a particular elevation. Nevertheless, the trends observed from the exceedance curves computed from the modelled and measured flow depths differ. In the case of the numerical model, flow depths become thinner the longer is the distance from the seaward boundary. The measurements indicate a decrease, then an increase and finally a decrease of the flow depths. The expected behavior is the one indicated by the modelled flow depths given that friction dissipates the water energy as the events propagate along the crest. Then, further study is required to comprehend why the flow depths obtained from the experiments show such tendency, and to validate the flow depths obtained from the numerical model.

Regardless of the differences in trends observed from the flow depth exceedance curves, the modelled flow depths are some orders of magnitude larger than the measured ones. In fact, for the most extreme events, the modelled flow depths represent a high percentage of the wave height themselves, which is not expected. This overestimation of the flow depths is strongly connected to the overprediction of the overtopping discharge. The bias factor of the flow depths varies in a wide range, depending on the distance to the seaward boundary and the exceedance probability. Nevertheless, it is unclear how it is connected to the bias factor of the non-dimensional mean overtopping discharge. It might be happening that the development of the overtopping process in the numerical model has an influence in the extracted flow depths. In addition, having more overtopping discharge in the numerical simulations influences the detection of the number of events (more events are captured in the numerical model than in the experiments), and in the constant layer of water that is formed (layer formed because water cannot infiltrate through the crest wall), which is thicker in the numerical model.

It was observed that the trend of the low exceedance probability part of the exceedance curves is different for the measured and modelled flow velocities. For the former, they decrease with increasing distance from the vertical part of the crest wall, which is the expected behavior given that

the energy gets dissipated as events propagate along the crest. For the later, they increase with more distance from the vertical component of the crest wall until a point when they start to decrease. In opposition, for the high exceedance sector of the exceedance curves, the modelled flow velocities also decrease the closer they were extracted to the port side. When comparing the magnitude of the flow velocities, it was found that the flow velocities occurring during the physical model tests were higher for the most extreme events, and smaller for the events occurring more frequently.

The differences in the trends of the flow velocity exceedance curves can partly be explained by the method of calculation of the flow velocities. In the case of the physical model tests, they were approximated based on the time it took for the events to displace in between consecutive pins in the layer thickness gauge. As for the flow velocities of the numerical model, they were depth averaged. In other words, the computation methods are not comparable. Also, in the situation when there is flow moving towards the sea, this would only be considered in the modelled flow velocities given the nature of their extraction and computation. In addition, the influence of the overprediction of the overtopping discharge is also visible from the flow velocity exceedance curves, as more events were captured from the simulations.

Given the differences in trends, and magnitude of the measured and modelled flow depths and velocities, it can be concluded that the numerical model is not accurate enough to reproduce them. There is a strong connection in the overprediction of the modelled overtopping discharge and the incapacity of the numerical model to properly reproduce the flow depths and velocities. The distinct methods of extraction and computation of the measured and modelled flow velocities also makes it difficult to validate the numerical model. Despite that, the numerical model is still valuable to explain the physical processes that occur during the wave overtopping events. It can also be useful to further study the impact on the flow depths and velocities when changes are effectuated in the wave conditions and the configuration of the breakwater.

5. Influence of two parameters on the modelled flow depths and velocities

In the next subsection, a summary of the physical processes is effectuated. In the remaining subsections, the effects on the flow depths and velocities when varying the wave conditions and protrusions heights is presented by means of exceedance curves.

5.1. Observed physical processes

In this section, the physical processes happening during the wave overtopping events are depicted with screenshots taken from the numerical flume. For this purpose, the output of the hydrodynamics was obtained for very short timesteps (0.05 s). The results presented correspond to the simulations with the largest wave height and lowest wave steepness (H_{m0} = 0.16 m, and s_{op} = 0.015), with the breakwater configuration without the berm, without protrusion ($R_c - A_c$ = 0 m) and with the highest protrusion ($R_c - A_c$ = 0.08 m). The figures below present the evolution of one specific overtopping event. To ease the comparison process when there is a presence or absence of protrusion, the same event was used for both cases. Figure 27, Figure 28, Figure 29, and Figure 30 show the development of the surface elevation (|by means of the indicator function of the VOF method, F), and the vertical and horizontal velocities over time. The wave gauges and some probes (the ones with the highest elevation) were included in the figures, to help the reader comprehend how the overtopping event evolves in relation to the measuring devices. Below, an explanation of the occurring processes is found.

a) First, a wave with a sufficient height to overtop the structure approaches the seaward boundary of the crest wall (see Figure 27 a and b). What happens next, strongly depends on whether there is protrusion in the configuration of the breakwater.

b) When there is no protrusion (left panels), the event more easily overtops the breakwater. The pull of gravity might cause a small portion of the wave tongue to fall before it is able to overtop the structure (see Figure 27 c). When there is protrusion (right panels), the wave tongue impacts the wall. Then, part of the volume falls, and the remaining part is boosted until it reaches a higher elevation and overtops the breakwater (see Figure 27 d).

c) As soon as the event starts to overtop the structure, it seems to undergo projectile motion. Then, water might follow a parabolic trajectory. At this stage, the flow is dominated by gravity. This force acts in the vertical direction and causes variations in the vertical component of the velocity of the water particles. Then, as the mass of water moves upwards, it gets decelerated and as it moves downwards, it gets accelerated. When the event reaches its maximum height, its vertical velocity is zero. The horizontal velocity seems to remain constant during the parabolic travel time. This situation can be observed in Figure 28 (with protrusion) and Figure 29 (without protrusion). In these figures, the vertical velocities change color from red till blue, indicating a change of acceleration and direction. On the other hand, the color of the horizontal velocities barely changes.

d) The position of impact of the event at the horizontal part of the crest element depends on the protrusion height. It was observed that for the extremer events (higher waves), the distance covered by the event before hitting the horizontal component of the crest wall is longer when there is larger protrusion (see Figure 27 e and f). In addition, when there is protrusion, the impact against the wall causes the overtopping event to get deviated, and to take longer to fall and hit the horizontal part of the crest element.

e) After the event impacts the horizontal part of the crest wall, most of the water volume accelerates and moves towards the landward side of the structure. Nevertheless, a portion of it accelerates and deviates towards the seaward side (see Figure 27 e, f, g, and h). It can also be observed from these panels that water moves towards the seaward side, along the crest, at the same moment as water is still overtopping the structure. In other words, during the overtopping event,

there are positive and negative velocities at the same time. This type of flow is not an eddy since there is air above the seaward flow, and above this air, the overtopping jet to the portside is present. Additionally, as water propagates along the horizontal component of the crest element, friction acts upon it, and dissipates its energy.

f) Concerning the water volume that moves towards the seaward side, it does not fall from the structure due to the presence of the downward step (from the vertical part of the crest wall to the horizontal part of the crest wall). Instead, water moves upwards along the wall, until it reaches a velocity of zero in the vertical (see Figure 27 i and j). Then, it slowly falls to the horizontal part of the crest element and accelerates again towards the port side.

g) For the part of the water volume that propagates in the landward direction (to the port side), it was observed that for the extremer waves, the water gets more accelerated when the protrusion is higher (see Figure 30). It is suspected that this happens because the overtopping event reaches a higher elevation (at the peak of the parabolic motion) when there is a larger protrusion. This can be associated with more energy storage (potential energy) which is then released at the moment of the impact against the horizontal part of the crest wall.

h) For the studied overtopping event, it was observed that for a distance sufficiently far from the seaward boundary, the flow depths are thinner for the case with a larger protrusion (see Figure 27 g and h). This is the location where the flow depths have stabilized into a single overtopping layer of water after the impact of the event against the horizontal part of the crest wall.

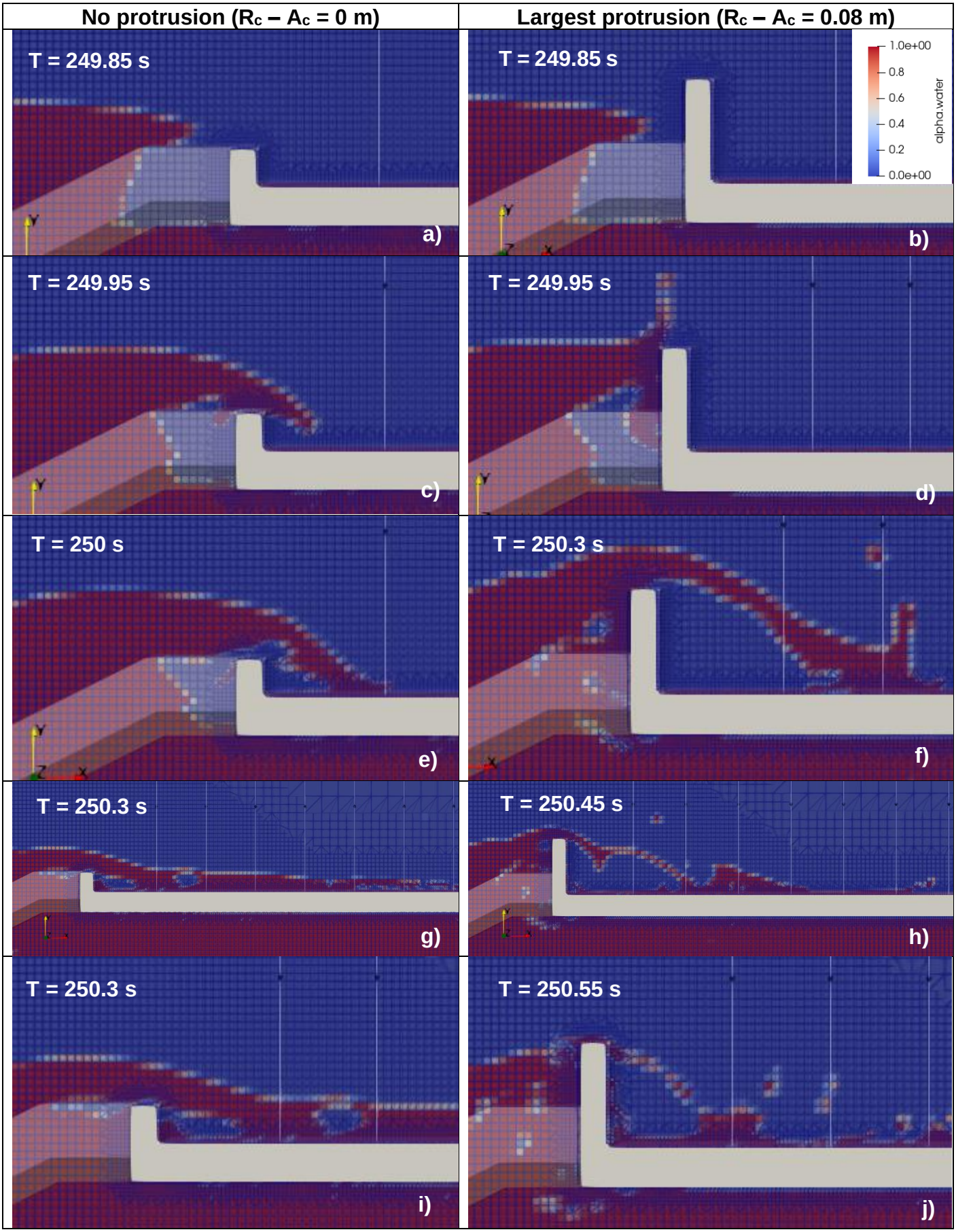

Figure 27. Evolution of one event after overtopping the breakwater with and without protrusion. Simulation with H_{m0} = 0.16 m and s_{op} = 0.015. The panels show the indicator function (it is red for water and blue for air). The black dots represent the probes located at 20 cm over the horizontal component of the crest wall. The vertical white lines indicate the location of the wave gauges. The regions with less opacity show the armor and filter layers.

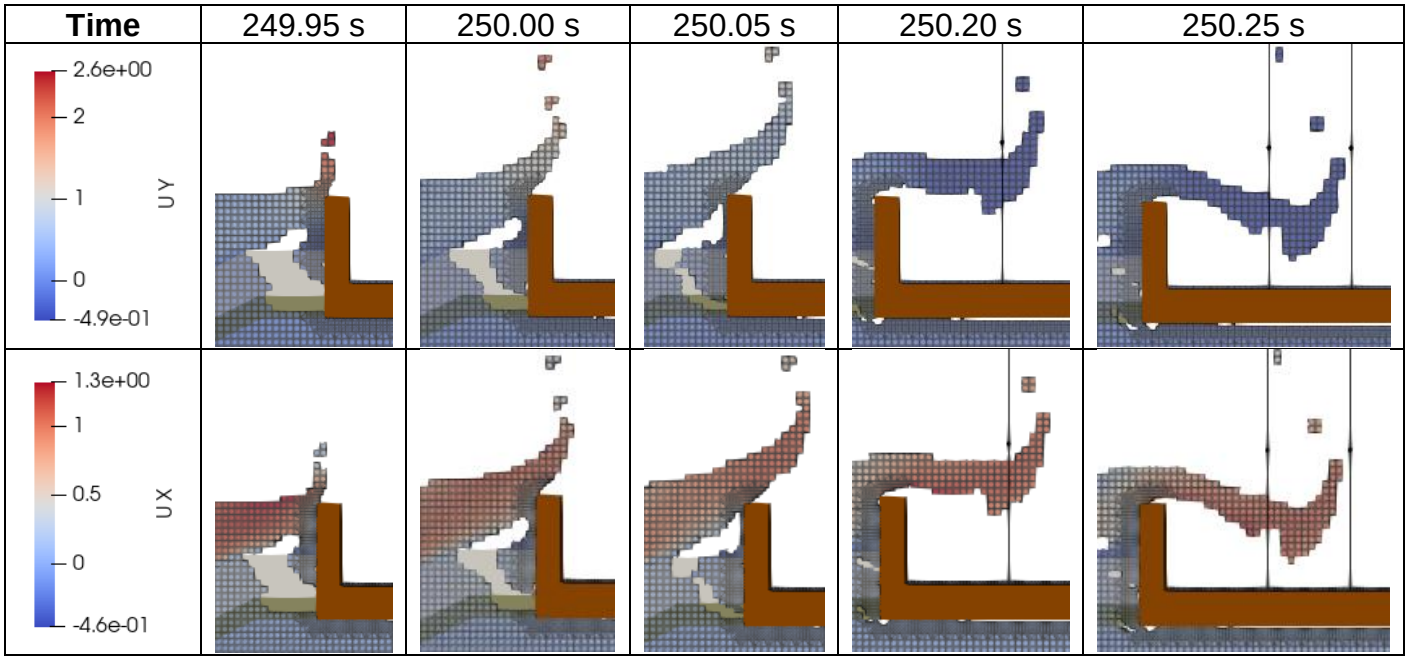

Figure 28. Vertical and horizontal velocities of an event while overtopping the breakwater with highest protrusion ($R_c - A_c$ = 0.08 m). Simulation with H_{m0} = 0.16 m and s_{op} = 0.015. The black dots represent the probes located at 20 cm over the crest. The vertical black lines indicate the wave gauges. The regions with less opacity show the armor and filter layers.

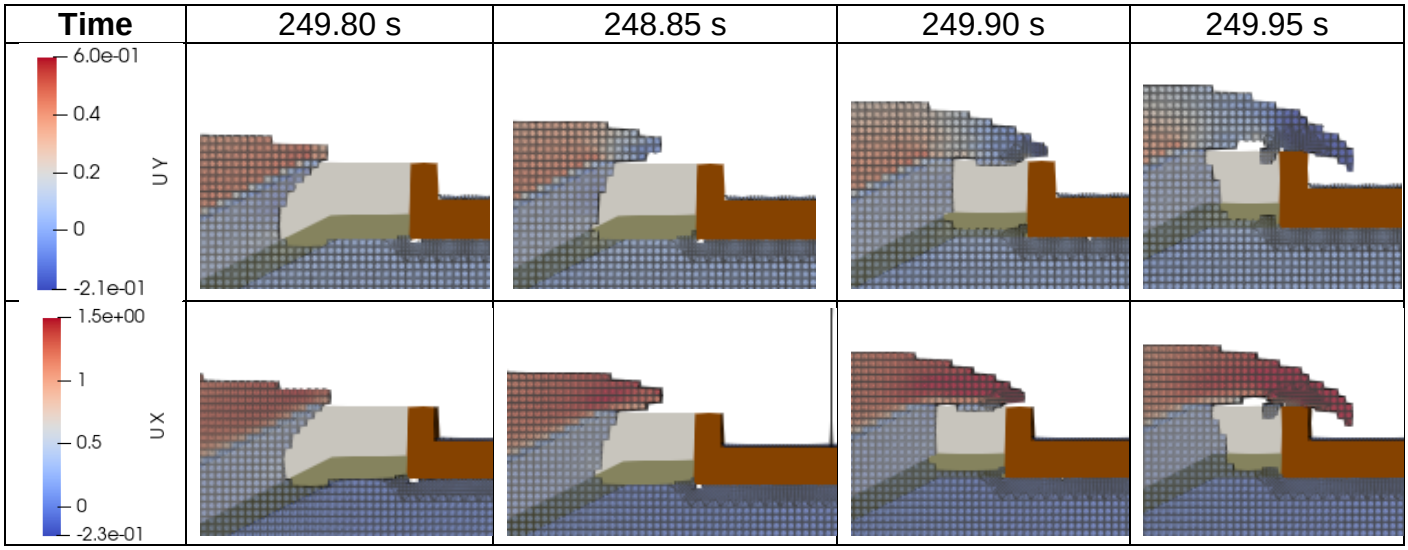

Figure 29. Vertical and horizontal velocities of an event while overtopping the breakwater without protrusion ($R_c - A_c$ = 0 m). Simulation with H_{m0} = 0.16 m and s_{op} = 0.015. The regions with less opacity show the armor and filter layers.

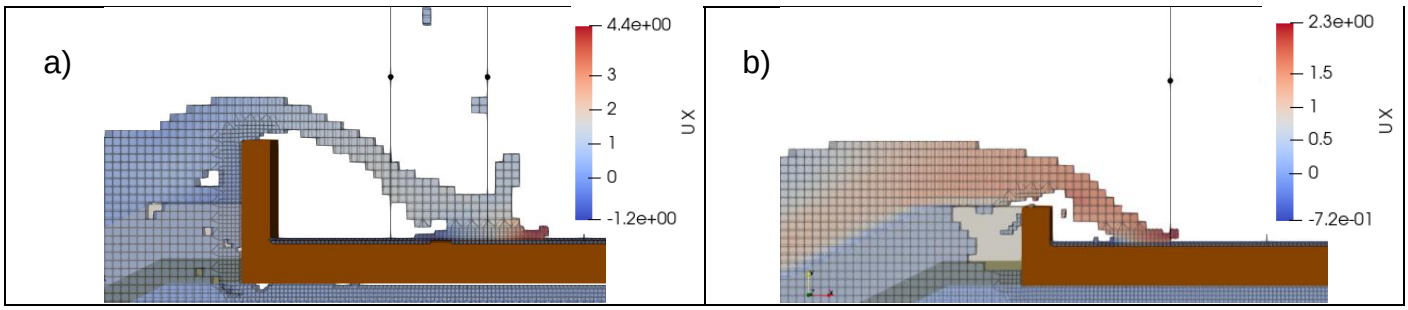

Figure 30. Event acceleration in the horizontal direction after the impact against the horizontal part of the crest element. Simulation with H_{m0} = 0.16 m and s_{op} = 0.015. a) largest protrusion ($R_c - A_c$ = 0.08 m), b) no protrusion ($R_c - A_c$ = 0 m). The black dots show the probes located at 20 cm over the horizontal part of the crest wall. The vertical black lines indicate the wave gauges. The less opaque regions present the armor and filter layers.

5.2. Variations in the wave conditions

Exceedance curves for the same wave condition and for different distances with respect to the vertical part of the crest wall are presented for two simulations, one with the lowest wave height and wave steepness (H_{m0} = 0.08 m with s_{op} = 0.015), and the other with the highest wave height and medium wave steepness (Hm0 = 0.16 m with sop = 0.027). Also, in different panels of the same figure, exceedance curves for different wave conditions at one particular location with respect to the vertical part of the crest wall are shown. All the exceedance curves were calculated taking the 1000 incoming waves into account. In addition, they are shown in such a way that, if they form a line of 45 degrees with respect to the horizontal axis, the shape of the distribution is Rayleigh.

5.2.1. Influence of the wave conditions on the flow depths

Figure 31 presents the flow depth exceedance curves at different locations with respect to the vertical component of the crest wall for the simulations with H_{m0} = 0.08 m and s_{op} = 0.015, in the left panel, and H_{m0} = 0.16 and s_{op} = 0.027, in the right panel. From both figures, it can be observed that the flow depths pertaining to exceedance curves computed at longer distances with respect to the vertical part of the crest wall, are smaller. Other researchers (e.g., Van Gent, 2002a; Cao et al., 2021b) have also found landward decreasing flow depths after performing physical model tests on impermeable coastal structures. They showed that the decay in the flow depths from the seaward leading edge was exponential. It can also be observed, from the two figures below, that there are fewer points in an exceedance curve, the farther the location is from the vertical component of the crest wall. This phenomenon occurs because the water energy gets dissipated the more distance the events cover along the horizontal part of the crest element. Then, the flow depth of some events can become smaller than the threshold and it is no longer captured.

When paying close attention to Figure 31, vertical jumps can be observed in the exceedance curves. These correspond to the definition of the threshold (h_c = 0.003 m for the simulation with H_{m0} = 0.08 m and s_{op} = 0.015, and h_c = 0.025 m for H_{m0} = 0.16 and s_{op} = 0.027). Also, many points are plotted at h_c = 0 m in both figures. This is the consequence of calculating the exceedance curves for the 1000 waves[17]. For the most part, they represent waves that were not able to overtop the crest wall. Nevertheless, among those points, there were also events that had a maximum value lower than the threshold (including those that couldn't be properly solved by the numerical model). Excluding the events with a maximum value smaller than the threshold is appropriate since the interest is primarily on the extremes. The most extreme events are the ones that cause instabilities to pedestrians, machinery and other equipment that might be standing on the crest during storms.

[17] The simulations were run for approximately 1000 waves. The real number of incident waves was calculated in a postprocessing step. The computed value was the one used for the estimation of the exceedance curves.

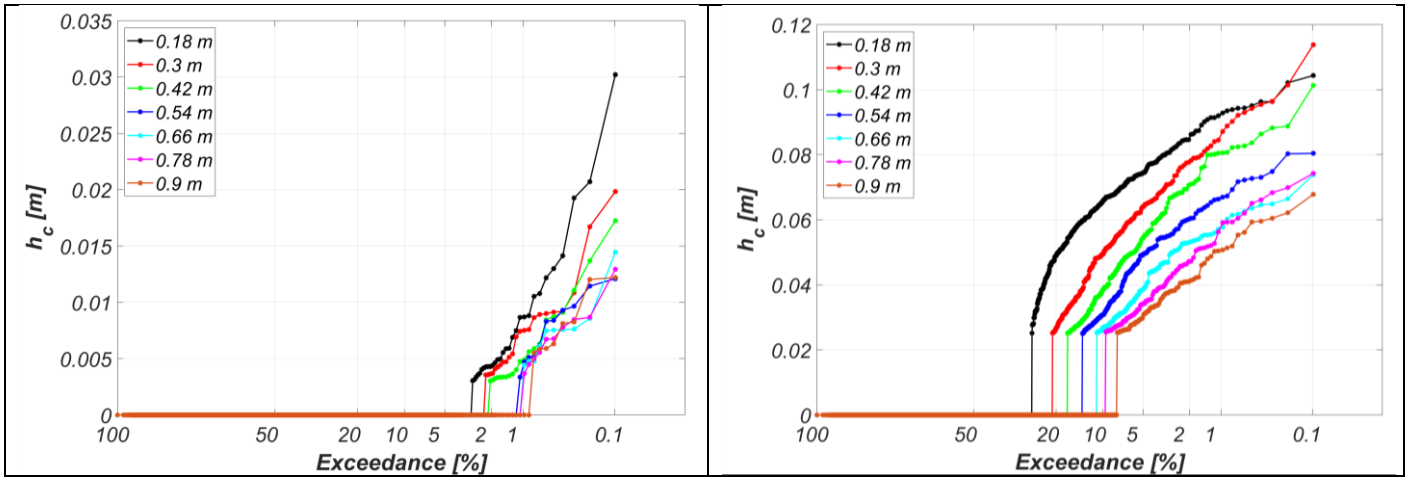

Figure 31. Flow depth exceedance curves for varying distances from the vertical part of the crest wall. The left panel shows the results for the simulation with H_{m0} = 0.08 m and s_{op} = 0.015, and the right panel for H_{m0} = 0.16 and s_{op} = 0.027. The curves were calculated in terms of the percentage of incoming waves. A line of 45 degrees indicates a Rayleigh distribution.

Figure 32 presents the flow depth exceedances curves for the different simulated wave conditions (in the same panel) and at diverse distances with respect to the vertical part of the crest wall (in the various panels). When comparing the consecutive panels, the same behavior captured in the past figure can be observed, that the flow depths decrease as the distance increase from the vertical part of the crest wall. When looking at one panel at the time, it can be observed that the higher the incident significant wave height, and the lower the wave steepness, the larger the flow depths. The same trend has also been observed by other researchers after performing physical model tests on dikes, seawalls, and rubble mound breakwaters (e.g., Van Gent, 2002a; Cao et al., 2021b; Mares-Nasarre et al., 2021). They reported the flow depths to be proportional to the Iribarren number and the wave height. If the Iribarren number and the wave height increased, the flow depths became deeper. The Iribarren number is inversely proportional to the (square root of the) wave steepness. Hence, the lower the wave steepness, the higher is the Iribarren number. It should be noted that the same tendency has been observed in the mean overtopping discharge, the higher the incident significant wave height and the lower the steepness, the larger the mean overtopping discharge. This has been found when performing both, physical model tests and numerical simulations (see for example, Van Gent et al., 2022; Irías Mata and Van Gent, 2023).

Since computing the flow depths exceeded by 2% of the incoming waves is common in literature, they are also presented in this section, specifically in Figure 33, where they are shown for all the wave conditions. It can be observed that the results for the smaller significant wave height with the two higher wave steepness have not been plotted. They were not included because these flow depths were zero regardless of the position with respect to the vertical component of the crest wall. In these cases, it could happen that only events with probabilities lower than 2% were able to overtop the structure. They could also be associated to the fact that the numerical model was not able to solve the very thin flow depths, and therefore, they were excluded with the definition of the threshold (see Appendix E.1, for example). The same trends that have already been discussed based on the exceedance curves can be observed in this figure.

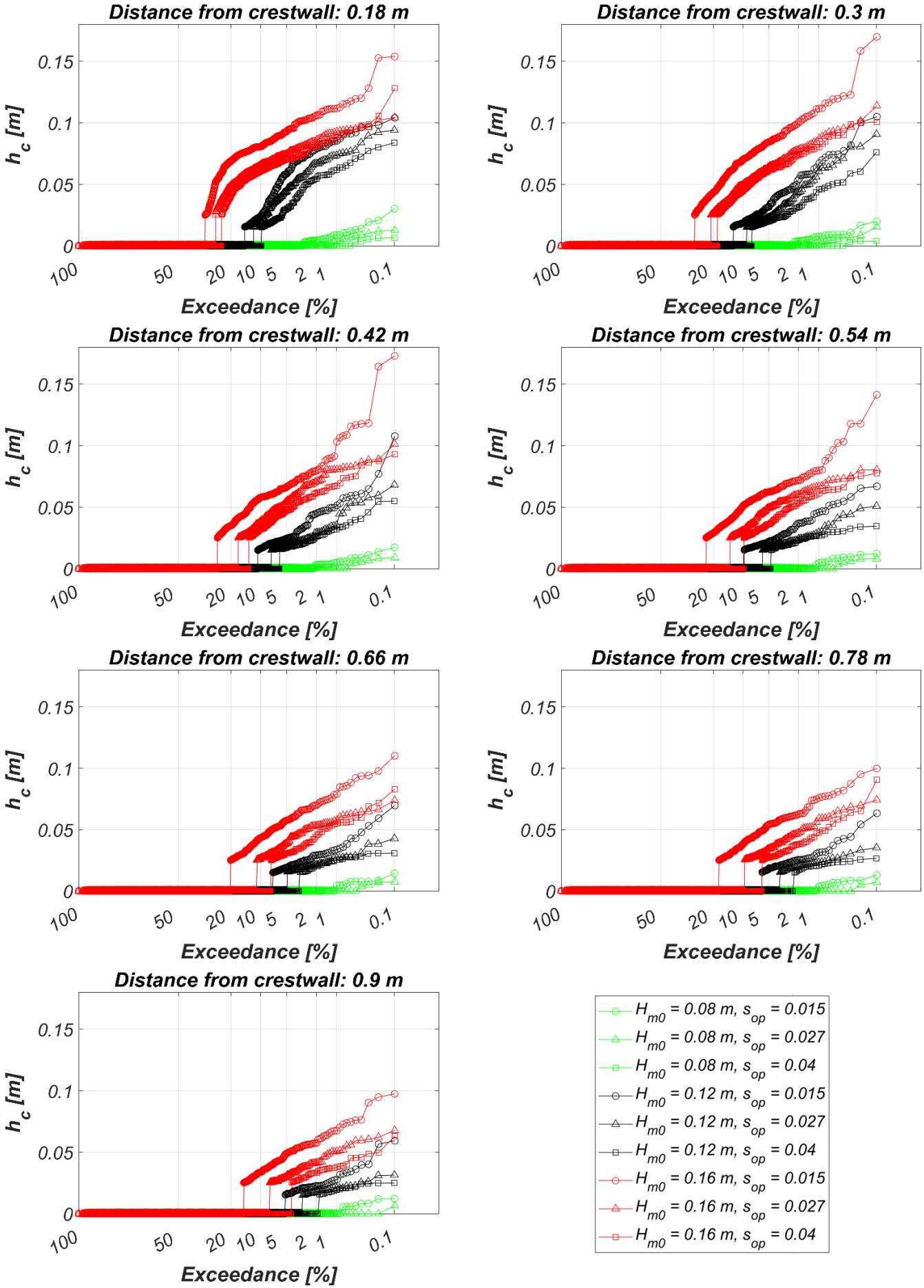

Figure 32. Flow depth exceedance curves for all simulated wave conditions at different positions from the vertical part of the crest wall. The curves were calculated in terms of the percentage of incoming waves. A line of 45 degrees indicates a Rayleigh distribution.

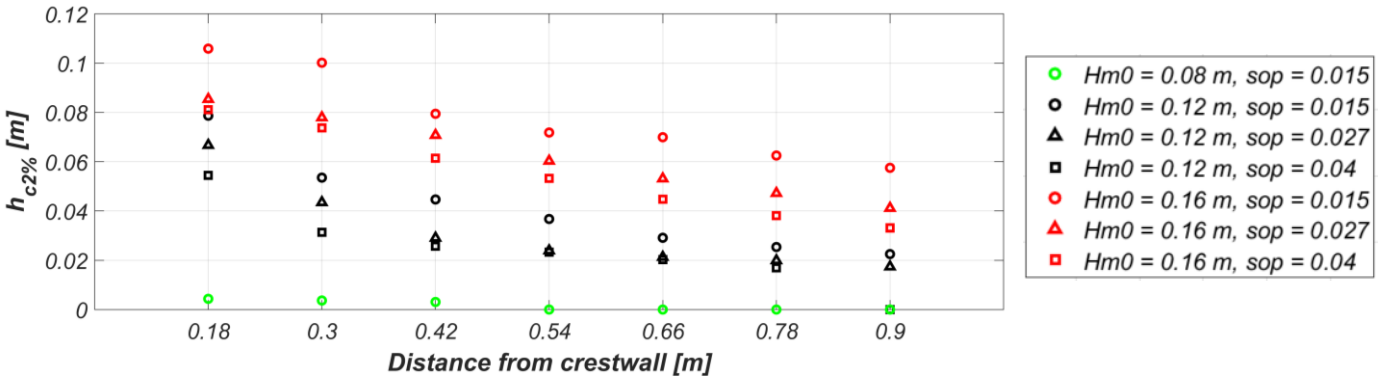

Figure 33. Flow depths exceeded by 2% of the incoming waves at different positions with respect to the vertical part of the crest wall. Results for all the wave conditions.

When paying close attention to the magnitude of the extremer flow depths, it can be inferred that they represent a high percentage of the significant wave height itself, which is not expected. It was found that in these cases, the events impacted the horizontal part of the crest element in between the measuring devices. Then, for the first instruments (the ones positioned closer to the seaside), the events are measured when they are still in the air, at the moment of collision with the horizontal part of the crest wall, or at the immediate moments after the impact. The behavior in this case cannot be compared to the one that is expected to happen once the events start propagating attached to (and along) the horizontal part of the crest wall (as a single layer of water). Situations when events collide with the horizontal part of the crest element in between measuring devices occur for larger incident significant wave heights, low exceedance probabilities and in closer distances with respect to the seaward boundary. Figure 34 shows examples of such situations. These snapshots were obtained from output saved from the numerical model at timesteps of 0.05 s. For such extreme events, more detailed analysis and future validation with physical model tests is required.

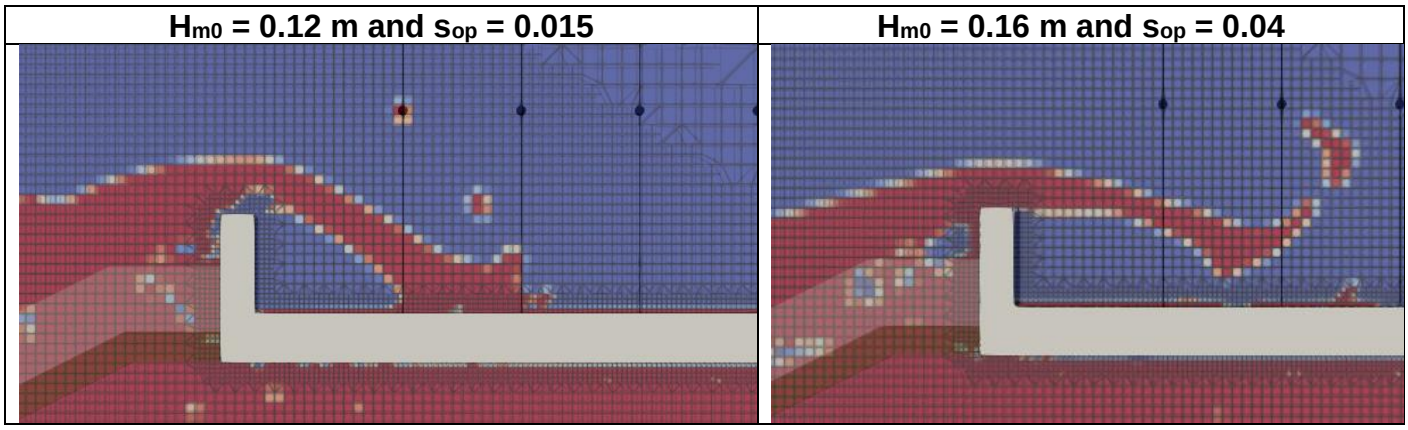

Figure 34. Example of situations when the events impact the horizontal part of the crest wall in between the measuring devices. The black lines indicate the position of the wave gauges and the black dots, the highest probes in the numerical flume. The regions with less opacity show the armor and filter layers.

For events that occur more often, it is expected that they follow the expected trends (as compared to the circumstances when events propagate attached to and along the crest). Such events are associated with smaller wave heights, and they might be able to impact the horizontal part of the crest wall before or near the first measuring instruments (closer to the seaside). It can be observed from the part of the exceedance curves associated to events with high exceedance probabilities, that the trends previously discussed are maintained (see Figure 32). In other words, the flow depths decrease for decreasing incident significant wave heights, for higher wave steepness, and for longer distances with respect to the vertical part of the crest wall.

5.2.2. Influence of the wave conditions on the flow velocities

It was stated in the previous section that for circumstances with larger incident significant wave heights, lower exceedance probabilities and in positions closer to the vertical part of the crest wall; the events collide with the horizontal part of the crest wall in between the measuring devices. When this happens, the trends (for flow depths) are different than the ones that are expected to occur once the events propagate attached to (and along) the crest as a single layer of water. The same situation happens for the flow velocities. Once the events move attached to (and along) the crest, it is expected that the velocities decrease with increasing distance from the vertical part of the crest element. The flow velocity decreases due to the dissipation of the water energy by friction. This was the behavior found when performing physical model tests for dykes (see Van Gent, 2002a, for example).

Figure 35 shows the flow velocity exceedance curves at different locations with respect to the vertical part of the crest wall for the simulations with H_{m0} = 0.08 m and s_{op} = 0.015, in the left panel, and H_{m0} = 0.16 and s_{op} = 0.027, in the right panel. In the case of the left panel, it can be observed that the flow velocities decrease with distance from the vertical part of the crest wall regardless of the probability of exceedance. This happens because the incoming waves are small enough (case with H_{m0} = 0.08 m) and reach the horizontal part of the crest element before the first or at the first measuring device (the one closer to the vertical component of the crest wall). For the right panel, it is clear that the low exceedance probability region of the exceedance curves does not follow the expected behavior when the events are propagating attached to (and along) the crest. In this case, it seems like the velocities are increasing the longer the distance is from the vertical part of the crest wall, until a point where they appear to slowly diminish. Then, the events are probably impacting the horizontal part of the crest wall in between the measuring devices.

To better understand the trend observed in the region of low exceedance probability of the exceedance curves (for cases with high incident significant wave heights), it must be kept in mind that the velocities are depth averaged. Then, two main causes were found to influence its behavior, both related to the fact that the events are colliding with the horizontal part of the crest wall in between the measuring devices. As it was described in section 5.1, when the events impact the horizontal part of the crest wall, there is a return flow towards the seaward side at the same moment that there is still water overtopping the structure. Hence, the first measuring devices capture water moving both, to the positive (landward) and negative directions (seaward). When performing the depth-averaging process, the magnitude of the positive velocities gets reduced by the negative ones. In addition to this, it was also mentioned in section 5.1, that once the events impact the horizontal part of the crest wall, they accelerate. This causes velocities to increase in positions closer to the port side.

In Figure 35, other characteristics that were already pointed out for the flow depth exceedance curves at different locations for the same simulation can also be observed. For example, the dissipation of the water energy also causes the flow velocities to drop below the threshold as the distance increases with respect to the vertical part of the crest wall. Hence, the longer the distance from the vertical part of the crest wall, the less points there are in the corresponding exceedance curves. The flow velocity exceedance curves were also computed for 1000 waves. Therefore, there were many points plotted at u_c = 0 m/s. Again, most of these points are associated to waves that did not overtop the structure. Nonetheless, among these points, there were also velocities smaller than the threshold, and others that couldn't be solved by the numerical model (also lower than the threshold). The threshold can be identified as the first value different than zero when inspecting the exceedance curves from higher to lower exceedance probability.

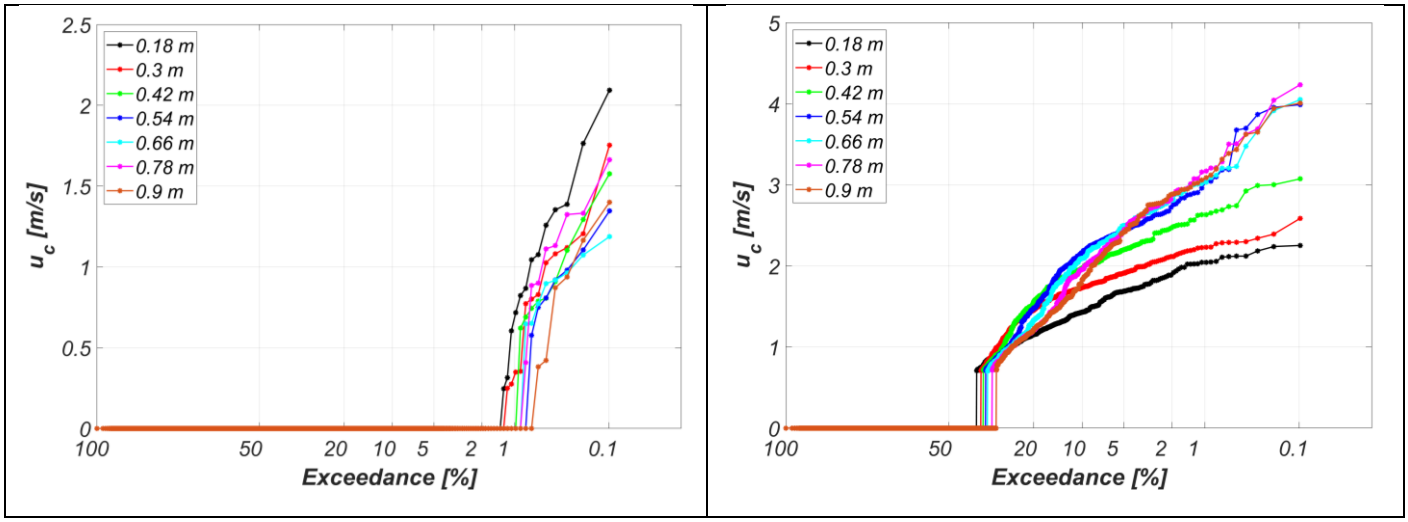

Figure 35. Flow velocity exceedance curves for various places from the vertical part of the crest wall. The left panel shows the results for the simulation with H_{m0} = 0.08 m and s_{op} = 0.015, and the right panel for H_{m0} = 0.16 and s_{op} = 0.027. The curves were calculated in terms of the percentage of incoming waves. A line of 45 degrees indicates a Rayleigh distribution.

Figure 36 presents the flow velocity exceedances curves for the various simulated wave conditions (in the same panel) and at different distances with respect to the vertical component of the crest wall (in the various panels). When looking at the consecutive panels, the trends discussed based on Figure 35 can be observed. For example, it is evident that for the simulations with H_{m0} = 0.12 m and 0.16 m, the behavior of the high exceedance probability part of the exceedance curves is affected by the impact of events, at the horizontal part of the crest wall, in between the measuring devices. When the attention is fixed at one panel at the time, it can be observed that the flow velocities are larger the higher the incident significant wave height, and the lower the wave steepness. Other researchers have also found the same trend from results obtained from physical model tests performed on dikes and rubble mound breakwaters (e.g., Van Gent, 2002a; Mares-Nasarre et al., 2021). They reported the dependence of the flow velocities, not only on the wave steepness, but on the Iribarren number.

More detailed analysis and future validation is required for the flow velocities extracted from the numerical model when the events collide with the horizontal part of the crest wall in between the measuring instruments. As it was mentioned, this happens for relative high incident significant wave heights, low exceedance probabilities and positions closer to the vertical component of the crest wall. In contrast, for events with high exceedance probabilities, it can be expected that the events reach the horizontal part of the crest wall before the first measuring devices (closer to the sea). Then, the trends should align with what is expected to happen when the events propagate attached to (and along) the crest. To show the validity of this argument, the exceedance curves at different positions with respect to the vertical part of the crest wall are presented in Figure 37 for the simulation with H_{m0} = 0.12 m and s_{op} = 0.015. This figure specifically shows a zoom in to the part of the exceedance curves with high exceedance probabilities. It can be observed that for this sector, the flow velocities (for the same exceedance probability) decrease the farther away they are measured from the vertical part of the crest wall. The same tendency, in the region of the exceedance curves with high exceedance probabilities, was found for the other simulations performed with various wave conditions.

In literature, it is common to show the trends of the flow velocities exceeded by 2% of the incoming waves. However, as discussed, they are part of the events associated with low exceedance probabilities. Hence, these events were reaching the horizontal part of the crest wall in between the measuring devices. Then, they were not measured when they were already propagating attached to (and along) the horizontal part of the crest wall. For this reason, they require further analysis and validation, and they are not presented in this section.

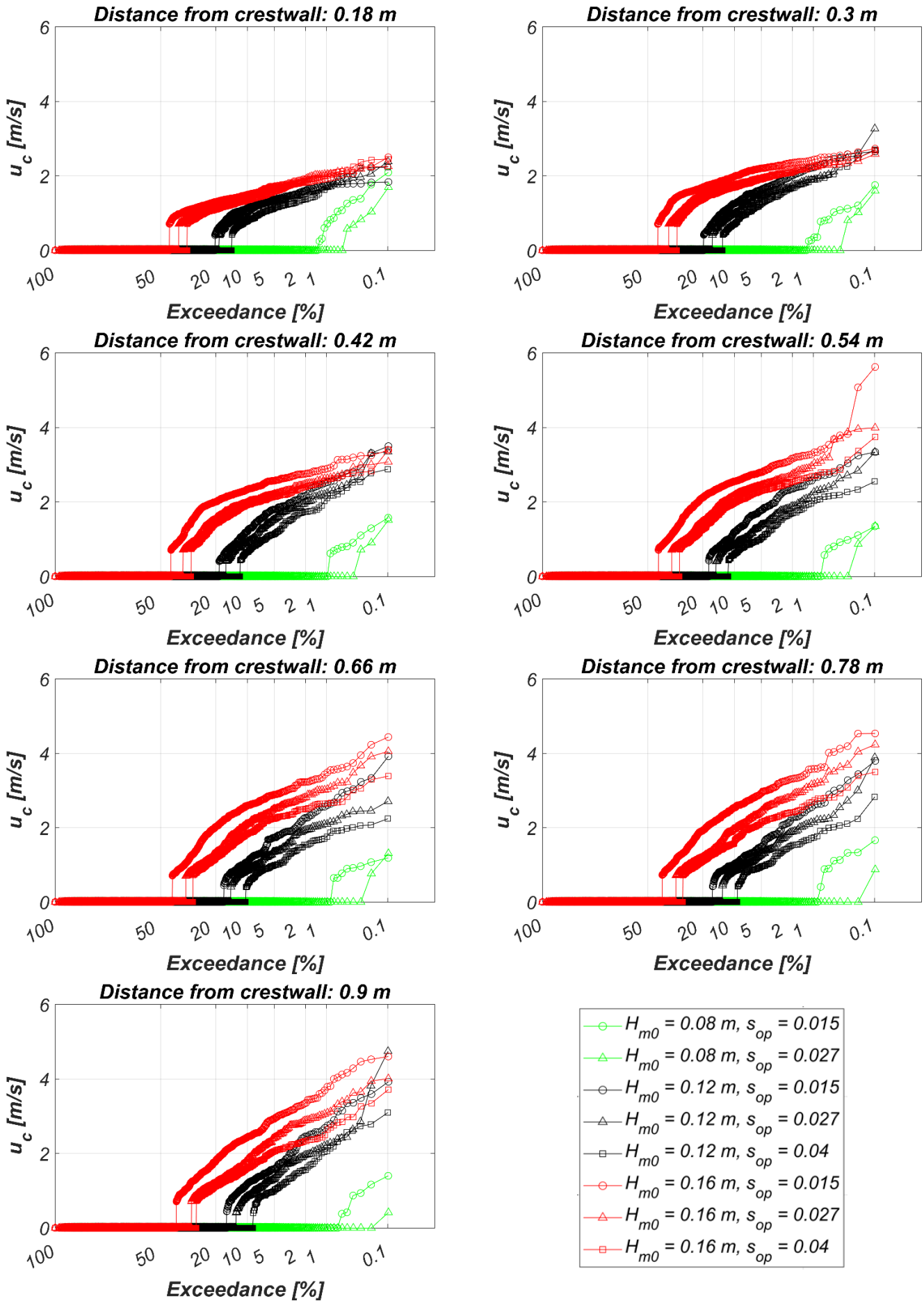

Figure 36. Flow velocity exceedance curves for all simulated wave conditions at different places with respect to the vertical part of the crest wall. The curves were calculated in terms of the percentage of incoming waves. A line of 45 degrees indicates a Rayleigh distribution.

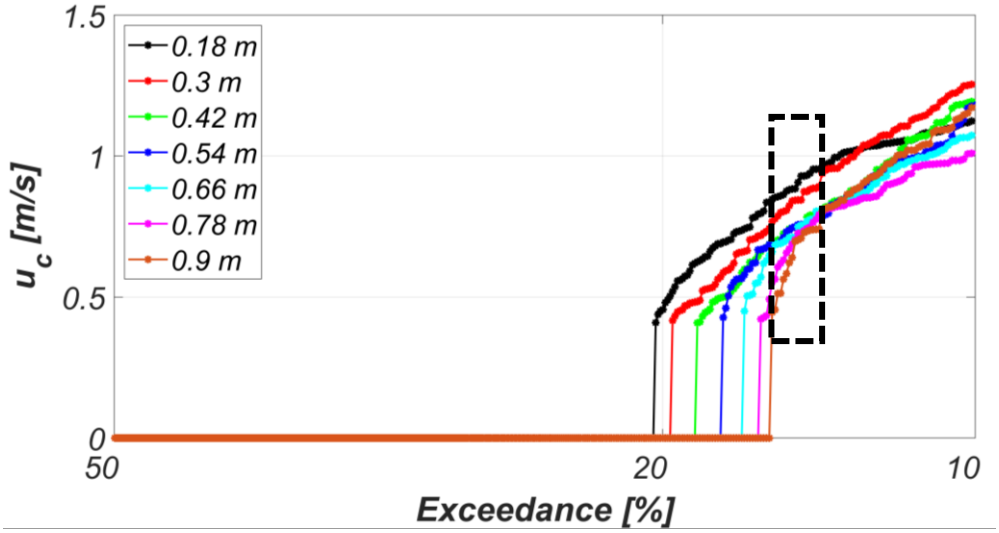

Figure 37. Zoom in to the high exceedance probability part of the exceedance curves computed at various distances from the vertical component of the crest wall. The black rectangle encloses the region of interest. Simulation with H_{m0} = 0.12 m and s_{op} = 0.015.

5.3. Variations in the protrusion height

In this section, the influence of changing the protrusion height is studied along with varying the wave steepness. All the cases were run with H_{m0} = 0.16 m. This value was chosen to ensure that even for the highest protrusion, the model would be able to solve the flow depths and velocities of the wave overtopping events. As it has been mentioned in section 5.2, the events collide with the horizontal part of the crest wall in between the measuring devices, the lower the exceedance probability, and the higher the incident wave height. In addition, as discussed in section 5.1, for extreme events, the higher the protrusion, the longer the distance covered by the event before it impacts the horizontal part of the crest wall. Figure 38 shows one of the extreme events after overtopping the breakwater, with and without protrusion. Notice how the distance covered by the event before hitting the horizontal part of the crest, is longer when there is more protrusion. For these cases with more protrusion, the events might end up hitting the horizontal part of the crest wall at the locations of the last measuring devices. Therefore, the trends of the flow depths and velocities do not follow the expected behavior once the events are propagating attached to (and along) the crest. Again, more detailed analysis and future validation is required for these situations.

s_{op} = 0.015 and R_c-A_c = 0.00 m	s_{op} = 0.015 and R_c-A_c = 0.08 m
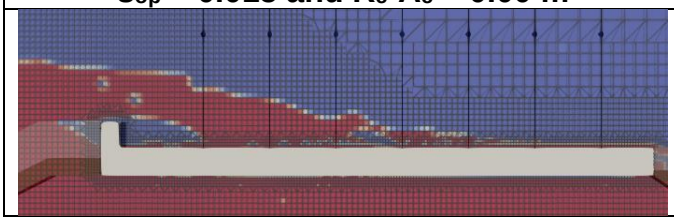	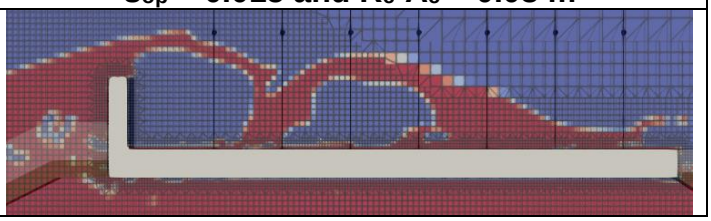

Figure 38. Examples of situations when the flow depths and velocities are extracted when the events are in the air or at the moment of impact against the crest. The black lines indicate the position of the wave gauges and the black dots, the highest probes in the numerical flume. The less opaque regions show the armor and filter layers.

Before presenting and discussing the results related to the effects that changing the protrusion height has on the flow depths and velocities, a first overview into the expected trends is made. For this purpose, it is assumed that the events are analyzed when they are already propagating attached to (and along) the crest as a single layer of water. From the analysis of the observed physical processes presented in section 5.1, it was mentioned that when there is protrusion, an overtopping event impacts the wall and part of its volume falls and cannot pass over the crest wall. Then, the higher

the protrusion, the less volume overtops the breakwater. This is described also in the expressions developed by Van Gent et al. (2022), which are based on physical model tests. Irías Mata and Van Gent (2023) also found this trend after carrying out numerical simulations in OpenFOAM®. It can be expected that the more volume overtops the structure, the deeper the flow depths would be. In case of the flow velocities, it was pointed out in section 5.1 that the higher the protrusion, the larger the flow velocities were. It is suspected that this applies in a situation in which the elevation reached by the event at the peak of the projectile motion, is higher when there is more protrusion.

Figure 39 and Figure 40 present the exceedance curves for the flow depths and flow velocities for various protrusion heights and wave steepness. To verify the trends explained in the previous paragraph, the events associated with high probability of exceedance are the ones to be analyzed. When paying close attention to this sector of the exceedance curves, it is observed that its behavior follows the expected trends. In the case of the flow depth exceedance curves, the flow depths are larger the smaller the protrusion is. This is more evident the longer the distance is with respect to the vertical part of the crest wall. For example, at a distance of 18 cm, which is the location of the first wave gauge, it is barely perceptible that the flow depths are larger when there is less protrusion. It can be deduced that when performing simulations with H_{m0} = 0.16 m, even the less extreme events end up hitting the horizontal part of the crest element almost at the location of the first measuring instrument. Nevertheless, for wave gauges located farther away from the vertical part of the crest wall, the number of events for which this tendency can be observed increases. This happens because as the events impact the horizontal part of the crest wall at the position of the first measuring devices, for the last measuring devices, the measured flow depths are the actual flow depths since the events have already stabilized into a single overtopping layer of water. A zoom in to the sector of the exceedance curves corresponding to the high exceedance probability events is shown in Figure 41.This allows the reader to observe the trends in more detail.

From Figure 41, it can be observed that even when the protrusion height is modified, the flow depths increase as the wave steepness decreases. In this figure, it can also be observed that there are less events captured the higher is the protrusion. This situation is expected since the higher is the obstacle, the same wave height is no longer able to overtop the structure. In Appendix E.3, a similar analysis to the one that has already been effectuated in this section, is carried out by means of flow depth timeseries (instead of exceedance curves).

It was previously stated that the flow velocities associated with the most extreme events, after the impact with the horizontal part of the crest element, are larger the higher is the protrusion. However, when observing the sector of the flow velocity exceedance curves associated with high exceedance probabilities, the opposite effect can be found. In other words, the flow velocities are larger the smaller is the protrusion (see Figure 40). In Figure 42, a zoom in to this zone of interest is presented, to ease the comparison process. In the same manner as for the flow depths, these trends are more evident for the measuring devices located at longer distances with respect to the vertical part of the crest wall. Having larger flow velocities for decreasing protrusion can be expected for events of high exceedance probabilities. In these cases, it is possible that the events do not reach a high elevation when overtopping the crest wall, even when the protrusion height is large. Then the flow velocity can be limited by the volume that is overtopping the crest wall, which is smaller in the case of higher protrusion. Also, from Figure 42, it can be observed that even when the protrusion height is changed, the flow velocities are larger for lower wave steepness.

In this section, the flow depths and velocities exceeded by 2% of the incoming waves are not going to be presented. They form part of the extremer events, the ones that collide with the horizontal part of the crest wall in between the measuring devices. Hence, they also require further study and validation with physical model tests.

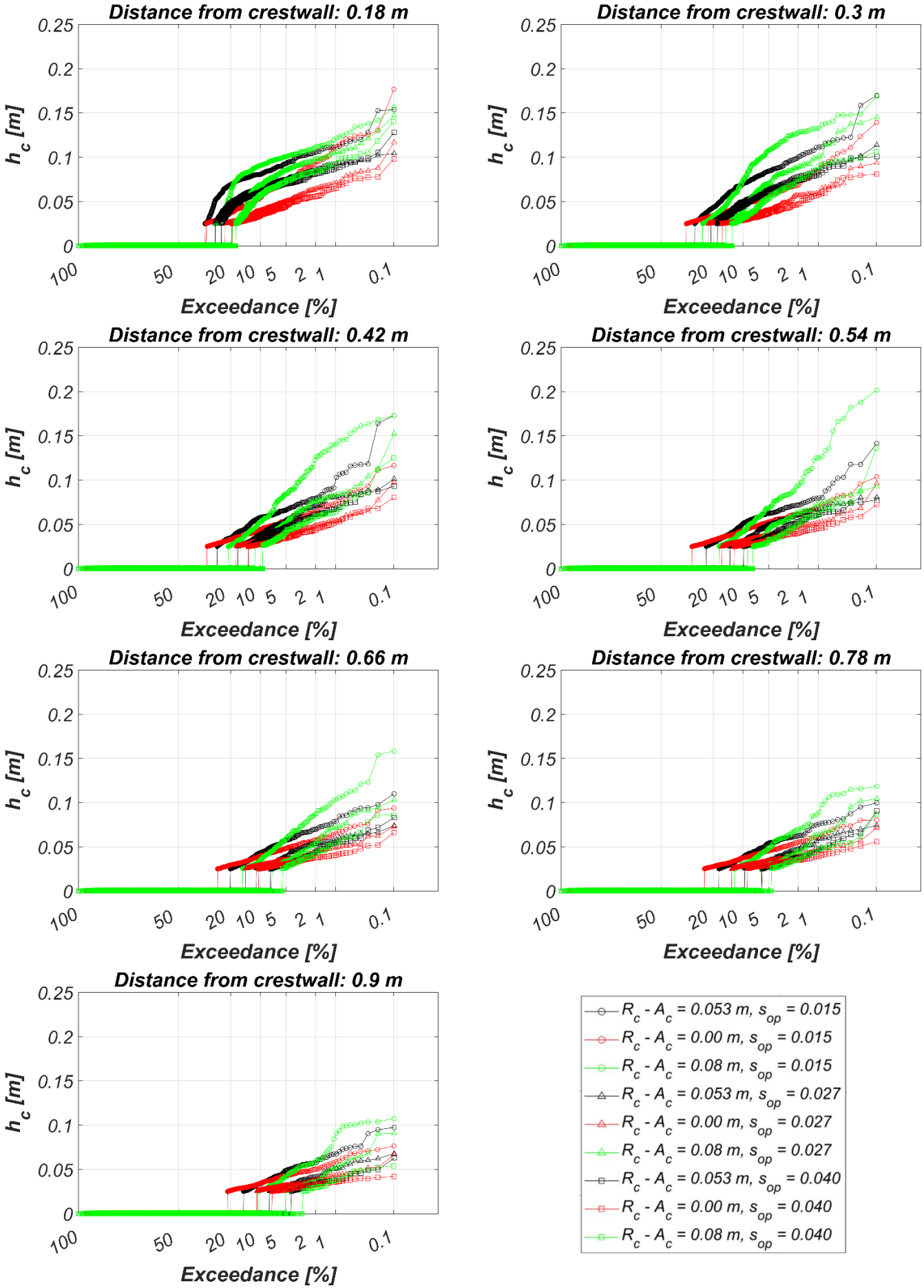

Figure 39. Flow depth exceedance curves for all simulated cases with H_{m0} = 0.16 m, with different wave steepness and protrusion heights. The curves were calculated in terms of the percentage of incoming waves. A line of 45 degrees indicates a Rayleigh distribution.

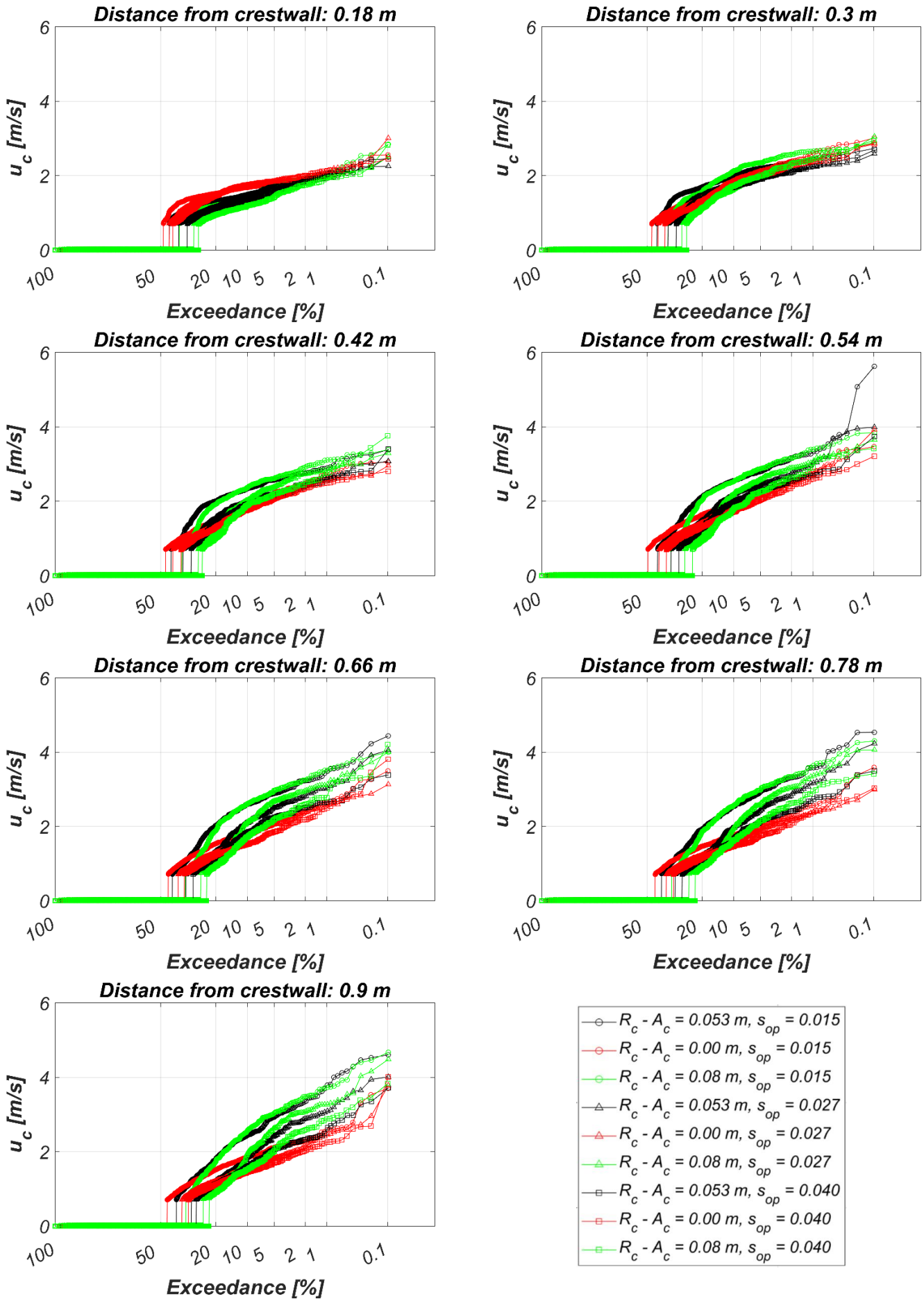

Figure 40. Flow velocity exceedance curves for all simulated cases with H_{m0} = 0.16 m, with different wave steepness and protrusion heights. The curves were calculated in terms of the percentage of incoming waves. A line of 45 degrees indicates a Rayleigh distribution.

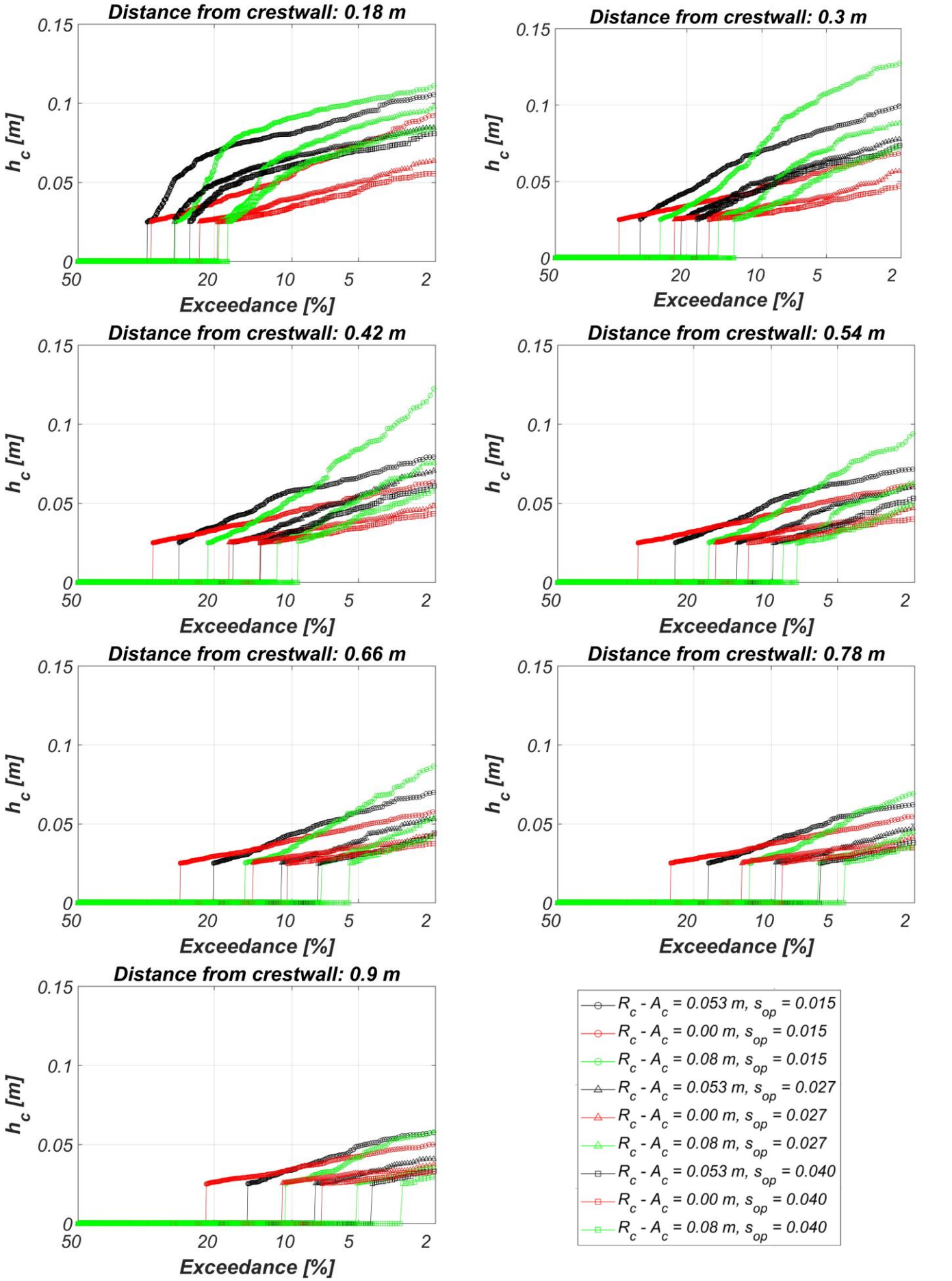

Figure 41. Zoom in to the high exceedance probability part of the flow depth exceedance curves obtained for different protrusion heights and wave steepness. Results for every location with respect to the vertical part of the crest wall.

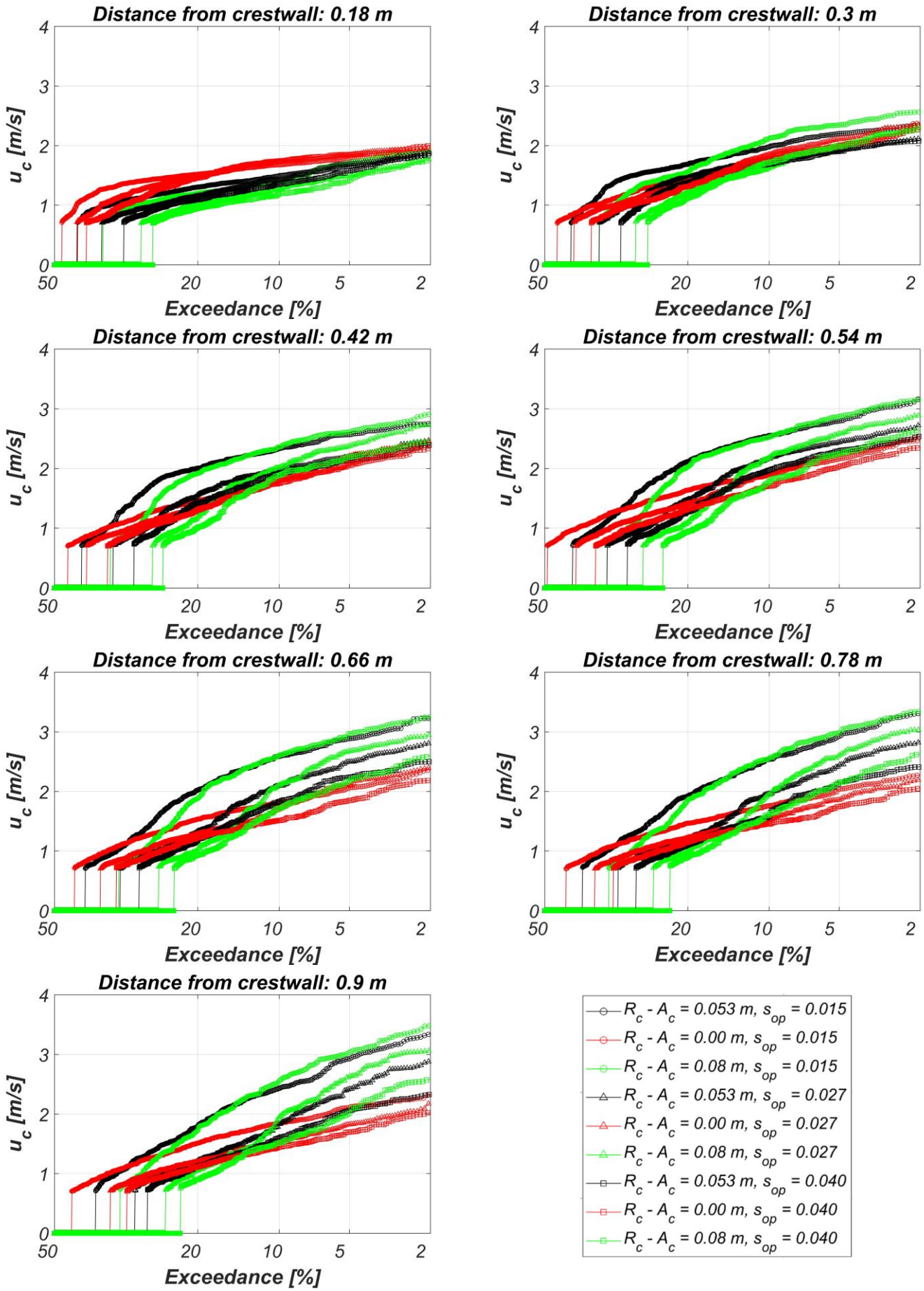

Figure 42. Zoom in to the high exceedance probability part of the flow velocity exceedance curves obtained for different protrusion heights and wave steepness. Results for every location with respect to the vertical part of the crest wall.

6. Discussion of results

In this section, limitations will be discussed about the physical model tests, numerical model, assumptions on the numerical model set-up, extraction and postprocessing of flow depths and velocities.

From the validation section of the flow depths and velocities, it seems there is a strong connection between the overpredicted overtopping discharge and the overestimation of the flow depths. The processes occurring during the overtopping event might also be dependent on the reasons of the overprediction of the discharge by the numerical model. For example, if the numerical model underestimates the dissipation due to wave breaking or if it shows too much resistance to the flow in the porous media, it could cause the waves to collide with the vertical component of the crest wall with more momentum. Consequently, the overtopping events could reach a longer distance with respect to the vertical part of the crest wall. Furthermore, in the current set-up of the numerical model, entrapped air couldn't be released (volume fractions in the VOF method smaller than 1). It is known that non-physical entrapped air affects the estimated forces, with OpenFOAM®, when the waves impact the vertical component of the crest wall (see Jacobsen et al., 2018, and Irías Mata, 2021). It might be possible that the presence of a non-physical volume of air also affects overtopping, and the resulting flow depths and velocities. Figure 43 shows an example of entrapped air (not released) during wave propagation and impact against the vertical part of the crest wall.

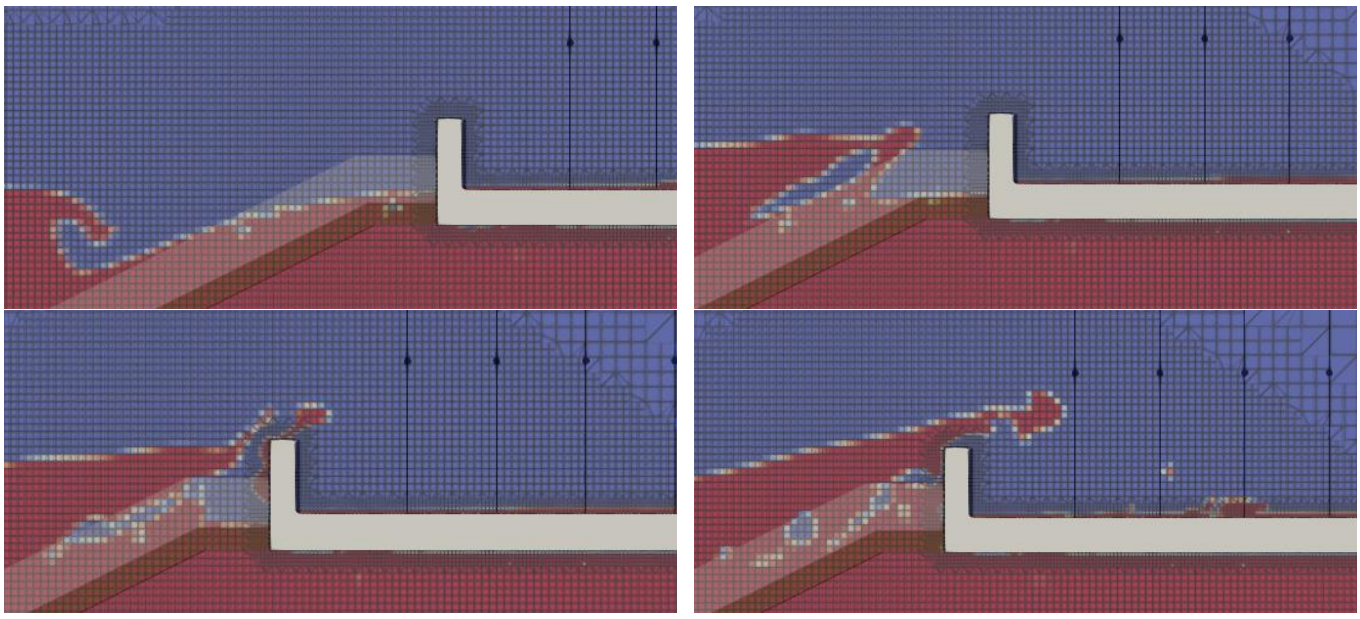

Figure 43. Example of entrapped air during wave propagation and impact with the vertical part of the crest wall. Simulation with H_{m0} = 0.16 m and s_{op} = 0.04. The regions with less opacity indicate the armor and filter layers.

According to the results presented in Chapter 5, it was found that for the extreme overtopping events, and especially for simulations with incident significant wave heights of 12 and 16 cm, that they hit the horizontal part of the crest element in between the measuring instruments (in the numerical model). However, the method used by the wave gauges do not allow to determine that this is happening. The (numerical) wave gauges sum up all the water found in a vertical plane and reference it with respect to the level at the top of the horizontal part of the crest wall. Therefore, it is not feasible to discern if the water is still completely in the air, impacting the horizontal part of the crest wall, or already propagating attached to (and along) the crest. In fact, the largest flow depths were found to coincide with moments in which the events were still in the air and colliding with the horizontal part of the crest element.

The hydrodynamics were captured in detail only for 100 seconds for some of the simulations. With these results it was concluded that the length travelled by the events before hitting the horizontal part of the crest wall is influenced by the incident significant wave height, the exceedance probability, and the protrusion height. The steepness of the wave might also affect this distance. Since the horizontal velocities increase for lower wave steepness, it might happen that events with lower wave steepness travel a longer distance before hitting the horizontal component of the crest wall. In addition, since only a small portion of the timeseries of some simulations was inspected, it is difficult to determine if there is a zone for which all the overtopping jets have already reached the horizontal part of the crest wall. Besides, it was observed that after the events collided with the horizontal part of the crest element, an additional distance is required for them to stabilize into a single overtopping layer of water such that the proper flow depths and velocities can be captured.

Concerning the flow velocities obtained from the numerical model, it was previously mentioned that they were depth-averaged and that only velocities occurring at the same time and positions as indicator functions of at least 0.5 were postprocessed. The depth-averaged flow velocities have as a disadvantage that they don´t fully describe all the processes that are happening at the same instant in time. This applies especially when the events impact the horizontal part of the crest element in between the measuring devices. After the impact, water flows towards the seaward side at the same moment as water is overtopping the breakwater. Hence, water moving towards the sea produces negative velocities which decrease the magnitude of the positive velocities associated with the overtopping event above.

Apart from the flow happening in two directions described above, for the positions where the event is already propagating along the crest, the magnitude of the flow velocities is affected by the constant layer of water below. This water, which cannot infiltrate through the impermeable crest element, is almost stagnant. Therefore, it reduces the magnitude of the depth-averaged flow velocities. Since the constant layer of water pertains to past overtopping events, it might happen that considering its low velocity is not appropriate when it comes to determining the thresholds causing destabilization of personnel and equipment standing on the crest of the breakwater. Further studies are needed to comprehend how to take this constant layer of water into account for the destabilization process.

Aside from the depth-averaging process, there were limitations in the method of extraction of the flow velocities. As mentioned, only when the indicator function at a particular time and position was larger than 0.5, the flow velocity would be considered. During the wave overtopping events, water could be dispersed into several cells or get accumulated into less cells, changing the value of the indicator function of these cells. Then a sudden drop of the indicator function caused disruptions in the flow velocity timeseries. An example of such a case can be observed in Figure 44.

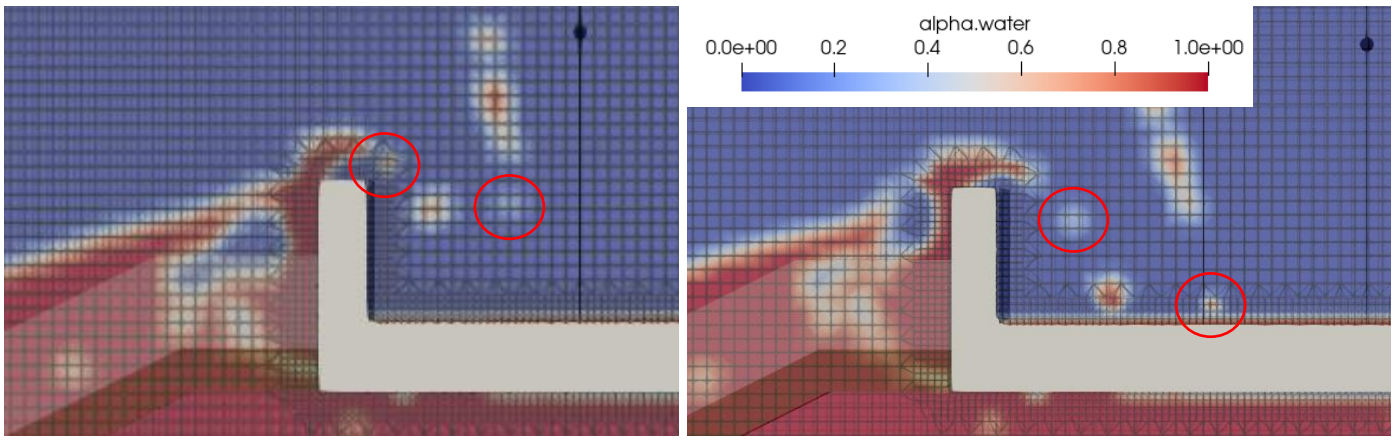

Figure 44. Example of water spreading into several cells and converging into less cells. Simulation with H_{m0} = 0.16 m and s_{op} = 0.04. The vertical black lines and the black dots show the position of the wave gauges and the highest probes. The regions with less opacity indicate the armor and filter layers.

The set-up of the numerical model included probes located till a maximum height of 20 cm above the level of the horizontal component of the crest wall. Nevertheless, for the most extreme events and for the breakwater configurations with more protrusion, it was observed that part of the overtopping events reached elevations even higher than the highest probes. Then, the depth-averaged flow velocities associated with these moments were not correctly computed. However, not characterizing properly such velocities is not relevant since what happens with the events high in the air is not of much interest for the stability of people or machinery standing on the crest of the breakwater.

With respect to the overall trends of the flow depths and velocities, it was observed that for the sector of the exceedance curves associated with a high probability of exceedance, the trends followed the expected behavior (as compared to events propagating attached to and along the horizontal part of the crest wall). This is because the events associated to such high probabilities of exceedance reached the horizontal part of the crest wall before the first measuring devices (the ones closer to the sea). Even though the model could reproduce the expected trends for the events of smaller magnitude, the primary interest is on the extreme events since these are the ones that cause more inconvenience to the people and equipment positioned on the crest. Nevertheless, it was found that the low probability of exceedance part of the exceedance curves corresponded to flow depths and velocities extracted when the events were still in the air or at the moment of impact against the horizontal component of the crest element. In this case, the trends are different than the ones observed when the events propagate attached to (and along) the crest. Therefore, a more detailed analysis and future validation is needed for the low probability of exceedance sector of the exceedance curves.

Decreasing the grid size around the crest wall would be quite computational expensive and would most likely not contribute to obtain more accurate flow depths and velocities. First of all, because it was already explained that the overestimation of the overtopping discharge is the dominant explanatory variable for the overprediction of the flow depths. Secondly, because from inspection of the timeseries, it seems it was possible to solve flow depths as thin as 0.003 m with the finest mesh (mesh of 0.005 m x 0.005 m). This fine mesh was more relevant when the flow depths were very thin. But it was checked that when augmenting is thickness, and especially for more extreme events, the benefit of it diminished. In addition, very thin flow depths in the physical model tests have scale effects (e.g., surface tension). Therefore, it is not necessary to reproduce such flow depths if it is not clear how they scale up to the prototype.

It is ambiguous how the overprediction of the overtopping discharge in the numerical model affect the modelled flow velocities. This is because the method to obtain flow velocities from the numerical model and physical model tests was different. Hence, they cannot be directly compared.

7. Conclusions and recommendations

7.1. Conclusions

In this research, a numerical model was set up in OpenFOAM® to simulate wave overtopping events on a rubble mound breakwater. The model was validated for wave propagation and overtopping with physical model tests. Two rubble mound breakwater configurations were used for validation: 1) with a crest wall and a berm, and 2) with a crest wall and without a berm. Then, the numerical model was used to evaluate the accuracy of OpenFOAM® to reproduce the flow depths and velocities happening at the crest during wave overtopping events. Furthermore, the model was utilized to analyze the effect of changing the protrusion height, and wave conditions on the flow depths and velocities. The sensitivity cases were carried out with a rubble mound breakwater configuration with a crest wall and without the berm. The different conditions simulated to study the influence on the flow depths and velocities included a H_{m0} in between 8 cm and 16 cm, a wave steepness (s_{op}) in between 0.015 and 0.04, and protrusion heights ($R_c - A_c$) in between 0 cm and 8 cm.

7.1.1. Optimal method of extraction of the flow depths and velocities at the crest of a rubble mound breakwater using OpenFOAM®

In the following, the answer to the first research sub-question is treated:

The extraction of the flow depths, from the numerical model, was feasible with the use of numerical wave gauges. The numerical wave gauges function in such a way that they sum up all the water they find in their vertical plane and place the resulting flow depth with respect to a reference level. Nonetheless, there was a restriction regarding the position of the lower tip of the wave gauges. It was found that when the lower tip of the wave gauges was located at the top of the horizontal part of the crest element, the flow depths were computed correctly. This is also the approach that is recommended to follow for future research on modelling flow depths during wave overtopping events with OpenFOAM®.

To compute the flow velocities in the numerical model, three methods were utilized: 1) numerical wave gauges and discharge sheets, 2) probes, and 3) output planes. When the flow velocities were estimated with the wave gauges and discharge sheets, by dividing the discharge by the respective flow depth, very high non-physical flow velocities appeared. They were the result of very thin flow depths or high overtopping discharges that were obtained for certain computational timesteps. The depth averaged flow velocities estimated with the probes and planes were similar in magnitude. Also, they didn't show high non-physical velocities. Postprocessing the flow velocities obtained with the planes was considerably more time consuming. Thus, the probes were the chosen method to calculate the flow velocities from the numerical model. Their use is also recommended for future research.

To accurately model the flow depths and velocities, a fine mesh composed of square cells of 0.005 m is needed around the crest element. With this fine mesh it is possible to solve flow depths as thin as 0.003 m.

7.1.2. Accuracy of flow depths and velocities, modelled with OpenFOAM®, at the crest of a rubble mound breakwater

The model results were compared to measurements taken from physical model tests. The performance of the numerical model was good when estimating incident waves. The computed spectral parameters (H_{m0} and $T_{m-1,0}$) had a bias factor slightly larger than 1. On the other hand, there was overestimation of the calculated overtopping discharge. The non-dimensional mean overtopping

discharge was overpredicted by a bias factor of 8. The overestimation of the overtopping discharge caused more overtopping events and larger flow depths in the numerical model (by several orders of magnitude). The method of extraction of the flow depths was similar for the experiments and the numerical model. Nevertheless, the method of extraction of the flow velocities was different. Hence, the computed flow velocities couldn't be validated. With this, the second research sub-question has been answered.

7.1.3. Physical processes occurring during the wave overtopping events

The physical processes occurring during wave overtopping events depend on the protrusion height:

a) Waves can more easily overtop the breakwater without protrusion. The situation is different when waves impact the vertical component of the crest wall with more protrusion. In this case, part of the volume falls into the sea and the rest gets boosted to a high elevation until it overtops the structure.
b) While overtopping the structure, the events seem to follow projectile motion. Gravity is the dominant force during their parabolic trajectory, and it affects their vertical velocities. Horizontal velocities remain almost constant during this travel time.
c) Once the events impact the horizontal part of the crest element, water quickly gets accelerated to the port and sea sides. As water propagates along the crest, friction acts upon it and dissipates its energy. The water that flows seaward moves at the same time as there is still water overtopping the breakwater. This water (moving towards the sea) later piles up against the vertical part of the crest wall and returns towards the port side.

In this subsection, the third research sub-question has been answered. It is remarkable to mention that, to this author's knowledge, this is the first time that flow in the seaward direction on the horizontal part of the crest wall has been observed.

7.1.4. Effects of changing the wave conditions and protrusion height on the flow depths and velocities at the crest of a rubble mound breakwater

For the specific conditions simulated with the numerical model, it was found that the extremer overtopping events reached the horizontal part of the crest wall in between the measuring devices. Therefore, the first measuring devices (the ones located closer to the sea) extracted the flow depths and velocities when the events were still in the air or at the moment of impact against the horizontal part of the crest element. Such circumstances happened for events associated with low exceedance probabilities and relative high incident significant wave heights. The observed trends in these situations were different than the expected ones when the events were already propagating attached to (and along) the horizontal part of the crest wall. More detailed analysis and further validation with physical model tests is required in these occasions.

In the case of the events with high probability of exceedance, they hit the horizontal part of the crest wall before or around the first measuring device (the one closer to the sea). Then, the observed trends corresponded to the expected behavior found once the events were already propagating attached to (and along) the horizontal part of the crest wall. For these events, it was found that the flow depths and velocities increased the larger the (significant) wave height and the lower the wave steepness. Also, the flow depths and velocities decreased the longer the distance with respect to the vertical part of the crest wall. In addition, for a smaller protrusion height, more events were captured, and their flow depths and velocities were larger. Moreover, even for varying protrusion heights, it was observed that the flow depths and velocities increased with lower wave steepness.

In the above, the answers to the fourth and fifth research sub-questions have been covered.

7.2. Recommendations

Based on the results obtained in this research, several recommendations are given for future studies in the topic of modelling flow depths and velocities during wave overtopping events in OpenFOAM®:

- For the specific set-up of the numerical model utilized during the present research, it was observed that the most extreme events were hitting the horizontal part of the crest element in between the measuring devices. Then, some of the measuring devices extracted the flow depths and velocities when the events were still in the air or at the moment of impact against the horizontal part of the crest wall. These extreme events are related to low exceedance probabilities and relative high incident significant wave heights. Therefore, they are the ones that compromise the security at the crest of rubble mound breakwaters the most. More detailed analysis and future validation with physical model tests is needed for these conditions.

- One of the limitations of the numerical model set-up used for the present research, was the impossibility to release entrapped air when modelling the wave-structure interactions. For future research, it is recommended to determine if the presence of non-physical volumes of air have an effect in the estimation of wave overtopping discharges, and flow depths and velocities.

- For the specific simulated breakwater configurations, it was found that the numerical model was not able to accurately solve the flow depths and velocities when small incident significant wave heights were used (i.e., H_{m0} = 0.08 m and 0.10). In addition, to simulate these wave conditions, very small grid cells were required, resulting in large computational times. Then, it is recommended to increase the incident significant wave heights to be simulated, to secure obtaining sufficient overtopping events and allowing the numerical model to solve the flow depths and velocities.

- When the wave gauges and discharge sheets were used to predict flow velocities, very high non-physical velocities were found. It was discovered that one of the reasons of these very high non-physical velocities was the extraction of very high overtopping discharges. More research concerning the causes of such high overtopping discharges is required.

- When performing physical model tests to validate the numerical modelling of flow depths and velocities at the crest of rubble mound breakwaters, it is encouraged to record the tests from a side view. Having information regarding the physical processes happening during the experiments would be beneficial to better comprehend what the physical instruments are measuring. It would also allow to compare if the collision point (with the horizontal part of the crest element) in the physical model tests and the numerical model is similar.

- For future validation of modelled flow depths and velocities at the crest of rubble mound breakwaters using physical model tests, it is necessary to come up with similar methods of calculation of the flow velocities.

- Future studies are needed to evaluate if the wave steepness affects the collision point of the overtopping events with the horizontal part of the crest wall.

- When overtopping occurs on a breakwater with a crest wall, water cannot be infiltrated through this impermeable element (the crest wall) and forms a constant layer of water. Additional research is needed to clarify how to take this constant layer of water into account when finding the overtopping flow parameters responsible for the destabilization of people or equipment standing on the crest of a rubble mound breakwater.

- More research is required to find the dependencies of the modelled flow depths and velocities on oblique waves. It is also paramount to determine if the model is capable of reproducing the trends found in literature (based on physical model tests), under more breakwater configurations (e.g., various seaward slopes, berm widths and berm levels, and the presence of a recurved parapet), depth-limited conditions and several foreshore slopes.

- Mares-Nasarre et al. (2019, 2021) found that the shape of the exceedance curves associated with exceedance probabilities lower than 2% is Exponential, in case of the flow depths, and Rayleigh, in case of the flow velocities. They fitted these distributions based on physical model tests on rubble mound breakwaters. It still remains to verify the shape of the same part of the exceedance curves when they are obtained from the numerical model.

8. References

Abt, S.R., Wittier, R.J., Taylor, A., Love, D.J., 1989. Human stabillity in a high flood hazard zone. J. Am. Water Resour. Assoc. 25, 881–890. https://doi.org/10.1111/j.1752-1688.1989.tb05404.x

Bae, H.U., Yun, K.M., Yoon, J.Y., Lim, N.H., 2016. Human stability with respect to overtopping flow on the breakwater. Int. J. Appl. Eng. Res. 11, 111–119.

Bosboom, J., Stive, M., 2022. Coastal Dynamics. TU Delft Open, Delft University of Technology, Delft, The Netherlands.

Cao, D., Chen, H., Yuan, J., 2021a. Inline force on human body due to non-impulsive wave overtopping at a vertical seawall. Ocean Eng. 219, 108300. https://doi.org/10.1016/j.oceaneng.2020.108300

Cao, D., Tan, W., Yuan, J., 2022. Assessment of wave overtopping risk for pedestrian visiting the crest area of coastal structure. Appl. Ocean Res. 120, 102985. https://doi.org/10.1016/j.apor.2021.102985

Cao, D., Yuan, J., Chen, H., Zhao, K., Liu, P.L.-F., 2021b. Wave overtopping flow striking a human body on the crest of an impermeable sloped seawall. Part I: Physical modeling. Coast. Eng. 167, 103891. https://doi.org/10.1016/j.coastaleng.2021.103891

Chen, H., Yuan, J., Cao, D., Liu, P.L.-F., 2021. Wave overtopping flow striking a human body on the crest of an impermeable sloped seawall. Part II: Numerical modelling. Coast. Eng. 168, 103892. https://doi.org/10.1016/j.coastaleng.2021.103892

Chen, W., Warmink, J.J., Van Gent, M.R.A., Hulscher, S.J.M.H., 2022. Numerical investigation of the effects of roughness, a berm and oblique waves on wave overtopping processes at dikes. Appl. Ocean Res. 118, 102971. https://doi.org/10.1016/j.apor.2021.102971

Chen, W., Warmink, J.J., Van Gent, M.R.A., Hulscher, S.J.M.H., 2021. Numerical modelling of wave overtopping at dikes using OpenFOAM®. Coast. Eng. 166, 103890. https://doi.org/10.1016/j.coastaleng.2021.103890

De Ridder, M.P., Kramer, J., Den Bieman, J.P., Wenneker, I., 2023. Validation and practical application of nonlinear wave decomposition methods for irregular waves. Coast. Eng. 183, 104311. https://doi.org/10.1016/j.coastaleng.2023.104311

Del Jesus, M., Lara, J.L., Losada, I.J., 2012. Three-dimensional interaction of waves and porous coastal structures. Coast. Eng. 64, 57–72. https://doi.org/10.1016/j.coastaleng.2012.01.008

EurOtop, 2018. In: Van der Meer, J.W., Allsop, N.W.H., Bruce, T., de Rouck, J., Kortenhaus, A., Pullen, T., Schüttrumpf, H., Troch, P., Zanuttigh, B. (Eds.). Manual on wave overtopping of sea defences and related structures (incl. Errata November 2019).

Franco, L., Gerloni, M., Van der Meer, J.W., 1994. Wave overtopping on vertical and composite breakwaters, in: Coastal Engineering 1994. Presented at the Proceedings of the twenty-four international conference.

Higuera, P., Lara, J.L., Losada, I.J., 2014. Three-dimensional interaction of waves and porous coastal structures using OpenFOAM®. Part II: Application. Coast. Eng. 83, 259–270. https://doi.org/10.1016/j.coastaleng.2013.09.002

Higuera, P., Lara, J.L., Losada, I.J., 2013a. Realistic wave generation and active wave absorption for Navier–Stokes models. Coast. Eng. 71, 102–118. https://doi.org/10.1016/j.coastaleng.2012.07.002

Higuera, P., Lara, J.L., Losada, I.J., 2013b. Simulating coastal engineering processes with OpenFOAM®. Coast. Eng. 71, 119–134. https://doi.org/10.1016/j.coastaleng.2012.06.002

Hirt, C.W., Nichols, B.D., 1981. Volume of fluid (VOF) method for the dynamics of free boundaries. J. Comput. Phys. 39, 201–225. https://doi.org/10.1016/0021-9991(81)90145-5

Holthuijsen, L., 2007. Waves in oceanic and coastal waters. Cambridge University Press.

Hsu, T.-J., Sakakiyama, T., Liu, P.L.-F., 2002. A numerical model for wave motions and turbulence flows in front of a composite breakwater. Coast. Eng. 46, 25–50. https://doi.org/10.1016/S0378-3839(02)00045-5

Irías Mata, M., 2021. Numerical estimation of wave loads on crest walls on top of rubble mound breakwaters using OpenFOAM. Delft University of Technology, Delft, The Netherlands.

Irías Mata, M., Van Gent, M.R.A., 2023. Numerical modelling of wave overtopping discharges at rubble mound breakwaters using OpenFOAM®. Coast. Eng. 181, 104274. https://doi.org/10.1016/j.coastaleng.2022.104274
Jacobsen, N.G., 2017. waves2Foam manual.
Jacobsen, N.G., Fuhrman, D.R., Fredsøe, J., 2012. A wave generation toolbox for the Open-Source CFD Library: OpenFoam®. Int. J. Numer. Methods Fluids 70, 1073–1088.
Jacobsen, N.G., Van Gent, M.R.A., Capel, A., Borsboom, M., 2018. Numerical prediction of integrated wave loads on crest walls on top of rubble mound structures. Coast. Eng. 142, 110–124. https://doi.org/10.1016/j.coastaleng.2018.10.004
Jacobsen, N.G., Van Gent, M.R.A., Wolters, G., 2015. Numerical analysis of the interaction of irregular waves with two dimensional permeable coastal structures. Coast. Eng. 102, 13–29. https://doi.org/10.1016/j.coastaleng.2015.05.004
Jensen, B., Jacobsen, N.G., Christensen, E.D., 2014. Investigations on the porous media equations and resistance coefficients for coastal structures. Coast. Eng. 84, 56–72. https://doi.org/10.1016/j.coastaleng.2013.11.004
Jonkman, S.N., Penning-Rowsell, E., 2008. Human Instability in Flood Flows. JAWRA J. Am. Water Resour. Assoc. 44, 1208–1218. https://doi.org/10.1111/j.1752-1688.2008.00217.x
Kobayashi, N., Wurjanto, A., 1989. Wave Overtopping on Coastal Structures. J. Waterw. Port Coast. Ocean Eng. 115, 235–251. https://doi.org/10.1061/(ASCE)0733-950X(1989)115:2(235)
Lara, J.L., Del Jesus, M., Losada, I.J., 2012. Three-dimensional interaction of waves and porous coastal structures. Coast. Eng. 64, 26–46. https://doi.org/10.1016/j.coastaleng.2012.01.009
Larsen, B.E., Fuhrman, D.R., Roenby, J., 2019. Performance of interFoam on the simulation of progressive waves. Coast. Eng. J. 61, 380–400. https://doi.org/10.1080/21664250.2019.1609713
Lin, P., Karunarathna, S.A., 2007. Numerical Study of Solitary Wave Interaction with Porous Breakwaters. J. Waterw. Port Coast. Ocean Eng. 133, 352–363. https://doi.org/10.1061/(ASCE)0733-950X(2007)133:5(352)
Liu, P.L.-F., Lin, P., Chang, K.-A., Sakakiyama, T., 1999. Numerical Modeling of Wave Interaction with Porous Structures. J. Waterw. Port Coast. Ocean Eng. 125, 322–330. https://doi.org/10.1061/(ASCE)0733-950X(1999)125:6(322)
Losada, I.J., Lara, J.L., Guanche, R., Gonzalez-Ondina, J.M., 2008. Numerical analysis of wave overtopping of rubble mound breakwaters. Coast. Eng. 55, 47–62. https://doi.org/10.1016/j.coastaleng.2007.06.003
Mares-Nasarre, P., Argente, G., Gómez-Martín, M.E., Medina, J.R., 2019. Overtopping layer thickness and overtopping flow velocity on mound breakwaters. Coast. Eng. 154, 103561. https://doi.org/10.1016/j.coastaleng.2019.103561
Mares-Nasarre, P., Gómez-Martín, M.E., Medina, J.R., 2020. Influence of Mild Bottom Slopes on the Overtopping Flow over Mound Breakwaters under Depth-Limited Breaking Wave Conditions. J. Mar. Sci. Eng. 8, 3. https://doi.org/10.3390/jmse8010003
Mares-Nasarre, P., Molines, J., Gómez-Martín, M.E., Medina, J.R., 2021. Explicit Neural Network-derived formula for overtopping flow on mound breakwaters in depth-limited breaking wave conditions. Coast. Eng. 164, 103810. https://doi.org/10.1016/j.coastaleng.2020.103810
Molines, J., Bayon, A., Gómez-Martín, M.E., Medina, J.R., 2019. Influence of Parapets on Wave Overtopping on Mound Breakwaters with Crown Walls. Sustainability 11, 7109. https://doi.org/10.3390/su11247109
Patil, A., 2019. Numerical investigation of nearshore wave transformation and surf zone hydrodynamics. Delft University of Technology, Delft, The Netherlands.
Roenby, J., Bredmose, H., Jasak, H., 2016. A computational method for sharp interface advection. R. Soc. Open Sci. 3, 160405. https://doi.org/10.1098/rsos.160405
Sandoval, C., Bruce, T., Burgess, K., 2017. Wave overtopping hazard to pedestrians: video evidence from real accidents, in: Coasts, Marine Structures and Breakwaters 2017. Presented at the ICE Coasts, Marine Structures and Breakwaters, ICE Publishing, Liverpool, UK, pp. 501–512. https://doi.org/10.1680/cmsb.63174.0501

Schüttrumpf, H., Möller, J., Oumeraci, H., 2002. Overtopping flow parameters on the inner slope of seadikes, in: Coastal Engineering 2002. Presented at the Proceedings of the 28th International Conference, World Scientific Publishing Company, Cardiff, Wales, pp. 2116–2127. https://doi.org/10.1142/9789812791306_0178

Shiach, J.B., Mingham, C.G., Ingram, D.M., Bruce, T., 2004. The applicability of the shallow water equations for modelling violent wave overtopping. Coast. Eng. 51, 1–15. https://doi.org/10.1016/j.coastaleng.2003.11.001

Suzuki, T., Altomare, C., Veale, W., Verwaest, T., Trouw, K., Troch, P., Zijlema, M., 2017. Efficient and robust wave overtopping estimation for impermeable coastal structures in shallow foreshores using SWASH. Coast. Eng. 122, 108–123. https://doi.org/10.1016/j.coastaleng.2017.01.009

Tuan, T.Q., Oumeraci, H., 2010. A numerical model of wave overtopping on seadikes. Coast. Eng. 57, 757–772. https://doi.org/10.1016/j.coastaleng.2010.04.007

Van Bergeijk, V.M., Warmink, J.J., Van Gent, M.R.A., Hulscher, S.J.M.H., 2019. An analytical model of wave overtopping flow velocities on dike crests and landward slopes. Coast. Eng. 149, 28–38. https://doi.org/10.1016/j.coastaleng.2019.03.001

Van den Bos, J.P., Verhagen, H.J., 2018. Breakwater design: Lecture notes CIE5300. Delft University of Technology, Delft, The Netherlands.

Van der Meer, J.W., Hardeman, B., Steendam, G.J., Schuttrumpf, H., Verheij, H., 2010. Flow depths and velocities at crest and landward sope of a dike, in theory and with the wave overtopping simulator. Coast. Eng. Proc. 1, 10. https://doi.org/10.9753/icce.v32.structures.10

Van Gent, M.R.A. 1994. The modelling of wave action on and in coastal structures, Coastal Engineering, 22 (3-4), 311-339.

Van Gent, M.R.A., 1995a. Wave interaction with permeable coastal structures. (PhD thesis). Delft University of Technology.

Van Gent, M.R.A., 1995b. Porous Flow through Rubble-Mound Material. J. Waterw. Port Coast. Ocean Eng. 121, 176–181. https://doi.org/10.1061/(ASCE)0733-950X(1995)121:3(176)

Van Gent, M.R.A., 2002a. Wave overtopping events at dikes, in: Coastal Engineering 2002. Presented at the Proceedings of the 28th International Conference, World Scientific Publishing Company, Cardiff, Wales, pp. 2203–2215. https://doi.org/10.1142/9789812791306_0185

Van Gent, M.R.A., 2002b. Coastal flooding initiated by wave overtopping at sea defences, in: Solutions to Coastal Disasters ’02. Presented at the Coastal Disasters Conference 2002, American Society of Civil Engineers, San Diego, California, United States, pp. 223–237. https://doi.org/10.1061/40605(258)21

Van Gent, M.R.A., 2001. Wave run-up on dikes with shallow foreshores. J. Waterw. Port Coast. Ocean Eng. 127, 254–262. https://doi.org/10.1061/(ASCE)0733-950X(2001)127:5(254)

Van Gent, M.R.A., Tönjes, P., Petit, H.A.H., Van den Bosch, P., 1994. Wave action on and in permeable structures. Presented at the Proceedings for the International Conference on Coastal Engineering (ICCE), pp. 1739–1753.

Van Gent, M.R.A., Wolters, G., Capel, A., 2022. Wave overtopping discharges at rubble mound breakwaters including effects of a crest wall and a berm. Coast. Eng. 176, 104151. https://doi.org/10.1016/j.coastaleng.2022.104151

Vanneste, D., Troch, P., 2015. 2D numerical simulation of large-scale physical model tests of wave interaction with a rubble-mound breakwater. Coast. Eng. 103, 22–41. https://doi.org/10.1016/j.coastaleng.2015.05.008

Wellens, P., Borsboom, M.J.A., Van Gent, M.R.A., 2010. 3D simulation of wave interaction with permeable structures. Coast. Eng. Proc. 1, 28. https://doi.org/10.9753/icce.v32.structures.28

Weller, H.G., Tabor, G., Jasak, H., Fureby, C., 1998. A tensorial approach to computational continuum mechanics using object-oriented techniques. Comput. Phys. 12, 620. https://doi.org/10.1063/1.168744

Wurjanto, A., Kobayashi, N., 1993. Irregular Wave Reflection and Runup on Permeable Slopes. J. Waterw. Port Coast. Ocean Eng. 119, 537–557. https://doi.org/10.1061/(ASCE)0733-950X(1993)119:5(537)

Xia, J., Falconer, R.A., Wang, Y., Xiao, X., 2014. New criterion for the stability of a human body in floodwaters. J. Hydraul. Res. 52, 93–104. https://doi.org/10.1080/00221686.2013.875073
Zijlema, M., Stelling, G., Smit, P., 2011. SWASH: An operational public domain code for simulating wave fields and rapidly varied flows in coastal waters. Coast. Eng. 58, 992–1012. https://doi.org/10.1016/j.coastaleng.2011.05.015

A. Description of the porosity model used to model the wave-structure interaction in OpenFOAM®

This section includes a brief description of the resistance-type porosity model by Jensen et al. (2014). This model is based on the Volume Averaged Navier-Stokes equations to account for the porosity effect. The continuity equation describes the divergence of the filter velocity being equal to zero:

$$\nabla u_f = 0 \qquad \text{Equation A- 1}$$

Where u_f is the filter velocity vector in Cartesian coordinates. It is the volume averaged ensemble averaged velocity over the total control volume, including the solids in the porous media.

The momentum equation for the porous media is as follows:

$$(1 + C_m)\frac{\partial}{\partial t}\frac{\rho u_f}{n} + \frac{1}{n}\nabla\frac{\rho u_f u_f^T}{n} = -\nabla p^* + gx\nabla\rho + \frac{1}{n}\nabla\mu\nabla u_f + F_p \qquad \text{Equation A- 2}$$

Where $\nabla = \frac{\partial}{\partial x} + \frac{\partial}{\partial y} + \frac{\partial}{\partial z}$, ρ is the density of the fluid, p* is the excess pressure, g is the gravity vector, μ is the dynamic molecular viscosity, n is the porosity of the permeable structure, t is time and $x = [x, y, z]$, is the Cartesian coordinate vector. Two extra terms C_m and F_p appear as a consequence of the volume averaging of the momentum equation. The F_p term accounts for the friction and pressure forces (form drag), and C_m, the acceleration forces that the porous media exerts on the flow. F_p is resolved by means of the extended Darcy-Forchheimer equation:

$$F_p = a\rho u_f + b\rho\|u_f\|_2 u_f \qquad \text{Equation A- 3}$$

The Darcy-Forchheimer consists of two terms, one linear and one non-linear. When the flow is laminar, the first one dominates (known as Darcy flow), when the flow is turbulent, the second dominates (known as Forchheimer flow). a and b are resistance coefficients. They are computed based on the formulations given by Van Gent (1995a), which are applicable for oscillatory flows:

$$a = \alpha_F \frac{(1-n)^2}{n^3}\frac{\mu}{\rho d_{n50}^2} \qquad \text{Equation A- 4}$$

$$b = \beta_F\left(1 + \frac{7.5}{KC}\right)\frac{1-n}{n^3}\frac{1}{d_{n50}} \qquad \text{Equation A- 5}$$

Where d_{n50} is the nominal median grain diameter and $KC = u_m T/(nd_{50})$, u_m is the maximum oscillating velocity and T is the period of oscillation. Van Gent (1995) calibrated the resistance coefficients from physical model tests and recommended the values $\alpha_F = 1000$ and $\beta_F = 1.1$.

To compute C_m, the added mass coefficient that accounts for the transient interaction between grains and water, the equation below was proposed in Van Gent (1995). Here γ_m is an empirical coefficient, approximated as 0.34:

$$C_m = \gamma_m \frac{1-n}{n} \qquad \text{Equation A- 6}$$

To track the deformations of the free surface, the Volume-of-Fluid method (VOF) was applied (originally developed by Hirt and Nichols (1981)). The air and water fluids are tracked by means of an indicator function (F). F is 0 for air and 1 for water, and it can hold intermediate values when both

fluids are mixed. To model the distribution of F, an advection equation is used. The indicator function can be employed to determine the spatial variation of the fluid properties, such as the density and viscosity:

$$\rho = \rho_w F + \rho_a (1 - F) \quad \text{Equation A- 7}$$

$$\mu = \mu_w F + \mu_a (1 - F) \quad \text{Equation A- 8}$$

Where the subscripts a and w refer to air and water, respectively. The equations above indicate that the density and viscosity are calculated based on the weighted average of air and water in each cell.

B. Grid sensitivity analysis for wave propagation

A grid sensitivity analysis was conducted to determine convergence in the wave propagation process. The objective was to find the coarsest grid mesh that did not longer have a strong impact in the estimation of the incident waves. For this purpose, it was chosen to simulate two physical model tests with the crest wall and without the berm (Th00151b and Th00402d, see Table 1). For these tests, the target values of the JONSWAP spectrum with a peak enhancement factor of 3.3, at the location of the wave gauge GRSM02, were H_{m0} = 0.08 m, T_p = 1.85 s, and H_{m0} = 0.12 m, T_p = 1.39 s, respectively. They had fictitious wave steepness[18] of s_{op} = 0.015, and s_{op} = 0.040, respectively). These tests were picked in such a way that they were representative of the wave conditions to be modelled to obtain the flow depths and velocities on the crest of the breakwater.

The numerical flume was constructed with a total length of 20.4 m and a height of 1.6 m. The first 9.4 m were defined as the inlet relaxation zone. Its length corresponds to the largest deep water wave length (L_{0p}) of all the tests performed, under normal incident waves, in the same campaign in the Delta Basin[19]. The last 2.13 m were defined as the outlet relaxation zone. The length of the outlet relaxation zone is of less relevance because, even though it is not fully non-reflective, the wave energy that gets reflected towards the wave paddle gets dissipated in the porous structure. For this reason, it was decided to use a value close to 2 m as a starting point, and not because this length was related to a particular portion of the any wave length of the tests. The porous breakwater was placed at 13.99 m from the inlet (configuration without the berm). To separate the incident and reflected waves, numerical wave gauges were positioned at distances corresponding to 1.59 m, 1.91 m, 2.41 m, 3.01 m, 3.34 m, and 4.04 m, respectively, from the toe of the breakwater (configuration without the berm). The distance between the end of the inlet relaxation zone and the first numerical wave gauge (from left to right) was set as 0.55 m. The closest wave gauge to the breakwater had the same location as the wave gauge in the physical model tests. Figure B- 1 a) presents the numerical set-up that was used for the grid sensitivity analysis.

[18] The fictitious wave steepness corresponds to the ratio between the significant wave height and the deep-water wave length, leading to: $s_{op} = \frac{H_{m0}}{1.56T_p^2}$.

[19] To take the largest deep water wave length of all the tests was a conservative approach taken by the author. But it was used as a starting point to perform the grid sensitivity analysis.

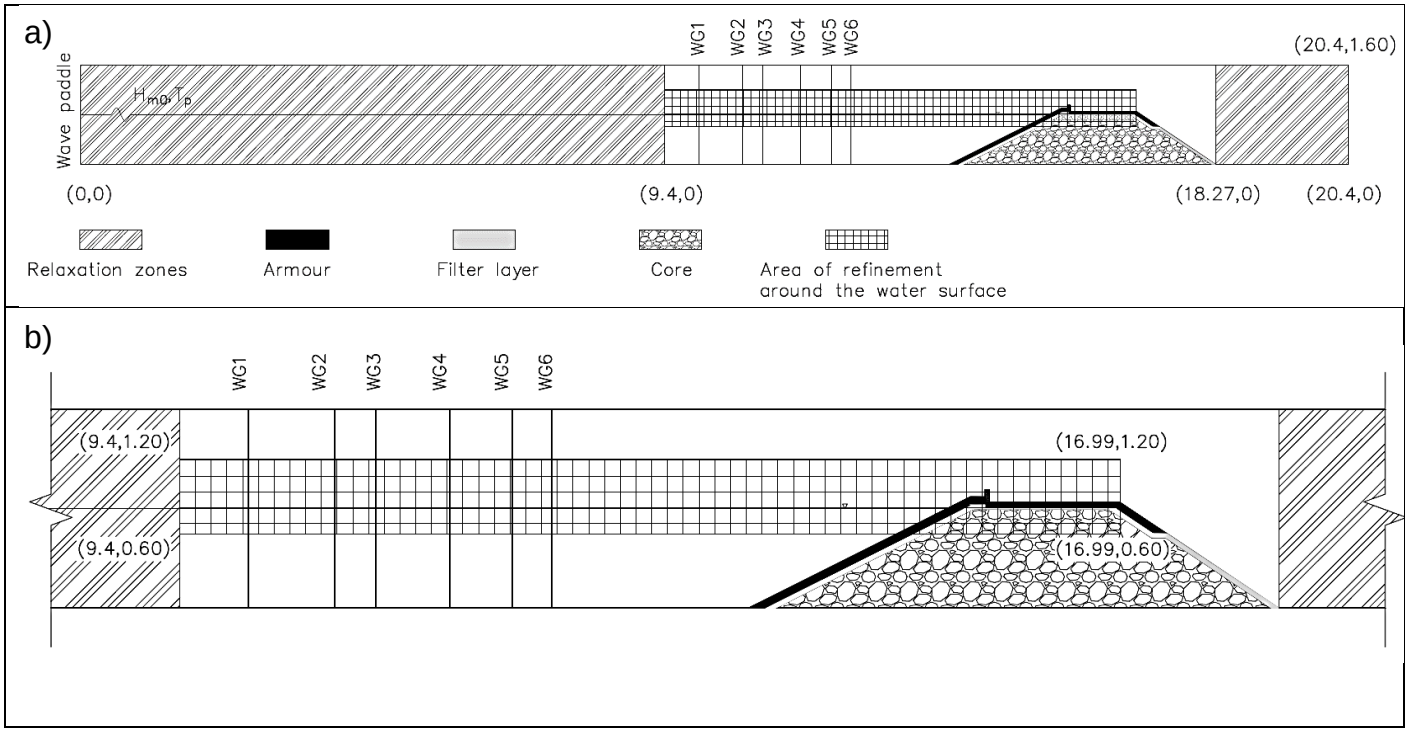

Figure B- 1. a) Numerical flume set-up to evaluate the influence of the grid on the wave propagation. b) Close-up of the area of refinement around the water surface. The coordinates are specified in meters. WG = wave gauge.

The cases were executed with a seed for random phase of 0, which generated the same time series of irregular waves for all the runs performed for each of the tests. This is essential to obtain comparable results when the grid is changed. The runtime for all the cases was set as 500 seconds. Hence, more than 250 waves were obtained for all the runs.

Initially, a base mesh with cells of 0.04 m x 0.04 m was created. Four different grid sizes around the water level ($\Delta x = \Delta y$ = 0.005, 0.01 m, 0.02 m, and 0.04 m) were analyzed. They were created by defining an area of refinement around the surface, which allowed different levels of refinement with respect to the base mesh. The area of refinement was located from the end of the inlet relaxation zone till the end of the crest of the breakwater (see Figure B- 1 b). The dimensions of the area of refinement around the water level were defined in such a way that the largest expected wave height[20] to be generated would be contained inside this zone. Three levels of refinement with respect to the base mesh were defined around the crest wall ($\Delta x = \Delta y$ = 0.005 m). The impermeable crest wall was removed from the numerical domain. To compare the impact of the different grid sizes on the wave propagation, the number of cells per significant wave height and wave length were plotted against the normalized computed significant wave height. The normalized significant wave height was calculated as the computed significant wave height with the actual grid size divided by the significant wave height computed with the finest grid size. The results are shown in Figure B- 2.

[20] The largest expected wave height was approximated as $2*H_{m0}$, as follows from the Rayleigh distribution in deep water (refer to (Holthuijsen, 2007) for more information). As rarest events could potentially occur and the physical model tests were performed in intermediate water, the area of refinement was extended a little bit more than what was calculated with $2*H_{m0}$.

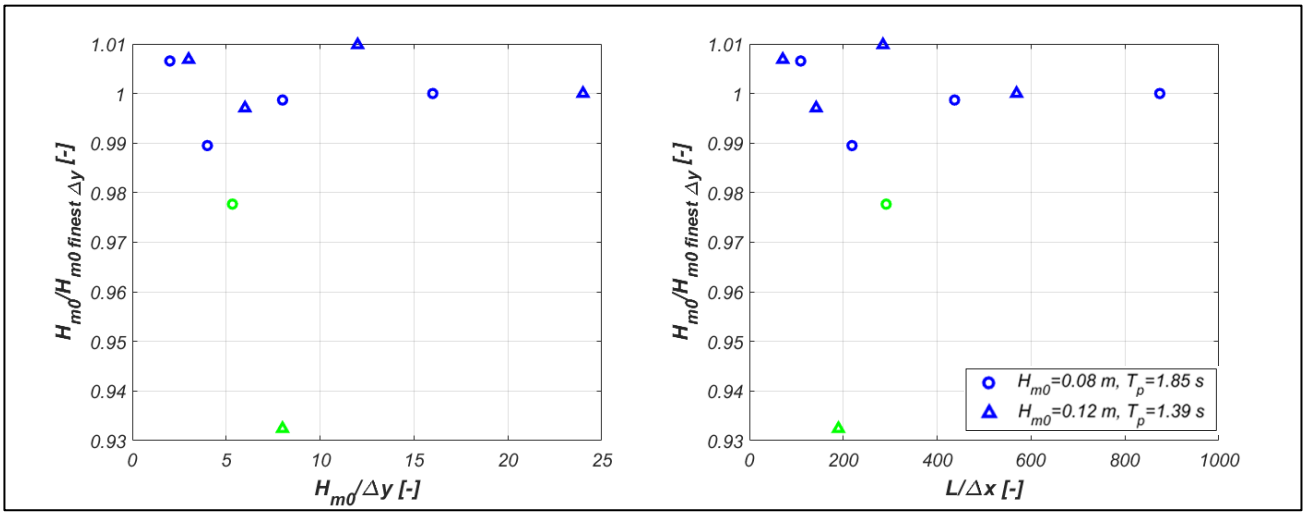

Figure B- 2. Effect of different grid sizes around the water level on the wave propagation. The circles represent the results of the test with the low wave height (Hm0 = 0.08 m) and low wave steepness (s_{op} = 0.015), and the triangles, the results of the test with the high wave height (Hm0 = 0.12) with high wave steepness (s_{op} = 0.040 m). The blue colors are obtained with a base mesh of 0.04 m x 0.04 m, and the green colors, with a base mesh of 0.06 m x 0.06 m.

As can be observed from Figure B- 2, when a base mesh of 0.04 m x 0.04 m is used, there is not a clear convergence in the estimation of the incident significant wave height as the mesh around the water surface is refined. The different grid sizes produce incident significant wave height values which are very close to each other. Overall, the incident significant wave height values were lower than the target values, by around 5% for the test with the lower H_{m0} and lower s_{op}, and by 14% for the test with the higher H_{m0} and higher s_{op}. Another case was run for both tests, where a different base mesh was created, with cells of 0.06 m x 0.06 m. Two refinement levels were applied to the surface around the water level, which means that the cells around the water surface had grid sizes $\Delta x = \Delta y = 0.015$ m. The grid size around the crest wall was $\Delta x = \Delta y = 0.0075$ m (also, three levels of refinement were applied in this case). However, there is a larger deviation in the calculation of the incident significant wave height with respect to the approximated value when the finer base mesh of 0.04 m x 0.04 m was employed. It was observed that with this coarser base mesh, the estimated incident significant wave height decreased (see Figure B- 2).

To further comprehend the effect of the grid size on the wave propagation, the total significant wave height[21] along the flume, the wave spectrum obtained with the incident waves, and the exceedance curve of the incident waves were obtained for each of the previously discussed mesh variations, and for both tests. The wave spectrum and the exceedance curves were obtained for the incident waves computed at the location of the first numerical wave gauge (positioned at 4.04 m from the toe of the breakwater with the configuration without the berm). In this analysis, an extra case was included where the base mesh was configured with cells of 0.02 m x 0.02 m, and the grid size around the water surface was kept as $\Delta x = \Delta y = 0.01$ m (1 refinement level was applied within the area of refinement). Around the crest wall, the cell size was $\Delta x = \Delta y = 0.005$ m (with two refinement levels with respect to the base mesh). The results are shown in Figure B- 3.

[21] The significant wave height computed from the total surface elevation (with the sum of incident and reflected waves).

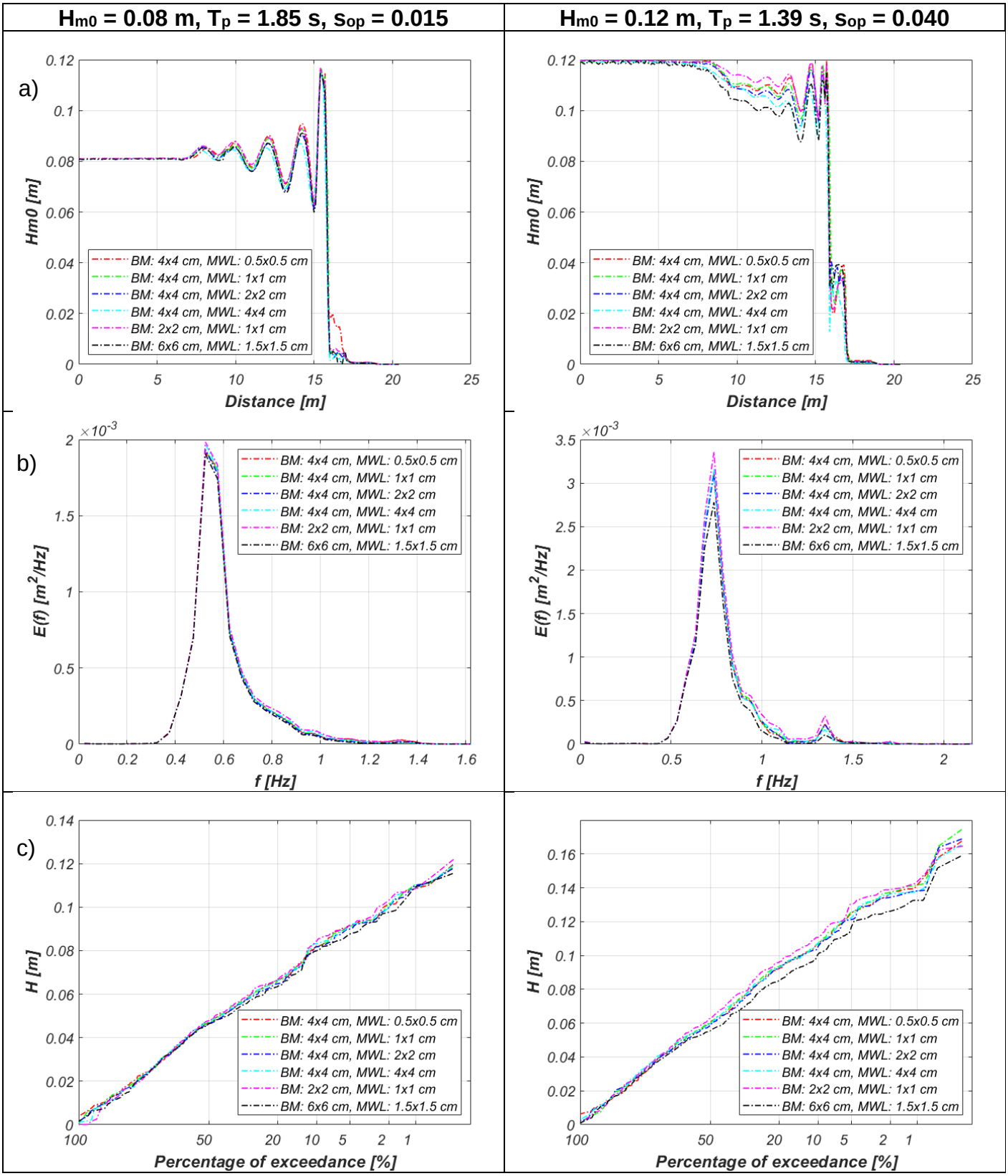

Figure B- 3. Grid effect on a) the significant wave height along the flume computed with the total surface elevation, b) the wave spectrum of the incident waves, and c) the exceedance curve of the incident waves. BM = base mesh, MWL = mesh around the water level.

Indeed, the larger deviations happen when the coarsest base mesh is used (the one with cells of 0.06 m x 0.06 m), the total significant wave height along the flume is lower, as well as the peak of the spectrum and the higher wave heights in the exceedance curve, with respect to the results obtained with the other mesh variations. Between the four different refinement levels around the water surface using the 0.04 m x 0.04 m base mesh, there are no noticeable differences in the exceedance curves and the wave spectrum. But it can be observed that the total significant wave height along the flume increases as the refinement level increases around the water surface for the base mesh created with 0.04 m x 0.04 m cells. Overall, the highest significant wave height along the flume was calculated when the base mesh with 0.02 m x 0.02 m was used. Since the interaction between the incident and reflected waves affect the overtopping events, an accurate representation of the total surface elevation is preferred. Even so, a balance must be found between accuracy and the use of computational resources. The base mesh of 0.02 x 0.02 m might offer the most accurate results, but there are areas away from the water surface, wish do not need such fine mesh (e.g., the region where the air flow is calculated). Hence, it is not the most efficient mesh. The grid with a base mesh of 4 cm x 4 cm, with a finer mesh of 0.5 cm x 0.5 cm around the water level produces the total significant wave height along the flume that is more similar to the one obtained with the base mesh of 0.02 x 0.02 m. Nonetheless, the computational time required to complete one of these runs, with only 500 seconds, was 11 days. Therefore, this option is even less practical than the one with the base mesh of 0.02 x 0.02 m. Finally, the grid with base mesh of 0.04 m x 0.04 m with grid cells around the water surface of $\Delta x = \Delta y = 0.01$ m is preferred since it offers an adequate balance between accuracy and computational efficiency. It was found that the difference between the computed incident significant wave height with the finest base mesh, 0.02 m x 0.02 m, and the coarser base mesh, 0.04 m x 0.04 m (with grid cells around the water surface of $\Delta x = \Delta y = 0.01$ m), was of 2% and 4%, for the tests with smaller and larger target wave height H_{m0}, respectively.

For the rest of the grid sensitivity analysis, the numerical set-up with the base mesh of 0.04 m x 0.04 m, with the mesh around the water level of 0.01 m x 0.01 m, with the length of the relaxation zones, and with the positions of the wave gauges mentioned at the beginning of this appendix section, will be referred to as the base case. As part of this sensitivity analysis, it was also decided to quantify the impact of some additional variations in the configuration of the numerical flume, with the objective of decreasing the demand of the computational resources of the model. The description of these variations is giving with respect to the base case:

1. The base mesh was divided into three regions. The top part, which comprised the elevations 1.20 m to 1.60 m, had grid cells with decreasing vertical dimension from the highest to the lowest position within the region. The ratio between the vertical dimensions of the top cell and the bottom cell was 2. The central region (from elevation 0.6 m to 1.20 m) had cells with an aspect ratio of 1:1 (0.04 m x 0.04 m). The bottom region, which extended from elevation 0 m to 0.60 m, had cells with increasing vertical dimension from the highest to the lowest cell. The ratio between the vertical dimensions of the top cell and the bottom cell was 0.8. The rest of the parameters were kept the same with respect to the base case.
2. The length of the inlet relaxation zone was changed as equal to the wave length computed with the linear wave theory, with the peak period and the actual water depth. This leads to different inlet relaxation zone lengths for each numerical flume destined to reproduce the results of each of the tests that were picked to carry out the grid sensitivity analysis. The rest of the parameters were kept the same with respect to the base case.
3. The length of the outlet relaxation zone was increased to 4.73 m. This corresponds to half the longest deep water wave length of all the tests of the same campaign at the Delta Basin. The rests of the parameters were kept the same as in the base case.
4. The distance between the end of the inlet relaxation zone and the first numerical wave gauge was defined as 2 m (the original distance was 0.55 m). The other parameters were maintained as in the base case.
5. The outlet relaxation zone was shortened to 1.5 m. This is in the same order of magnitude as half the wave length computed with the peak period and actual water depth for the second

test, the one with higher wave height and higher wave steepness. For this reason, this variation applies only for the second test used for calibration. The rest of the parameters were kept the same with respect to the base case. This variation was implicitly taken into account for the first test, the one with lower wave height and wave steepness, since the length of the outlet relaxation zone for the base case was in the same order of magnitude as half the wave length computed with the peak period and actual water depth for the first test (2 m).

All the variations with respect to the base case are presented in Figure B- 4.

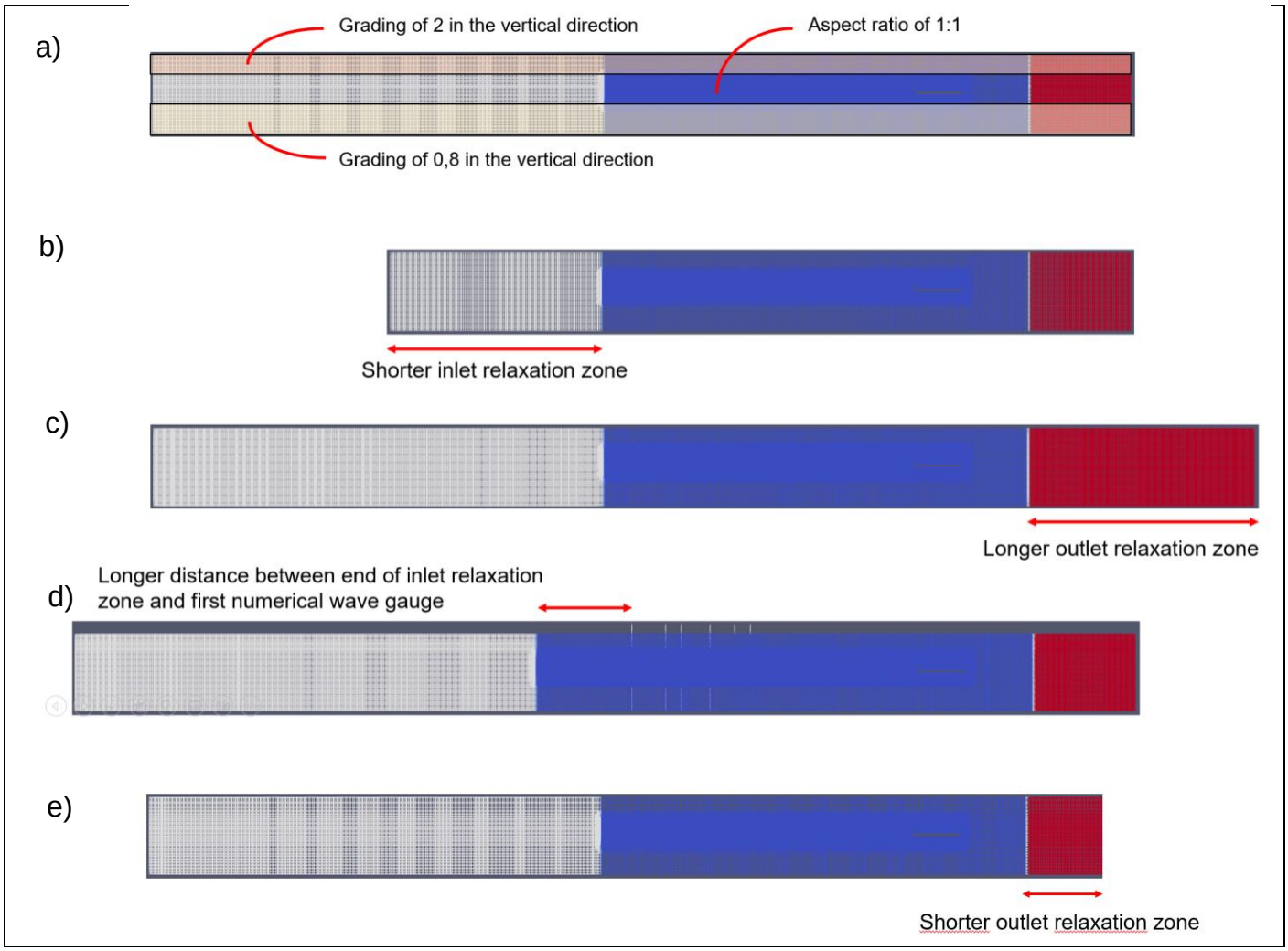

Figure B- 4. Additional changes to the numerical model to evaluate convergence in the wave propagation. a) Variation 1. b) Variation 2. c) Variation 3. d) Variation 4. e) Variation 5.

For all the variations, the cells located around the water surface were created with an aspect ratio of 1, because as suggested by Jacobsen et al. (2012), it approximates better wave breaking. Jacobsen et al. (2012) also mentions that, in most engineering applications, the results are invariant to the air flow caused by the wave motion. For this reason, it was suggested that savings in computational time could be obtained when calculations would be limited to the cells filled with water. Nevertheless, this is not currently possible in OpenFOAM®, and hence, the flow in air and water are both computed. Therefore, as a method of compensation for the use of computational resources to approximate the air flow, a grading different than 1 was applied in the vertical direction in the upper region of the base mesh in the first variation (see Figure B- 4 a). In addition, the interest of the present research is on the estimation of the flow depths and velocities at the crest of a rubble mound breakwater. Hence, there is no need to accurately estimate the boundary layer. For this reason, also a grading different than 1 was applied in the vertical direction of the lower region of the base mesh in the first variation (see Figure B- 4 a).

The relaxation zones, the method employed in waves2foam to absorb reflected waves, form part of the computational domain. Hence, the longer the relaxation zones, the more the computations would last. For applications of wave propagation with a porous structure, it is a common practice to set the inlet relaxation zone as one wave length, and the outlet relaxation zone as half the wave length. Defining a non-reflective relaxation zone based on the wave length was first suggested in Jacobsen et al. (2012). The outlet relaxation zone does not have the need to be as long as the inlet relaxation zone, since the energy that is reflected back (towards the wave paddle) is further dissipated by the porous structure. To study the variations in the wave propagation due to the length of the relaxation zones, the variations 2, 3 and 5 (only for the test with higher wave height and wave steepness) were performed.

The fourth variation was executed to discard an influence in the wave propagation result when the distance between the end of the inlet relaxation zone and the first numerical wave gauge changed.

For the test with the smallest target wave height (H_{m0} = 0.08 m) and lower steepness (s_{op} = 0.015), the absolute relative percentage of error with respect to the significant wave height as computed with the base case were of 0.5%, 0.8%, 0.7%, and 0.8%, for the variations 1, 2, 3, and 4, respectively. And, for the test with the largest target wave height (H_{m0} = 0.12 m) and higher steepness (s_{op} = 0.040), the absolute relative percentage of error with respect to the significant wave height computed with the original case were of 1.5%, 0.5%, 0.5%, 1.8%, and 2.3% for the variations 1, 2, 3, 4, and 5, respectively. The effect of all the variations on the significant wave height along the flume, the incident energy spectrum, and the exceedance curve of the incident waves can be observed on Figure B- 5 (for both tests).

From these last sensitivity analysis cases, it was found that the computational efficiency of the model could indeed be further improved. This can be reached by defining the length of the inlet relaxation zone as equal to the wave length computed with the peak period and the water depth, by using an outlet relaxation zone equal to half the wave length computed with the peak period and actual water depth, by using aspect ratios different that 1:1 in mesh zones away from the water surface, and by choosing the short distance (0.55 m) between the end of the inlet relaxation zone and the first numerical wave gauge.

Even though the results in wave propagation showed that it is possible to apply a grading in the vertical direction in the upper region of the base mesh, it was decided to discard this option. The author had the concern on whether having aspect ratios different than 1 would affect the computation of the flow depths and velocities in the zones where the overtopping events occur. This could be the case since both velocities, the vertical and horizontal ones, are relevant to correctly predict the overtopping process. Some time was spent trying to apply the grading in just a sector of the upper region, mainly in the parts where the waves were only propagating. However, this idea didn't turn to be successful because some errors showed up when SnappyHexMesh was run. In addition, it was found that it is needed to have cells with aspect ratios close to 1 in the surfaces that are snapped with the SnappyHexMesh tool, otherwise the convergence is slow, and failure can happen.

For the final configuration applied for the wave propagation, refer to section 2.2.3, in the main text.

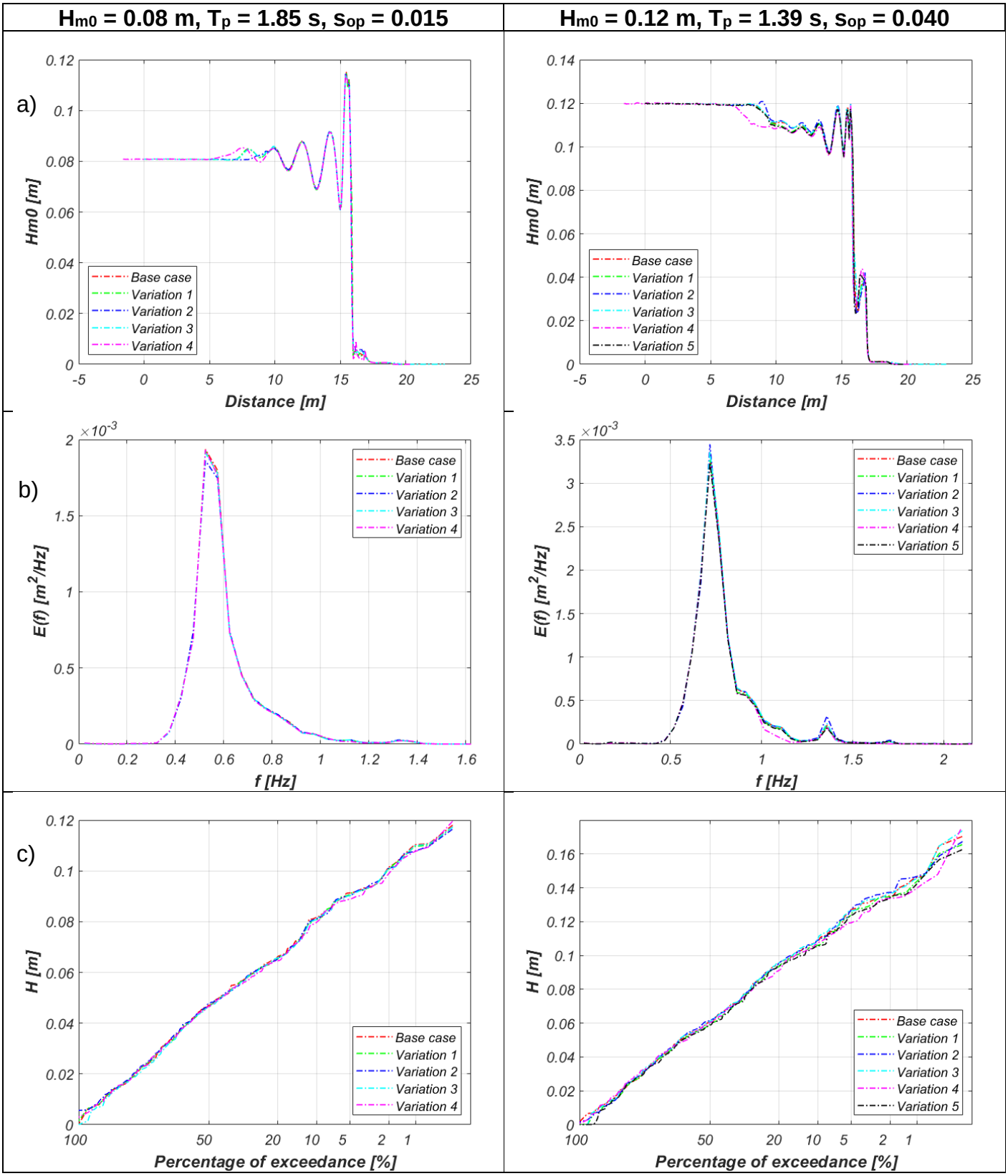

Figure B- 5. Effect of the additional variations of the numerical model on a) the significant wave height along the flume, b) the wave spectrum of the incident waves, and c) the exceedance curve of the incident waves.

C. Extraction of flow depths and flow velocities from the numerical flume

Several steps were taken to analyze the output from the wave gauges, discharge sheets, probes, and planes that were utilized to extract the flow depths and velocities from the numerical model. The most relevant findings will be explained in this section.

C.1. Mass continuity

It was necessary to determine whether the mass was conserved during the wave overtopping events. For this purpose, several discharge sheets were placed on the horizontal part of the crest wall of the breakwater, spaced at 4 cm intervals. The test with ID Th00155 was chosen for this analysis (H_{m0} = 0.1 m, T_p = 2.07 s, see Table 1). From all the tests without the berm picked to be modelled in OpenFOAM®, it was the one with the highest non-dimensional mean overtopping discharge (slightly surpassing the upper recommended limit of non-dimensional mean overtopping discharge of 1E-3). Therefore, more overtopping events could be observed in a shorter amount of time. This was advantageous because some of the simulated tests took up to 9 days in total when they were run for 1000 waves. Figure C- 1 presents the cumulative volume of water passing through the consecutive discharge sheets located on the breakwater crest for the test with ID Th00155 for 1000 waves[22].

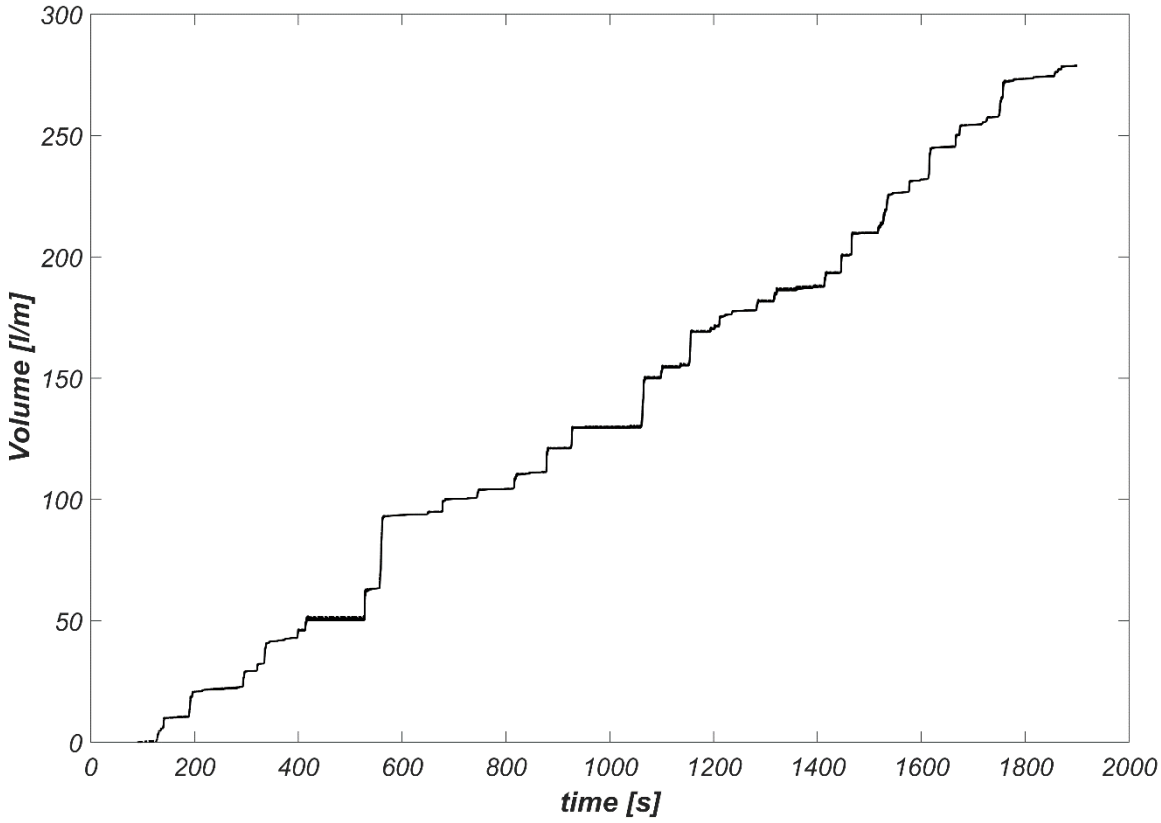

Figure C- 1. Cumulative overtopped volume passing through all the discharge sheets. All the lines are plotted in black.

[22] Note that the mass continuity check could have been performed with less waves than 1000.

It seems from Figure C- 1, that only one curve is shown. However, what happens is that all the curves were plotted one on top of the other. Then, this means that the mass of the overtopping events was conserved during the whole simulation, as the total overtopped volume of water passed through all the discharge sheets.

C.2. Flow depths

To extract the flow depths occurring during the wave overtopping events, several wave gauges were placed in the crest region of the breakwater. Initially, the separation between these devices was set as 4 cm[23]. The same test with ID Th00155 (see Table 1) was chosen to analyze the results due to its highest non-dimensional mean overtopping discharge (more overtopping events are expected in less time, as explained in section C.1). The runtime of the simulation was 600 seconds (289 waves were generated).

As a starting point, the bottom tip of the wave gauges was placed at the elevation 0.80 m, which corresponds to the lower edge of the crest element. Figure C- 2 shows the associated configuration. Note that some wave gauges were located outside of the crest element, in the porous part of the breakwater. These wave gauges were excluded from the analysis. Only the wave gauges positioned between x = 16.08 m and x = 16.80 m were considered (see Figure 16). Since the crest wall is an impermeable element, it was expected that when the upper elevation of the horizontal part of the crest wall would be subtracted from the water surface elevation, the flow depths from the overtopping events would be obtained. Once this procedure was performed, for the author's surprise, it was found that negative flow depths were obtained. Extracting the flow depths from several wave gauges for each computational timestep results in a large amount of data. Therefore, a simple way of visualizing what happened was to plot a histogram which shows specific surface elevation occurrences for all the wave gauges during the whole simulation (see Figure C- 3).

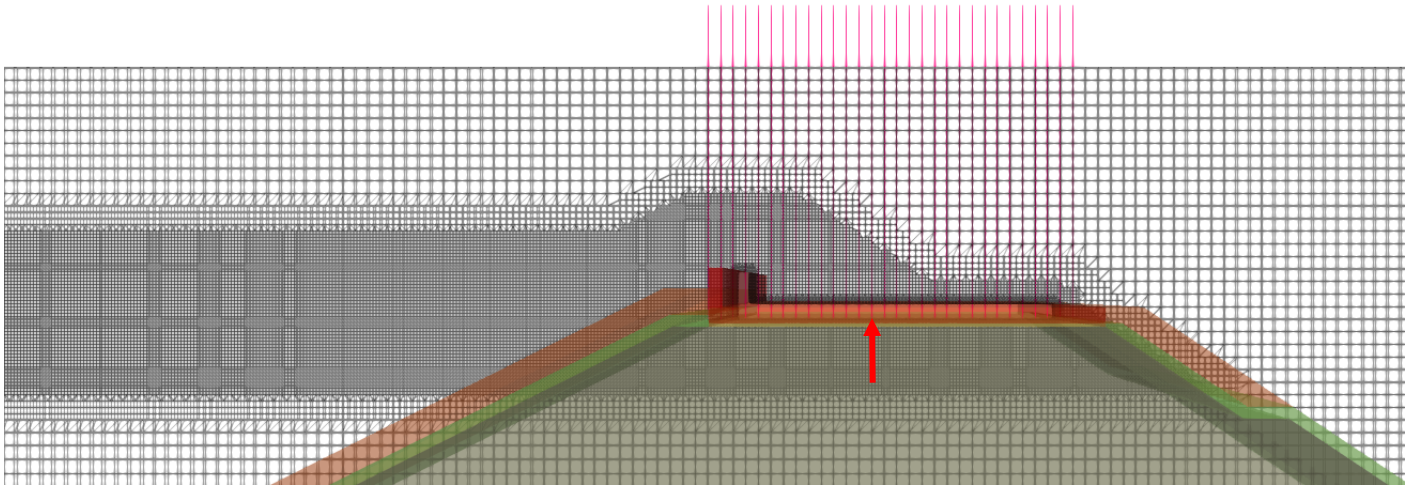

Figure C- 2. Set-up of wave gauges with their lower tip at the bottom part of the crest wall.

The shape of the histogram shown in Figure C- 3 is not the relevant feature, but the water surface elevations themselves. During great part of the computational time, the surface elevations were between 0.80 m and 0.85 m, which coincide exactly with the lower and upper parts of the horizontal part of the crest element. This was unexpected, since water is not supposed to go through this impermeable element. The apparent presence of water inside the crest wall could be attributed to the possibility that the wave gauges were capturing water flow through the permeable region below.

[23] The separation of the numerical instruments was defined, initially, as 4 cm. Nevertheless, the final configuration included a spacing of 12 cm between adjacent measuring devices (see section 2.2.10).

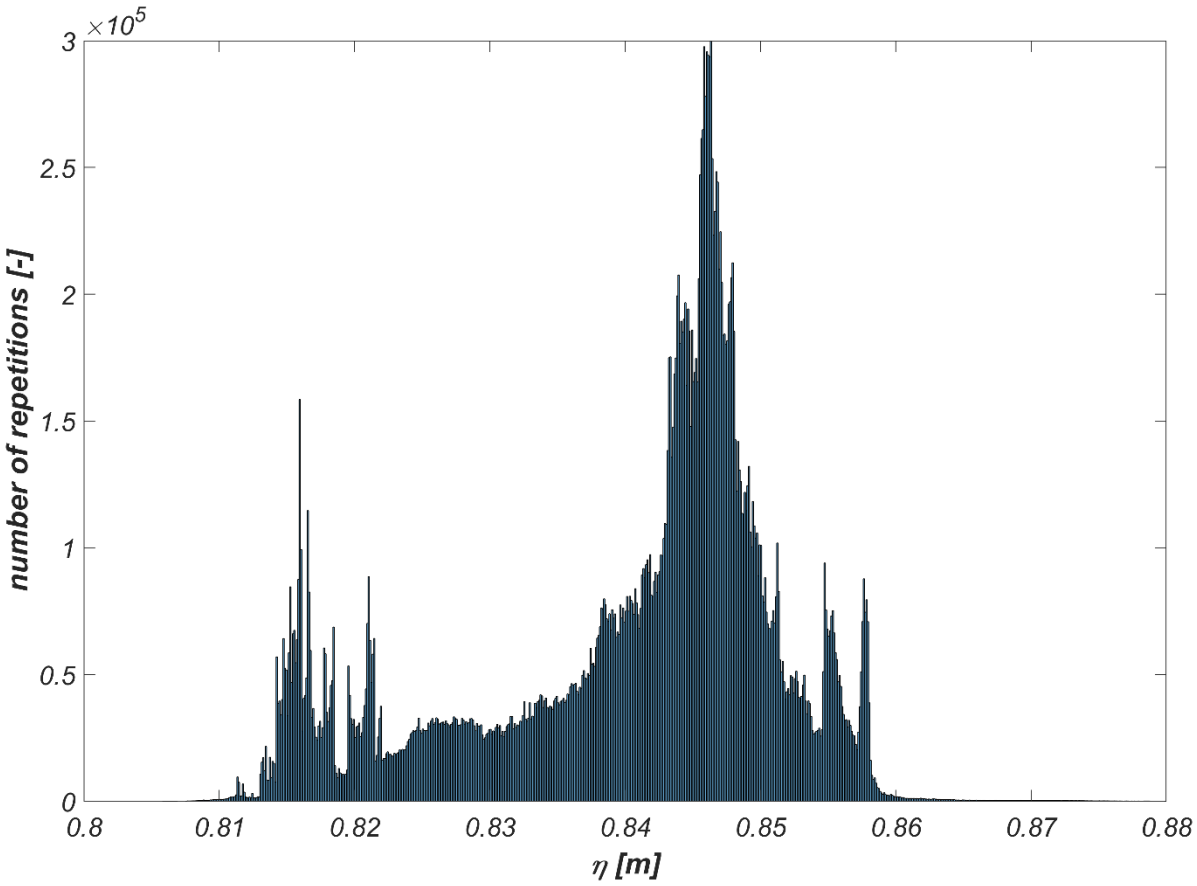

Figure C- 3. Surface elevation histogram for all wave gauges and computational time steps when the lower tip of the wave gauges is placed at 0.80 m.

Another simulation of the same test (Th00155) was carried out where the lower tip of the wave gauges was moved to the upper edge of the horizontal part of the crest wall (see Figure C- 4 for the new configuration). It was also run for 600 seconds. Again, some of the wave gauges were placed in the porous region, but only the ones located between x = 16.08 m and x = 16.80 m were analyzed. The resulting histogram of water surface elevations for all the wave gauges and computational timesteps is shown in Figure C- 5.

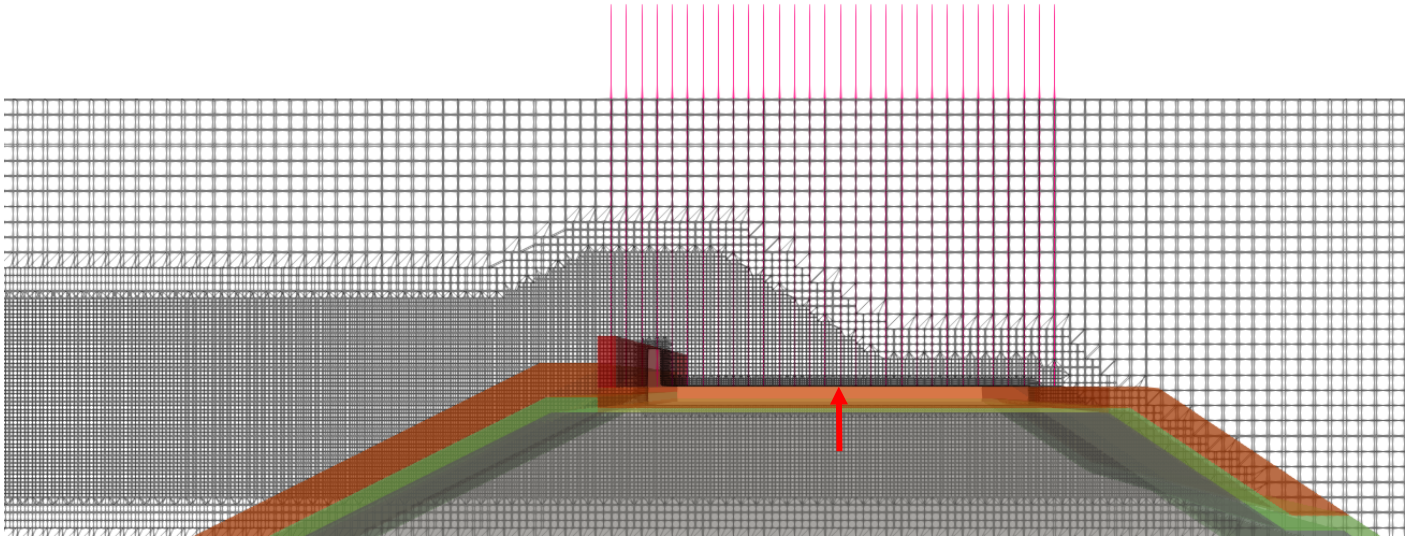

Figure C- 4. Set-up of wave gauges with their lower tip at the upper part of the crest wall.

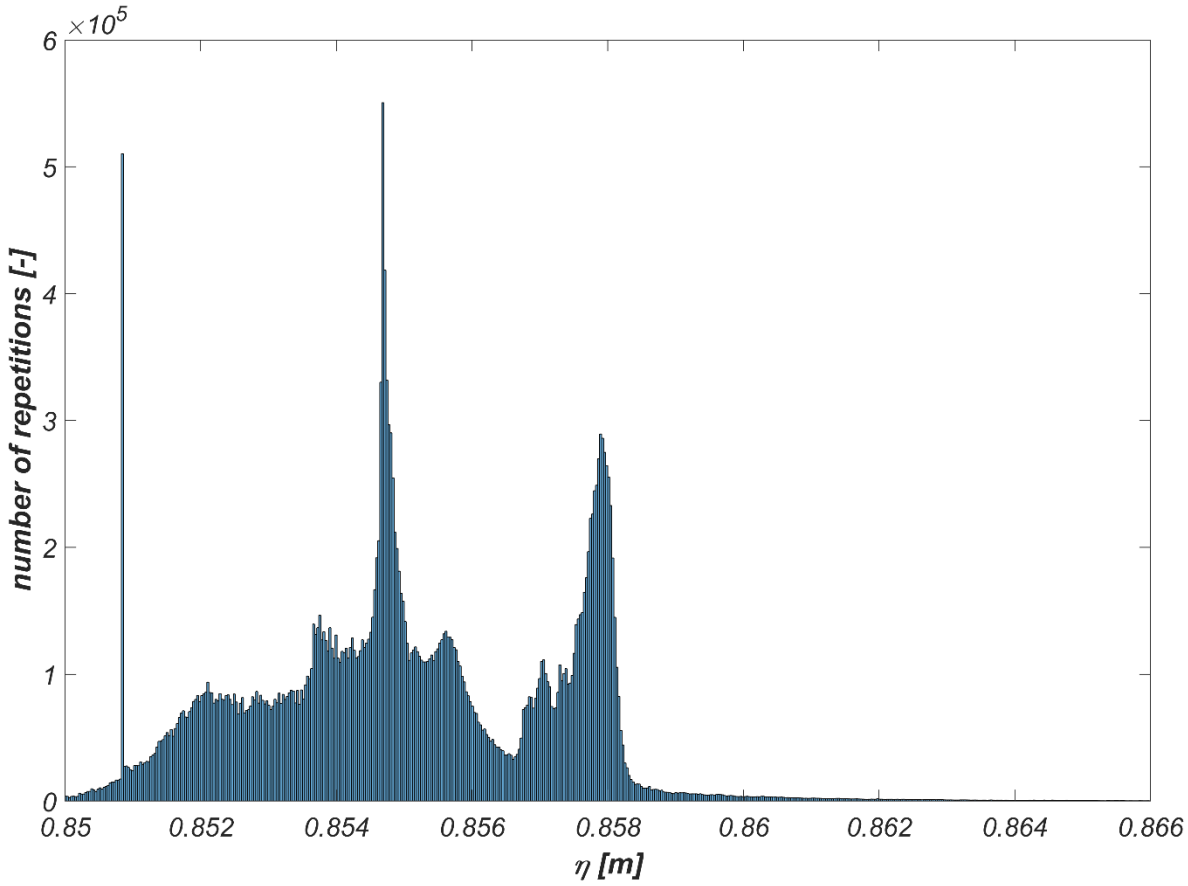

Figure C- 5. Surface elevation histogram for all wave gauges and computational time steps when the lower tip of the wave gauges is placed at 0.85 m.

As it can be observed from the figure above, the water surface elevations during the overtopping events were all above the upper edge of the horizontal part of the crest wall (0.85 m). This follows common sense as the lower tip of the wave gauges were placed completely on top of the horizontal part of the crest wall. It captures the attention that the shape of the histogram is different than the one obtained when the wave gauges were located at the bottom of the crest element.

One way to find out what was happening with the output from the wave gauges was to check the flow depths at different moments in time. While the simulations were running, OpenFOAM® saved the hydrodynamics of the entire numerical flume at 20 seconds intervals. This can be compared as taking a picture of an instant of time of the entire numerical domain. Hence, visual comparisons could be effectuated with the flow depths time series obtained from the wave gauges.

It was decided to analyze the output of the wave gauge located at 16.20 m (see Figure 16). Figure C- 6 a) and b) shows the flow depth time series when the lower tip of the wave gauge is placed at the bottom and upper edges of the horizontal part of the crest element, respectively. To avoid having negative flow depths when the lower tip of the wave gauge is located at the bottom of the crest wall, the elevation of the bottom edge of this impermeable element was subtracted from the water surface elevations. In this case, these flow depths are not computed correctly, as the thickness of the horizontal part of the crest element was included, but it eased the comparison process. The elevation at the top of the horizontal part of the crest wall was subtracted from the water surface elevations in the case when the lower tip of the wave gauges was located at the upper edge of the horizontal part of the crest wall. Technically, the resulting flow depths should correspond to the physical ones.

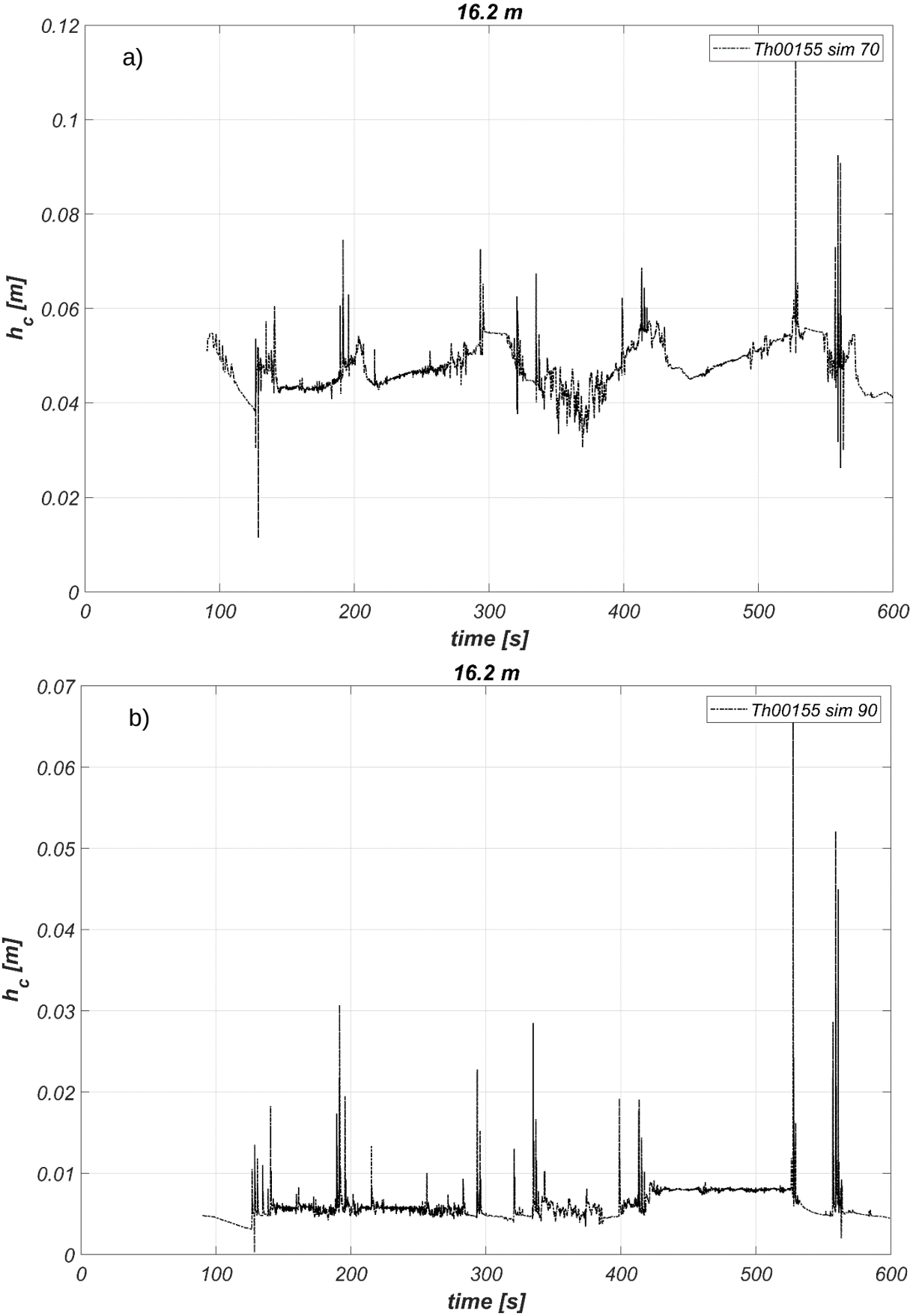

Figure C- 6. Flow depth time series at x = 16.20 m (coordinates of the numerical flume) when the lower tip of the wave gauge is placed at the bottom edge (a) and upper edge (b) of the horizontal part of the crest element.

Ignoring the magnitude of the flow depths, what it is interesting to observe is the shape of the timeseries themselves. They are not the same. For example, in Figure C- 6 a), the timeseries suggest there is a continuous increase of the flow depth from the second 220 till 300, while in b), it seems the flow depth is almost constant. Figure C- 7 shows the output of the numerical flume at different moments in time (220 s, 240 s, and 260 s), with a closer look in the region of interest. Here, the red colors are associated with an indicator factor of 1 (water), and the blue colors are related to an indicator factor of 0 (air). As it has been described before (see section 2.2.3), the mesh consists of grid cells of 0.5 cm around the crest wall. Then, if it is imagined that the water that is present close to the horizonal part of the crest wall would be compressed, flow depths close to 0.5 cm would be obtained. The flow depths in the consecutive frames of Figure C- 7 are almost the same, with a small drop in the flow depth from a to b. Therefore, it can be concluded that the timeseries presented in Figure C- 6 a) does not correspond to what is occurring in the numerical model. Instead, the magnitude of the flow depths presented in the timeseries of Figure C- 6 b) are similar to the visual representations of Figure C- 7.

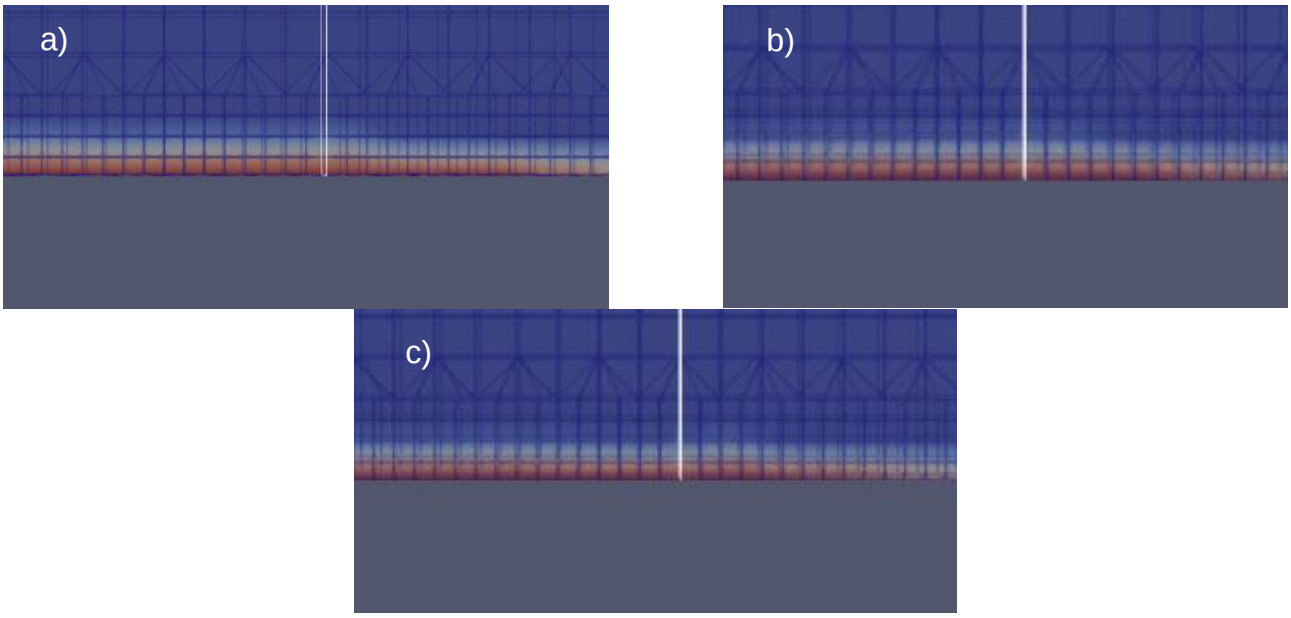

Figure C- 7. Output of the numerical flume for different moments in time. a) at 220 s, b) at 240 s, and c) at 260 s. The white plane indicates the wave gauge positioned at x = 16.20 m.

Another visual inspection was carried out for a different wave gauge. Figure C- 8 presents the timeseries for the wave gauge located at 16.48 m (see Figure 16). Once again, the shape of the timeseries is different. When looking at this figure carefully, it can be observed that the peaks that are present in b) are also in a) but with a different stretching. For example, from 200 to 260 seconds, both timeseries show that the flow depths are decreasing, with a sudden peak in between. The output from different instants in time (200, 220, 240, and 260) of the numerical domain are shown in Figure C- 9. Again, when it is imagined that the water present in the cells, is squeezed in the vertical direction, the magnitude of the flow depths coincides with the timeseries presented in Figure C- 8 b). Overall, it can also be observed from the timeseries shown in Figure C- 8 a), that when there is a decrease, or an increase in the flow depth, it happens for several centimeters rapidly, which can't be possible as the flow depths barely surpass 0.5 cm for most of the time (see Figure C- 9).

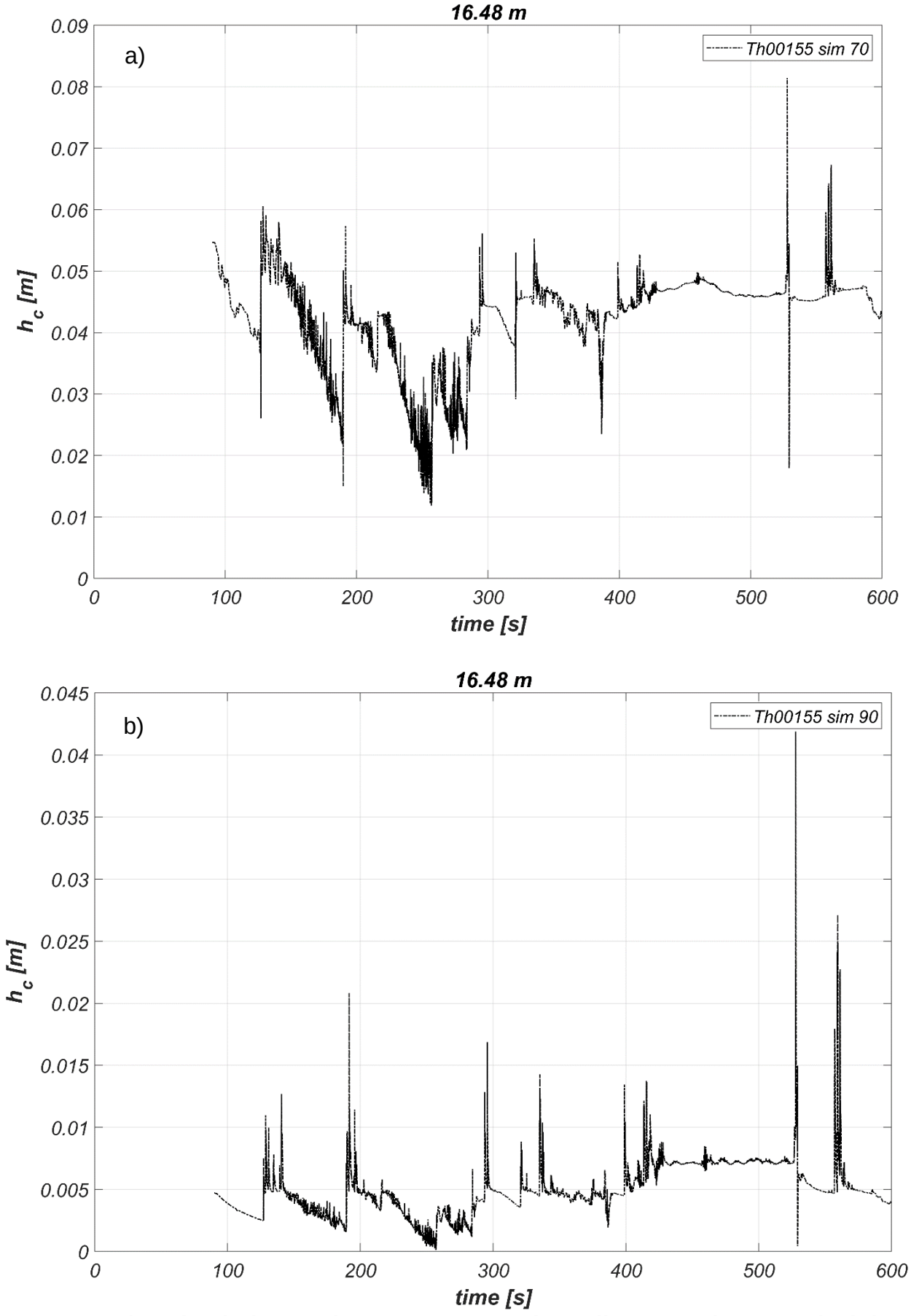

Figure C- 8. Flow depth time series at x = 16.48 m (coordinates of the numerical flume) when the lower tip of the wave gauge is placed at the bottom edge (a) and upper edge (b) of the horizontal part of the crest wall.

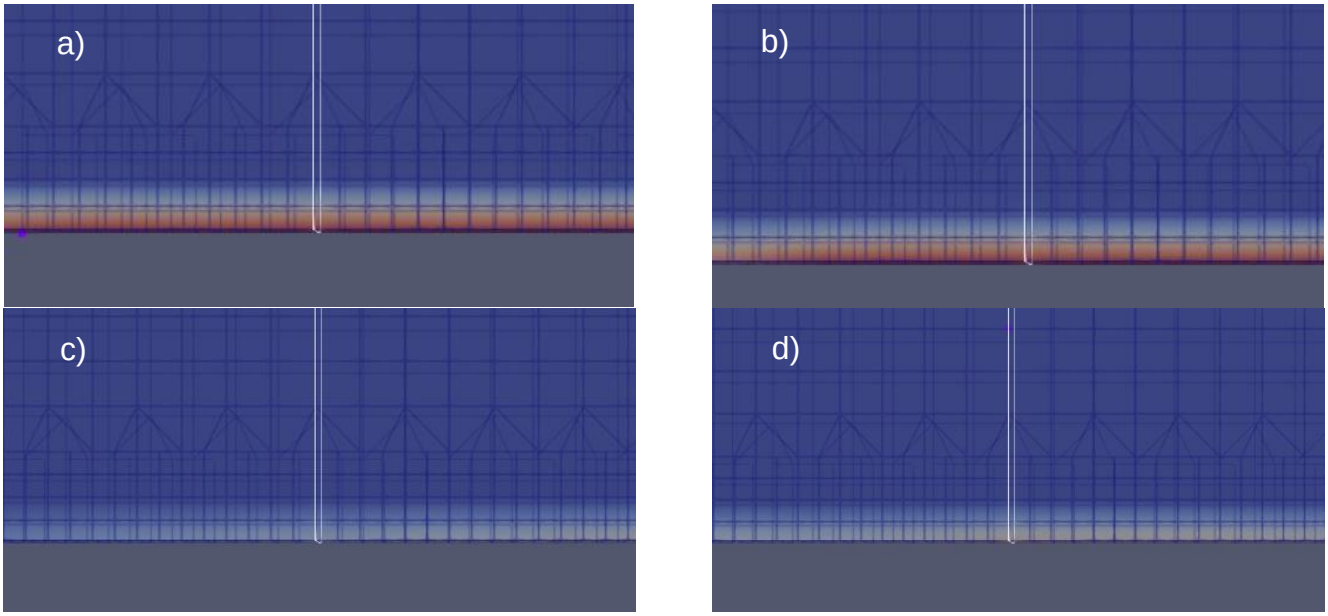

Figure C- 9. Output of the numerical flume for different instants. a) at 200 s, b) at 220 s, c) at 240 s, and d) at 260 s. The white plane indicates the location of the wave gauge at 16.48 m.

To verify if the output extracted when the wave gauges were placed with their lower tip at the top of the horizontal component of the crest wall was correct, an additional case was run. This time the lower tip of the wave gauges was located at the middle of the horizontal part of the crest element (see Figure C- 10). Less wave gauges were defined; they were separated at 12 cm intervals between x = 16.08 m and x = 16.80 m. The simulation was also run for 600 s. Figure C- 11 presents the timeseries of the flow depth at x = 16.44 m (see Figure 16), when a) the lower tip of the wave gauges is located at the top of the horizontal component of the crest wall, and b) when the lower tip of the wave gauges is located at the middle of the horizontal part of the crest wall. To compute the flow depths when the lower tip of the wave gauges is placed at the middle of the horizontal part of the crest element, the elevation of the top of the horizontal component of the crest wall was subtracted from the water surface elevations. Therefore, they should coincide with the physical flow depths. As it can be observed from Figure C- 11, the timeseries coincide. By visual inspection, it was checked that the flow depth timeseries were the same for the other wave gauge locations. The histogram which shows the number of repetitions of a given surface elevation for all wave gauges was not computed. The reason is that the last simulation contained less wave gauges. Hence, the shape of the histogram could have been influenced by this aspect.

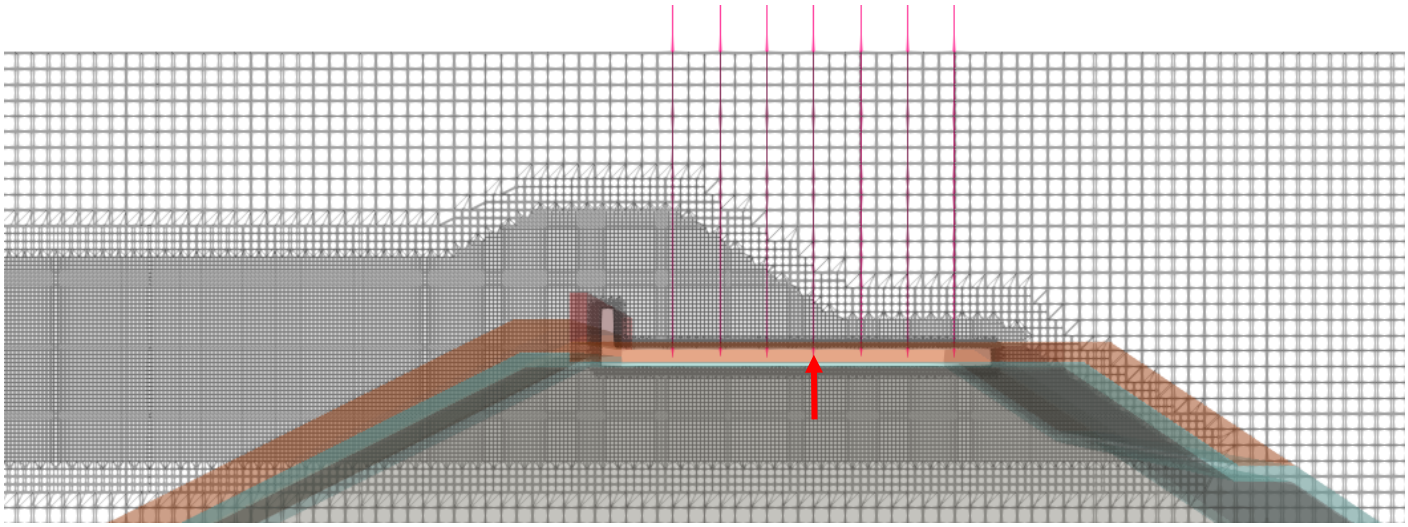

Figure C- 10. Configuration of wave gauges with their lower tip at the middle of the horizontal part of the crest wall.

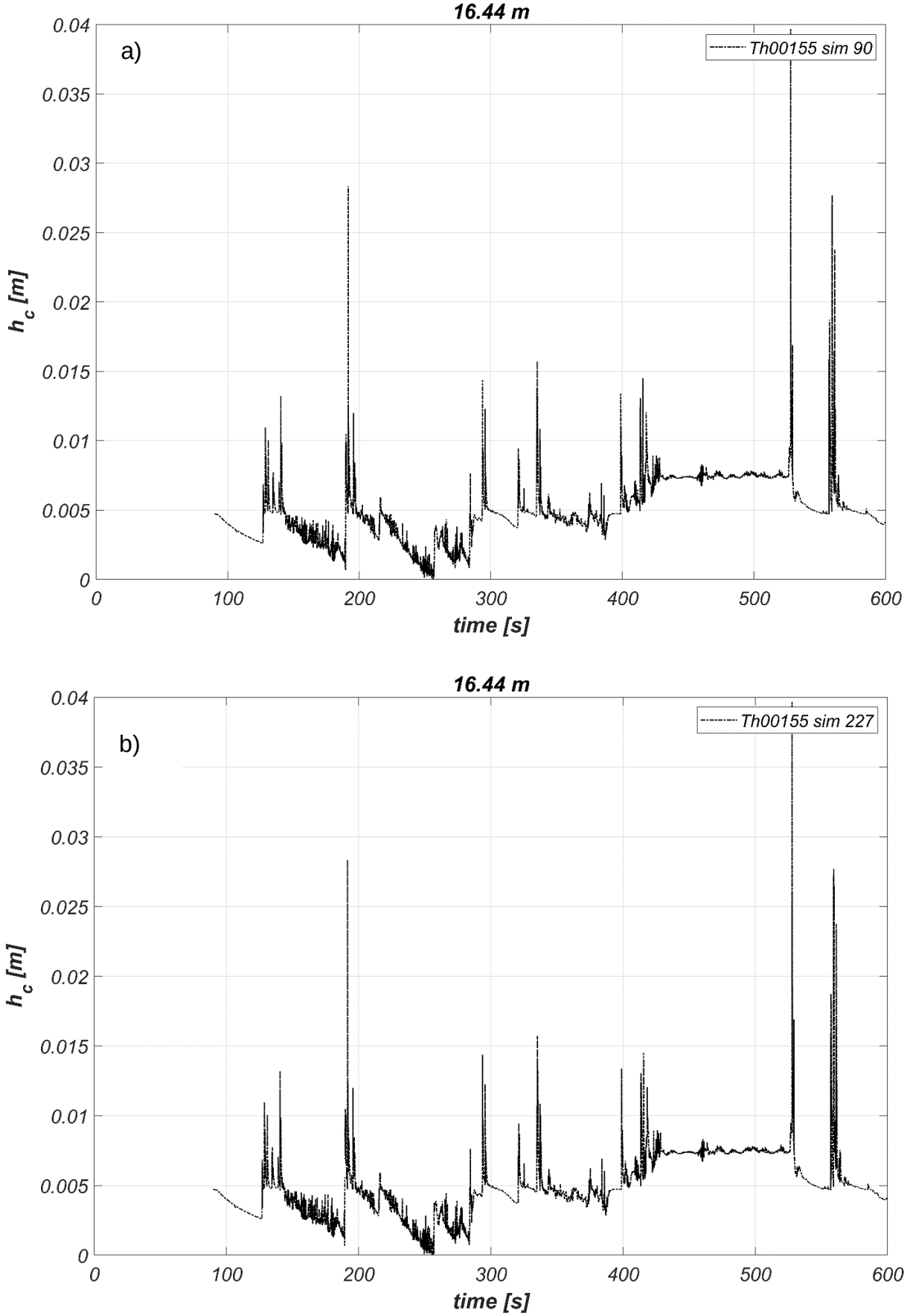

Figure C- 11. Flow depth time series at x = 16.44 m (coordinates of the numerical flume) when the lower tip of the wave gauge is placed at the top (a) and at the middle (b) of the horizontal component of the crest wall.

From the previous discussion, it can be concluded the set-ups in which the wave gauges are placed at the top and at the middle of the horizontal component of the crest wall, are the correct ones.
So far, it only has been checked which is the right position to place the wave gauges to obtain correct flow depths. It still remains to verify the method of extraction of the flow depths by these measuring devices. The waves2foam manual (see Jacobsen, 2017) does not mention anything regarding this aspect. A hypothesis is that the wave gauges sum all the water they find in their vertical plane and place it at a reference level, in a similar manner as physical wave gauges function. To prove this hypothesis, a simulation of 100 seconds was run with another test, Th00152 (see Table 1). In this case, the output of the entire numerical flume was saved each 0.05 s. Figure C- 12 a) shows one instant in time (t = 205.9 s) when an overtopping event is still in the air when its information is extracted by the first numerical wave gauge (x = 16.08 m). When the associated flow depth timeseries is analyzed for the same instant in time (see Figure C- 12 b), it can be inferred that indeed the wave gauge summed up the water it found in the air and placed it at the top of the horizontal part of the crest wall[24].

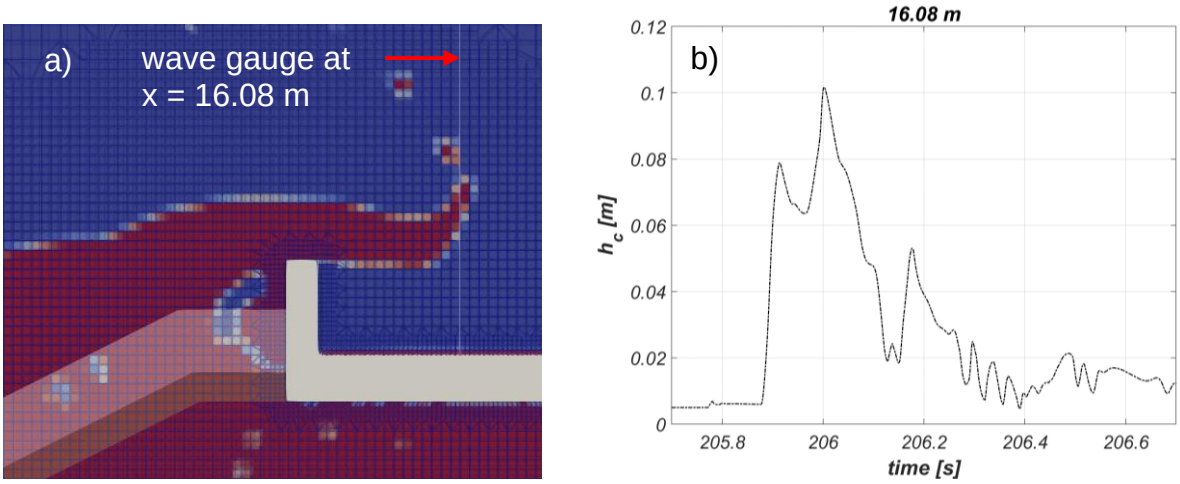

Figure C- 12. Example of the method of extraction of the flow depths by the numerical wave gauges. Simulation with H_{m0} = 0.12 and s_{op} = 0.015. a) Instant t = 205.9 s when the flow depth of the overtopping event is being measured at the first wave gauge (x = 16.08 m). b) Flow depth timeseries around the same instant in time (t = 205.9 s).

Due to the variation in results in the measured surface elevations when the wave gauges were placed at the upper or lower edges of the horizontal part of the crest element, it was decided to investigate if there was a change in the results in the overtopping discharges. Using the test with ID Th00155, the cumulative overtopping discharges were computed when the discharge sheets were located at the upper or lower boundaries of the horizontal part of the crest wall. The results are presented in Figure C- 13. As it can be observed, the curve of cumulative overtopping discharge is the same for both options. Then, the discharges were calculated correctly even when the discharge sheets were placed starting at the bottom of the impermeable element.

It is possible to locate the wave gauges within the horizontal component of the crest wall as long as their lower tip is not very close to its bottom. In this case, they measurements might get polluted with the flow going through the permeable part of the breakwater. It seems the discharge sheets don't present this problem. For further variations carried out in this research, the author decided to use the configuration with the wave gauges and discharge sheets starting at the top of the horizontal component of the crest wall. In this way, it is possible to secure obtaining reliable results. This set-up (instruments at the top of the horizontal part of the crest element) is also what the author would recommend for future researchers that need to simulate similar structures in OpenFOAM®.

[24] It has to be reminded that the flow depths were obtained from subtracting the elevation of the upper edge of the horizontal part of the crest wall from the water surface elevations. With this statement it is clear that the wave gauges reference the flow depths with respect to the upper edge of the horizontal part of the crest wall.

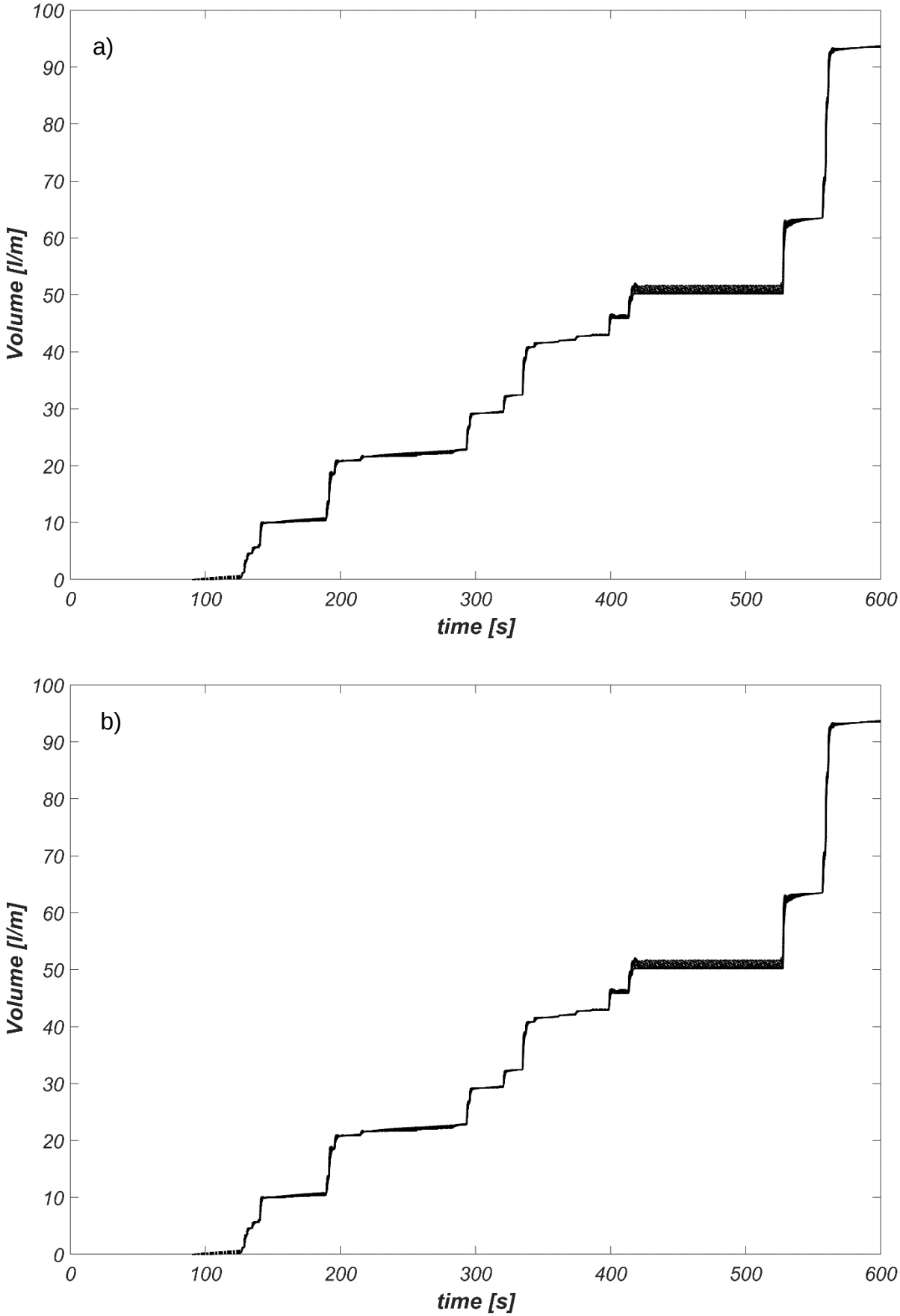

Figure C- 13. Cumulative overtopping discharge when: a) the discharge sheets were defined starting at 0.85 m, b) the discharge sheets were defined starting at 0.80 m. All the lines are plotted in black.

C.3. Flow velocities

As has been mentioned before, when the simulations were run for 1000 waves, they took several days to complete (7 to 9 days). This was a problem, especially at this stage when several methods of extraction of flow velocities needed to be tested and compared. In principle, running the simulation for 1000 waves is not needed when the objective is to compare the flow velocities obtained from different measuring devices. However, it was still necessary to have quite some overtopping events. As the chosen physical model tests had an upper limit of non-dimensional mean overtopping discharge, the overtopping events were not happening very often. Therefore, it was decided to tackle this problem by defining the breakwater as an impermeable structure in OpenFOAM®. Then, frequent overtopping events were expected as water could no longer infiltrate in the structure. The crest wall was also eliminated from the numerical model.

To compare the different methods of extraction of flow velocities, the test with ID Th00402d was chosen (H_{m0} = 0.12 m, T_p = 1.39 s, see Table 1). It is not the test with the highest non-dimensional mean overtopping discharge among the tests that were picked for the validation process, but this is no longer required as the number of overtopping events increase with an impermeable breakwater. The set-up of the numerical flume was almost kept the same. The main difference is that the porous media equations (see section 2.2.1) are not used for the calculation. The length of the numerical domain and the relaxation zones were not modified. The outlet relaxation zone could have been completely removed from the numerical flume since the waves cannot be transmitted through an impermeable structure. Not removing the outlet relaxation zone only has an impact in the computational time of the simulation (it is longer if it is kept), and not in the results. Figure C- 14 presents the configuration of the numerical flume with the impermeable structure. The area occupied by the breakwater was removed from the domain. The SnappyHexMesh utility refines the mesh around surfaces that are removed from the domain. This is the reason why the mesh is finer in the front and rear slopes of the breakwater, and not because it was required for the computation. The runtime was defined as 100 seconds for all the simulations (corresponding to roughly 70 waves). Only for these cases the spin-up time was computed as the time it took the waves to propagate from the wave paddle till the breakwater and back, and not as 90 seconds, as was stated in section 2.2.7.1.

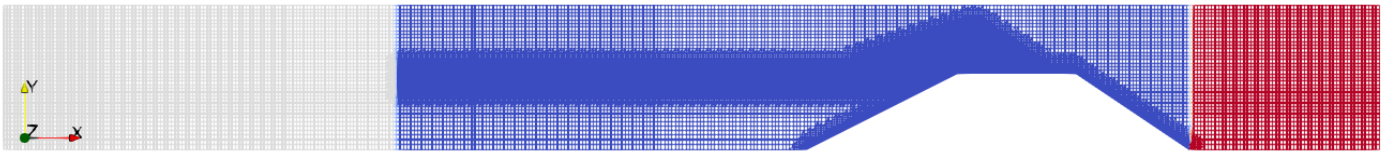

Figure C- 14. Configuration of the numerical flume with an impermeable breakwater (test with ID Th00402d). The gray and red regions indicate the relaxation zones.

C.3.1. Method 1: Discharge sheets and wave gauges

This method consists of computing the velocities from the division of the discharge per unit of width by the flow depth, measured at different horizontal positions on the crest, and for each computational timestep. To extract the discharges and the flow depths, discharge sheets and wave gauges were used. The discharge sheets and wave gauges were located at the same horizontal positions, at each 12 cm, from x = 16.08 m till x = 16.80 m. Section 2.2.9.2 explains the configuration that was used in more detail (see also Figure 16). Figure C- 15 presents the resulting depth-averaged flow velocities for the locations x = 16.32 m and x = 16.56 m.

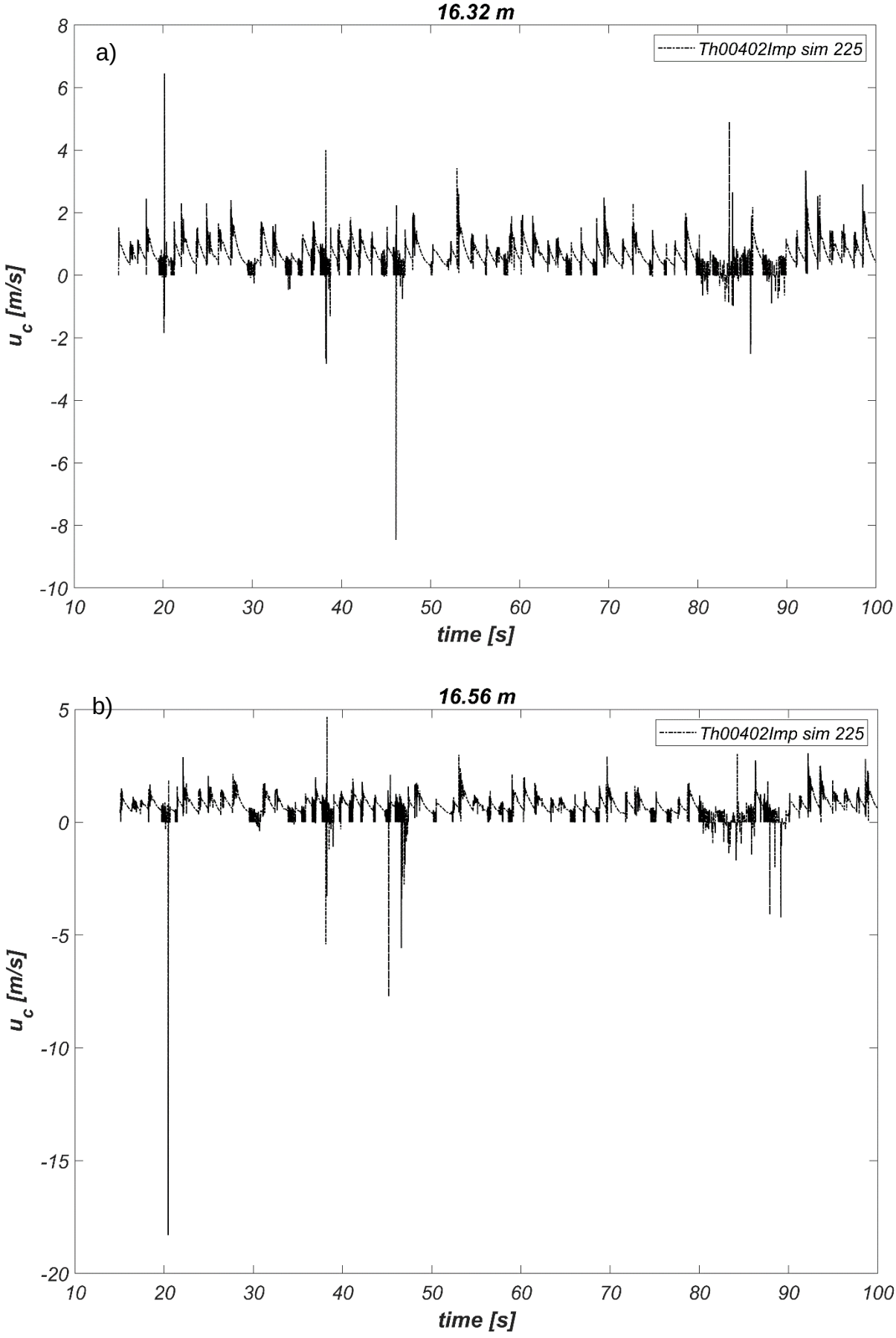

Figure C- 15. Depth-averaged flow velocities obtained with discharge sheets and wave gauges at the locations a) x = 16.32 m, and b) x = 16.56 m.

As can be observed from the previous figures, some of the depth-averaged velocities have a high non-physical magnitude. Upon detailed inspection, it was observed that they are caused by either very small flow depths, or by very high overtopping discharges. In the first case, when the overtopping discharge is divided by a very thin water layer, a very high flow velocity is obtained. In the second case, when a very high discharge is divided by a (non-small) flow depth, it also results in a very high flow velocity. Figure C- 16 shows a histogram of the flow depths obtained for all the computational times and all the wave gauges. It can be observed that there are many occurrences of flow depths close to zero, some of which are responsible for the high non-physical velocities.

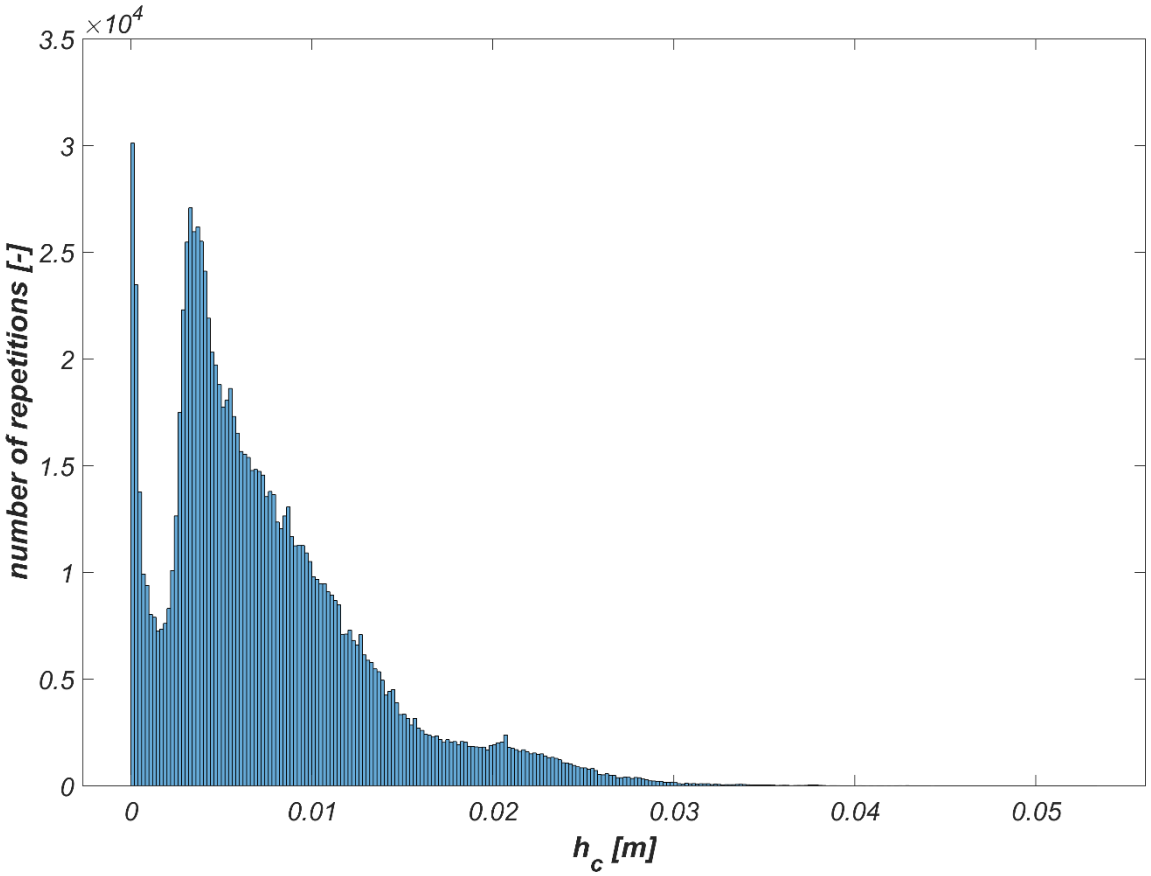

Figure C- 16. Flow depth histogram for all computational timesteps and all the wave gauges.

The output of the discharge sheets and the water gauges was requested in runtime. Therefore, it was assumed that it was possible to make the division of the overtopping discharges over the flow depths for all the horizontal positions for each computational time step since they should be extracted at the same instant of time. Nevertheless, it was decided to prove the validity of this supposition. Since there were thousands of computational timesteps, a quick way to perform the check, was to compute a histogram of the difference between the timesteps at which the flow depths were extracted and the timesteps at which the overtopping discharges were requested. The result is shown in Figure C- 17. It can be concluded that the difference is sufficiently small, and the assumption was correct.

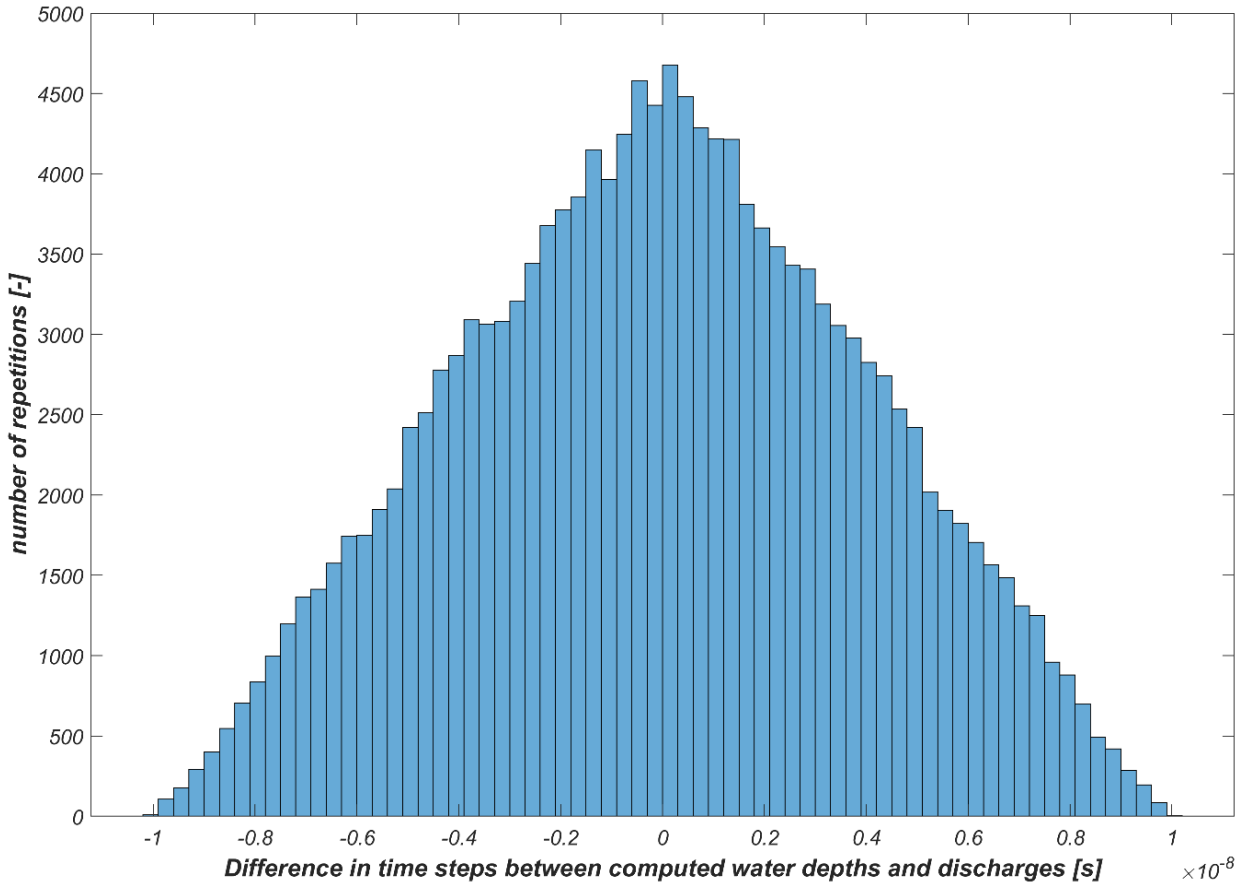

Figure C- 17. Histogram of the difference in timesteps at which the flow depths and discharges are extracted.

C.3.2. Method 2: Probes[25]

Flow velocities (in the x-direction) were extracted from specific points of the domain. For this purpose, probes were located at each 12 cm, in the horizontal direction, from x = 16.08 m till x = 16.80 m (see Figure 16). In the vertical direction they were placed at the cell centers, and from the elevations y = 0.85 m till y = 1.05 m. In a postprocessing step, the flow velocities were depth averaged. Section 2.2.9.2 provides a more detailed description of the probes' set-up, and the depth-averaging procedure. In this case, Equation 7 was used to compute the depth-averaged velocities and only the velocities for which their associated indicator function was higher than 0.7 were taken into account. In Figure C- 18 the timeseries of the depth-averaged velocities, for the case of analysis, is shown for x = 16.20 m, and x = 16.68 m. The results are presented together with the timeseries of the depth-averaged velocities computed from the planes (see section below).

C.3.3. Method 3: Planes

Planes were located at each 12 cm, in the horizontal direction, from x = 16.08 m till x = 16.80 m (see Figure 16). The velocities (in the x-direction) were extracted from the cell edges in the vertical direction. Only the flow velocities that occurred in the elevations from y = 0.85 m till y = 1.05 m were considered. In a postprocessing step, the flow velocities were depth averaged. Section 2.2.9.2 provides a more detailed description of the planes' set-up, and the depth-averaging approach (Equation 7 was used). Figure C- 18 presents the timeseries of the depth-averaged velocities, for both the planes and the probes, for x = 16.20 m, and x = 16.68 m. The maximum velocities occurring at each horizontal location for all the timesteps (total time = 100 s) is presented in Figure C- 19.

[25] Probes here refer to the numerical probes. They shall not be confused with the measuring devices that are used in physical model experiments.

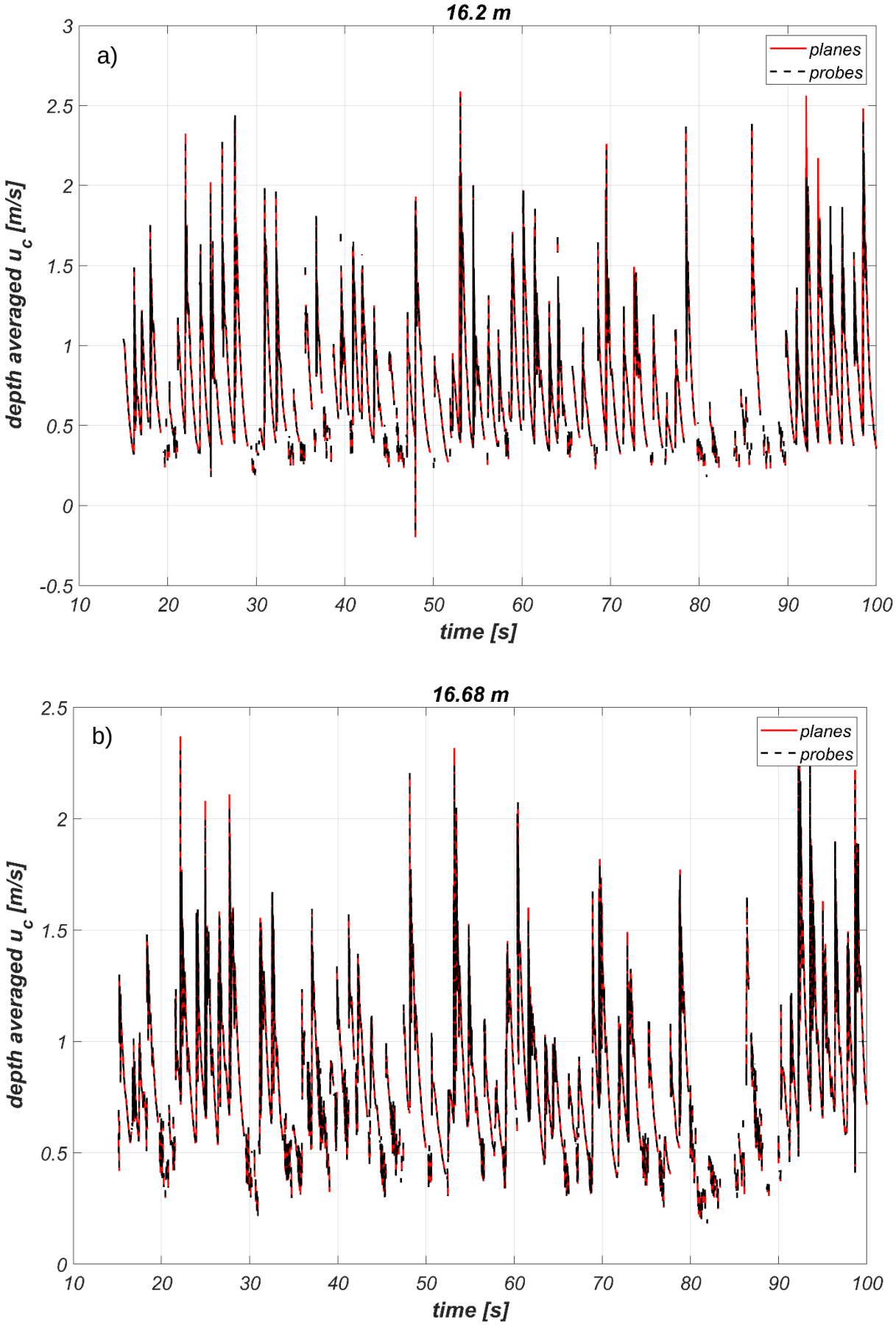

Figure C- 18. Depth-averaged flow velocities obtained with the probes and planes at the locations a) x = 16.20 m, and b) x = 16.68 m.

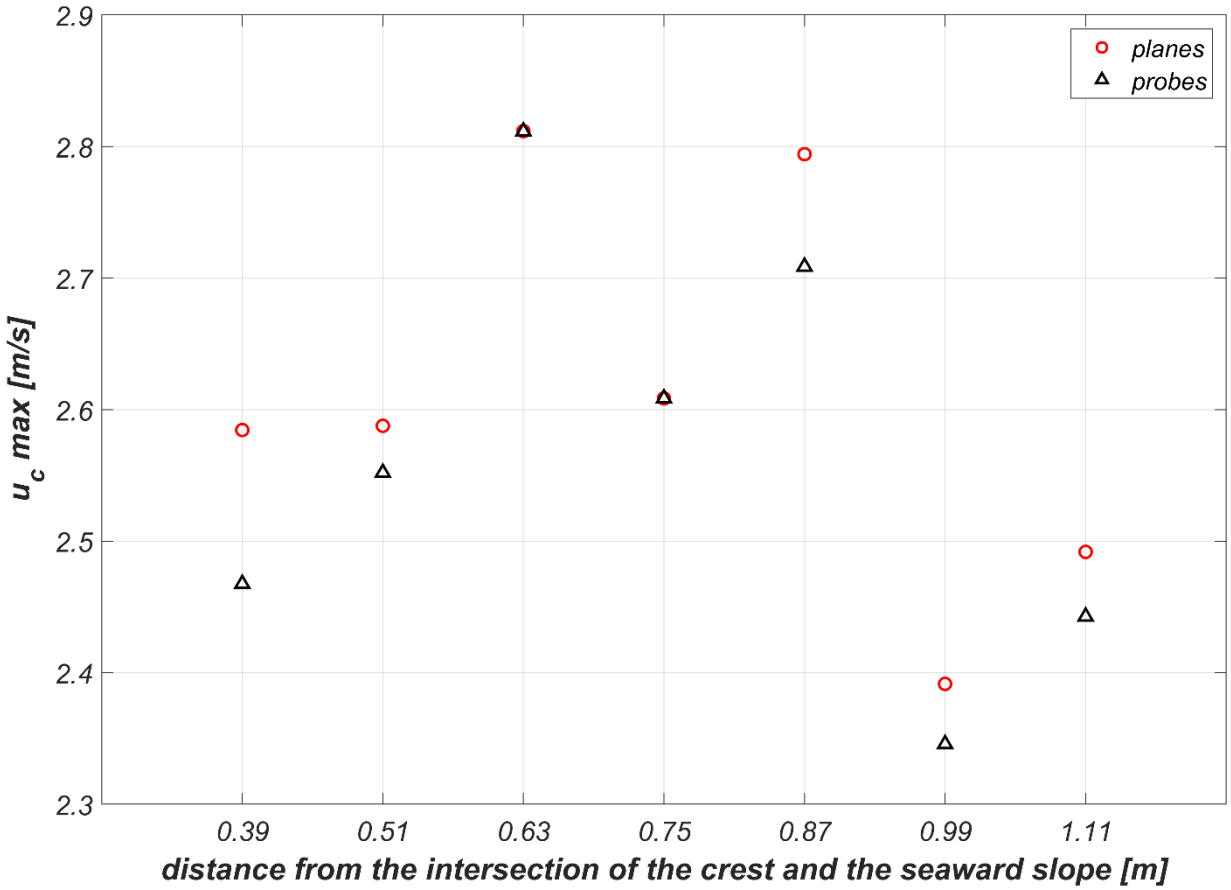

Figure C- 19. Maximum depth-averaged flow velocities at each location and for all computational timesteps. The distance is giving with respect to the intersection in between the crest and the seaward slope (x = 15.69 m, in numerical coordinates).

It can be observed, from Figure C- 18 and Figure C- 19, that the two methods produce almost the same results. There are only small differences in the magnitude of the flow velocities for some computational timesteps, and the maximum depth-averaged flow velocities are in the same order of magnitude. It seems these last two approaches are better in reproducing depth-averaged flow velocities than the first method (the one that used discharge sheets and wave gauges). Also, in the sense that when either the probes or the planes are used, the magnitudes of the flow velocities are limited (there are no overestimated velocities present). In addition, when the first method was tested, it was tried to set a low threshold limit for which smaller flow depths would be taken as zero for that instant in time. In this way, the chance of getting very high flow velocities due to very thin flow depths would decrease. The problem is the definition of this threshold value, as it cannot be based on something purely physical but numerical. Anyway, with the first method, very high non-physical velocities also occur due to very high overtopping discharges. Therefore, it is discouraged to use the first method to compute the flow velocities during wave overtopping events.

In Figure C- 19, the maximum depth-averaged flow velocities for all the computational timesteps and locations are presented. It is worth mentioning that a more robust approach to draw conclusions on the similarity of both methods (probes and planes), would have been to estimate the depth-averaged flow velocities exceeded by a certain percentage of incoming waves for each location. However, for this specific simulation, where an impermeable breakwater was used, there is so much overtopping that separating individual overtopping events is unachievable. In spite of the impossibility to compute the exceedance curve for this case, from visual inspection of the timeseries, it is clear that both methods give similar results.

Even though the probes and the planes produce the same results, there is still the need to choose which of the two methods is the desired one for future validation of the flow velocities during wave overtopping events. The answer lies in the postprocessing time of both methods. In the case of the probes, a limited number of output text files are created during the simulation. Nevertheless, when the planes are used, text files are created for each computational timestep, which results in an immense quantity of files that need to be read in a postprocessing script. For the test that was analyzed in these sections (Th00402d), and for only 100 seconds, 7.5 hours were needed to read all the files. The output of the probes could be read in a matter of minutes[26]. Thus, the selected method is the one based on the probes.

C.4. Grid sensitivity analysis for the computation of flow depths and velocities

A grid sensitivity analysis was performed on the mesh around the crest to determine its impact on the estimation of the flow depths and velocities (depth-averaged). For the computation of the depth averaged velocities, Equation 8 was used. Initially, the mesh surrounding the crest was composed of grid cells with a size $\Delta x = \Delta y = 0.005$ m. The thickness of this finest mesh was 2 cm. Such mesh (around the crest) was utilized for the sensitivity analysis concerning wave propagation, and for the validation of the incident waves and mean wave overtopping discharges. Further refinement of the grid cells around the crest was unattainable due to the substantial increase in computational time it would imply. Therefore, only three cases were considered for the grid sensitivity analysis. The first one, where the initial mesh was used ($\Delta x = \Delta y = 0.005$ m with a thickness of 2 cm). The second one, where the thickness of the finest mesh was increased. The thickness was defined as 20 cm since it corresponds to the maximum vertical distance that was taken into account for the location of the probes. For the third case, the finest mesh was completely removed from the numerical domain. In other words, the mesh around the crest is the same as the mesh around the water level ($\Delta x = \Delta y = 0.01$ m, see Table 3). Figure C- 20 shows a representation of the three variations performed in this section.

[26] When simulations are run for 1000 waves, reading the files generated by the probes can take around 1 hour or even more. Nevertheless, it is still feasible compared to reading the data generated by the planes for the same runtime, which could take several days.

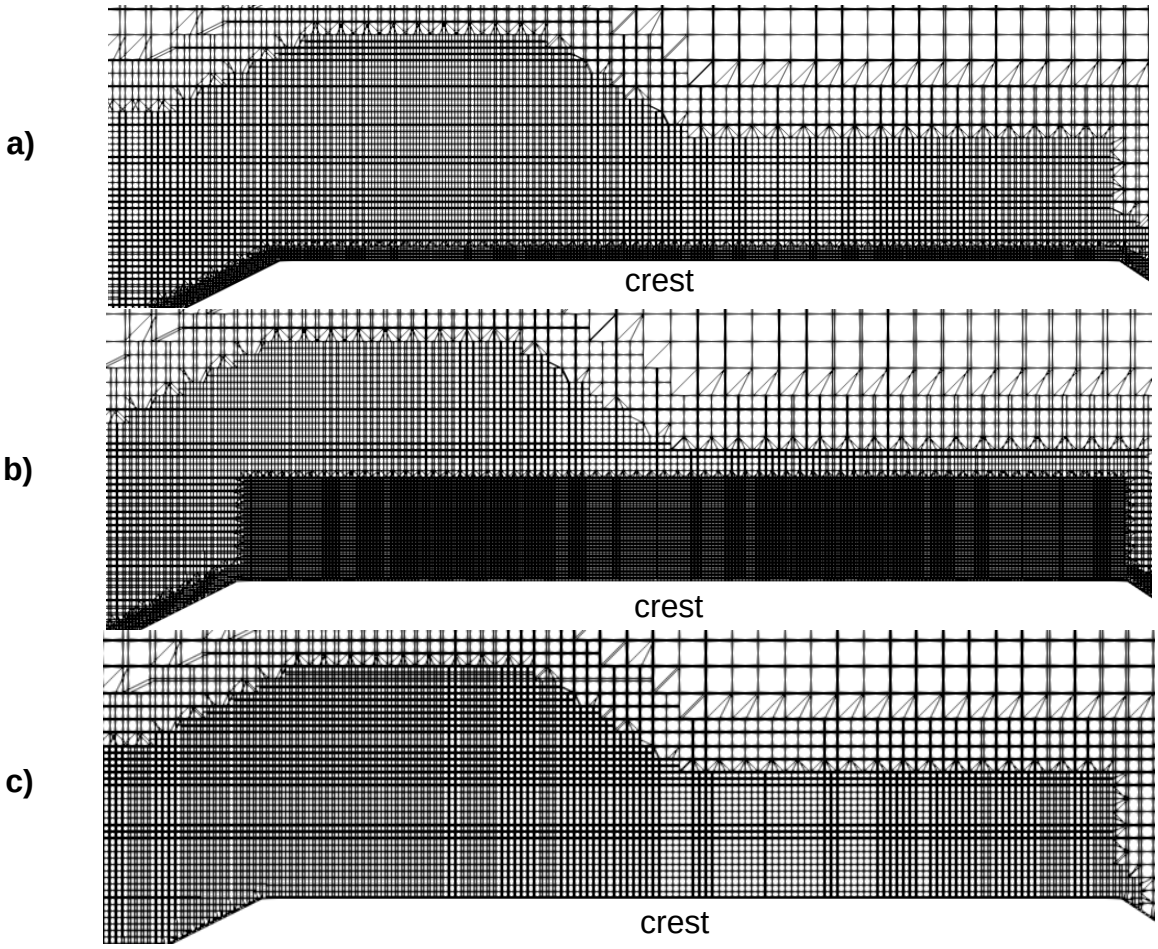

Figure C- 20. Variations in the mesh around the crest for the grid sensitivity analysis. Case with a) original finest mesh with grid cells of $\Delta x = \Delta y = 0.005$ m and thickness of 2 cm, b) original finest mesh with 20 cm of thickness, c) finest mesh removed.

The sensitivity analysis was performed with the test with ID Th00402d (H_{m0} = 0.12 m, T_p = 1.39 s, see Table 1). To reduce the computational time and get more overtopping events for the same runtime, it was decided to use an impermeable breakwater (same strategy used for section C.3). The distance between the end of the inlet relaxation zone and the toe of the breakwater was shortened, and the crest wall was removed. This set-up was no longer representative of the original conditions of the test Th00402d. However, the interest here was to capture the differences in the estimation of the flow depths and velocities when the grid around the crest element was varied. Hence, these adjustments were valid. The runs were carried out with more than 250 waves. In addition, the wave energy is not capable of penetrating the impermeable structure. For this reason, the length of the outlet relaxation zone was shortened. Figure C- 21 presents the configuration of the numerical flume used to perform the grid sensitivity analysis around the crest.

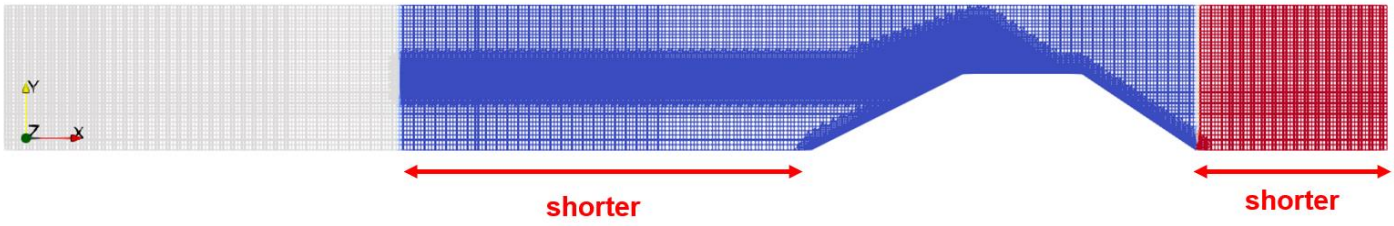

Figure C- 21. Numerical flume set-up to perform the grid sensitivity analysis around the crest. The gray and red regions represent the relaxation zones. The lengths indicated as shorter refer to the corresponding lengths of the original set-up for the test Th00402d.

Figure C- 22 shows part of the timeseries of the flow velocities extracted at the location x = 16.32 m (see Figure 16). From visual inspection, it can be observed that there is more noise in the flow velocities when they are calculated when the finest mesh is totally removed from the numerical domain. This noise is more noticeable especially when the flow velocities decrease in magnitude. On the other hand, the flow velocities follow a similar pattern when they are computed when the finest mesh is included in the domain, regardless of its thickness. This trend was also observed for other moments in time and for the other locations.

Figure C- 23 presents the maximum velocities at each location and for all computational timesteps when they are computed for each of the mesh variations around the crest. These velocities seem to be in a similar order of magnitude. Although it can also be observed that the maximum flow velocities computed when the finest mesh is removed tend to be smaller with respect to the maximum flow velocities computed when the finest mesh is included. Nonetheless, it cannot be concluded that the extremes calculated when the finest mesh is removed are, in general, smaller than the ones computed when the finest mesh is included in the numerical model. A more appropriate methodology to carry out this evaluation, would be to compute the flow velocities exceeded by a certain percentage of incoming waves (e.g., $u_{c2\%}$). However, for this particular simulation, there is so much overtopping that it was impossible to separate the individual overtopping events. Therefore, a figure showing the flow velocities exceeded by a certain percentage of incoming waves for the different locations with respect to the seaward slope cannot be presented.

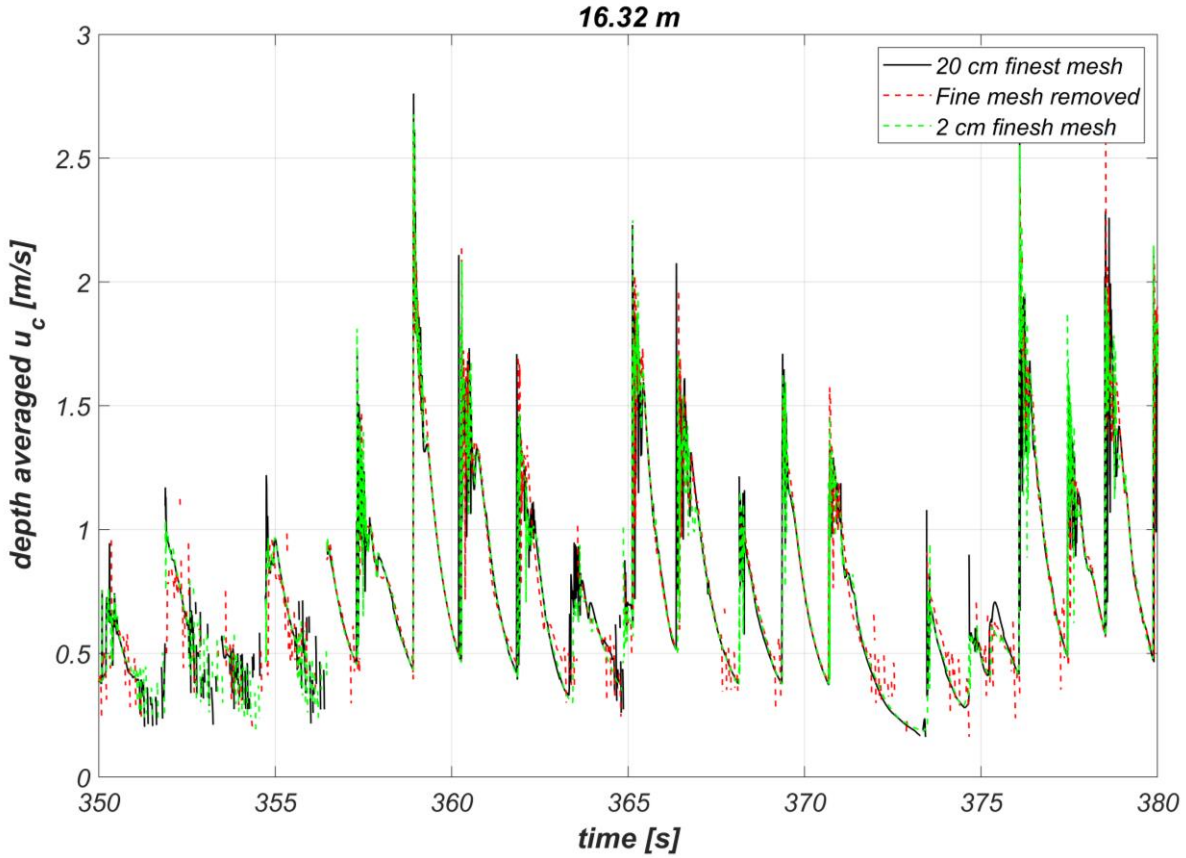

Figure C- 22. Depth-averaged flow velocities timeseries for the location x = 16.32 m with variations in the mesh around the crest of the breakwater.

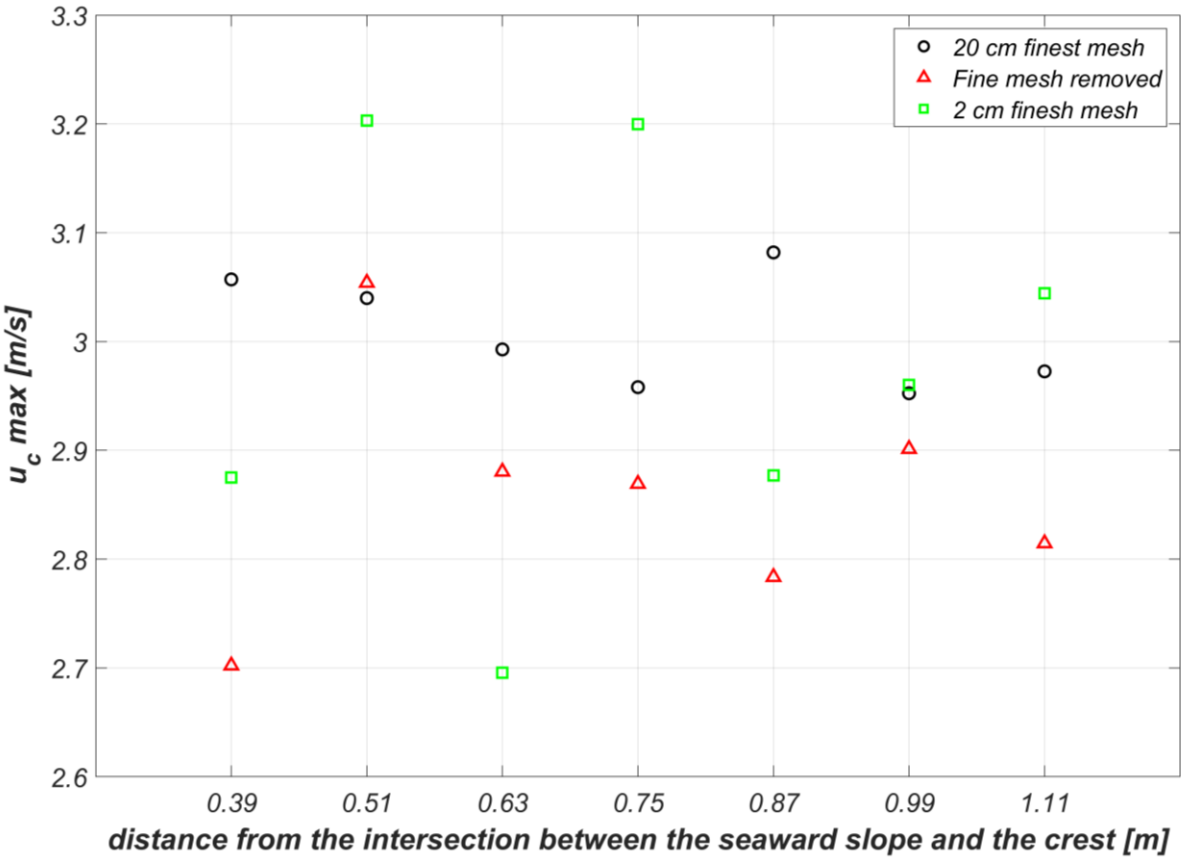

Figure C- 23. Maximum depth-averaged flow velocities at each location and for all computational timesteps. A bit more than 250 waves were considered. The distance is given with respect to the intersection between the seaward slope and the crest (x = 15.69 m).

Figure C- 24 presents part of the timeseries of flow depths extracted at the position x = 16.32 m (see Figure 16). It can be observed that, in the same manner as for the timeseries of the flow velocities, there is more noise on the computation of the flow depths when the finest mesh is completely removed from the domain. The signal of the flow depths when they are calculated with the finest mesh, either with a thickness of 2 cm or 20 cm, is similar. The same trend was observed for other locations and other moments in time.

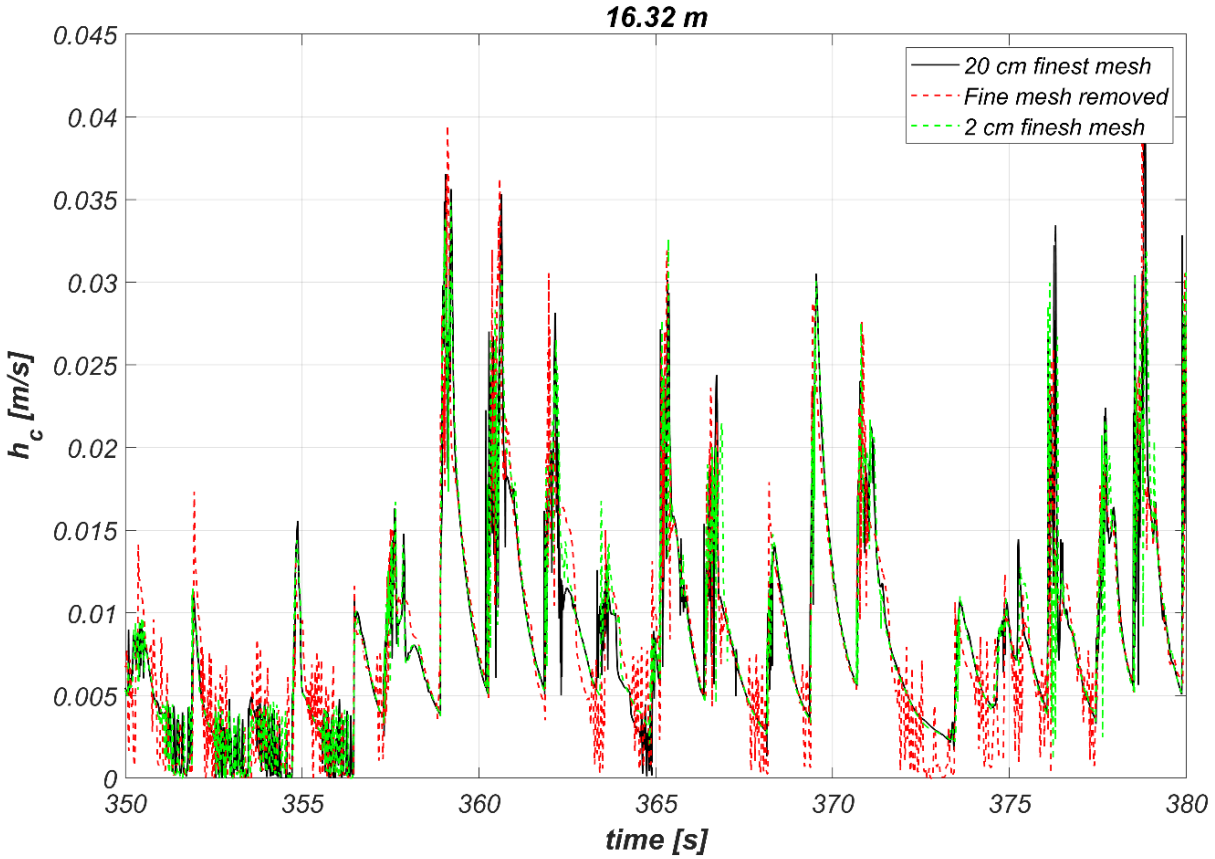

Figure C- 24. Flow depths timeseries for the location x = 16.32 m with variations in the mesh around the crest of the breakwater.

Figure C- 25 show the maximum flow depths at each location and for all computational timesteps. This time, it was not found that the maximum flow depths were smaller when the finest mesh was removed from the numerical flume. As was mentioned for the flow velocities, a better methodology to capture the behavior of the extremes due to variations in the mesh surrounding the crest, would be to calculate the flow depths exceeded by a certain percentage of incoming waves for the different locations on the crest. Nevertheless, for this simulation it was unfeasible to separate individual overtopping events. Hence, such a plot was not presented in this section.

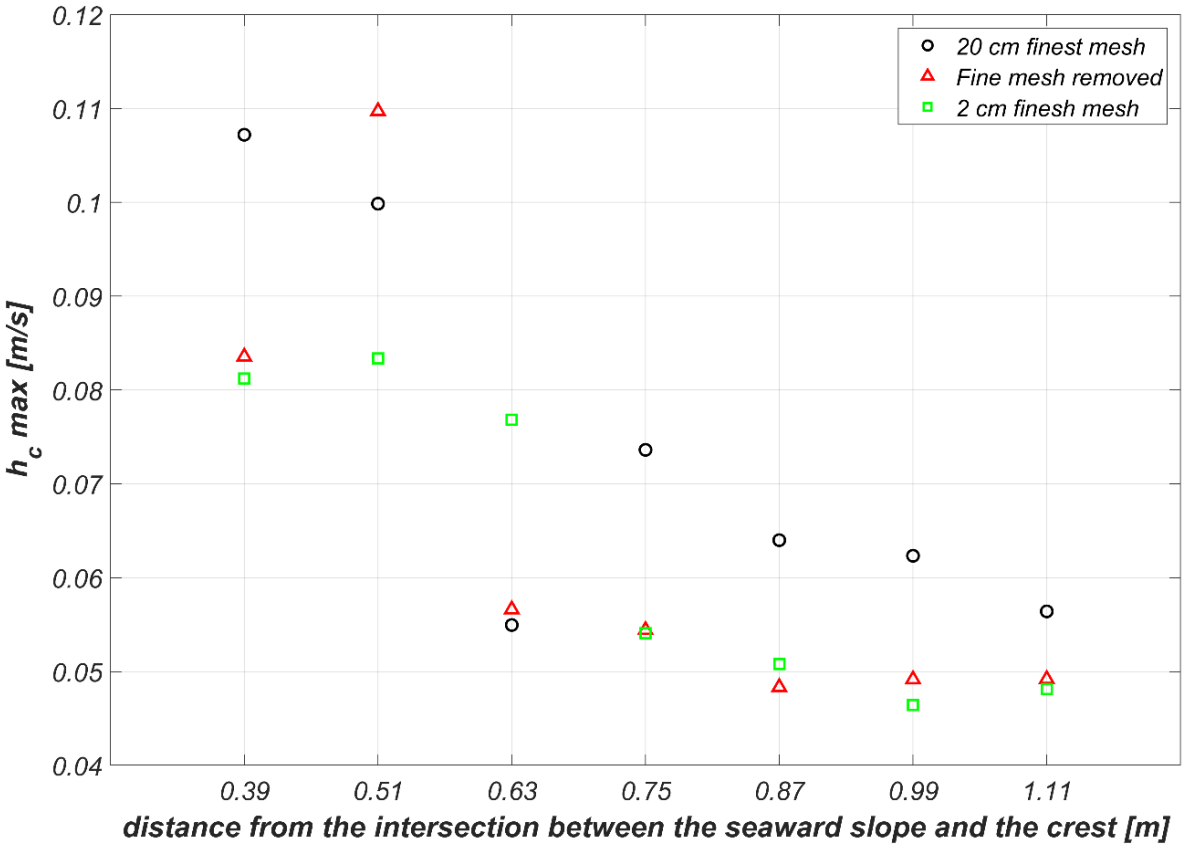

Figure C- 25. Maximum flow depths at each location and for all computational timesteps. A bit more than 250 waves were considered. The distance is given with respect to the intersection between the seaward slope and the crest (x = 15.69 m).

From the previous paragraphs, it can be concluded that it is required to incorporate the finest mesh in the numerical flume to better resolve the flow depths and flow velocities. Removing the finest mesh leads to higher inaccuracies, especially when dealing with low flow depths and velocities. Although it was not possible to verify it with a more robust method (e.g., by computing the flow depths and velocities exceeded by a certain percentage of incoming waves for all the horizontal positions on the crest), removing the finest mesh might also affect the computation of the extreme flow depths and velocities. When the finest mesh was kept in the numerical domain, but the thickness was varied, not significant differences were observed in the timeseries signal. Using a thicker finest mesh (20 cm) increase the computational time of the simulations. Therefore, the option that allows a better balance between accuracy and computational efficiency is the one where the finest mesh is kept but with the thickness of 2 cm (the original set-up).

D. Comparison between measured and computed wave energy spectra

In this section, a visual comparison is made between the measured and computed wave energy spectra (see Figure D- 1 and Figure D- 2). In general, differences can be observed in the peak of the spectrum, but also in the concentration of energy in different parts of the spectrum. More energy in the frequencies smaller than the peak frequency and less energy in the frequencies higher than the peak frequency are responsible for the overestimation of the spectral wave period in the numerical simulations.

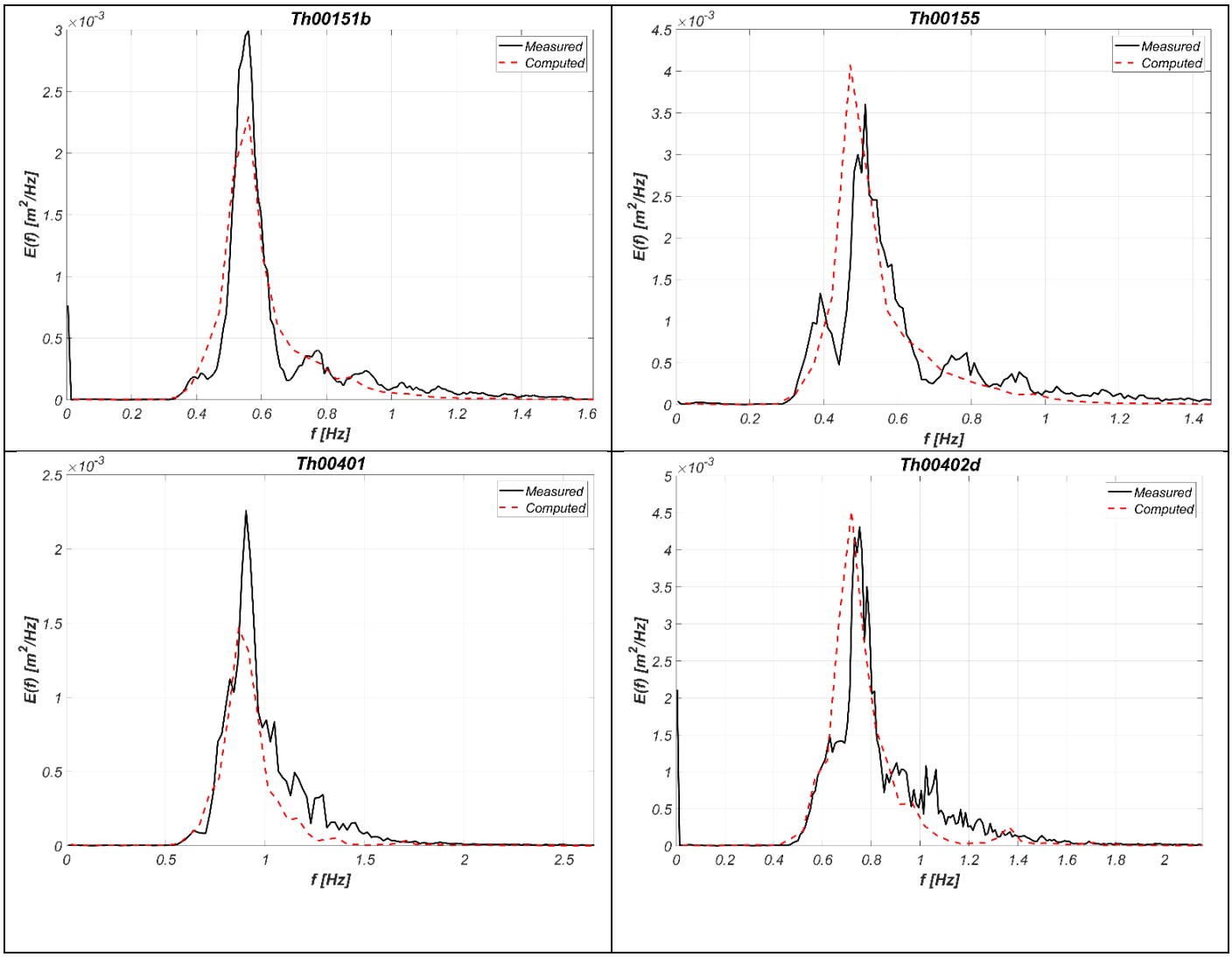

Figure D- 1. Comparison of measured and computed wave energy spectra associated to the breakwater configuration without the berm. The ID of the tests is indicated above each plot.

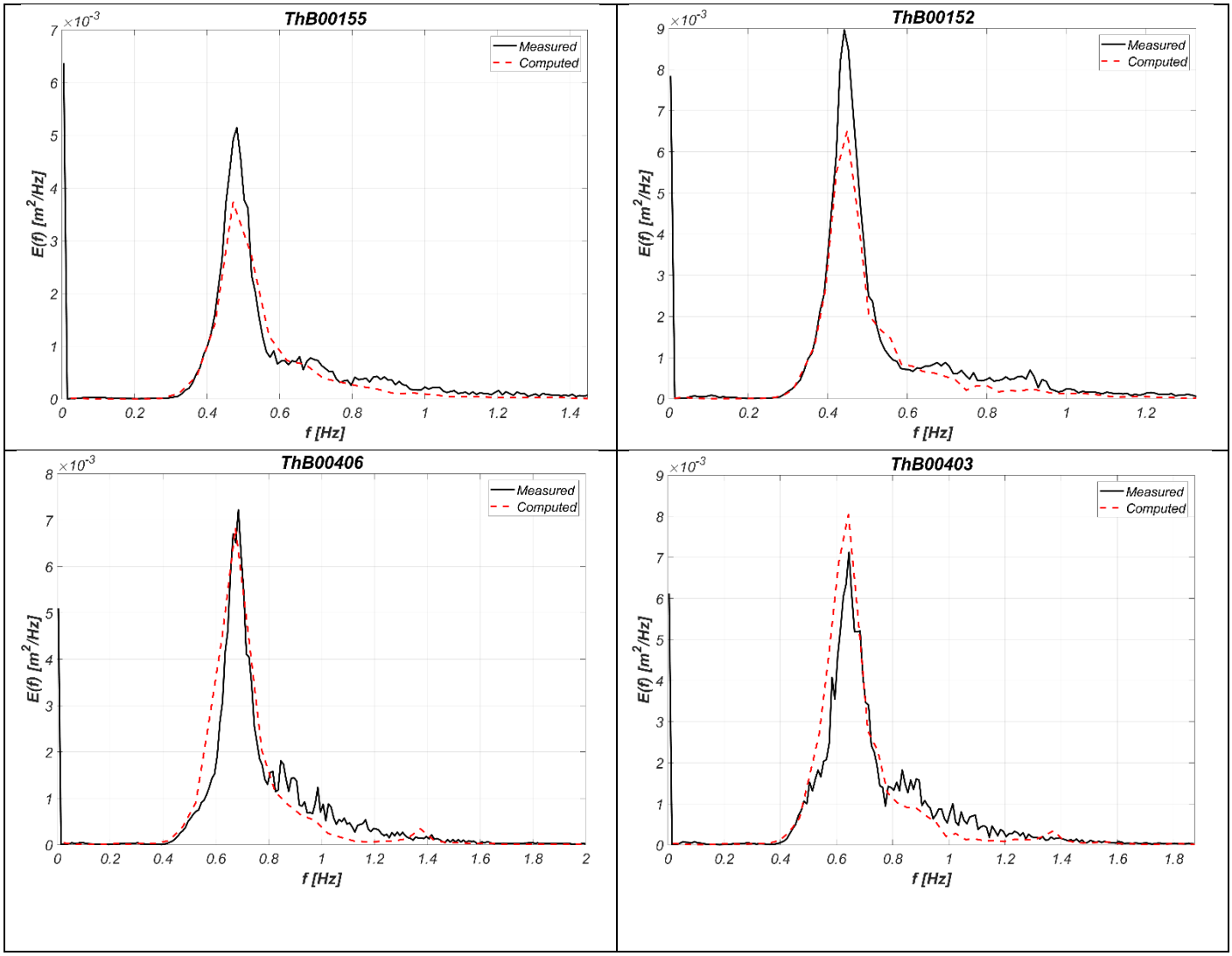

Figure D- 2. Comparison of measured and computed wave energy spectra associated to the breakwater configuration with the berm. The ID of the tests is indicated above each plot.

E. Additional results concerning the numerical modelled flow depths and velocities

E.1. Incapability of the numerical model to resolve thin flow depths

For the simulations carried out with the smaller wave height (Hm0 = 0.08 m), only a few events were able to overtop the breakwater crest wall. For some of these events, the flow depths couldn't be solved by the numerical model because they were very thin. As the energy gets dissipated as the events move along the crest and the flow depths decrease even more, this problem gets aggravated. See Figure E- 1 below.

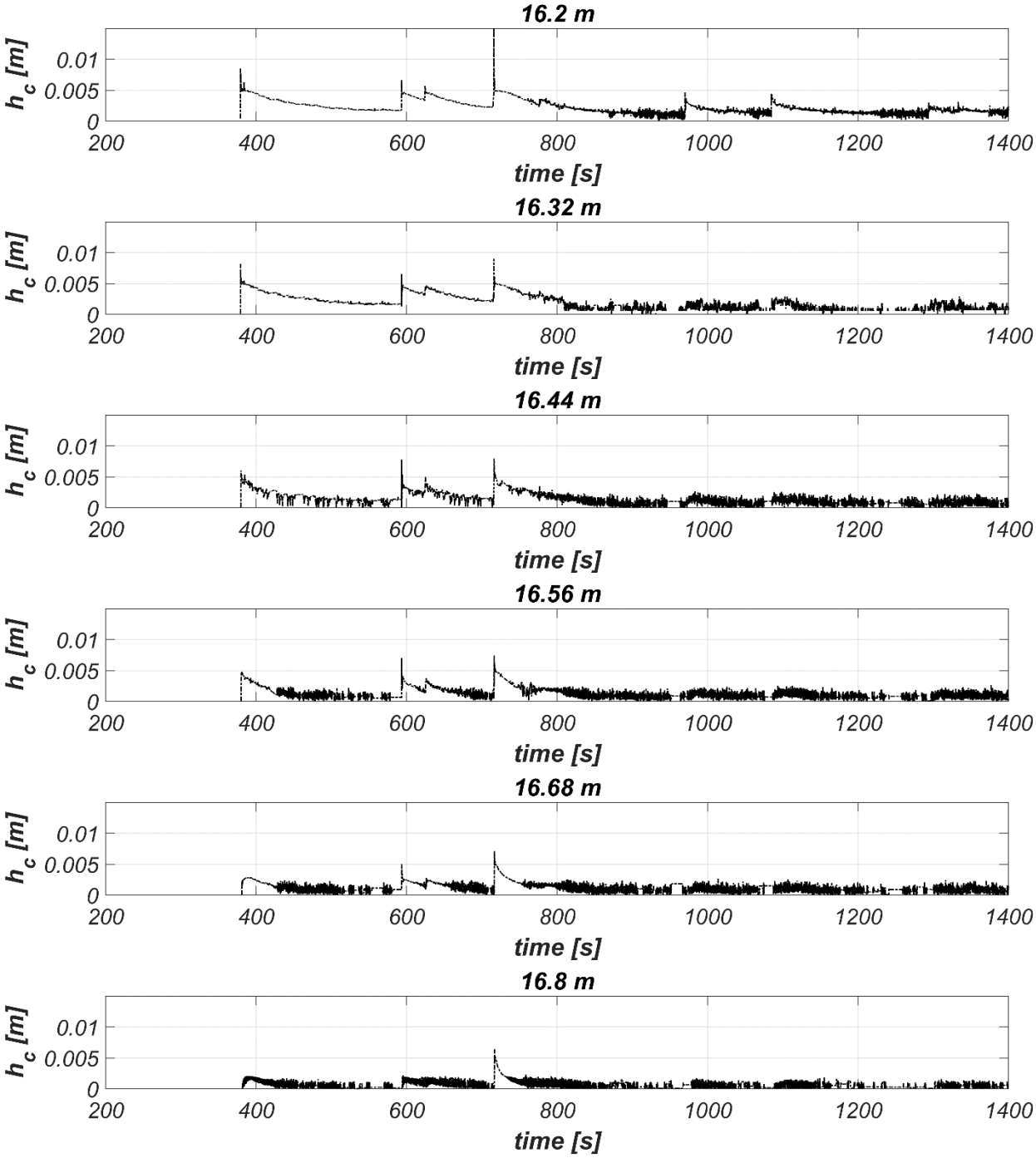

Figure E- 1. Flow depth timeseries at different locations with respect to the vertical component of the crest wall. Case with H_{m0} = 0.08 and s_{op} = 0.027. The timeseries at x = 16.08 m is not shown.

E.2. Additional aspects regarding the computation of flow velocities

While inspecting the hydrodynamics of the numerical flume during wave overtopping events, it was found that high air flow velocities occurred. These flow velocities were even higher than the ones from water. Also, sometimes non-physical droplets appeared high in the numerical domain. These represented additional reasons to use a filtering to postprocess the water flow velocities. Air and the non-physical droplets usually had low indicator functions associated to them. Therefore, a minimum indicator function of 0.5 was considered appropriate to take the flow velocities into account for the depth-averaging process (see 2.2.9.2). The two figures below present examples of non-physical droplets and high air flow velocities.

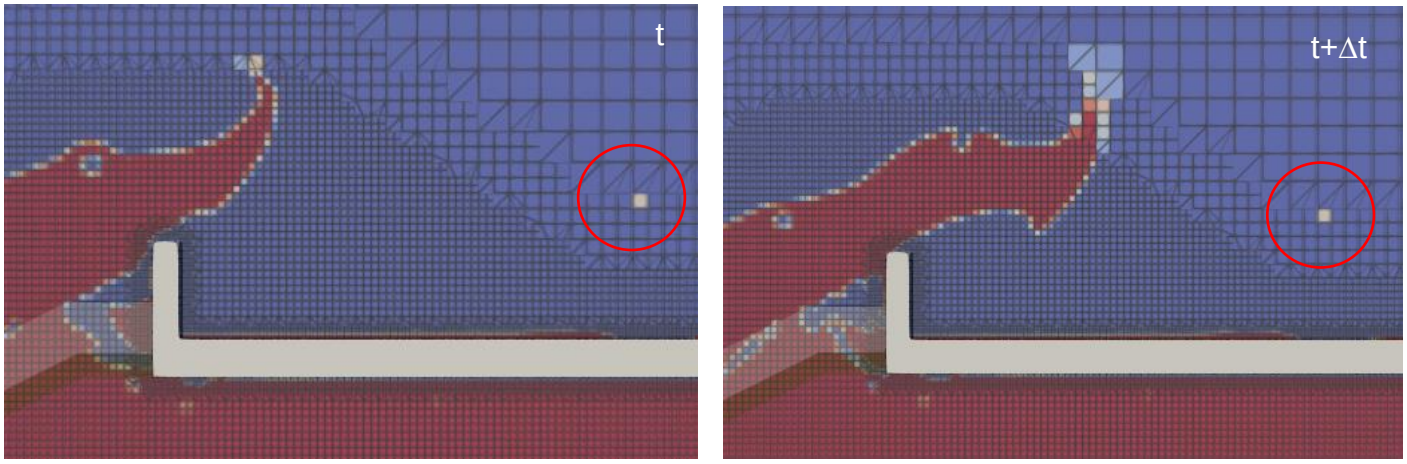

Figure E- 2. Example of non-physical droplet. Simulation with H_{m0} = 0.16 m and s_{op} = 0.015. The regions with less opacity indicate the armor and filter layers.

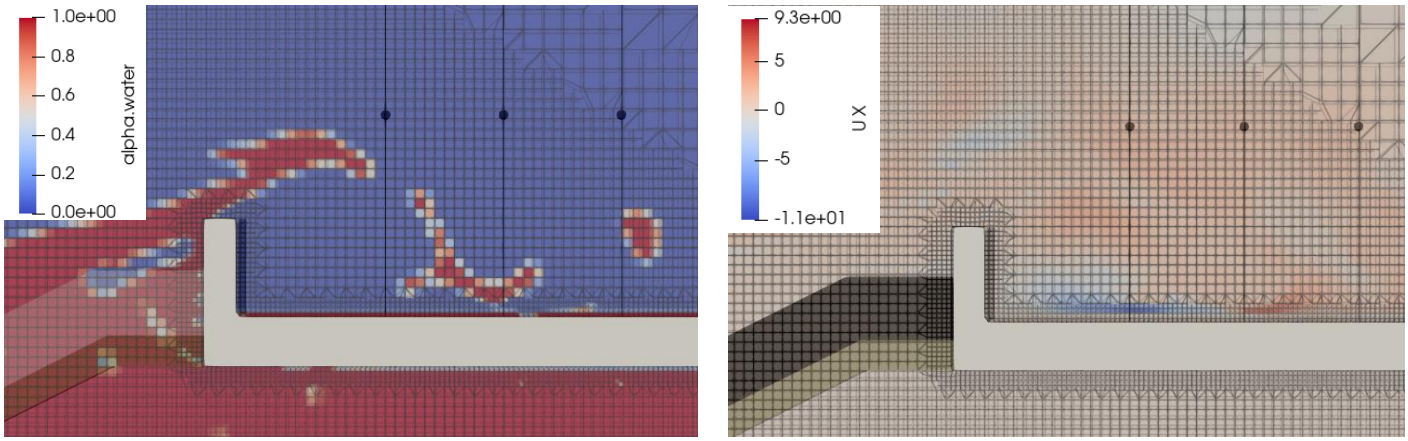

Figure E- 3. Example of high air flow velocities. Simulation with H_{m0} = 0.16 m and s_{op} = 0.04. The black lines and the black dots show the position of the wave gauges and highest probes. The regions with less opacity indicate the armor and filter layers.

E.3. Consistency check in the flow depth and velocity timeseries

It is indispensable to ensure that the flow depth and velocity timeseries are consistent. In other words, the events that are captured in one of them should also be present in the other one for the same moments in time. To tackle this requirement, it was decided to plot the discharge, the flow depth and velocity timeseries at each location with respect to the vertical part of the crest wall. The discharge was measured only at one position (on top of the vertical component of the crest wall). Figure E-2 presents an example of these type of figures. It was obtained specifically for the simulation with H_{m0} = 0.08 m and s_{op} = 0.015, at the location closest to the vertical part of the crest wall (x = 16.08 m). In this occasion, there are limited overtopping events. For this reason, it was feasible to plot the entire duration of the simulation. It can be observed that for the most part, the

three time signals are consistent. Upon further inspection, it can be observed that a large discharge or flow depth does not necessarily produce a large flow velocity. This supports the finding presented in Mares-Nasarre et al. (2019), which states that the flow depths and velocities with the same exceedance probability are not correlated.

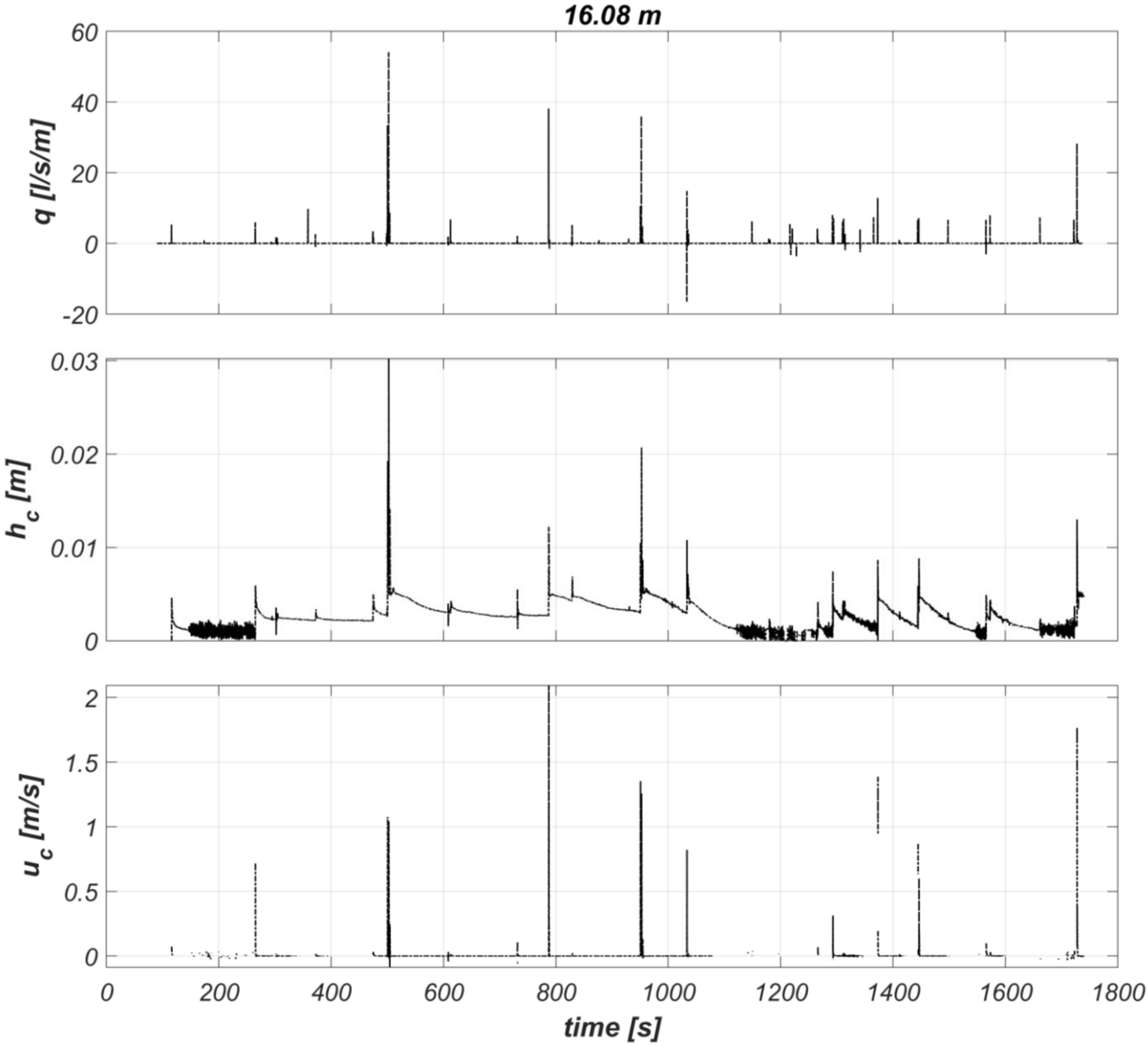

Figure E- 4. Comparison between the discharge, flow depth and velocity timeseries for the simulation with H_{m0} = 0.08 m and s_{op} = 0.015.

Figure E-3 presents a portion of the flow depth and flow velocity timeseries for the simulation with H_{m0} = 0.16 m and s_{op} = 0.015 (for x = 16.20 m). The peak flow depths and velocities are highlited through vertical lines, in red and green, respectively. In this case, since there were much more overtopping events, presenting the entire time signal was not feasible. For the specific zoom in shown below, it can be observed that the events are captured around the same moments in time for both, the flow depth and velocity timeseries. It can also be observed that the peaks do not happen at the same time (there is a timelag in between the red and green lines). Mares-Nasarre et al. (2019) also found, from physical model tests, that the peaks of the flow depths and velocities do not occur simultaneously.

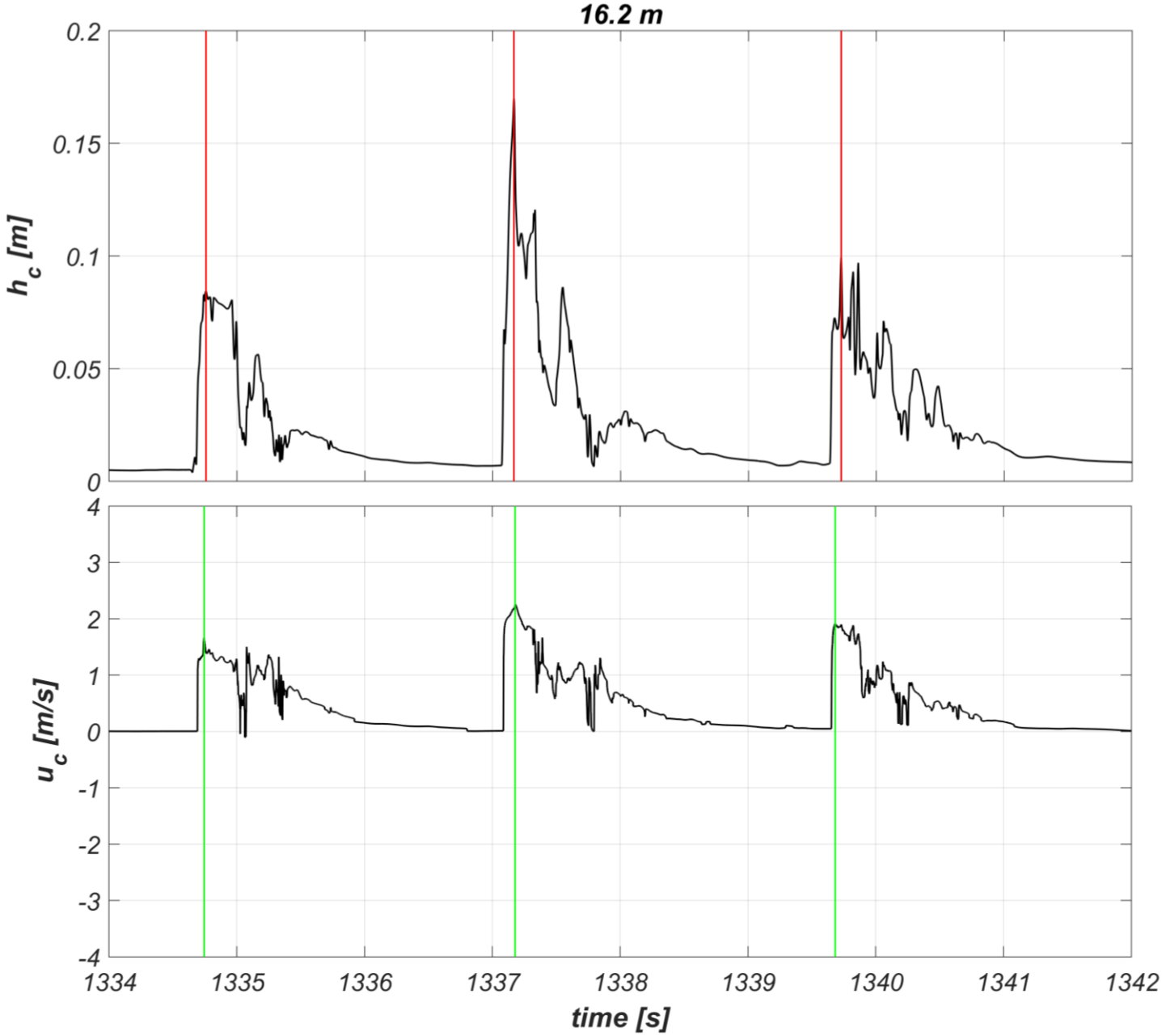

Figure E- 5. Comparison between the flow depth and flow velocity timeseries for the simulation with H_{m0} = 0.16 m and s_{op} = 0.015. The peak flow depths and velocities are highlighted with vertical lines, in red and green, respectively.

E.4. Observed trends from flow depth timeseries with and without protrusion

In section 5.3, it was explained that for the events with high exceedance probabilities it was possible to observe that flow depths are deeper when there is less protrusion in the breakwater configuration. The same conclusions can be obtained when looking at the flow depths timeseries directly. Consider for example, Figure E- 6. It shows 100 seconds of the timeseries of the simulations effectuated with Hm0 = 0.16 m and sop = 0.015 m, for the situations without protrusion ($R_c - A_c$ = 0 m), and the largest protrusion ($R_c - A_c$ = 0.08 m). The timeseries are shown for some of the measuring devices. It can be observed that for very small flow depths captured at the position located closer to the vertical part of the crest wall (e.g., around t = 244 s), the flow depths are smaller when there is a larger protrusion. In subsequent panels, and for increasing distances with respect to the vertical component of the crest wall, these small flow depths decrease even more. On all occasions they are thinner when there is a higher protrusion. In these circumstances, the events impact the horizontal part of the crest element before the first measuring instrument.

For events that have a bit lower exceedance probability (e.g., around t = 210 s), their flow depths measured in the first wave gauges are larger when there is more protrusion. Nevertheless, in subsequent panels, the flow depths decrease more when there is more protrusion till a point when they are even smaller than the flow depths occurring when there is no protrusion. This happens because these events hit the horizontal part of the crest element in between the first positioned measuring devices. Once the events stabilize (into a single overtopping layer of water), the flow depths become smaller when there is more protrusion compared to when there is no protrusion. For the most extreme events (e.g., around t = 237 s), and when there is more protrusion, it can happen that they do not stabilize (into a single overtopping layer of water) on time before they reach the last wave gauge. In this case, the trends observed do not align with the expected trends once the events are propagating along the crest.

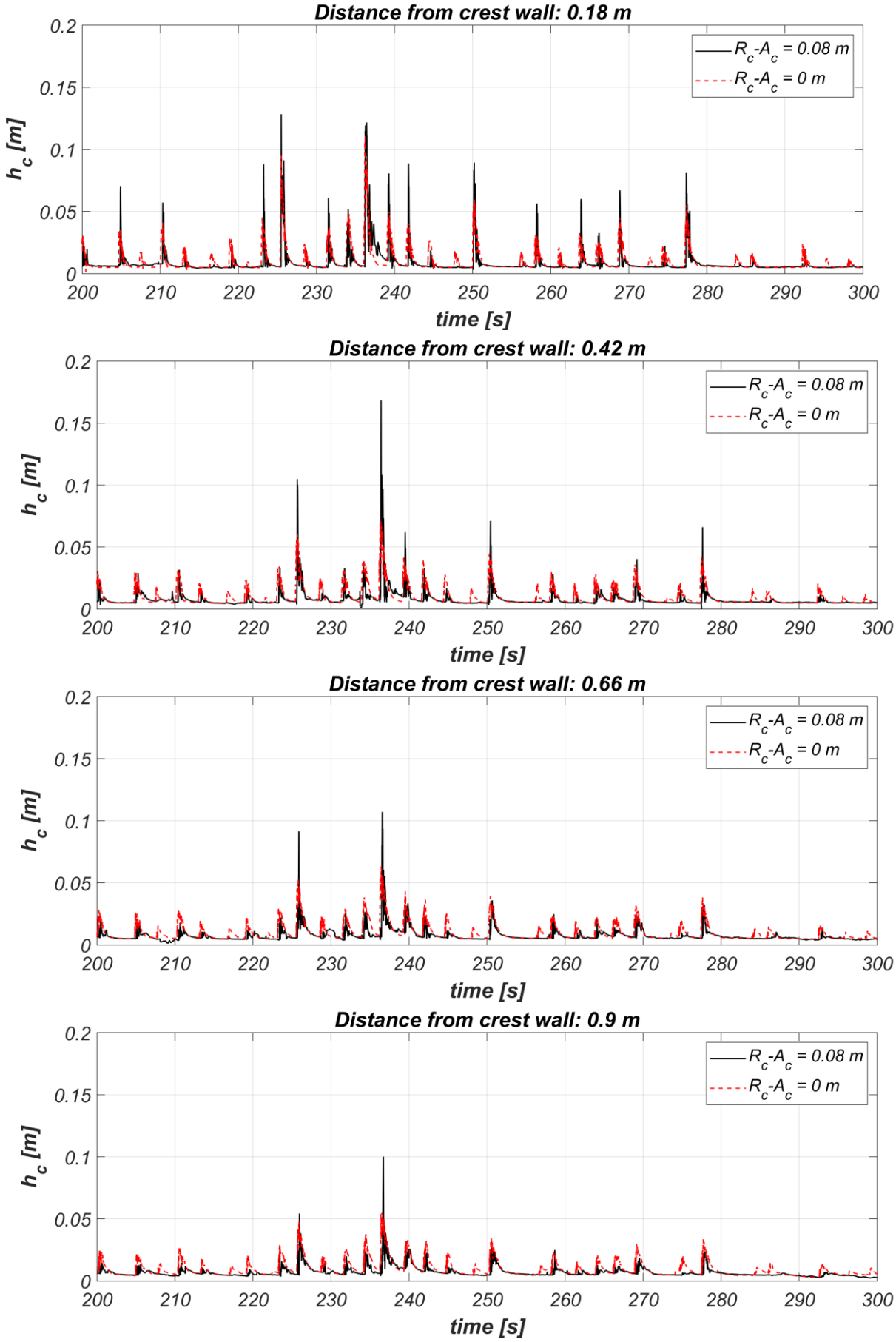

Figure E- 6. 100 seconds of the flow depth timeseries of the simulation performed with H_{m0} = 0.16 m and s_{op} = 0.015, with and without protrusion, R_c-A_c = 0 m, and 0.08 m, respectively.

F. Modelled and measured flow depths and velocities

The objective of this section is to determine how accurate is the numerical model to reproduce the flow depths and velocities. For this purpose, exceedance curves have been computed for six physical model tests based on measured and modelled flow depths and velocities. The flow depth exceedance curves are presented in Figure F- 1 and Figure F- 2, and the flow velocity exceedance curves are shown in Figure F- 3 and Figure F- 4. The exceedance curves are presented for different locations with respect to the vertical component of the crest wall. As it was previously mentioned in section 2.2.9, it was not possible to extract the information from the numerical and physical models at the same locations. Nevertheless, the positions of the numerical instruments covered the locations of the physical measuring devices. The results from the figures below are presented, from top to bottom, for the tests with ID: Th00402d, Th00406, Th00403c, ThB00152, ThB00156 and ThB00403, respectively. The reader is referred to Table 2 for an overview of the wave conditions associated to each test.

Regarding the flow depths, the left panels of Figure F- 1 and Figure F- 2 show the comparison of the flow depth exceedance curves computed from both, the measured and modelled flow depths. The right panels show a zoom in to the exceedance curves calculated from the measurements. When focusing on the trends of the flow depth exceedance curves computed at different locations, it is observed from the numerical model results, that the flow depths decrease with increasing distance from the vertical part of the crest wall. This is the expected trend given that friction dissipates the water energy as the events move along the crest. However, the exceedance curves calculated from the measured flow depths show a different behavior (see right panels). With longer distance from the vertical component of the crest wall, the measured flow depths decrease in magnitude, they increase later, and finally, decrease again. The output obtained from both, the numerical and physical wave gauges is similar. They sum up all the water they find in the vertical, at each timestep, and reference it to a particular elevation. Since the tendency shown by the exceedance curves computed from the measured flow depths is different than expected, further analysis is needed to comprehend why this is the case.

Regardless of the differences in trends, the flow depths computed from the numerical model are several orders of magnitude larger than the measured ones. A major cause of this difference is the overprediction of the overtopping discharge. As it was previously stated in section 4.2, the computed non-dimensional mean overtopping discharge is a (bias) factor 8 of the measured one. Despite that, it does not seem to be a clear connection between this factor and the one in between the modelled and measured flow depths. The factor in between the modelled and measured flow depths varies in a wide range depending on the location with respect to the vertical component of the crest wall, and the exceedance probability. Furthermore, the low exceedance flow depths obtained from the numerical model represent a high percentage of the wave height themselves, which is not expected. It seems that the overtopping discharge itself is not the only explanatory variable for these differences. It can happen that the evolution of the overtopping process also influences the flow depths extracted from the numerical model.

The effect of the overprediction of the overtopping discharge in the numerical model was not detected only in the magnitude of the flow depths. It was also observed, from a qualitative comparison of the timeseries of the measured and modelled flow depths, that the constant thin layer of water, the one that was formed because overtopped water couldn’t infiltrate the impermeable crest element, was deeper in the numerical simulations than in the physical model tests. In addition, more events were captured in the numerical model.

Concerning the computation of the flow depth exceedance curves of the physical model tests, it was observed that the constant thin layer of water varied in magnitude depending on the position of the layer thickness gauge pins. If a constant threshold would have been defined for all the pins, for the

locations with larger constant thin layers, more events would have been captured. Therefore, the threshold was adjusted to the constant thin layer of water pertaining to each location. Even after modifying the threshold depending on the position, it was observed that the number of events did not always decrease for increasing distances with respect to the vertical component of the crest wall. Since the number of events is not considerably larger in any of the locations with respect to the previous one, it is assumed that this effect has a limited impact on the exceedance curves. When more events are captured, it enlarges the exceedance curve on the left, which is the part associated with high exceedance probability events. As a trial, the constant thin layer of water was removed from the timeseries. The resulting exceedance curves didn’t change appreciably with respect to the ones presented in Figure F- 1 and Figure F- 2. In addition, even though the threshold was defined to be at least of 5 mm, it can happen that the sector of the exceedance curves associated with high exceedance probabilities is influenced by scale effects.

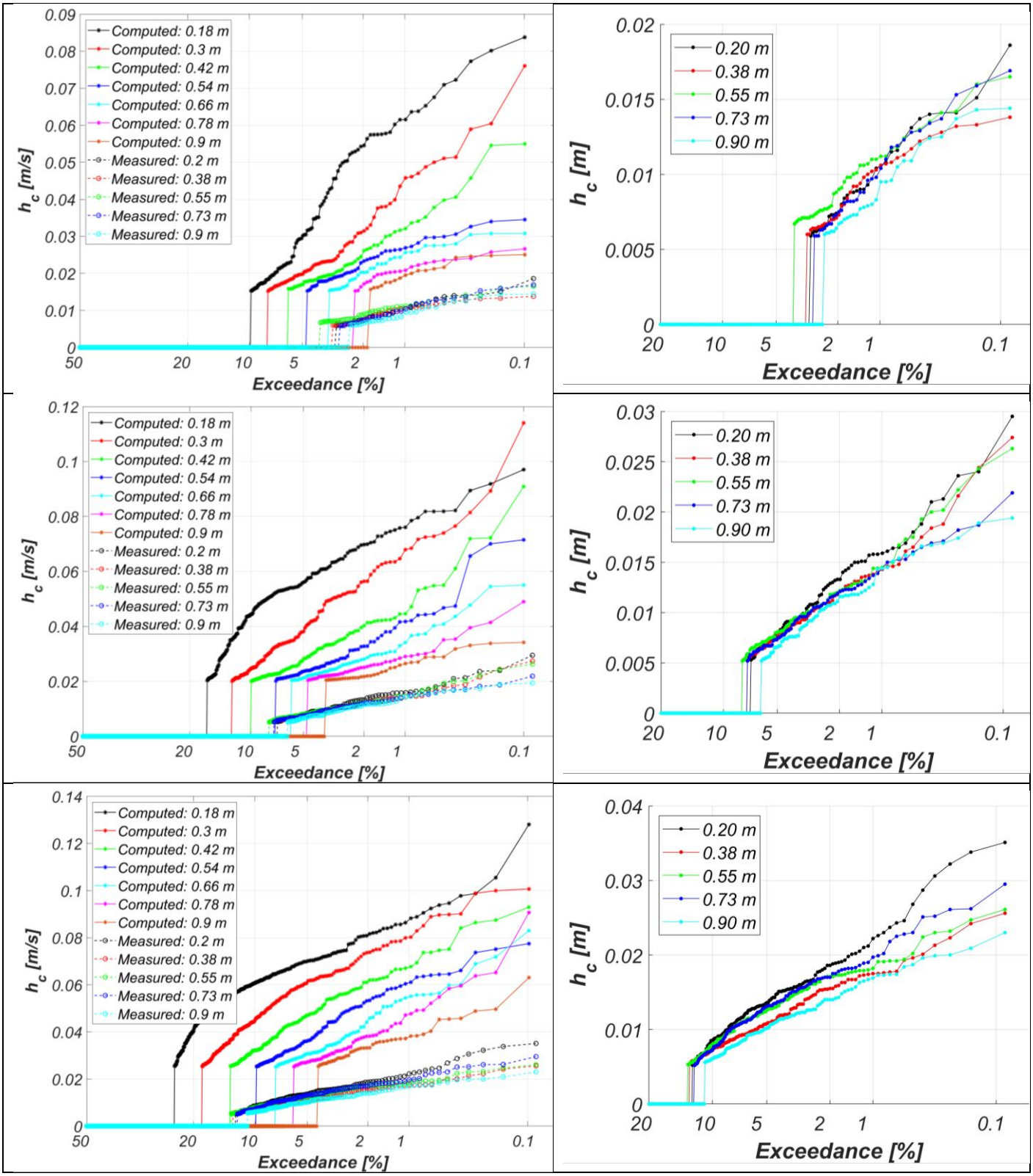

Figure F- 1. Comparison of exceedance curves obtained from the measured and simulated flow depths (left panels). The right panels show a zoom in to the exceedance curves computed from the measurements. The labels indicate the distance with respect to the vertical part of the crest wall.

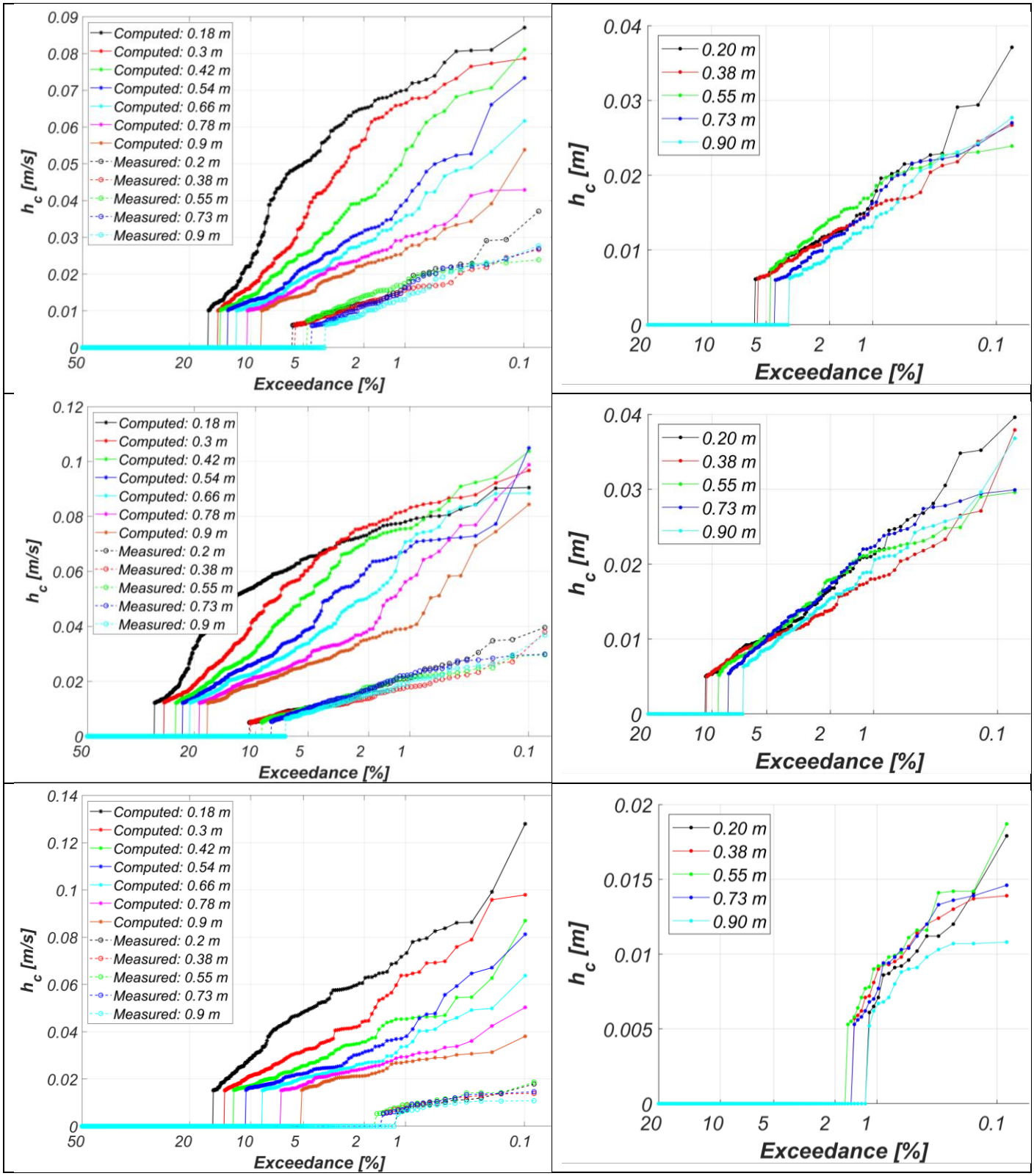

Figure F- 2. Comparison of exceedance curves obtained from the measured and simulated flow depths (left panels). The right panels show a zoom in to the exceedance curves computed from the measurements. The labels indicate the distance with respect to the vertical part of the crest wall.

With respect to the flow velocities of the physical experiments, it was previously mentioned in section 5.1, that they were estimated based on the time it took for the events to move from one pin to the other in the layer thickness gauge. For a particular pin location, it was verified that an event would have passed through the previous pins (the ones towards the seaward side with respect to the pin in question). Otherwise, the event would have not been considered as valid. Given the method of computation of the flow velocities, they were representative of the positions in between pins. Since the layer thickness gauge was composed of five pins, the velocities are associated to four locations only. The comparison between the flow velocities extracted from the numerical model and the physical model tests is carried out in terms of exceedance curves. The results are presented in the left panels of Figure F- 3 and Figure F- 4. The right panels of the same figures show a zoom in of the exceedance curves computed from the simulated flow velocities, specifically the high exceedance probability part.

The exceedance curves calculated from the measurements show a behavior such that the flow velocities decrease the longer the distance is with respect to the vertical part of the crest wall. This is consistent with what is expected since the water energy gets dissipated as the events flow along the crest. On the other hand, the exceedance curves calculated based on the modelled flow velocities show a different trend. It can be observed for the most extreme events, that with increasing distance from the vertical part of the crest wall, the flow velocities also increase till a point where they start to decrease. The flow velocities that were obtained from the numerical model were depth averaged, and this can possibly explain the difference in behavior with respect to the flow velocities of the physical model tests. For example, it was observed that negative velocities were present during the simulations. In the case of the flow velocities extracted from the physical model tests, flow in the negative direction was not taken into account. The events that occur more often in the numerical model (high exceedance probability part of the exceedance curves), also show a similar trend to the one observed from the flow velocities computed from the measurements. They also decrease with increasing distance from the vertical part of the crest wall.

When focusing on the magnitude of the flow velocities, it can be observed that for the events with a low probability of occurrence, they are larger in the physical model tests than in the simulations. The reverse situation is observed when comparing the flow velocities associated to events with higher probability of exceedance. Since the flow velocities were not directly measured during the experiments, it could happen that the accuracy of the method with which they were computed is not good enough. In addition, the influence of the overprediction of the computed overtopping discharge can also be recognized from the flow velocity exceedance curves, as more events were captured with the numerical model.

The flow velocities computed from the numerical model and the experiments are not directly comparable. The first one gives the flow velocity depth averaged at one instant in time for one location, while the second one is an average of the time it took for an event to displace in the horizontal direction. The distinct methods of extraction and computation of the measured and modelled flow velocities makes it difficult to validate the numerical model. Even with this limitation, the difference in trends, and magnitude of the measured and modelled flow depths and velocities are indicative that the numerical model is not accurate enough to reproduce them. There is a strong connection in the overprediction of the overtopping discharge and the incapacity of the numerical model to correctly model the flow depths and velocities. Despite that, the numerical model can be useful to explain the physical processes that occur during the wave overtopping events. It can also be helpful to analyze the effect that diverse wave conditions and breakwater configurations have on the flow depths and velocities.

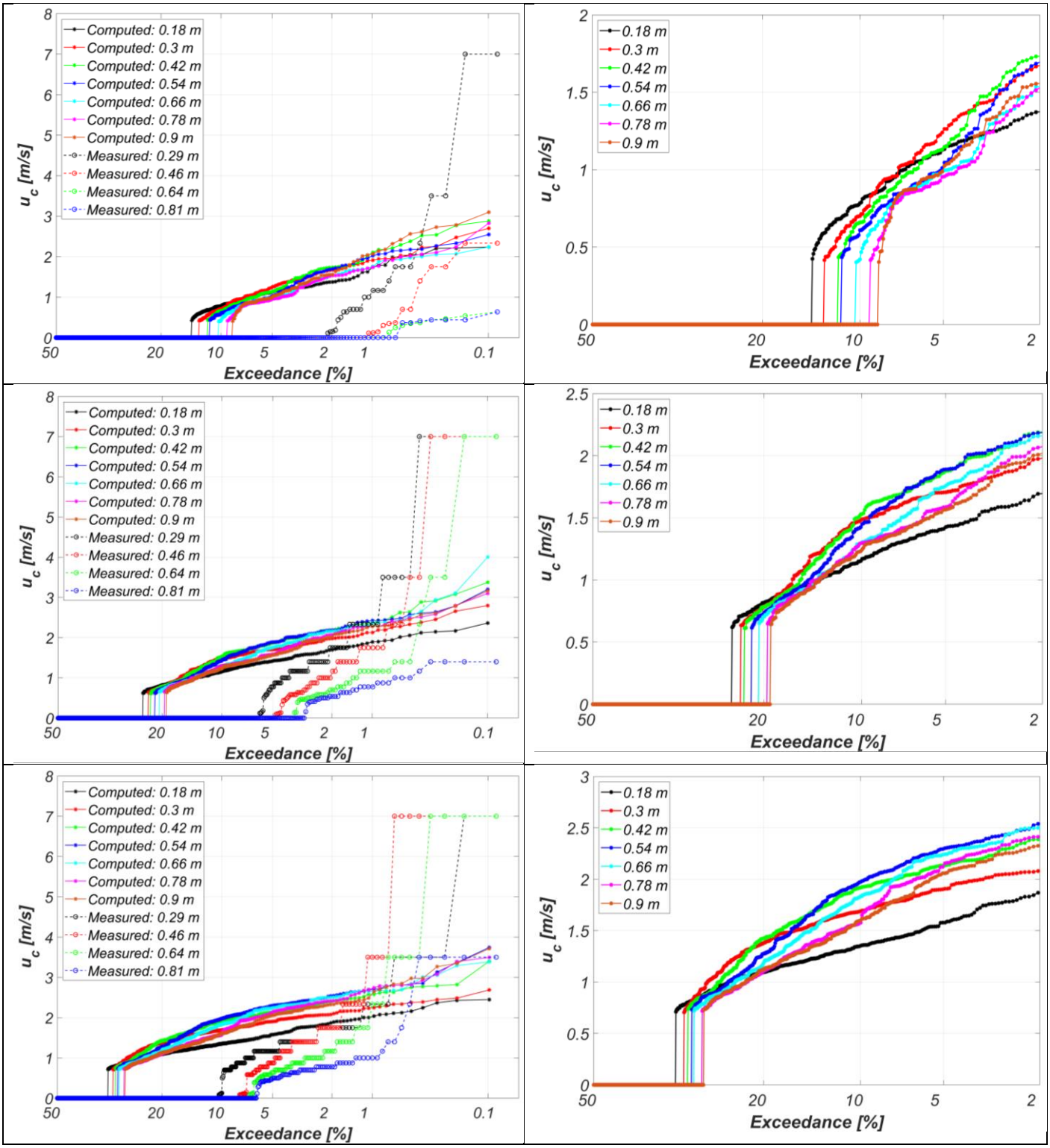

Figure F- 3. Comparison of exceedance curves obtained from the measured and simulated flow velocities (left panels). The right panels show a zoom in to the exceedance curves computed from the results of the numerical model. The labels indicate the distance with respect to the vertical part of the crest wall.

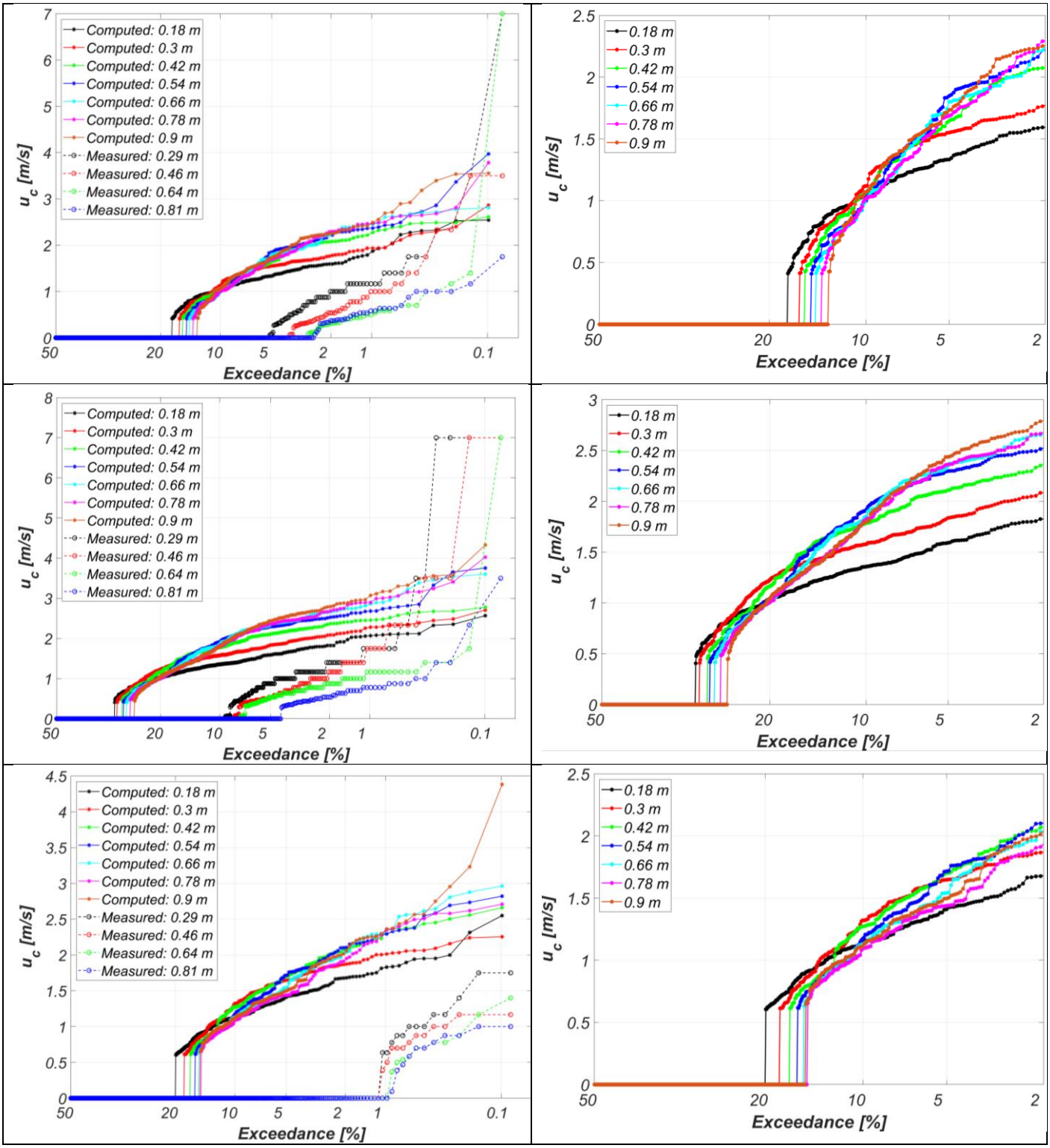

Figure F- 4. Comparison of exceedance curves obtained from the measured and simulated flow velocities (left panels). The right panels show a zoom in to the exceedance curves computed from the results of the numerical model. The labels indicate the distance with respect to the vertical part of the crest wall[27].

[27] For the computation of the depth-averaged velocities for the test ThB00152 (top panels in Figure F- 4), only the velocities and indicator functions (F) of the probes located in the first 19 cm on top of the horizontal part of the crest element were used. For all the other simulations, the first 20 cm were taken into account, as was explained in section 2.2.9. An exception had to be made for this specific test, since the memory of the computer was not sufficient to extract the information from all the probes. From the author's perspective, the omission of data corresponding to this extra centimeter is not going to change the trends in the flow velocity exceedance curves.